EXPERIMENTAL AND THEORETICAL STUDIES

OF WEAKLY BOUND COMPLEXES

A thesis submitted for the degree of

Doctor of Philosophy

of the University of Oxford

by

Andrew E. Barton

St. John's College

Trinity Term, 1980

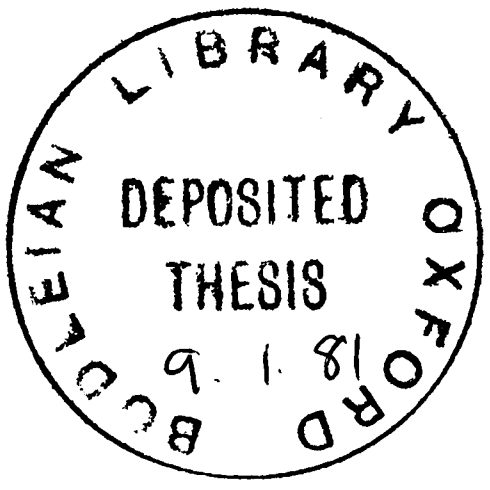

EXPERIMENTAL AND THEORETICAL STUDIES OF WEAKLY BOUND COMPLEXES

A thesis submitted for the degree of

Doctor of Philosophy

of the University of Oxford

by

Andrew E. Barton

St. John's College

Trinity Term, 1980

ABSTRACT

This thesis is concerned with some experimental and theoretical studies of weakly bound complexes. These complexes have binding energies of the order of a few kilojoules per mole, and consequently do not behave like normal chemical substances. The KrHCl complex and its isotopic forms, and NeDCl and its isotopic forms are studied in detail in the microwave and radiofrequency regions by Molecular Beam Electric Resonance (MBER) spectroscopy. The NeDCl complex is the first neon complex to be studied by microwave spectroscopy. Several new spectroscopic constants are identified from the experimental data of both systems, and all spectral features down to the resolution of the apparatus (about 1.5 kHz) have been explained. A model for the large amplitude vibrations that these complexes exhibit is proposed. Equilibrium structures and vibrationally averaged structures are subsequently derived for them.

A more thorough analysis of atom-diatomic molecule interactions is made by deriving potential energy surfaces from the experimental data for the complexes. This method is analogous to the Born-Oppenheimer separation method for electronic and vibrational motion in molecules. The new experimental parameters, particularly DQ, the centrifugal distortion of the nuclear quadrupole coupling constant for the chlorine nucleus, help to fix the amount of coupling between the bending and stretching motions of the complex on the potential energy surface. The limitations of these derived surfaces are also examined. The method is extended to diatomic molecule - diatomic molecule complexes, and a potential energy surface for one of these complexes, $(HF)_2$, is derived.

Refocussing studies on polyatomic complexes such as $(CO_2)_2$ are also presented, and the relationship between proposed gas phase structures and those of molecular crystals is discussed.

For Anne, the one who helped me most of all

Acknowledgements

This is the first D. Phil. thesis produced by a member of the molecular beams group at Oxford. I hope that it is the first of many. Grateful thanks must go primarily to my supervisor, Brian Howard, whose lively encouragement and enthusiam for all things van der Waals has been the start of many interesting studies, some of which are outlined in this thesis. Thanks are also due to Pat Langridge-Smith, and several Part II students, notably Dave Howlett, Alex Chablo, and especially Valerie Clements, who have provided a happy atmosphere in which to work over the past two years or so. Special thanks must go to Jeremy Hutson for his obsession with computers and for the use of his Born-Oppenheimer program. I am also very grateful to Peter Bosanquet for the loan of drawing equipment. Financial support by the SRC and the Physical Chemistry Laboratory is gratefully acknowledged. Last, but by no means least, I must thank my wife, Anne, without whom....

CONTENTS

		page
CHAPTER 1:	INTRODUCTION	
1.1	Bulk properties and molecular beam scattering	2
1.2	Complex formation and structure determination	5
1.3	Theoretical studies	12
CHAPTER 2:	THE MOLECULAR BEAM ELECTRIC RESONANCE SPECTROMETER	
2.1	The Rabi spectrometer	23
2.2	The source chamber: molecular beam formation	25
2.3	The buffer and main chambers: molecular beam deflection	33
2.4	The detector chamber and measurement of spectra	43
CHAPTER 3:	MOLECULAR BEAM ELECTRIC DEFLECTION STUDIES	
3.1	The carbon dioxide dimer	55
3.2	Bonding in van der Waals dimers	64
CHAPTER 4:	THE KRYPTON - HYDROGEN CHLORIDE SYSTEM	
4.1	KrHCl isotopes	72
4.2	KrDCl	92
4.3	Analysis of results	102
4.4	Charge transfer in KrHCl	116
4.5	Conclusion	120
CHAPTER 5:	THE NEON - DEUTERIUM CHLORIDE SYSTEM	
5.1	Introduction	126
5.2	Experimental	128
5.3	Interpretation of results	133
5.4	Comparison of inert gas - HCl (DCl) series	141
CHAPTER 6:	THE RARE GAS...HX SERIES	
6.1	Comparison of Ar, Kr...HX series	152
6.2	ArHI studies	159
6.3	ArHF studies	161

CHAPTER 7: THE BORN-OPPENHEIMER APPROXIMATION APPLIED TO VAN DER WAALS COMPLEXES

A. Atom - diatom complexes

7.1 Zeroth-order solution (BOARS level) 166

7.2 Non-adiabatic corrections (CBO level) 171

7.3 Convergence and isotope effects 174

7.4 Intermolecular potential surfaces from molecular beam data 175

B. Diatom - diatom complexes

7.5 The hydrogen fluoride dimer 192

7.6 Method (BOARS level) 195

7.7 Spectroscopic parameters 200

7.8 Convergence and correction terms (CBO level) 201

7.9 Results and discussion 204

APPENDICES

A. Refocussing of molecules in electric deflection experiments

B. Spin-spin and spin-rotation interactions in van der Waals molecules

C. Deuterium quadrupole effects in van der Waals spectra

D. Appendix to chapter 7

CHAPTER 1: INTRODUCTION

Chemists have recognised for a long time that long-range attractive and short-range repulsive forces exist between molecules in the gas phase[1]. These forces characterise potential energy surfaces[2], and bound states can exist in their wells for every case except possibly He_2[3]. The interactions that produce them, however, are much weaker than the normal 'chemical' type of interaction, and complex dissociation energies are usually only of the order of 1% of chemical bond dissociation energies. An extreme example of this is for $(H_2)_2$, which has a dissociation energy of 0.03 kJ mol^{-1} (2.4 cm^{-1})[4], compared with the dissociation energy of H_2 which is 432.6 kJ mol^{-1} (36,133 cm^{-1})[5]. These weak binding energies are of the same order of magnitude as kT, the thermal energy at room temperature, and so binary collisions of the complex with other species are likely to lead to the breaking up of the complex. The lifetimes of these weakly bound complexes, or van der Waals complexes as they are called, will normally be short and the study of individual complexes is likely to be difficult. Because of this the subject branches into two main areas: (i) a study of the potential energy surfaces from bulk phase measurements, and molecular beam scattering measurements of the monomer constituents of the complex; and (ii) the synthesis and study of discrete van der Waals complexes leading to an inference of potential energy surfaces. Research in the latter area has only begun in the last ten years or so, and the contents of this thesis fall into it.

An account of the two main areas will be given, emphasising the information on the potential energy surface that an individual experiment gives. For most polyatomic complexes the only information that can be derived at present is of vibrationally averaged structures, although in this thesis a potential energy surface for a diatom-diatom van der

Waals molecule is derived.

A number of interesting and comprehensive reviews have also appeared in the last few years on both the study of van der Waals molecules and the derivation of associated potential energy surfaces[6,7].

1.1 Bulk properties and molecular beam scattering

The measurement of bulk properties such as viscosity and second virial coefficients has provided the major source of experimental information for the derivation of potential energy surfaces. Unfortunately, there is a limit to the amount of information that can be extracted from such data. Whilst it is possible to derive a macroscopic quantity from a known potential energy curve or surface, by appropriate statistical averaging, the inverse route (or 'data inversion') is more difficult, and the uniqueness of the derived microscopic interaction is open to question.

Early attempts to determine intermolecular potentials were made by studying virial coefficients of inert gas pairs. The virial coefficients are defined by the equation

$$\frac{pV}{nkT} = 1 + \underset{\sim}{n}B(T) + \left(\underset{\sim}{n}\right)^2 C(T) + \ldots \qquad (1.1)$$

where $$B(T) = \frac{2\pi\alpha}{3Tk}\int_0^\infty \Delta \exp(-\phi/T)\,d\phi$$

$C(T) \equiv$ integration over 3 particles

and $\Delta = r_L^3 - r_R^3$, $\alpha = \exp(\varepsilon/T)$ and $\phi = V/k + \varepsilon$. r_L and r_R are the inner and outer coordinates of the potential energy well at ϕ, where ϕ is the potential energy (in K) measured from the bottom of the well. The second virial coefficient $B(T)$ is a function of temperature. In the high temperature region $B(T)>0$ and the dominant contributions to it come from a sampling of the repulsive wall region. At lower temperatures $B(T)<0$ and the contribution from the attractive well dominates.

Unfortunately B(T) measurements do not determine V(R) uniquely[8]. $3B(T)/2\pi\alpha$ is the Laplace transform of Δ, and only the well width as a function of depth and the repulsive region may be determined together. Also many different (though very similar) potentials can be found that reproduce the data. Theoretically only if $V \geq 0$ (totally repulsive) or $V \leq 0$ (totally attractive) would it be possible to determine V(R) uniquely (semiclassically), although recently it has been pointed out that the continuity of the function for these two parts may allow a complete inversion to be made[9]. Analyses of the inert gas - inert gas potential have been done by Smith and co-workers[10]. The data for the inert gas pairs was also of sufficient quality that the use of the simple Lennard-Jones (12-6) form was discredited[11].

Transport properties of gases provide similar data. Diffusion coefficients[12], thermodynamic properties[13], and viscosity data[14] have all been studied to determine V(R) or improve existing parameterisations. However, statistical averages are again required, for example[15] in the case of viscosity, η:

$$\eta^{-1} \propto \int_0^\infty v^7 e^{-\mu v^2/2kT} dv \int_0^\pi \sin^2\theta \frac{d\sigma}{d\Omega} \sin\theta d\theta \qquad (1.2)$$

where the first integral is a velocity average, and the second is an angular weighting average over the differential scattering cross-section, $\left(\frac{d\sigma}{d\Omega}\right)$. Trial potentials must again be used to fit the experimental data.

The addition of molecular beam scattering data has greatly improved the determination of the potentials for light atom-atom systems. Two types of information are available; differential cross-sections and integral cross-sections. The incident relative kinetic energy of the colliding pair may often be varied as well. The observation of rainbow oscillations in the differential cross-sections[16] provides information on the width of the potential well. Forward scattering, low velocity

beam data allow the determination of the long range part of the attractive well, whereas high velocity, small angle scattering provides data that sample the repulsive wall. The attractive potential may be uniquely determined in favourable cases via semiclassical techniques, for example ArKr[17], but the usual approach has been to combine scattering and bulk data in a determination of a highly parameterised potential surface and fit all the data, for example Ar_2[18] and mixed dimers[19]. The data serve to complement each other; for example, beam results usually have considerable uncertainty in the well depth, but together with low temperature B(T) data the well depth can be determined much more precisely. The use of such data allows atom-atom potentials to be determined quite precisely.

In the case of atom-molecule and molecule-molecule interactions, the potential depends not only on a single distance coordinate but is also a function of angular variables, *i.e.* a potential surface describes the interaction rather than a potential curve. Consequently it is possible to extract information not simply as a distance dependence of the interaction, but only as some angular averaged quantity. Experimentally, differential cross-sections have been measured using crossed molecular beams and the resulting data used to determine isotropic potentials for such species as ArHCl[20], and XeHF[21]. These cross-sections also contain inelastic scattering contributions, and this accounts for small discrepancies in fitting the data, but does not change the derived isotropic potentials significantly[22]. A similar approach was taken for describing the hydrogen-hydrogen interaction[23], where the anisotropic contributions to the potential energy surface are likely to be small[4]. The data for polyatomic systems, for example the Ar..CO_2 interaction[24] which is highly anisotropic has only been explained at present with fits to simple atom-atom type potentials. In subsequent years more information should become available describing both the anisotropic and

isotropic parts of the potential energy surface[25], and Buck has recently developed a method for inverting scattering data for atom-diatom systems with the diatom component having a large rotational spacing[26].

1.2 Complex formation and structure determination

The formation and study of van der Waals complexes has led to an increasing amount of high quality data becoming available for potential surface determination, especially for the more anisotropic systems. The formation and experimental study of such complexes generally falls into two main areas. These are bulk (equilibrium) studies and molecular beam (non-equilibrium) studies. Theoretical studies have also grown apace with this work.

A. Bulk gas (equilibrium) studies

The spectra of such complexes are much more difficult to obtain than the spectra of chemically bound species, because of the large bond lengths (R ~ 2-5 Å), and the small binding energies (1-20 kcal mol^{-1}). The weak binding energies make it difficult to produce relatively large concentrations of complex in equilibrium with its monomer constituents. For example, in argon gas at room temperature and 1 atmosphere pressure, approximately 0.09% of argon is in the form of dimers[27]. Increasing the pressure and lowering the temperature increases the mole fraction of dimers but it also lowers spectral resolution since, as previously stated, the strength of the van der Waals bond is of the same order of magnitude as kT (at room temperature ≡ 200 cm^{-1}), and so the complex will usually not survive a collision with a monomer before it breaks up. Thus the complex lifetime, τ_c, will be simply the time between collisions, or of that order of magnitude. In the spectroscopy between two states of van der Waals molecules the collisional linewidth will be given by[7]:

$$\Gamma\ (cm^{-1}) \simeq 4.2 \times 10^{-4}\ \sigma\rho\sqrt{T\mu^{-1}} \qquad (1.3)$$

where μ is the reduced mass of the complex, $\sigma\ [Å^2]$ ($\simeq 2\pi\hbar^2 B_{o\mu}^{-1}$) is the

total collision cross-section, B_0 is the complex rotational constant, and ρ (in amagat) is the density of the system. It will be possible to determine the complex structure only if rotation lines can be resolved, *i.e.* the rotational constant must be greater than the collisional line-width. Despite these drawbacks several studies have been successful especially in the infrared region.

(i) Infrared spectroscopy

$(HF)_2$[28] and $(HCl)_2$[29] were resolved because of the large transition probability for infrared absorption, which allowed lower pressures to be used. The binding energy of both complexes is about 10^3 cm^{-1} (see chapter 7) which also increases the collisional lifetime. The major problem in obtaining spectra for these systems is the presence of monomer spectra which overlap and swamp any dimer spectra in certain regions. This has been overcome in the case of complexes like $(HCl)_2$ and $(HF)_2$ by looking in the forbidden Q branch region. No successful spectral analyses of these spectra have yet been forthcoming, however, mainly because many vibration-rotation levels of the complex are populated at the experimental temperatures usually employed, and a great deal of overlapping of lines occurs[30].

Rank[31] and Pimentel[32] have observed transitions in ArHCl in the HCl stretching region. Again, no full analysis has been possible yet. However, the latter group have examined the temperature dependence of the intensity of the complex spectra, and derived an apparent well depth of 420 ± 175 cm^{-1}. A similar value was reported for ArHBr[33]. Several assumptions about the coupling of bending and stretching modes had to be made for both analyses, and the value is in considerable disagreement[32] with that of Farrar and Lee[20]. The discrepancy is due mainly to the incorrectness of the IR analysis, which assumed that the extinction coefficient for the complex was not temperature dependent. Re-analysis of the data by Boom[34] suggests a well depth of 100-200 cm^{-1}, essentially

in agreement with the scattering data.

The most thorough study to date of the infrared spectrum of a van der Waals complex has been by McKellar and Welsh on the X..H_2 complex, where X is an inert gas atom[35], H_2[36], N_2 and CO[37]. The advantage of this system is that hydrogen has a small mass so that B_0 will be large, and the rotational structure can be resolved despite large values of the linewidth Γ. The vibrational spectrum of the hydrogen molecule is also electric dipole forbidden, so only weak quadrupole and pressure-induced spectra are seen, and these are of comparable intensity with the spectra of the complex. Low pressures (< 1 atmos.) reduce pressure broadening effects to acceptable limits and temperatures of ~ 80 K and a 165 m path length were used to obtain the spectra. Considerable fine structure was seen due to rotation of the complex together with internal rotation of the hydrogen. Simple pseudodiatomic analyses indicated intramolecular distances (X..H_2) of ~ 4-4.3 Å. Le Roy was able to fit anisotropic surfaces to the data which included effects due to the stretching of the diatomic molecule bond[7,38].

Rather less detail has been resolved in the infrared spectra of complexes such as $(CO_2)_2$[39], and the complexes formed by O_2, N_2[40], and NO[41]. Interpretation in terms of simple structural models only has been possible. The CO_2 dimer work suggested that the equilibrium structure was T-shaped, but this proposal will be questioned in chapter 3 and another structure will be proposed. Similar structural analyses have been attempted for the hydrogen halide dimers from their diffuse spectra[29]. In contrast, Raman spectroscopy is a poor technique for studying these complexes, as the shifts from the exciting line are small and obscured by fly-by collisions[42].

(ii) Microwave spectroscopy

Structural studies and simple force constant analyses in the infrared by Thomas[43] have complemented those of Millen using microwave

spectroscopy. These studies have been mainly on the more strongly bound dimers such as HCN..HF[44], H_2O..HF[45], CH_3CN..HF[46], and $(HCN)_2$[47], and have yielded little information on potential energy surfaces.

(iii) Far infrared spectroscopy

Far infrared studies of van der Waals molecules probe directly the low frequency bending and stretching modes of the complex. Spectra have been recorded for inert gas - HCl complexes, and a tentative assignment of the spectra in terms of bending mode excitation has been made[48]. Rather more studies on rotational line broadening have been done and anisotropic potentials fitted. This technique is described with reference to KrHCl in chapter 4.

(iv) Electronic spectroscopy

Extra information on atom-atom systems has come from the electronic spectra of these complexes. Following the work of Balfour on Mg_2[49], and Tanaka and Yoshino on Ar_2[50], spectra have been observed and analysed for a variety of inert gas pairs. The spectra are usually taken in absorption since the excited state of the van der Waals species is generally more tightly bound than the ground state, and so by the Franck-Condon principle, transitions in emission will occur to the repulsive wall of the ground state, yielding continuum spectra. If both the rotational and vibrational spacings can be resolved, exact semiclassical potential curves can be determined by the RKR inversion technique[51]. The first observation of rotational structure was made on Ar_2[52]. If only the vibrational spacings are known, one RKR equation can still be used to determine the width of the potential as a function of the well depth[53]. The data is usually combined with bulk phase data to determine an improved potential curve. All the inert gas dimers have been analysed in this way, as have several alkali dimers[54-56].

B. Molecular beam studies

Dimers and higher polymers may be formed readily by an isentropic expansion through a supersonic nozzle into a vacuum. Conditions may be varied to produce either large clusters of atoms or molecules, or restricted to dimer formation (the term 'bimer' is often used to mean a system where the two component monomers may or may not be identical). Dimer mole fractions in excess of 1% have been reported for Ar_2[57,58] in expansions, as well as clusters of up to 50 argon atoms. The nature of the expansion results in all the molecules travelling with very similar velocities. This narrow range of velocities corresponds to a very low translational temperature, and temperatures less than 1 K are easily achieved[59]. Rotational and vibrational temperatures also decrease, the rotational temperature following the translational temperature quite closely, but the vibrational temperature lagging behind (~ 50-100 K, typically)[59,60]. The distributions, however, are non-Boltzmann and so the concept of 'beam temperatures' is slightly false[59,61]. The absence of collisions provides an ideal situation in which to do spectroscopy since both collisional broadening and Doppler broadening (using a perpendicular photon source) are negligible. High spectral resolution is achieved (typically, 1 part in 10^7), and the spectra are relatively simple since any species are in their lowest quantum states[62].

Levy and co-workers have utilised these advantages in their study of complexes of inert gases with iodine by crossing the molecular beam with a dye laser beam, in the technique of laser-induced fluorescence (LIF). The laser is kept near an electronic transition in the iodine molecule and the wavelength scanned. The total fluorescence at right angles to the two beams is then monitored. Levy applied this technique in an iodine-seeded helium beam at a frequency close to ~~the~~ the $B\ ^3\Pi_{o_u^+} \leftarrow X\ ^1\Sigma_{o_g^+}$ vibronic band of I_2, and obtained the fluorescence excitation spectrum of HeI_2 and He_2I_2[59]. Analysis of this indicated

that: (a) the complex predissociated in a short time (~ picoseconds) into He and I_2^* which then fluoresced, the lifetime of the upper state decreasing as the vibrational excitation of the iodine increased[63]; (b) the rotational structure of the bands indicated that the molecule had a non-linear structure in both ground and excited electronic states[64]; (c) electronic predissociation lifetimes to iodine atoms and helium were longer than predissociation and fluorescence lifetimes[64,65]. The dispersion of this fluorescence yielded valuable data on the predissociation process. It was found that the complexes generally fell apart to give iodine excited with one less vibrational quantum than the complex[66,67].

No rotational structure could be completely resolved for the heavier complexes, but the well depths of the potentials could be measured from the dispersed fluorescence spectra. The anharmonicity of the iodine potential curve means that the quanta of vibration decrease in energy as the quantum number (v) increases. Searching for the disappearance of the single quantum decay process in XI_2 (X = He, Ne, Ar) as v increased then bracketed the dissociation energy within two vibrational quanta. By this method HeI_2 was found to have a dissociation energy of 13.6-14.8 cm^{-1}[68]. This is the value of the dissociation energy of XI_2^*. To this must be added the blue shift of the fluorescence excitation spectrum which measures the difference between the ground and excited well depths. D_0 for HeI_2 is then about 18.8 ± 0.6 cm^{-1}. Levy has fitted atom-atom potentials to these results[68]. Vibrational relaxation cross-sections have also been estimated from the dispersed fluorescence spectrum[69].

Polyatomic complexes with inert gases have also been studied and well-defined structures obtained. These include He-tetrazine, He_2-tetrazine, He-benzene, He_2-benzene, and $HeNO_2$[70]. Similar studies have also been done on NaNe and NaAr[71] and Cu_2[72], with full RKR analyses

attempted. Similar studies using a two-photon ionization technique have also been described, and initial results for Na_3 reported[73].

Several other spectral regions have been explored. The use of a diode laser to obtain the infrared spectrum of $(N_2O)_2$[74] yielded a broad band which suggested a predissociation lifetime of between 10^{-12} and 10^{-4} seconds. Similar work on $(CO_2)_2$ indicates that rotational predissociation of the complex is occurring[61]. The use of a bolometer as a sensitive beam detector by these authors is expected to increase in importance.

Photoelectron spectroscopy[75], electron diffraction[76], and reactive scattering[77] have also been used to study beams of van der Waals complexes.

In the microwave and radiofrequency regions the Rabi spectrometer[78], with the advantages of a supersonic expansion source, was first used by Klemperer in the study of $(HF)_2$[79]. The spectrometer at Oxford will be described in the next chapter. Radiofrequency and microwave spectroscopy generally yield information on the vibrationally averaged structure of the complex if polyatomic in nature, but for the simpler complexes spectroscopic information can be used to determine the form of the potential near the well minimum. Structures have been obtained for the following complexes: ArHCl[80], ArHF[81], $(H_2O)_2$[82], ArClF[83], ArOCS[84], KrClF[85], HFClF[86], HFHCl[87], $ArBF_3$[88], BF_3CO[88], N_2BF_3[88], $ArCO_2$[89], XeHCl[90], ArO_3[91], ArMeCl[92], KrHCl[93], ArHBr[94], NeDCl[95], $(NO)_2$[96], N_2OHF[97] and CO_2HF[97]. Non-rigid structures are indicated for the complexes from hyperfine structure and dipole moment studies, usually because of the incompatibility of the data if rigid structures are proposed[80,91]. The properties and information content of such data is the subject of this thesis. Structural information is also available from refocussing studies, and the validity of this technique will be discussed in chapter 3.

Flygare and co-workers have developed a pulsed-microwave pulsed-beam Fourier transform spectrometer, and studied high J states (8 - 12 GHz) of KrHCl[98], KrHF[99], KrHBr and ArHBr[100]. This method is discussed further in chapter 4.

1.3 Theoretical studies

A large number of theoretical studies intent on providing information on the intermolecular potentials have grown up alongside the experimental studies. They divide into two main areas: (a) semi-classical and quantum mechanical studies either of the effects of collisions or of the dissociation of the complex; (b) *ab initio* or related studies of the structure and potential energy surface for the complex.

(i) Semiclassical and quantum mechanical studies

Whilst the potential curve for atom-atom interactions is well-defined, for more complex systems it is a function of many coordinates requiring a huge amount of information to construct a complete surface. Neilsen and Gordon[101] approached this task by developing a semiclassical method for calculating rotationally inelastic scattering cross-sections for atom-diatom collisions (classical paths, quantised rotational states). They then utilised data for ArHCl[102] that gave information about this process. These included spectral line shifting and pressure broadening, proton magnetic resonance relaxation times, Raman scattering, and rotational relaxation and sound absorption. Semiclassical evaluation of linewidths involves an integration over the probabilities of changing rotational levels for the diatom during a collision, which in turn leads to lifetime uncertainty and broadening. The proton magnetic resonance spectra of gases[103] measure T_1 and T_2 processes. They depend on the reorientation angle of the angular momentum vector produced by a

collision which depends on the anisotropic potential. Using these data with an isotropic potential from transport data enabled several anisotropic potentials to be tested. The best potentials, however, produced equilibrium structures for ArHCl which were very different from MBER results[104]. Higher quality data has since become available, and a re-analysis is necessary.

Studies of vibrational predissociation lifetimes have followed the observations that HeI_2^* ($B\ ^3\Pi$) has a lifetime of about 10^{-10} seconds which decreases on increasing vibrational excitation of the I_2 sub-unit. For $(Cl_2)_2$, however, a lifetime of $\geq 10^{-4}$ seconds was indicated[77], as was the case for ether-hydrogen bonded complexes[105]. Beswick[106] has explained the short lifetimes of HeI_2 and related species by solving the close-coupled scattering equations and relating the widths of the resulting resonances to the vibrational predissociation lifetimes. On a qualitative basis, vibrational- translational energy transfer was predicted to be inversely related to the mismatch of vibrational quantum sizes for the diatom stretching vibration and the van der Waals stretching frequency[107]. Child[108] has indicated that vibrational predissociation channels leaving the diatom in excited rotational states are favoured over simple vibrational-rotational energy transfer. Ewing has also found this for hydrogen-bonded complexes. He suggests that the predissociation process is inefficient when there is poor Franck-Condon overlap between vibrational wavefunctions which characterise the bound complex A-H*..B and the wavefunctions of the separated fragments[109].

For diatom-diatom complexes several modes of energy transfer can occur. Channels involving rotational and vibrational excitation of the products of predissociation are again favoured over simple vibration-translation energy transfer[109,110]. For $(I_2)_2$[77], the longer lifetime compared with HeI_2 is due to the poorer overlap in the outgoing translational channel with the van der Waals stretching wavefunction, due to

the larger reduced mass for the system.

The role of rotational predissociation in these molecules has been discussed[111].

Further work in the predissociation field may relate the dependence of the intermolecular potential to the eigenstate of the diatomic sub-unit.

(ii) *Ab initio* and related studies

Numerous *ab initio* studies have been undertaken to date on weakly bound complexes[112]. In the course of this thesis, reference will be made to the relevant studies that exist. Potential surfaces have been fitted to *ab initio* calculations for several complexes[113]. The work of Yarkony *et al.*[114] on a surface for $(HF)_2$ will be discussed in chapter 7. Calculations are not completely reliable due to the small differences in large quantities (monomer and dimer energies) that have to be calculated. Monomer properties are frequently badly estimated by small basis sets, and effects due to basis set superposition errors[115,116]. Some of these problems have been highlighted for the formic acid dimer[117].

A method for the solution of the large amplitude motion that these complexes exhibit is presented in chapter 7 following the work of Holmgren *et al.*[118]. Other models proposed by Sørensen[119] and Wallace[120] have been developed which describe the motion from the starting point of small vibrations. These are to be expected to work reasonably well for van der Waals complexes like KrClF but the large amplitude motions in complexes like NeDCl cannot be modelled correctly[119].

Information on anisotropic potential surfaces is therefore small at present. Most surfaces are not able to predict data from other experimental sources than the ones from which they have been derived. In this thesis the inert gas - hydrogen halide series is studied (chapters 4, 5 and 6) and the extent of motion of the complexes is indicated, from derived potential energy surfaces (chapter 7). The validity and range

of the potential surfaces is also discussed. A potential energy surface is also derived for $(HF)_2$ from the extensive data which now exists for it[79,121].

References to Chapter 1

1. J.H. Jeans, The Dynamical Theory of Gases, (University Press, Cambridge, 1904); D.E. Stogryn and J.O. Hirschfelder, J. Chem. Phys., *33*, 942, (1960).

2. Examples of such forces are multipole forces, dispersion forces and induction forces. Hydrogen-bonded complexes are included as van der Waals complexes by consensus of opinion and provide an approximate upper limit of ~80-100 kJ mol^{-1} to the binding energy.

3. Y. Tanaka and K. Yoshino, J. Chem. Phys., *50*, 3087, (1969).

4. J.F.C. Verbene, Ph.D. Thesis, (Nijmegen, Netherlands, 1979).

5. G. Herzberg, Spectra of Diatomic Molecules, (Van Nostrand, N.Y., 1950).

6. W. Klemperer, Ber. Bunsenges. Phys. Chem., *78*, 128, (1974); G.E. Ewing, Acc. Chem. Res., *8*, 185, (1975); B.J. Howard, in MTP International Review of Science, (Butterworths, London, 1975), vol. 2, chapter 3; G.E. Ewing, Can. J. Phys., *54*, 487, (1976); B. Blaney and G.E. Ewing, Ann. Rev. Phys. Chem., *27*, 553, (1976); R.E. Smalley, L. Wharton and D.H. Levy, in Chemical and Biochemical Applications of Lasers, (Academic Press, N.Y., 1977), vol. 2, chapter 1; Acc. Chem. Res., *10*, 139, (1977); W. Klemperer, Faraday Disc. Chem. Soc., *62*, 179, (1977); D.H. Levy, Adv. Chem. Phys., (1980), to be published.

7. R.J. Le Roy, J.S. Carley and J.E. Grabenstetter, Faraday Disc. Chem. Soc., *62*, 169, (1977); Adv. Chem. Phys., *42*, 353, (1980).

8. J.O. Hirschfelder, C.F. Curtiss and R.B. Bird, Molecular Theory of Gases and Liquids, (Wiley, N.Y., 1964).

9. D.A. Jonah and J.S. Rowlinson, Trans. Farad. Soc., *62*, 1067, (1966); E.B. Smith, Faraday Div. Symposium, (University College, London, 1977), Paper F.1.

10. G.C. Maitland and E.B. Smith, Mol. Phys., *24*, 1185, (1972); *ibid.*, *29*, 1759, (1975).

11. R.D. Weir, I.W. Jones, J.S. Rowlinson and G. Saville, Trans. Farad. Soc., *63*, 1320, (1967).

12. W. Hogervorst, Physica, *51*, 77, (1971); A.S. Kalelka and J. Kestin, J. Chem. Phys., *52*, 4248, (1970).

13. J.K. Lee, D. Henderson and J.A. Barker, Mol. Phys., *29*, 429, (1975).

14. D.W. Gough, G.C. Maitland and E.B. Smith, Mol. Phys., *24*, 151, (1972).

15. R.G. Gordon, Lecture notes, Oxford, (1978).

16. R.D. Levine and R.B. Bernstein, Molecular Reaction Dynamics, (Clarendon Press, Oxford, 1974), chapter 3.

17. U. Buck, J. Chem. Phys., *54*, 1923, (1971); *ibid.*, *54*, 1929, (1971); U. Buck, F. Huisken, H. Pauly and J. Schleusener, J. Chem. Phys., *68*, 3334 (1978).

18. J.M. Parson, P.E. Siska and Y.T. Lee, J. Chem. Phys., *55*, 5762, (1971); *ibid.*, *56*, 1511, (1972).

19. C.Y. Ng, Y.T. Lee and J.A. Barker, J. Chem. Phys., *61*, 1996, (1974); C.H. Chen, P.E. Siska and Y.T. Lee, J. Chem. Phys., *59*, 601, (1973); J.J.H. van den Biesen, F.A. Stokvis, E.H. van Veen and C.J.N. van Meijdenberg, Physica A, *100*, 375, (1980).

20. J.M. Farrar and Y.T. Lee, Chem. Phys. Lett., *26*, 428, (1974).

21. C.H. Becker, P.W. Tiedemann, J.J. Valenti, Y.T. Lee and R.B. Walker, J. Chem. Phys., *71*, 481, (1979).

22. U. Buck and P. McGuire, Chem. Phys., *16*, 101, (1976).

23. J.M. Farrar and Y.T. Lee, J. Chem. Phys., *57*, 5492, (1972).

24. H.J. Loesch, Chem. Phys., *18*, 431, (1976).

25. Lectures given at "Pair interactions between molecules", Faraday Div. Symposium, (Imperial College, London, 1977).

26. R.B. Gerber, V. Buch and U. Buck, J. Chem. Phys., *72*, 3596, (1980).

27. E. Buluggiu and C. Foglia, Chem. Phys. Lett., *1*, 82, (1967).

28. G.A. Kuipers, J. Mol. Spectrosc., *2*, 75, (1958); D.F. Smith, J. Mol. Spectrosc., *3*, 473, (1959); W.F. Herget, N.M. Gailar, R.J. Lovell and A.H. Nielsen, J. Opt. Soc. Am., *50*, 1264, (1960); J.L. Himes and T.A. Wiggins, J. Mol. Spectrosc., *40*, 418, (1971).

29. M. Larvor, J.-P. Houdeau and C. Haeusler, Can. J. Phys., *56*, 334, (1978).

30. L.S. Bernstein and C.E. Kolb, J. Chem. Phys., *71*, 2818, (1979).

31. D.H. Rank, B.S. Rao and T.A. Wiggins, J. Chem. Phys., *37*, 2511, (1962); D.H. Rank, P. Sitaram, W.A. Glickman and T.A. Wiggins, J. Chem. Phys., *39*, 2673, (1963).

32. A.W. Miziolek and G.C. Pimentel, J. Chem. Phys., *65*, 4462, (1976).

33. A.W. Miziolek and G.C. Pimentel, J. Chem. Phys., *66*, 3840, (1976).

34. E.W. Boom, private communication.

35. A. Kudian and H.L. Welsh, Can. J. Phys., *49*, 230, (1971); A.R.W. McKellar and H.L. Welsh, J. Chem. Phys., *55*, 595, (1971); Can. J. Phys., *50*, 1458, (1972).

36. A. Watanabe and H.L. Welsh, Phys. Rev. Lett., *13*, 810, (1964); A.R.W. McKellar and H.L. Welsh, Can. J. Phys., *52*, 1082, (1974).

37. A. Kudian, H.L. Welsh and A. Watanabe, J. Chem. Phys., *43*, 3397, (1965); *ibid.*, *47*, 1190, (1967).

38. R.J. Le Roy and J. van Kranendonk, J. Chem. Phys., *61*, 4750, (1974).

39. L. Mannik, J.C. Stryland and H.L. Welsh, Can. J. Phys., *66*, 1826, (1971).

40. G. Henderson and G.E. Ewing, J. Chem. Phys., *59*, 2280, (1973); Mol. Phys., *27*, 903, (1974); C.A. Long and G.E. Ewing, J. Chem. Phys., *58*, 4824, (1973); C.A. Long, G. Henderson and G.E. Ewing, Chem. Phys., *2*, 485, (1973).

41. C.E. Dinnerman and G.E. Ewing, J. Chem. Phys., *53*, 626, (1970); *ibid.*, *54*, 3660, (1971).

42. C.E. Morgan and L. Frommhold, Phys. Rev. Lett., *29*, 1053, (1971).

43. R.K. Thomas, Proc. Roy. Soc. A, *325*, 133, (1971); *ibid.*, *344*, 579, (1975).

44. A.C. Legon, D.J. Millen and S.C. Rogers, Chem. Phys. Lett., *41*, 137, (1975).

45. J.W. Bevan, A.C. Legon, D.J. Millen and S.C. Rogers, J.C.S. Chem. Comm., 341, (1975).

46. J.W. Bevan, A.C. Legon, D.J. Millen and S.C. Rogers, J.C.S. Chem. Comm., 130, (1975).

47. A.C. Legon, D.J. Millen and P.J. Mjoberg, Chem. Phys. Lett., *47*, 589, (1977).

48. E.W. Boom, D. Frenkel and J. van der Elsken, J. Chem. Phys., *66*, 1826,(1977); E.W. Boom and J. van der Elsken, (to be published).

49. W.J. Balfour and R.F. Whitlock, Can. J. Phys., *50*, 1648, (1969).

50. Y. Tanaka and K. Yoshino, J. Chem. Phys., *53*, 2012, (1970).

51. E.A. Mason and L. Monchick, Adv. Chem. Phys., *12*, (Wiley-Interscience, N.Y., 1967), page 329.

52. E.A. Colbourn and A.E. Douglas, J. Chem. Phys., *65*, 1741, (1976).

53. Y. Tanaka and K. Yoshino, J. Chem. Phys., *50*, 3087, (1969); *ibid.*, *53*, 2012, (1970); *ibid.*, *57*, 2964, (1972); Y. Tanaka, K. Yoshino and D.E. Freeman, J. Chem. Phys., *59*, 5160, (1973); *ibid.*, *61*, 4880, (1974); Y. Tanaka, W.C. Walker and K. Yoshino, J. Chem. Phys., *70*, 380, (1979), (in emission).

54. G.C. Maitland and E.B. Smith, Mol. Phys., *22*, 861, (1970); *ibid.*, *27*, 867, (1974); G.C. Maitland, Mol. Phys., *26*, 513, (1973); R.A. Aziz, Mol. Phys., *30*, 1409, (1975).

55. References in table II of M. Waldman and R.G. Gordon, J. Chem. Phys., *71*, 1325, (1979).

56. E.J. Breford and F. Engelke, Chem. Phys. Lett., *53*, 282, (1978); J. Chem. Phys., *71*, 1994, (1979).

57. R.E. Leckenby, E.J. Robbins and P.A. Trevalion, Proc. Roy. Soc. A, *280*, 409, (1964); R.E. Leckenby and E.J. Robbins, Proc. Roy. Soc. A, *291*, 389, (1966).

58. T.A. Milne and F.T. Greene, J. Chem. Phys., *47*, 4095, (1967); *ibid.*, *52*, 1552, (1970); D. Goulomb, R.E. Good and R.F. Brown, J. Chem. Phys., *52*, 1545, (1970).

59. R.E. Smalley, D.H. Levy and L. Wharton, J. Chem. Phys., *64*, 3226, (1976).

60. G.M. McClelland, K.L. Sanger, J.J. Valenti and D.R. Herschbach, J. Phys. Chem., *83*, 947, (1979).

61. T.E. Gough, private communication.

62. R.E. Smalley, L. Wharton and D.H. Levy, J. Chem. Phys., *63*, 4977, (1975).

63. K.E. Johnson, L. Wharton and D.H. Levy, J. Chem. Phys., *69*, 2719, (1978).

64. R.E. Smalley, L. Wharton and D.H. Levy, J. Chem. Phys., *68*, 671, (1978).

65. G. Kubiak, P.S.H. Fitch, L. Wharton and D.H. Levy, J. Chem. Phys., *68*, 4477, (1978).

66. W. Sharfin, K.E. Johnson, L. Wharton and D.H. Levy, J. Chem. Phys., *71*, 1292, (1979).

67. J.E. Kenny, K.E. Johnson, W. Sharfin and D.H. Levy, J. Chem. Phys., *72*, 1109, (1980).

68. J.A. Blazy, B.M. DeKoven, T.D. Russell and D.H. Levy, J. Chem. Phys., *72*, 2439, (1980).

69. T.D. Russell, B.M. DeKoven, J.A. Blazy and D.H. Levy, J. Chem. Phys., *72*, 3001, (1980).

70. R.E. Smalley, L. Wharton and D.H. Levy, J. Chem. Phys., *68*, 2487, (1978); S.M. Beck, M.G. Liverman, D.L. Monts and R.E. Smalley, J. Chem. Phys., *70*, 232, (1979); R.E. Smalley, L. Wharton and D.H. Levy, J. Chem. Phys., *66*, 2750, (1977).

71. R. Ahman-Bitar, W.P. Lapatovich, D. Pritchard and I. Renham, Phys. Rev. Lett., *39*, 1657, (1977); R.E. Smalley, D.J. Auerbach, P.S.H. Fitch, D.H. Levy and L. Wharton, J. Chem. Phys., *66*, 3778, (1977); J. Tellinghuisen, A. Ragone, M.S. Kim, D.J. Auerbach, R.E. Smalley, L. Wharton and D.H. Levy, J. Chem. Phys., *71*, 1283, (1979).

72. D.R. Preuss, S.A. Pace and J.L. Gole, J. Chem. Phys., *71*, 3553, (1979).

73. A. Herrmann, S. Leutwyler, E. Schumacher and L. Wöste, Chem. Phys. Lett., *62*, 216, (1979).

74. T.E. Gough, R.E. Miller and G. Scoles, J. Chem. Phys., *69*, 1558, (1978).

75. P.M. Dehmer and J.L. Dehmer, J. Chem. Phys., *69*, 125, (1978); F. Carnovale, M.K. Livett and J.B. Peel, J. Chem. Phys., *71*, 255, (1979).

76. P. Audit, J. Phys., (Paris), *30*, 192, (1969); L. Janzen and L. Bartell, J. Chem. Phys., *50*, 3611, (1969).

77. D.L. King, D.A. Dixon and D.R. Herschbach, J. Am. Chem. Soc., *96*, 3328, (1974); D.A. Dixon and D.R. Herschbach, Ber. Bunsenges. Phys. Chem., *81*, 145, (1977).

78. T.C. English and J.C. Zorn, in "Methods in Experimental Physics", (Academic Press, N.Y., 1973), Vol. III, Part B; P. Kusch and V.W. Hughes, Handbüch der Physik, (Springer-Verlag, Berlin, 1959), vol. 37, page 1.

79. T.R. Dyke, B.J. Howard and W. Klemperer, J. Chem. Phys., *56*, 2442, (1972).

80. S.E. Novick, P. Davies, S.J. Harris and W. Klemperer, J. Chem. Phys., *59*, 2273, (1973); S.E. Novick, K.C. Janda, S.L. Holmgren, M. Waldman and W. Klemperer, J. Chem. Phys., *65*, 1114, (1976); J.M. Hutson and B.J. Howard, J. Chem. Phys., to be published.

81. S.J. Harris, S.E. Novick and W. Klemperer, J. Chem. Phys., *60*, 3208, (1974).

82. T.R. Dyke and J.S. Muenter, J. Chem. Phys., *60*, 2929, (1974); T.R. Dyke, J. Chem. Phys., *66*, 492, (1977); T.R. Dyke, K.M. Mack and J.S. Muenter, J. Chem. Phys., *66*, 498, (1977).

83. S.J. Harris, S.E. Novick, W. Klemperer and W.E. Falconer, J. Chem. Phys., *61*, 193, (1974).

84. S.J. Harris, K.C. Janda, S.E. Novick and W. Klemperer, J. Chem. Phys., *63*, 881, (1975).

85. S.E. Novick, S.J. Harris, K.C. Janda and W. Klemperer, Can. J. Phys., *53*, 2007, (1975).

86. S.E. Novick, K.C. Janda and W. Klemperer, J. Chem. Phys., *65*, 5115, (1976).

87. K.C. Janda, J.M. Steed, S.E. Novick and W. Klemperer, J. Chem. Phys., *67*, 5162, (1977).

88. K.C. Janda, L.S. Bernstein, J.M. Steed, S.E. Novick and W. Klemperer, J. Am. Chem. Soc., *100*, 8074, (1978).

89. J.M. Steed, T.A. Dixon and W. Klemperer, J. Chem. Phys., *70*, 4095, (1979).

90. K.V. Chance, K.H. Bowen, J.S. Winn and W. Klemperer, J. Chem. Phys., *70*, 5157, (1979).

91. R.L. DeLeon, K.M. Mack and J.S. Muenter, J. Chem. Phys., *71*, 4487, (1979).

92. J.M. Steed, L.S. Bernstein, T.A. Dixon, K.C. Janda and W. Klemperer, J. Chem. Phys., *71*, 4189, (1979).

93. A.E. Barton, T.J. Henderson, P.R.R. Langridge-Smith and B.J. Howard, Chem. Phys., *45*, 429, (1980).

94. K.C. Jackson, P.R.R. Langridge-Smith and B.J. Howard, Mol. Phys., *39*, 817, (1980).

95. A.E. Barton, D.J.B. Howlett and B.J. Howard, Mol. Phys., to be published.

96. C.M. Western, P.R.R. Langridge-Smith, S.E. Novick and B.J. Howard, Mol. Phys., submitted for publication.

97. W. Klemperer, 6th High Resolution Spectroscopy Conference, (Tours, 1979), Paper G.1.

98. T.J. Balle, E.J. Campbell, M.R. Keenan and W.H. Flygare, J. Chem. Phys., *71*, 2723, (1979); *ibid.*, *72*, 922, (1980).

99. E.J. Campbell, M.R. Keenan, L.W. Buxton, T.J. Balle, P.D. Soper, A.C. Legon and W.H. Flygare, Chem. Phys. Lett., *70*, 420, (1980).

100. M.R. Keenan, E.J. Campbell, T.J. Balle, L.W. Buxton, T.K. Minton, P.D. Soper and W.H. Flygare, J. Chem. Phys., *72*, 3070, (1980).

101. W.B. Nielsen and R.G. Gordon, J. Chem. Phys., *58*, 4131, (1973).

102. W.B. Nielsen and R.G. Gordon, J. Chem. Phys., *58*, 4149, (1973).

103. A.M. Leonardi-Cattolica, K.O. Prins and J.S. Waugh, J. Chem. Phys., *54*, 769, (1971).

104. A.M. Dunker and R.G. Gordon, J. Chem. Phys., *64*, 354, (1976).

105. G.N. Robertson, Philos. Trans. Roy. Soc. A, *286*, 25, (1977), and references therein.

106. J.A. Beswick and J. Jortner, J. Chem. Phys., *69*, 512, (1978); S.B. Woodruff and D.L. Thompson, J. Chem. Phys., *71*, 376, (1979).

107. J.A. Beswick and J. Jortner, J. Chem. Phys., *68*, 2277, (1978).

108. M.S. Child, Farad. Disc. Chem Soc., *62*, 307, (1977).

109. G.E. Ewing, J. Chem Phys., *72*, 2096, (1980).

110. J.A. Beswick and J. Jortner, Chem. Phys. Lett., *65*, 240, (1979). J. Chem. Phys., *71*, 4737, (1979).

111. J.A. Beswick and A. Requera, J. Chem. Phys., *72*, 3018, (1980).

112. See, for example, P. Kollman, J. Am. Chem. Soc., *99*, 4873, (1977).

113. T.F. Ewing, J. Detrich and R.W. Cann, J. Chem. Phys., *69*, 4662, (1978); K.T. Tag and J.P. Toennies, J. Chem. Phys., *68*, 5501, (1978); G.C. Nielsen, G.A. Parker and R.T. Pack, J. Chem. Phys., *66*, 1396, (1977); *ibid.*, *69*, 3268, (1978); G.A. Parker, R.L. Snow and R.T. Pack, Chem. Phys. Lett., *33*, 399, (1975).

114. D.R. Yarkony, S.V. O'Neill, H.F. Schaefer III, C.P. Baskin and C.F. Bender, J. Chem. Phys., *60*, 855, (1974).

115. S.F. Boys and F. Bernardi, Mol. Phys., *19*, 558, (1970).

116. H. Lischka, J. Am. Chem. Soc., *96*, 4761, (1974).

117. F.H. Smit, J.L. Derissen and F.B. van Duijneveldt, J. Chem. Phys., *69*, 4241, (1978).

118. S.L. Holmgren, M. Waldman and W. Klemperer, J. Chem. Phys., *67*, 4414, (1977); *ibid.*, *69*, 1661, (1978).

119. G.O. Sørensen, in Topics in Current Chemistry, (Springer-Verlag, Berlin, 1979), vol. 82; 6th High Resolution Spectroscopy Conference, (Tours, 1979), Paper C.8.

120. R. Wallace, Chem. Phys., *37*, 93, (1979); Chem. Phys. Lett., *67*, 442, (1979).

121. T.R. Dyke, B.J. Howard and W. Klemperer, J. Chem. Phys., to be published.

CHAPTER 2: THE MOLECULAR BEAM ELECTRIC RESONANCE SPECTROMETER

2.1 The Rabi Spectrometer

The Molecular Beam Electric Resonance (MBER) spectrometer is a combination of the Rabi electric resonance spectrometer[1] and a molecular beam supersonic nozzle system[2,3]. The MBER spectrometer was used in the work described in this thesis to obtain the microwave and radiofrequency spectra of KrHCl and NeDCl. Descriptions of the spectrometer have appeared elsewhere, but a brief review will be given here, especially concentrating on a numerical estimation of relevant quantities.

A schematic diagram of the parts of the spectrometer is shown in figure 2.1, together with the dimensions of the apparatus. The spectrometer consists of four vacuum chambers which are built of stainless steel. They are the source chamber, the buffer chamber, the main chamber and the detector chamber. Each section is pumped separately, since an enormous pump would be required to pump the whole chamber, and also because the source chamber can be designed to take the greatest gas load. The source chamber is pumped by a $9\frac{5}{8}$" (throat diameter) Edwards E09 vapour diffusion pump, fitted with an Edwards P9L6 pneumatic gate valve above it. The latter is interlocked to close whenever a seal breaks in the source chamber to prevent charring of the diffusion pump oil. The presence of the valve, however, cuts down the pumping speed from 2500 litres s^{-1} to around 1000 litres s^{-1}. It is backed by an Edwards ISC450B rotary pump, which pumps at 450 litres min^{-1}. The pumping requirements of the buffer and main chambers are lower than this. The former uses a 5" E04 vapour diffusion pump and the latter a 7" E06 pump, with pumping speeds of 600 and 1300 litres s^{-1} respectively. They are fitted with refrigerated chevron baffles to stop oil contaminating the chambers. This decreases breakdown potentials for the high voltage electric fields. Both are backed by the same Edwards ES330

Figure 2.1 *Schematic view of the spectrometer. Distances are in cm. * labels the buffer fields either side of the C field. The stopwire is mounted between the first buffer field poles, and can be moved laterally to obstruct the beam. Only one pole of the deflecting magnet is shown for clarity.*

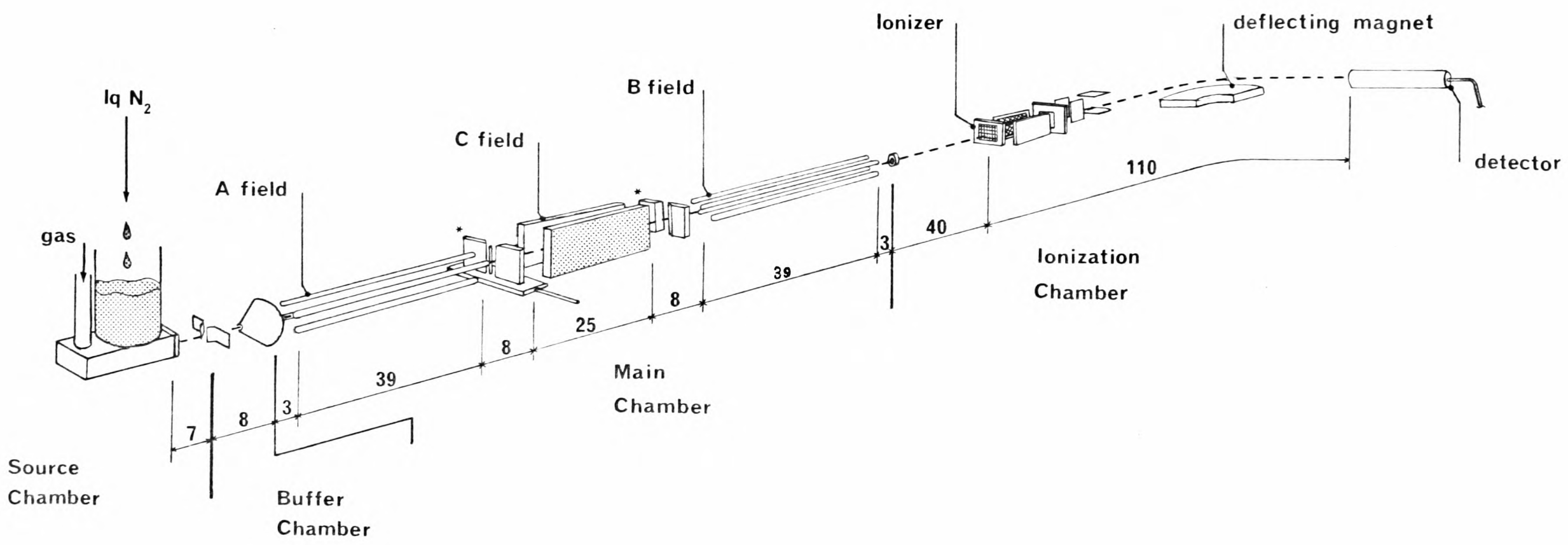
lq N_2
gas
A field
B field
C field
Ionizer
deflecting magnet
detector
110
40
3
39
8
25
8
39
3
8
7
Source
Chamber
Buffer
Chamber
Main
Chamber
Ionization
Chamber

rotary pump (330 litres min^{-1}). The pumping requirements for the ionizing and detecting chamber are more stringent and will be described later. Each of the chambers can be isolated for maintainance purposes, and their separate functions are described below.

2.2 The source chamber: molecular beam formation

The beam is formed by expanding a suitable mixture of gases through a supersonic nozzle. The gases are pre-mixed in either of two one litre bottles (Monel, and stainless steel, Hoke Ltd.) and the mixture is fed through a system of Monel piping to the nozzle block. The composition of the mixture is monitored by a Matheson (8 atmos.) pressure gauge, and the flow of gas through the system is controlled by a Nupro fine needle-valve (model SS-4SG). The nozzle itself is a small hole drilled in a stainless steel block. Nozzles of 35 μm and 50 μm were used in the experiments. They are produced by drilling with successively smaller drills into the upstream side of the block to within a few tenths of microns from the downstream side, and then drilling in with a jeweller's drill from that side[4]. The block is bolted on to a hollow copper mount which is connected to the gas handling manifold. An indium wire ring is compressed between the nozzle block and the copper mount to ensure a gas-tight seal. The entire system is fixed to a liquid nitrogen reservoir, and the temperature can be regulated by simultaneous cooling and heating by passing current through heating wire wrapped around the nozzle block and copper mount. The temperature of the nozzle is measured with a chromel-alumel thermocouple, with one end fixed to the nozzle block and the other kept in a flask of melting ice. The emf is measured by a digital voltmeter and the temperature read off an appropriate calibration table. Careful addition of coolant can stabilise the temperature to within 5° over many hours. The reservoir itself is connected to an inlet pipe which is fixed to a screw and bellows system which allows the height of the nozzle to be adjusted. These are in turn

mounted on to a plate driven by a threaded bolt which allows the horizontal position of the nozzle to be adjusted as well. The whole system is bolted to the source chamber.

Three factors are responsible for the observation of spectra: (a) correct expansion conditions for the formation of cool beams of the complex; (b) correct positioning of the nozzle with respect to the first slits; and (c) alignment of the nozzle with the rest of the apparatus. The sensitivity of the observed spectra to these conditions was not fully appreciated for some time[5]. Solution of the problems associated with (a) leads to easy solutions of (b) and (c), but the solution of (a) requires an understanding of the process of adiabatic cooling during supersonic expansions.

The equations governing supersonic expansions were first discussed by Kantrowitz[6] and Kistiakowsky[7]. When a beam is formed from a low pressure source the flow is purely effusive, and the gas in the beam is a true thermodynamic reflection of the gas in the source. When the source pressure is raised the gas enters the beam through a free-jet expansion, and the gas now behaves like a bulk fluid with its own thermodynamic parameters. During the expansion random thermal motion is converted into directed mass flow so that the translational temperature (defined in terms of the velocity distribution width) decreases while the velocity of flow increases. To get some idea of the flow rate of the beam consider a typical expansion of argon (used for many van der Waals experiments as a carrier gas). In the experiments described in this thesis stagnation temperatures of ~ 170 K are used and the stagnation pressure is usually about 500 torr. If the thermal energy is converted into mass flow a (maximum) beam velocity (v_m) of 325 m s^{-1} is indicated for the argon expansion. During the expansion the process of cooling is approximately isentropic in nature and conservation of energy requires that

$$H_S = H + \tfrac{1}{2}mv^2 \tag{2.1}$$

where H_S is the enthalpy of the gas before expansion and v is the (increasing) velocity of mass flow as the expansion proceeds. The corresponding temperature, T, downstream of the expansion is then given by the equation

$$H_S - H = c_p(T_S - T) \tag{2.2}$$

treating the heat capacity c_p as a constant. T is a valid temperature only if there is thermodynamic equilibrium between all degrees of freedom. Experimentally this is met for noble gas expansions. The Mach number of a gas, M, is defined as the ratio of the flow speed v to the speed of sound, c, at the corresponding temperature, T. Since $c = (\gamma kT/m)^{\frac{1}{2}}$, and $\gamma = c_p/c_V$, then

$$M = v(m/\gamma kT)^{\frac{1}{2}} \tag{2.3}$$

and so

$$\tfrac{1}{2}M^2\gamma kT + c_pT = c_pT_S \tag{2.4}$$

where T_S is the stagnation temperature.

Rearranging

$$T = \frac{T_S}{1 + \tfrac{1}{2}(\gamma - 1)M^2} \tag{2.5}$$

The velocity distribution is approximately Maxwellian with an extra velocity dependence caused by the mass flow, and is $N(V) \propto V^3T^{-\frac{3}{2}}e^{-\frac{m}{2}(V - v)^2/T}$ [8]. More extensive theoretical calculations indicate that M should increase without limit[9], but several factors go to make equation 2.5 invalid. The most important of these is that as the binary collision rate drops eventually there are too few collisions to ensure thermodynamic re-equilibration. At this point the thermodynamic parameters that characterise the expansion are 'frozen out' and a terminal Mach number, M_T, is reached. One model of this Mach number 'freezing' predicts that the terminal Mach number is given by[10]

$$M_T = \varepsilon(\Lambda/D)^{\frac{1 - \gamma}{\gamma}} \tag{2.6}$$

where Λ is the mean free path of the nozzle expansion, and ε is a characteristic of the gas in question. For the argon expansion this reduces to

$$M_T = 133(P_S D)^{0.4} \qquad (2.7)$$

where P_S is the stagnation pressure in atmospheres and D is the nozzle diameter in centimetres. For a 50 μm nozzle, $M_T = 11.7$, and using equation 2.5 yields a terminal translational temperature of 3.2 K. In a similar expansion Dymanus found near-Boltzmann behaviour for the rotational distribution of the seeded molecular beam[11], and the above temperature suggests a velocity spread (half width at half maximum) of about 45 m s^{-1}. The position of the transition from continuum to free-jet molecular flow for this terminal speed will be about 50 nozzle diameters or ~2 mm downstream of the nozzle[9].

In seeded beams of polyatomic molecules the corresponding population of states for various degrees of freedom follows the translational temperature. In particular the rotational temperature is usually found to be very close to the translational temperature[11,12]. Herschbach[12] has investigated this with laser-induced fluorescence and his data suggested a rotational temperature of 3.8 K. Dymanus[11] in his study of a seeded OCS/argon expansion fitted a rotational temperature of 3.5(7) K under similar conditions. Vibrational temperatures lag behind these low temperatures somewhat, and depend on the cross-sections for vibrational relaxation between the molecule and diluent gas under study. For an iodine-seeded expansion a vibrational temperature of ~120 K would be expected. An exact understanding of the importance of various contributions to vibrational and rotational relaxation in the molecular beam formation process is not available yet, but it appears as if relaxation of both modes occurs via metastable and stable complex formation. Levy[12] has found that the rotational relaxation mechanism appears to be dominated by collisions which form these metastable complexes. The

complex flies apart upon vibrational relaxation with concomitant extensive rotational relaxation due to conservation of angular momentum (in the exit channel μvb must equal ΔJ, where b is the exit channel impact parameter). For polyatomic beams the increased heat content (measured by a small γ) leads to higher terminal temperatures. For a pure CO_2 expansion, a terminal Mach number of 6 is calculated and a terminal translational temperature of 24 K estimated. Travis *et. al.*[13] have measured a rotational temperature of 32 K for this expansion. Similar temperatures have been measured by Dymanus[11], and so in view of this seeded inert gas beams are used in most MBER experiments.

The formation of stable complexes requires a termolecular collision, the role of the third body being to remove excess energy. (This energy gain increases the translational temperature of equation 2.5 slightly.) The processes leading to the formation of complexes are probably quite complex, but an estimate of the amount of Ar_2 in the beam can be made by considering the termolecular reaction

$$\underset{m}{3Ar} \underset{\alpha}{\overset{\beta}{\rightleftharpoons}} \underset{c}{Ar_2} + Ar$$

where m, c are the number densities and α, β the rate constants. The first order differential equation as a function of downstream distance (z) is

$$\frac{dm}{dz} = -\frac{2m}{z} - \left(\frac{\beta}{v}\right)m^3 + \frac{\alpha}{v}mc \qquad (2.8)$$

Solution of this equation is difficult, but it is easily solved if the back reaction is ignored. Consequently an overestimate of the Ar_2 concentration will be made. Solution yields

$$\frac{c}{m} \simeq \frac{1}{2}\left(\sqrt{1 + \frac{2\beta m_s^2 D}{3v}} - 1\right) \qquad (2.9)$$

at large z, where D is the nozzle diameter[9]. For the argon expansion the value of β is not known but using a typical value of 10^{-32} cm^6 $molecules^{-2}$ s^{-1} [14] gives a value of c/m of ~ 1%.

The dependence of dimer formation on stagnation pressure and nozzle diameter has also been extensively studied. Throughput of gas is limited by the pumping speed of the diffusion pump and is proportional to $P_S D^2$; dimer mole fraction is generally considered to be approximately proportional to $P_S{}^2 D$ [15]. Use of high pressures and small nozzle sizes are therefore favoured, but for small nozzle sizes the cross-sections become more channel-like in appearance and the equations break down[9].

The parts of the free-jet expansion are shown in figure 2.2. We initially used a laser drilled nickel shim as a nozzle source which was bolted on to the nozzle block with a retainer. The retainer was drilled so as to produce a funnel shape for the expanding gas on the downstream side. A semi-angle of 60° was used, being thought sufficient according to figure 2.2, but this arrangement caused considerable rotational heating of the beam. Thus while for the calibrant OCS (4% in Ar) a 15% refocussing[†] was seen, with negligible flop-out of the $J,M_J = 1,0$ state in the refocussed beam, using the same shim soldered to the block with no obstacle downstream gave 150% refocussing, and 60% of this refocussing was found to flop out on applying the $J = 1$, $M_J = 0 \rightarrow \pm 1$ resonance frequency (see later). Comparing the $J = 2$ signal a rotational Boltzmann temperature of 4.6 K was indicated in good agreement with Dymanus' results[11].

During the expansion a non-negligible fraction of beam is scattered at large angles, and in the original nozzle design the retainer scattered these molecules back into the path of the beam causing shock waves which resulted in the high rotational temperatures and poor

[†]The percentage refocussing is given by $(\text{Ref.} - \text{St.}).(\text{F.b.} - \text{St.})^{-1} \times 100$, where F.b. is the full-beam strength, Ref. is the refocussed intensity, and St. is the finite stopped beam intensity ($\sim$10% of F.b.). This quantity is independent of detector efficiency. Values can be larger than 100% because of the space-gathering characteristics of the A focussing field.

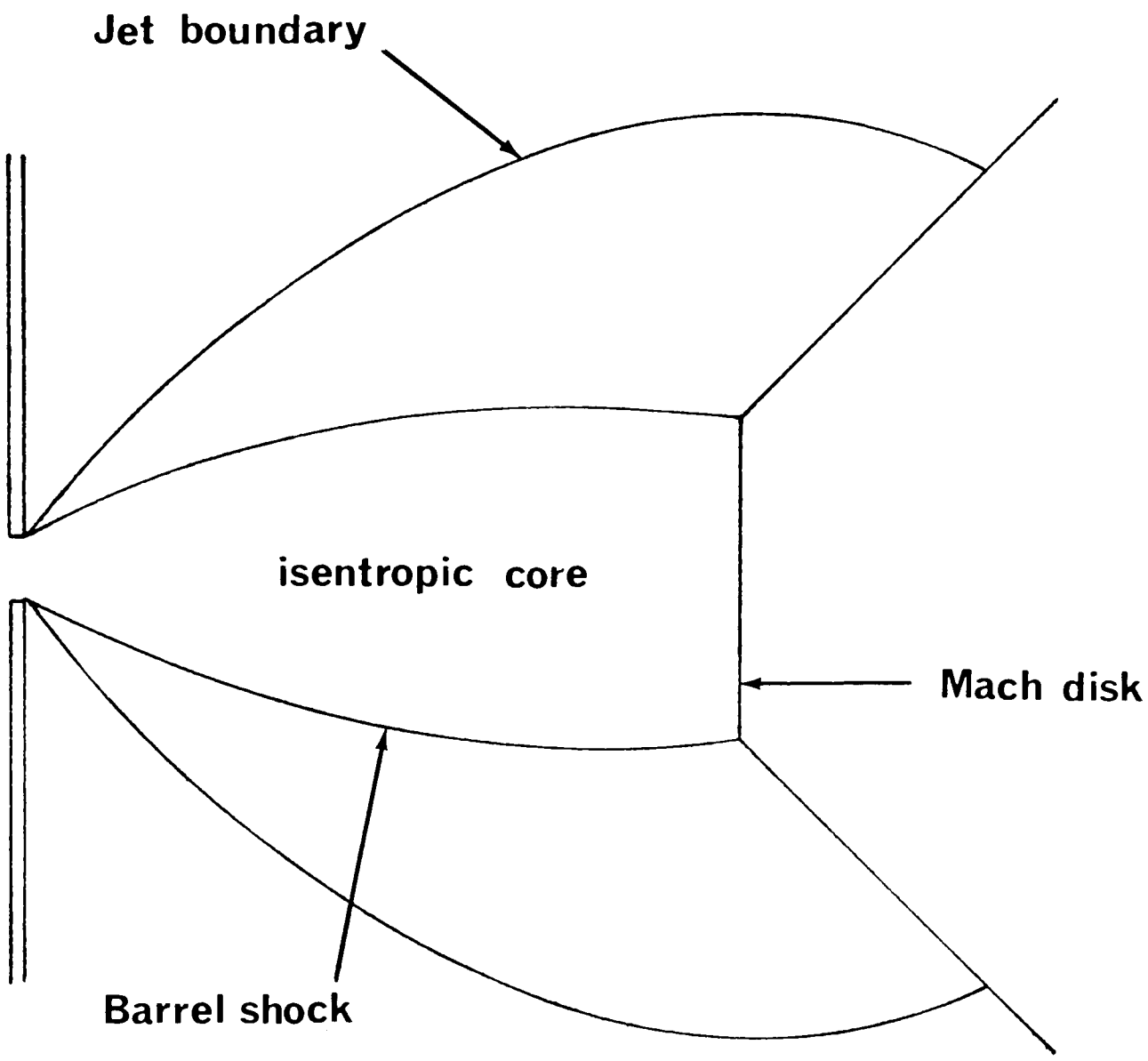

Figure 2.2 Shock patterns surrounding the expanding gas of a free jet.

refocussing of low J states that were found. The realisation of the importance of this process led to the use of nozzles that had no obstacles on the downstream side. This produced signal/noise ratios which improved on those of the old nozzles by at least an order of magnitude. Further shock effects are caused by the presence of background gas and collimating slits or skimmers. Experimental and theoretical work suggests that gas near the centreline of the beam is unaffected by background gas until it reached a so-called Mach disk[9,16]. The distance to the Mach disk, z_M, is given by

$$z_M = \frac{2}{3} D \left(\frac{P_S}{P_o} \right)^{\frac{1}{2}} \qquad (2.10)$$

where P_o is the source chamber pressure, and P_S is the stagnation

pressure. For the argon expansion through a 50 μm nozzle in the Oxford spectrometer where the source diffusion pump and gas flow speed give a value of P_o of 10^{-4} torr, this makes z_M equal to 7.5 cm, far beyond the transition to free molecular flow. The concept of a Mach disk is one that should be strictly applied only in continuum flow conditions, and hence the Mach disk is very diffuse under the experimental conditions of the expansion. Levy[12] works with higher stagnation pressures and very much larger source chamber pressures, and hence his Mach disk distance is about 2 cm, and is more pronounced. Therefore placing the nozzle source for the Oxford spectrometer at a distance greater than about 7.5 cm would affect the formation of the beam, because of background scattering. If the distance is reduced scattering of molecules into the beam from the slits appears to become increasingly important, and the beam intensity falls. This is shown for a nitrogen expansion in figure 2.3. The source/slit distance was therefore fixed at 7 cm.

The turn-over in intensity is due to scattering of the molecules out of the beam. This is because the local density of background molecules in front of the nozzle increases as the backing pressure increases because of the fixed pumping speed of the source chamber pump. A similar dependence on the intensities of rotational lines occurs because of the heating effect of these unwanted collisions. This effect has been observed for the OCS transition mentioned earlier, and by Dymanus[11] for ℓ-doubling transitions in OCS. Working at these higher pressures requires efficient skimmer systems therefore.

Alignment of the main (straight-through) beam is not critical within several thousandths of an inch (1 thou ≡ 25 μm), but with the incorporation of a stop-wire (see figure 2.1 and text below) alignment of the source, stopwire and detector increases this criticality, and alignment of the horizontal and vertical positions (due to skewing of the beam) of the source to within 25 μm becomes necessary for

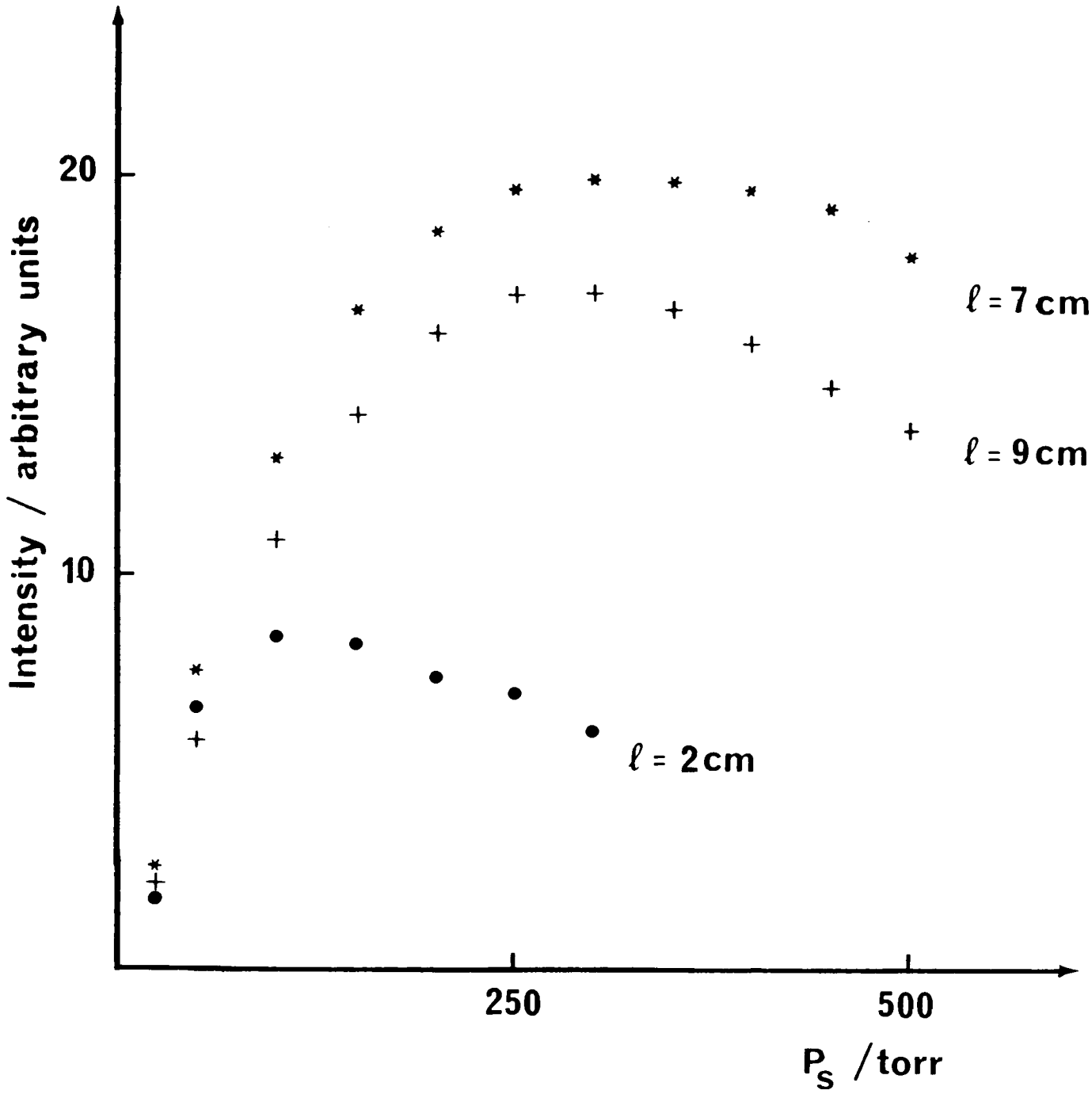

Figure 2.3 Saturation of N_2 mass peak (m/e = 28) as a function of source pressure. ℓ is the distance from the nozzle to the first slits. The intensity of the standard r.f. OCS transition shows a similar dependence.

optimisation of signal.

2.3 The buffer and main chambers: molecular beam deflection

(a) Focussing fields

The beam passes through adjustable slits into the next stage of differential pumping, the buffer chamber. This is maintained at about 10^{-5} torr, and the beam travels for only a few centimetres before

passing into the main chamber at 10^{-6} torr.

In a Rabi-type experiment, the beam is formed in a particular quantum state by passing through a non-uniform electric field. The use of these state selecting inhomogeneous fields, called A and B fields, limits the technique to molecules and complexes having a permanent dipole moment. A polar molecule experiences a force, F, in an inhomogeneous electric field that tends to move it towards a location that minimises its energy. This force is given by $\mathbf{F} = -\nabla W(E)$, where $W(E) = \langle -\mu . \mathbf{E} \rangle$ is the Stark energy. For the majority of complexes studied the leading term in this expansion indicates that $W \propto E^2$, a second-order Stark effect. The case of first-order Stark effect focussing will be considered in the next chapter. The inhomogeneous field is supplied by a quadrupolar arrangement of rods shown in figure 2.1. If the distance from the centreline of the field to the rods is R, then it can be easily seen that the value of the electric field at a distance r from the centreline for such a quadrupole arrangement of rods with hyperbolic cross-sections is[17]

$$|E| = \frac{2V_o r}{R^2} \qquad (2.11)$$

where $\pm V_o$ are the potentials applied to the rods. Molecules exhibiting second-order Stark effects thus experience a simple harmonic force when passing through the fields. Molecules with positive Stark effects are focussed towards the beam axis, and molecules in negative Stark states are deflected away from the axis.

The conventional "flop-out" mode of operation, which the Oxford spectrometer operates in, consists of cutting out the straight-through beam with a stop-wire and deflecting positive Stark state molecules around it by applying large voltages to the A field. The molecules that are in negative Stark states are deflected away from the axis and are subsequently pumped away. Whilst the A field acts as a state selector,

Figure 2.4 "Flop-out" mode of the molecular beam spectrometer. δ is the stop-wire which shadows the detector. If transitions occur from the focussing state α to the defocussing state β in the C field region, then a decrease of beam flux is monitored.

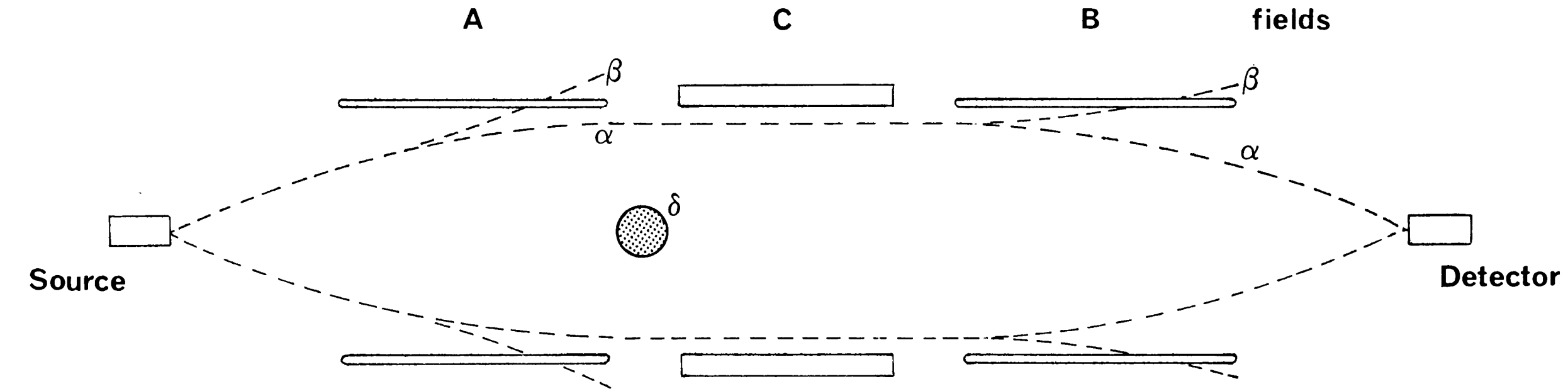

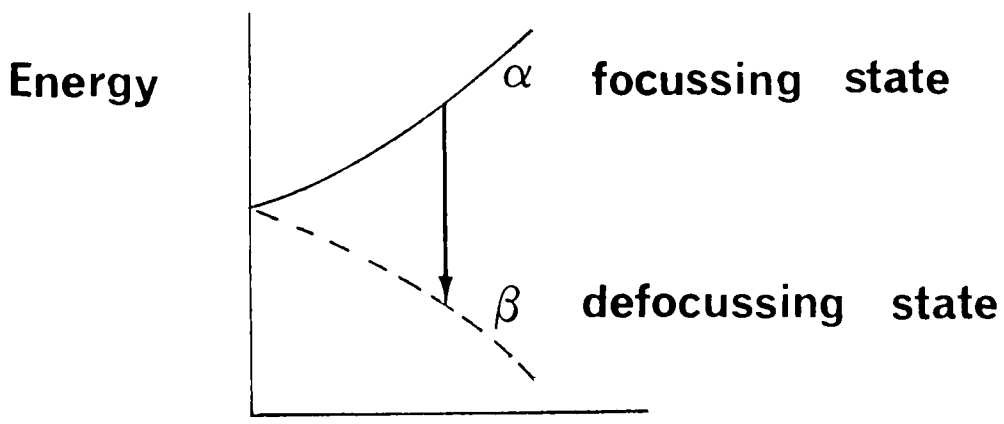

the B field acts as a state analyser. Molecules that are focussed by the A field then pass through the B field where they are focussed on to the detector if they have remained in positive Stark states. This provides a constant refocussed beam flux at the detector. In the C field region radiation is applied and if a transition to a negative Stark state occurs for molecules in a particular eigenstate then these molecules are lost from the beam on passing through the B field and a beam flux change is monitored at the detector (see figure 2.4).

The A and B fields are identical in construction in the Oxford spectrometer. Each comprises two 39 cm rods and two 38 cm rods, with a 0.95 cm ($\frac{3}{8}$") diameter. They are held in the arrangement shown in figure 2.1 by a gantry constructed of machined glass in which a cloverleaf pattern is cut to provide a larger breakdown path across the spacers[18]. The two longer rods are bolted above the shorter rods with the overlap facing the C field, and are alternately grounded and connected to a + 0-30 kV Brandenburg 807R power supply. The rods, however, are not hyperbolic but circular in cross-section. The restoring force therefore contains higher order terms (r^{4n+2}, where $n \geq 1$)[19]. The first correction term can be minimised by taking the distance from the centreline to the rods as (1/1.15)×(rod diameter), giving a rod separation of 1.26 cm and an aperture radius of ~ 4mm. Aberration effects are also present[20]. Bennewitz[20] has shown that there is a limiting field beyond which a state with a positive Stark effect becomes defocussing. Since the electric field increases with distance from the beam axes there is an effective focussing aperture for each molecule which depends on the rotational constant and its quantum state Stark coefficient. In practice, molecules with low rotational constants in low rotational states have small apertures for focussing by the A field, and for these cases the beam has to be aligned more precisely. The alignment of the components in the main chamber is achieved with a small He-Ne gas laser,

(Spectra-Physics 155).

The presence of the buffer fields (see figure 2.1) and the longer rods is due to the effect of loss of quantum state identity of the beam molecules on passing out of the A field or entering the B field. An abrupt change in electric field can cause so-called Majorana transitions[21]. They occur because the abrupt field changes will have Fourier components with a wide range of frequencies which can cause unwanted transitions (and loss of beam intensity). The buffer fields smooth out these sudden changes in field strength between the A, B, and C fields. They are usually kept at about twice the C field voltage, although above 500 V cm^{-1} little effect on observed transitions is seen.

(b) C field construction

Transitions are induced in the C field region by applying radio-frequency or microwave radiation to the beam. Two types of C field are in use: (i) a parallel-plate C field, for frequencies less than ~200 MHz, and (ii) a strip-line C field, for the region 200 MHz to ~2 GHz.

The first C field is constructed of two parallel, optically flat glass plates (25 × 8 × 2 cm), which are gold plated, separated by precision quartz spacers. The parallelism is ensured by observing the fringes (Haidinger's fringes[22]) produced by irradiation with monochromatic visible light (usually the sodium D lines). This produces plates that are parallel to within one wavelength of the light used. Radiofrequency radiation is applied from a radiofrequency oscillator to the plates. To enable both the $\Delta M_J = 0$ and the $\Delta M_J = \pm 1$ transitions to be seen, the r.f. field must have components parallel and perpendicular to the static field. To do this the gold plate is broken along the line of the beam as shown in figure 2.5, and alternate plates grounded to r.f.[23]. To overcome problems with the inhomogeneous fields at the edges of the plates, the r.f. field stops 2.5 cm short of each edge, and only the static d.c. field is applied to this part. Microwave radiation is coupled into the resonance

region through either a length of open-ended X-band waveguide (8-40 GHz) or via an S-band coaxial-to-waveguide transformer and horn (1.8-8 GHz), both above the C field (see figure 2.6a). The polarisation axis of the waveguide is such that for the dominant TE_{10} mode the electric vector of the microwave radiation is parallel to the d.c. field[24]. Only $\Delta M_J = 0$ transitions will then be expected, but as microwave lines are usually

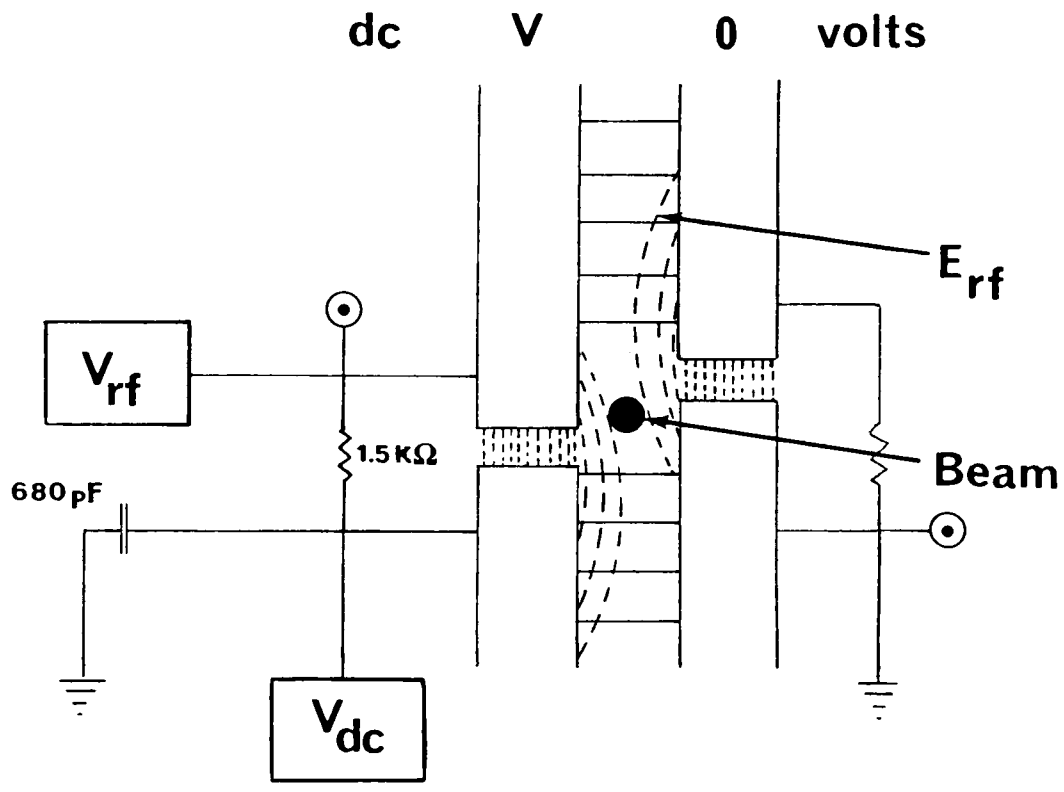

Figure 2.5 Voltage source for parallel-plate C field arrangement.

measured at zero field this is not a disadvantage. The radiation is applied perpendicular to the beam in the spectrometer to cut down Doppler broadening of the spectral lines to a minimum (see below).

The parallel-plate C field will produce uniform radiation fields only for radiation with wavelengths much longer than its dimensions *i.e.* < 350 MHz. As the frequency increases the possibility of standing waves and irregular lineshapes increases. Also standing waves can be set up in the cable connections. These standing waves can be most readily avoided by making the C field part of a properly terminated

a.

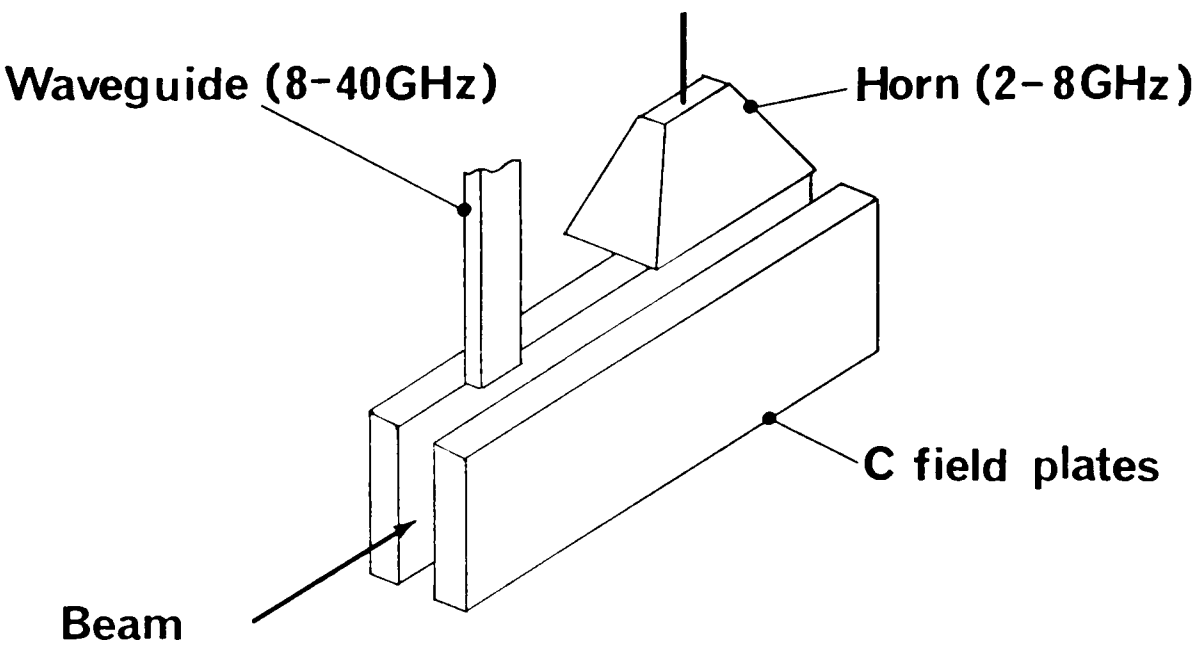

b.

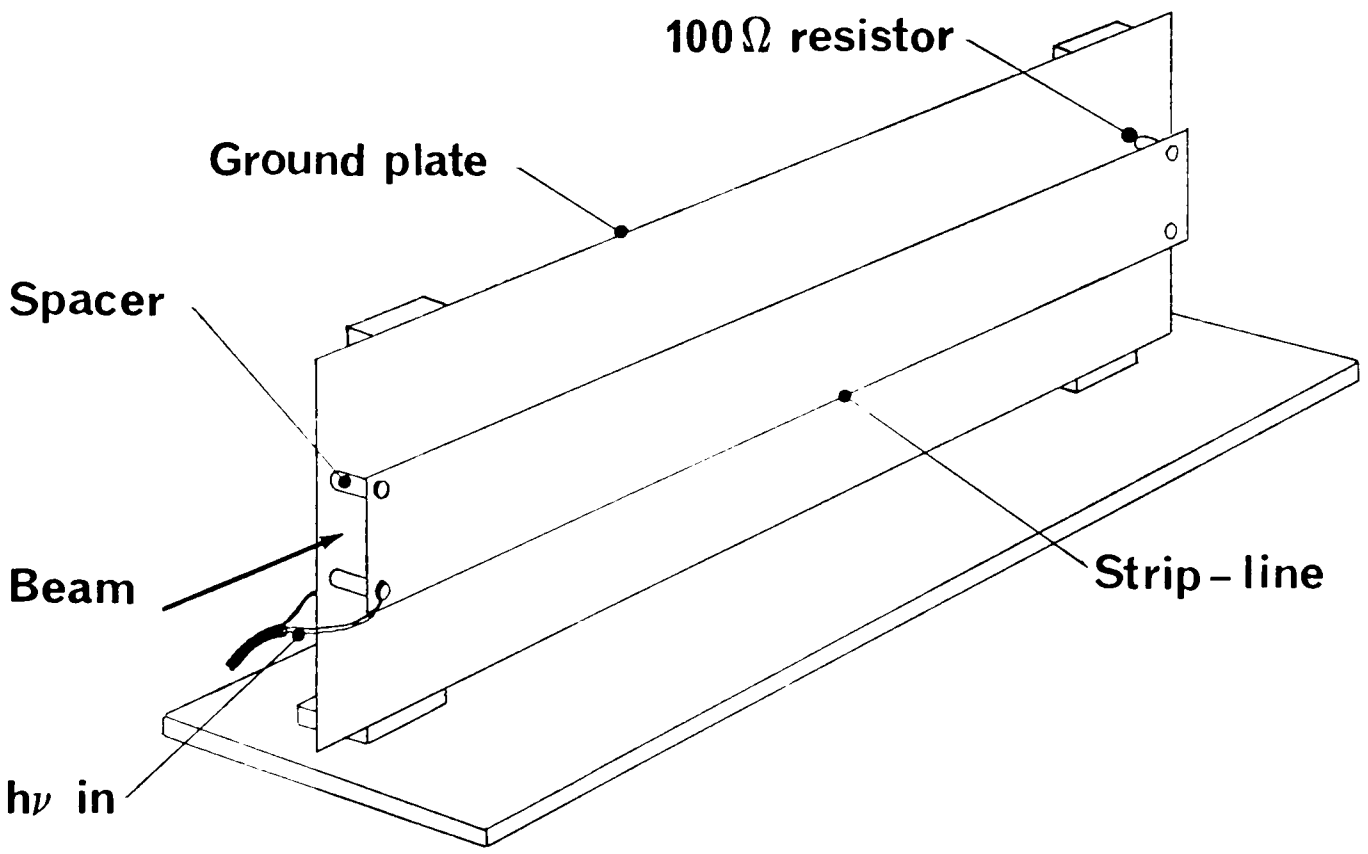

Figure 2.6 *a. Parallel-plate C field arrangement*

b. Strip-line C field construction. The strip-line dimensions are 1.6" × 10" and the teflon spacer length is 0.32".

transmission system using the strip-line C field, thus avoiding these mismatch problems. As the radiation is propagated in 50 Ω coaxial cable a resistance of 50 Ω at the end of the transmission line eliminates reflected waves, and the system behaves as one of infinite length[25]. The construction of the strip-line C field by the author follows the design of Muenter[26] and is outlined in figure 2.6b. The strip-line is connected to the earth plate by 0.32" teflon spacers, with teflon bolts. The characteristic impedance is only determined by the spacing to width ratio of the strip-line, and should be ~ 5 for a 50 Ω impedance[27]. The termination is made by two 100 Ω, $\frac{1}{4}$ W carbon resistors in parallel.

To test this field against the parallel-plate C field, transitions from 0 - 2 GHz in the hyperfine Λ-doubling spectra of $^{14}N^{16}O$ were studied. NO has a great many lines between 200 MHz and 2 GHz[28,29]. Several of the diamagnetic $^2\Pi_{\frac{1}{2}}$ transitions were studied[29], see table 2.1.

Table 2.1 NO Λ-doubling transitions

	J	Ω	F_+	F_-	frequencies /MHz	focussing voltages A	B /kV
$^{14}N^{16}O$	0.5	0.5	0.5	1.5	225.936	11.5	5.5
			1.5	1.5	431.191	11.5	5.5
	1.5	0.5	1.5	1.5	651.543	22	14
			2.5	2.5	801.196	22	14
	2.5	0.5	3.5	3.5	1160.747	30	28
	3.5	0.5	4.5	4.5	1514.768	30	30
$^{15}N^{16}O$	0.5	0.5	0	1	482.621	12	7.5
(0.04% abundance)							

In each case the power was cut down to try to produce linewidths of around 1 kHz, approximately the theoretical limiting linewidth (see below). The power requirements were very different for the two C fields. At around 500 MHz narrow linewidths (~ 1.5 kHz FWHM) could be achieved for both types but the strip-line field required ~ 10 dB less power. At 1 GHz the value was ~ 20 dB and no transition could be seen at 1.5 GHz using the parallel-plate C field, due to reflections in the line. Figure 2.7 is of the 801 MHz transition which shows this phenomenon. Muenter[26] has reported that linewidths of 5 kHz could be seen for transitions up to 5 GHz. The present strip-line C field was tested using the $J,F = 1,\frac{5}{2} \leftarrow 2,\frac{5}{2}$, and the $3,\frac{5}{2} \leftarrow 2,\frac{5}{2}$ transitions in $ArH^{81}Br$ and $ArH^{79}Br$ respectively at 4423.122 and 6616.620 MHz[30]. Linewidths of ~ 10 kHz were seen for both transitions with poorer signal/noise ratios than by using the S-band horn. This does not imply that uniform radiation fields exist however since the Doppler width will be about 2x kHz for a frequency of x GHz. More power is also required and inevitable power broadening will occur in order to achieve good lineshapes.

(c) Spectrometer calibration and resolution

The advantage of the MBER spectrometer is the very accurate measurement of transition frequencies that is possible because of the lack of most broadening effects. The natural linewidth of microwave lines is very small, ~ 10^{-7} Hz at 1 GHz. Also Doppler broadening is kept to a minimum by passing the radiation in perpendicular to the direction of the beam. The factor that limits the linewidth (apart from power broadening) is the finite time that the molecule spends in the C field resonance region (20 cm). The corresponding uncertainty broadening for a beam velocity of 325 m s^{-1} is ~ 1.6 kHz. The theory for a two-level system has been calculated by Klemperer[31], who finds that the lineshape is a Lorentzian attenuated by a power dependent $\sin^2$ function. This can lead to peculiar lineshapes such as that shown in figure 4.4.

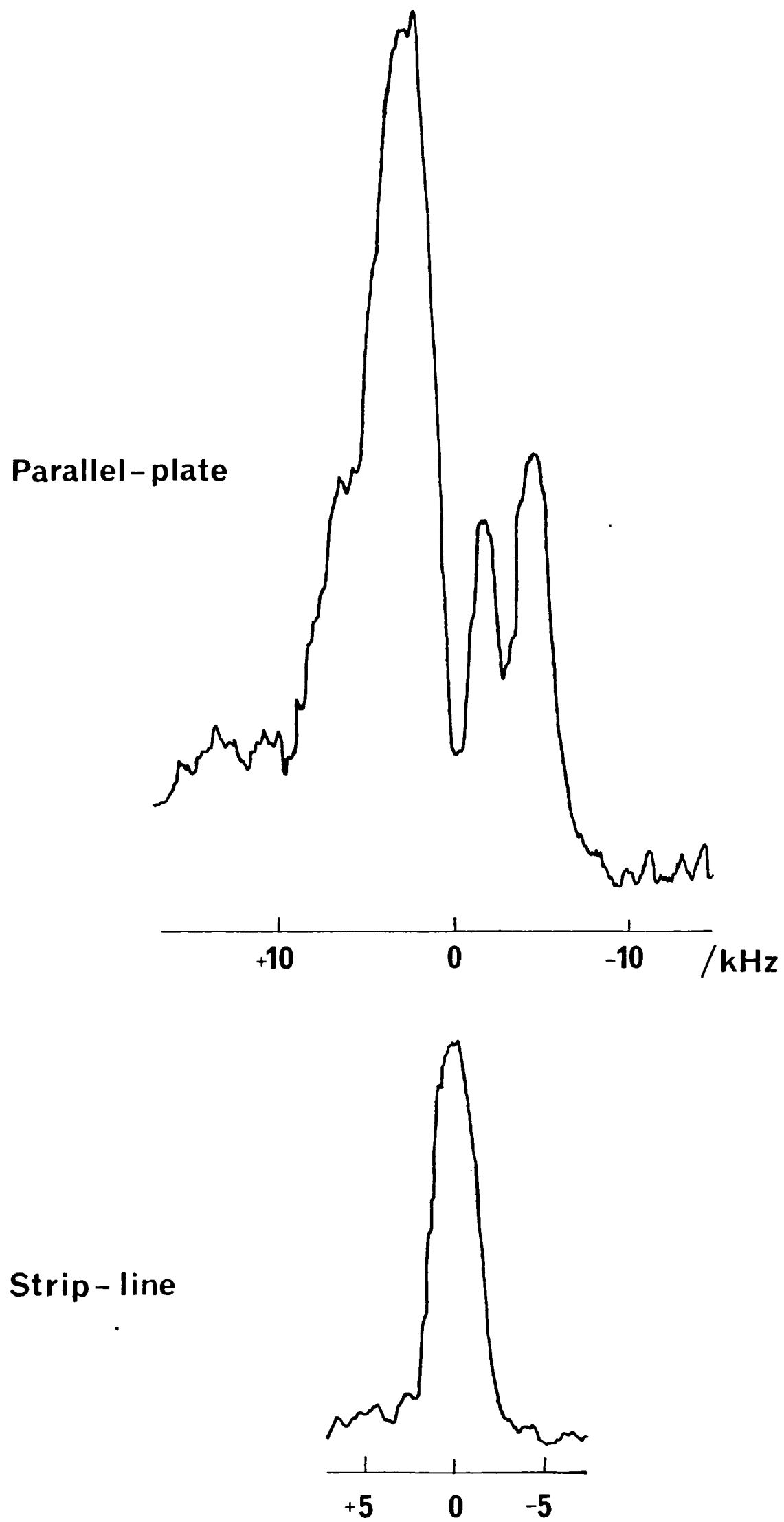

Figure 2.7 $^{14}N^{16}O$ *801 MHz transition using both C fields*

From the lineshapes of HCN a beam velocity and a velocity spread were calculated, but some doubt on the result has been put forward by Wicke[32] because of the neglected velocity selection that the quadrupole fields can cause.

The limiting linewidth can be reached readily for r.f. transitions but for transitions in the S-band horn and especially for the X-band waveguide (2.3 cm long) the radiation spreads out giving rise to some Doppler broadening. At 5 GHz linewidths of 5 kHz are usual, while at 10 GHz lines of ~ 10 kHz (FWHM) are exceptional (see chapters 4 and 5).

For measurements of Stark effects and hence dipole moments a value for the C field spacing must be found. It is calculated by comparing the transition frequency of a molecule with the frequency in a spectrometer with a known C field spacing. The $J = 1$, $M_J = 0 \rightarrow \pm 1$ transition of OCS is used[33]. For the Oxford spectrometer a C field spacing of 1.0270(2) cm was found. This spacing is checked periodically, as is the alignment of the whole system because of vibrational effects caused by the rotary pumps.

2.4 The detector chamber and the measurement of spectra

The intensity of the molecular beam is measured by a mass spectrometer arrangement. The ionizer is shown in figure 2.8, and operates by electron bombardment[34]. The electrons are produced by a heated tungsten filament which is coated with thoria by electrophoresis to reduce the work function. The grid and anode are maintained at approximately the same potential, about +100 V with respect to the cathode. The geometry of the gun is designed so that a space-charge limited flow of electrons exists between grid and anode plate through which the beam passes[35]. This pile up of flux of electrons causes a lowering of potential in the centre of this region (see figure 2.9). Positive ions formed in this region will then be trapped in this potential. The grid and anode are angled away from each other and the charge between the plates increases.

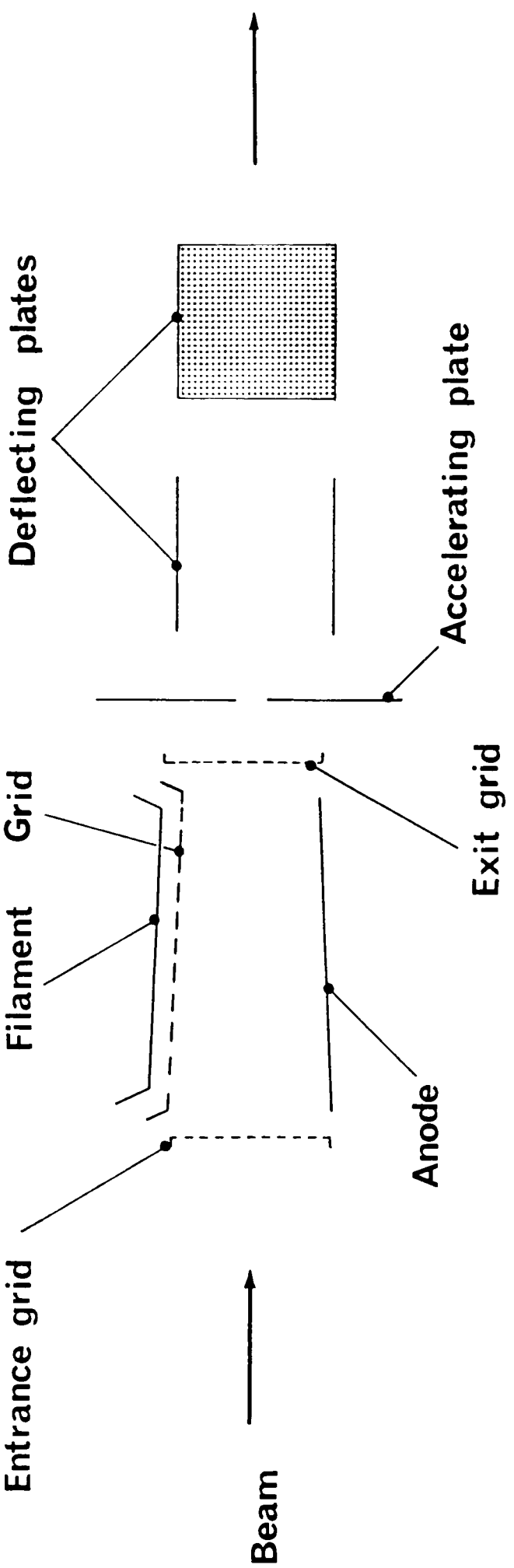

Figure 2.8 Schematic diagram of the ion gun apparatus

The potential minimum therefore deepens towards the exit end of the ionizer, and ions are consequently driven in this direction and collimated to a certain extent by the potential shape. The entrance and exit grids serve to contain the space-charge within the grid and plate

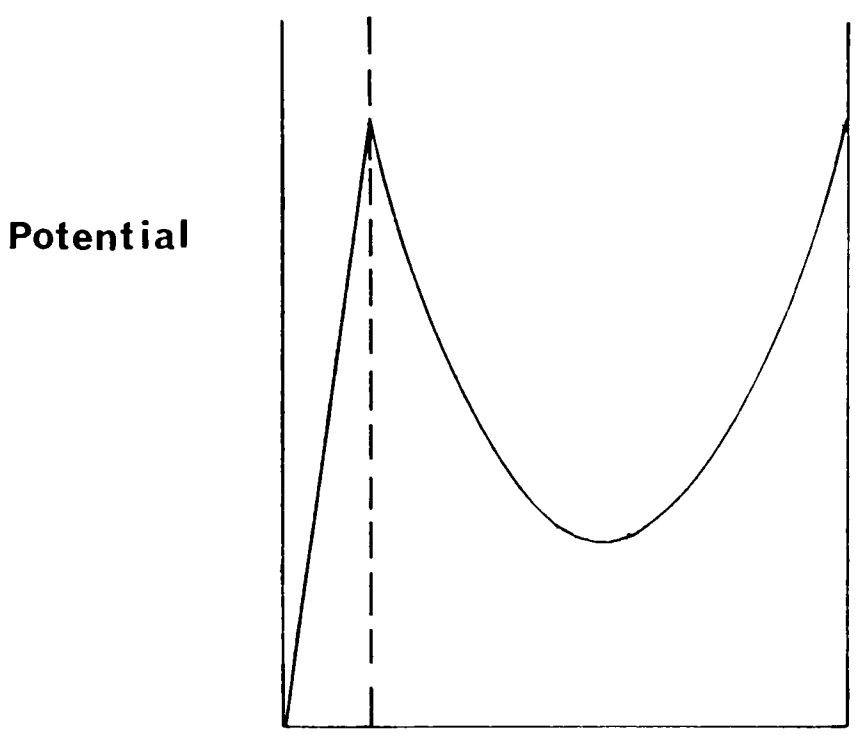

Figure 2.9 Potential distribution for ion gun. The current density is greatest at the potential minimum.

region. The ions are ejected with a small spread of velocities, but the entire assembly is kept at +2.8 kV by a HP6516A (3.5 kV d.c.) power supply. A grounded exit plate then accelerates the positive ions to a uniform velocity, and so consequently ions of a given mass/charge ratio (m/e) are bent at a similar angle by the deflecting magnet on to the detector. The deflecting magnet is water-cooled, and the detector is an EMI 9643/4B electron multiplier tube. This generation of tubes gives a gain of $\sim 3 \times 10^3$ at an accelerating voltage (electron multiplier, E.M. voltage) of 1.6 kV [36], with a maximum gain of 3×10^5 at 2.5 kV. Horizontal and vertical deflecting plates are used to deflect the ion beam

on to the detector. Typical operating characteristics are shown in table 2.2.

Table 2.2 Ion gun operating characteristics

$d_{cath \rightarrow grid}$ 0.7 mm	Area of entrance grid 0.25 × 0.5 cm
$d_{grid \rightarrow anode}$ 3.0 mm	$l_{filament}$ 8 cm
$V_{filament}$ = 6.5 V	V_{anode} = +90 V
$I_{filament}$ = 13 A	I_{anode} = 180 mA
	V_{grid} = +110 V
$V_{accel.}$ = 2.8 kV	I_{grid} = 90 mA
$V_{horiz\ defl.}$ = 150 V	$V_{ent\ grid}$ = ~ +60 V
$V_{vert\ defl.}$ = 145 V	$V_{exit\ grid}$ = +80 V

The chamber is pumped by an AEI JD8 diode ion pump (8 l s^{-1}), a P120 triode ion pump (120 l s^{-1}), and a Vacuum Generators ST2 Titanium Sublimation pump. The pumping speed for inert gases such as argon is only about 20 litre s^{-1} in total and so the background of argon builds up with continuous usage. The system is purged every month or so by letting ~ 10^{-1} torr of air into the system and pumping out through the main chamber. In this way pressures of 5×10^{-9} torr may be achieved although the average working pressure is ~ 5×10^{-8} torr.

To gain an estimation of the detector efficiency, consider the number of molecules reaching the detector and the aperture of the ionizer entrance slit. For OCS at m/e = 60, a beam of 0.06×10^{-7} Amps at E.M. voltage of 1.6 kV is found, at a source pressure of 1×10^{-4} torr. If an angular distribution of $\cos^4\theta$ is assumed[15], then the integration

suggests that $(2.6 \times 10^{18}) \times (1.4 \times 10^{-5}) = 3.6 \times 10^{13}$ molecules s^{-1} reach the ionizer entrance. The ion current corresponds to $20 \times (0.06 \times 10^{-7})/3000 \times (1.6 \times 10^{-19}) = 2.5 \times 10^{8}$ ions s^{-1}. Since ~ 90% of OCS breaks up in the gun and only about 50% of the ions are detected[37], then an ionization efficiency of 0.014% is calculated. The value for inert gases appears to be about ten times larger at about 0.1%. (Commercial instruments have an efficiency of only 10^{-4}%.) This calculated efficiency is about an order of magnitude lower than that found by Weiss[34], though most workers now doubt his figures[35,37].

The resolution of the mass spectrometer system is about one part in a hundred. The background has several large peaks due to the ionizer producing Th^{+} to Th^{5+}, ThO^{+} and ThO^{2+}, due to the thoria coating on the filament. Peaks due to air, water vapour, and the poorly pumped inert gases are also present. These aid calibration of the spectrometer, since the magnet characteristics fluctuate with time, and deviations of 1 to 2 volts at 35 volts (m/e ≃ 100) are usual. The peaks, however, can be a nuisance if they occur at the same m/e as the species being studied.

The signal/noise ratio is given ideally by the equation[34]

$$\left(\frac{N^{2}_{\text{ion beam}}}{N_{\text{total}}}\right)^{\frac{1}{2}} \tau^{\frac{1}{2}} \qquad (2.12)$$

where τ is the detector time constant. For the ion beam discussed, with little background this will be about 10^{4} ($\tau = 10$s). In favourable cases the flop-out beam may actually be detected as a beam flux change in the current, but usually signal/noise ratios are much less. To combat this the radiation is 100% amplitude modulated at 14.3 Hz and the same waveform is fed to a phase-sensitive detection system. The detection system is a Keighly 610CR Electrometer which acts as a low noise amplifier and a Brookdeal 9401 lock-in amplifier (phase sensitive detector/amplifier). A 14 Hz narrow band pass pre-amplifier was also used to avoid overloading the p.s.d.. Time constants of 3 or 10 seconds were usual, with

scanning of the transition in both directions to overcome shifts in the apparent positions of lines due to time constant effects. The scanning speed is such that three or four time constants are allowed for the linewidth. Clearly, in searching for transitions the narrowness of the MBER spectral lines means that noise broadened searches must be carried out to diminish search times.

Sources of radiation are as follows:

(i) Radiofrequency sources

The r.f. source is a Schlumberger 4601 (0-180 MHz) frequency synthesiser. The output is continuous and scan rates can be under either manual or computer control. The arrangement for r.f. work is shown in figure 2.10a. The r.f. source power can be amplified by an Electronic Navigation Industries 40dB broadband power amplifier, and up to 1 W into 50 Ω cable (7 V) is supplied to the C field. The scan time is cut down by applying frequency modulation from an internal 400 or 1000 Hz source in the frequency synthesiser. The d.c. voltage for Stark effect measurements is produced by a Fluke 415B power supply and measured by a Fluke 895A differential voltmeter, (0-1100 V), which is accurate to better than 1 part in 10^4.

(ii) Microwaves sources

Frequencies from 100 MHz to 18 GHz are generated using a Hewlett-Packard HP8620C mainframe with plug-in modules covering the range 0.1 to 18 GHz [38]. Unlevelled power outputs range from 10-50 mW. All the units can be scanned manually or under computer control, as well as being noise broadened at the level of 20 MHz/volt. Usually a 2 kHz sinewave from the r.f. synthesiser is used for this, in a configuration similar to figure 2.10a. All frequency measurements are referred to the timebase of an HP5345A electronic counter (accurate to better than 1 part in 10^8). This consists of a mainframe and a series of plug-in heterodyne converter units for measurements up to 18 GHz. The

a.

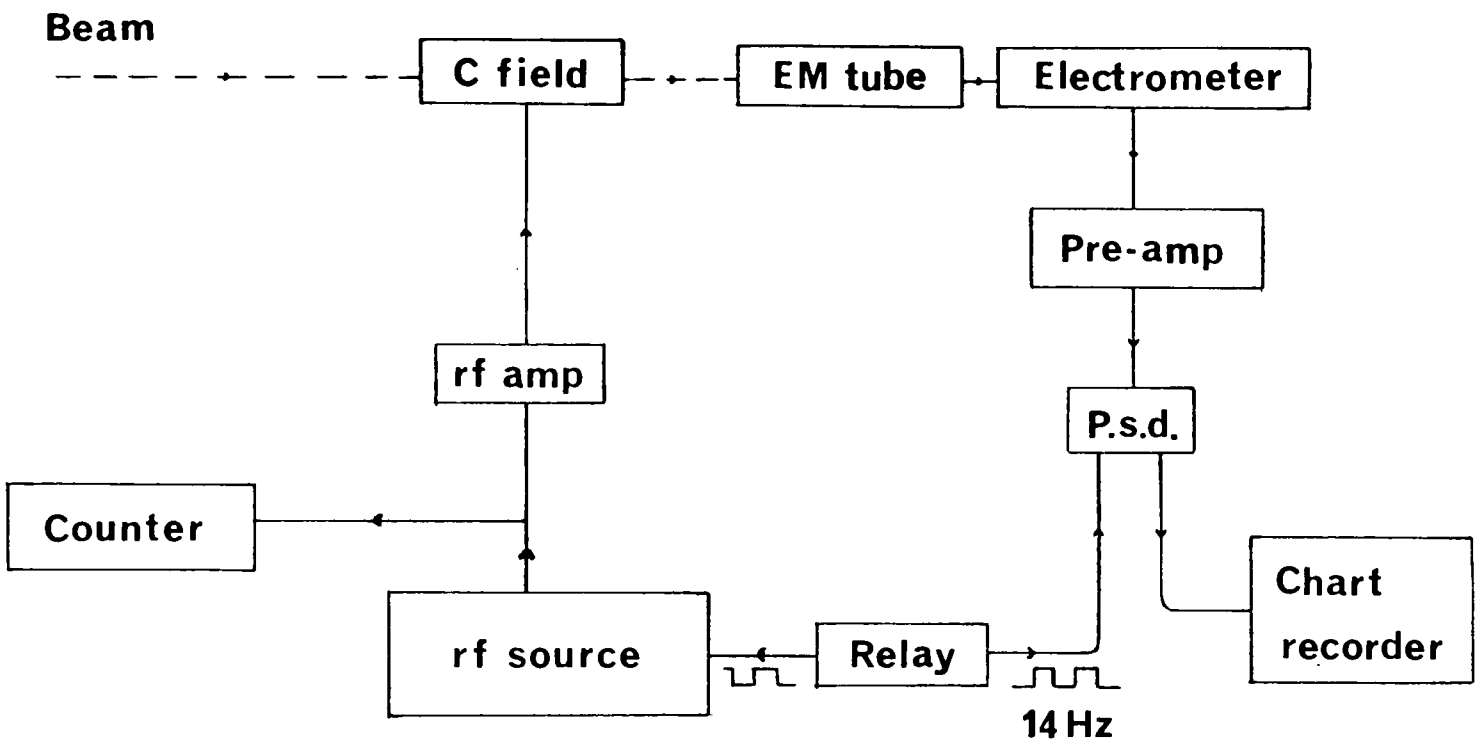

b.

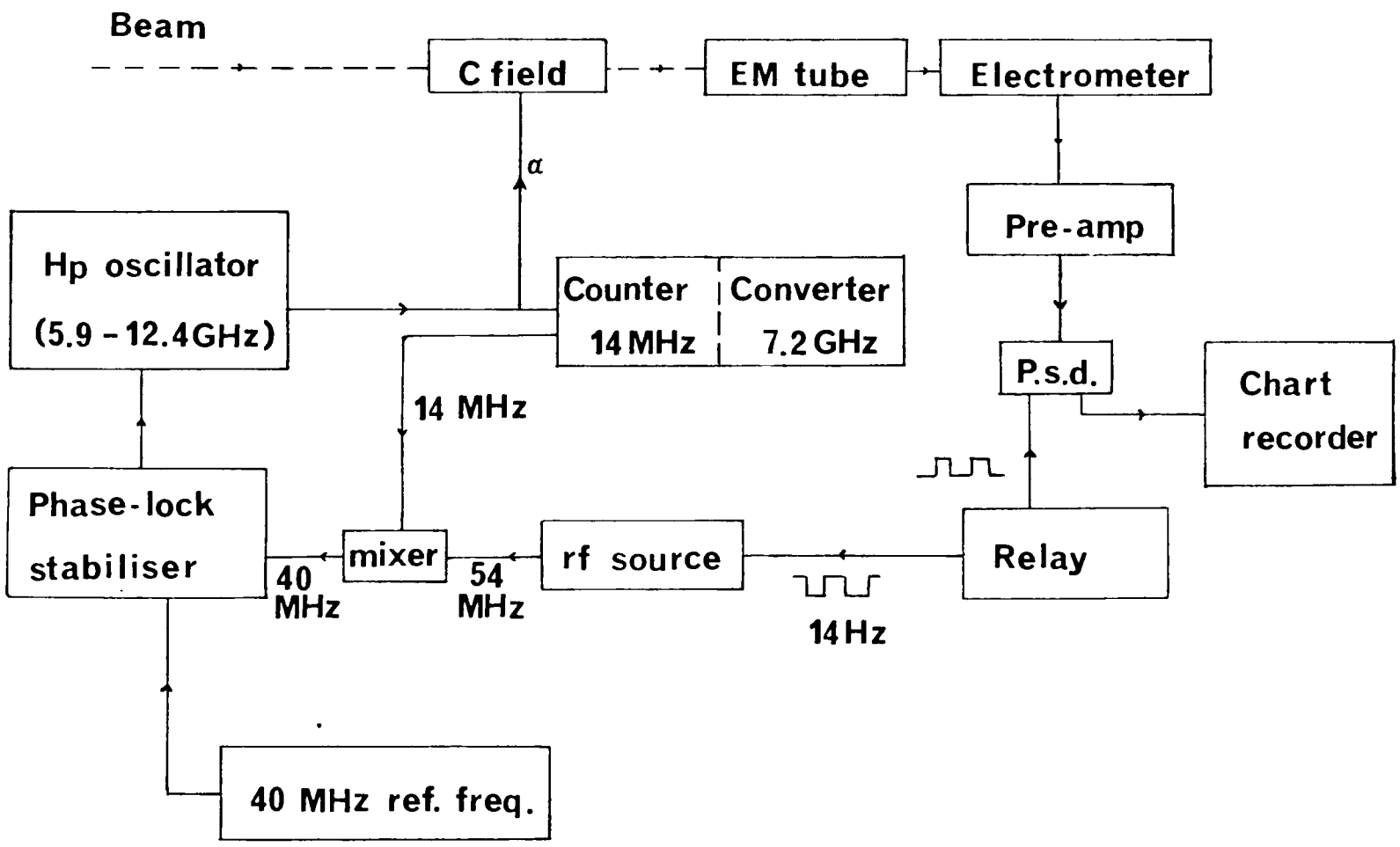

Figure 2.10 a. *Set-up for radiofrequency measurements;*
b. *Set-up for phase-locked microwave measurements.*
α *labels phase-locked 7214 MHz supply.*

heterodyne converters subtract multiples of 50 or 200 MHz from the frequency, and the residual (in the range 0 to 50 or 200 MHz) is supplied to the counter to be measured. The harmonic is indicated by the converter and the residual frequency is available as output (see configuration b, below).

For accurate microwave measurements phase-locking of the frequency source must be used. This employs a feedback system by an error voltage being generated from the difference between a reference frequency and the CW source frequency. The electronics to do this is contained in a Microwave Systems MOS-5 microwave frequency stabiliser. Part of the microwave power from the source oscillator is fed to the stabiliser and mixed with a harmonic of one of ten 15 MHz crystal oscillators (total range 14.998 - 15.113 MHz) such that the beat frequency is ~ 40 MHz. This intermediate frequency (i.f.) is then amplified and compared with a 40.88 MHz stable reference, and the phase difference is used to generate an error voltage which is fed back to the microwave oscillator's frequency control electrode to lock its frequency to that of the crystal frequency. The locked frequency is therefore given by

$$f_L = n\, f_{15} \pm f_{40} \qquad (2.13)$$

where n is the harmonic number, f_{15} is the crystal frequency and f_{40} the reference frequency. The use of the HP counter gives the sign of equation 2.13. Several sources for the f frequencies can be used. (a) The usual configuration is to use the Schlumberger oscillator to provide the f_{40}. This is frequency modulated at 14.3 Hz with a square wave of x volts. On one cycle the dialled frequency will be produced but on the other portion this will be supplemented by an additional frequency $f_{40} + y$ kHz generated internally by the external voltage input of x volts. Two locking frequencies will then be present 180° out of phase with each other. If the 15 MHz crystal is now scanned two flop-out transitions

will be seen separated by y kHz (usually 50-100 kHz) and of opposite phase at the p.s.d.. If the two reference frequencies are measured then two measurements of the transition frequency are available. (b) In this configuration the internal microwave stabiliser crystals are disconnected and the difference frequency of the heterodyne converter of the counter (on the desired harmonic) is fed to a Hatfield mixer (Modulator 1750; 0.1 - 300 MHz, or 1754; 0.01 - 100 MHz). The r.f. oscillator also supplies a frequency about 40 MHz above or below this frequency, and the beat frequency is compared with the internal 40.88 MHz frequency of the stabiliser, which then produces the error voltage. The Schlumberger oscillator supplies the modulation again. Separate calibration of each phase scan must be done. The locked frequency follows variations in the r.f. oscillator frequency. The set-up is shown in figure 2.10b. More stable locks can be generated by this latter method but it is less convenient to use than configuration (a). (c) The configuration is similar to (b), but no modulation is supplied by the Schlumberger oscillator. Modulation is provided by a second Schlumberger oscillator, playing a similar role as in configuration (a)[39]. This allows cumulative phase-locking under computer control, the results being averaged on-line. The computer used is a Varian V71 minicomputer. An example of cumulative phase-locking is shown in figure 2.11 for the $J,F = 3,\frac{5}{2} \rightarrow 2,\frac{3}{2}$ transition of $^{84}KrH^{35}Cl$ (see chapter 4), at 7203.023 MHz. The lines have been broadened to about 20 kHz to show both phases of signal produced by this technique.

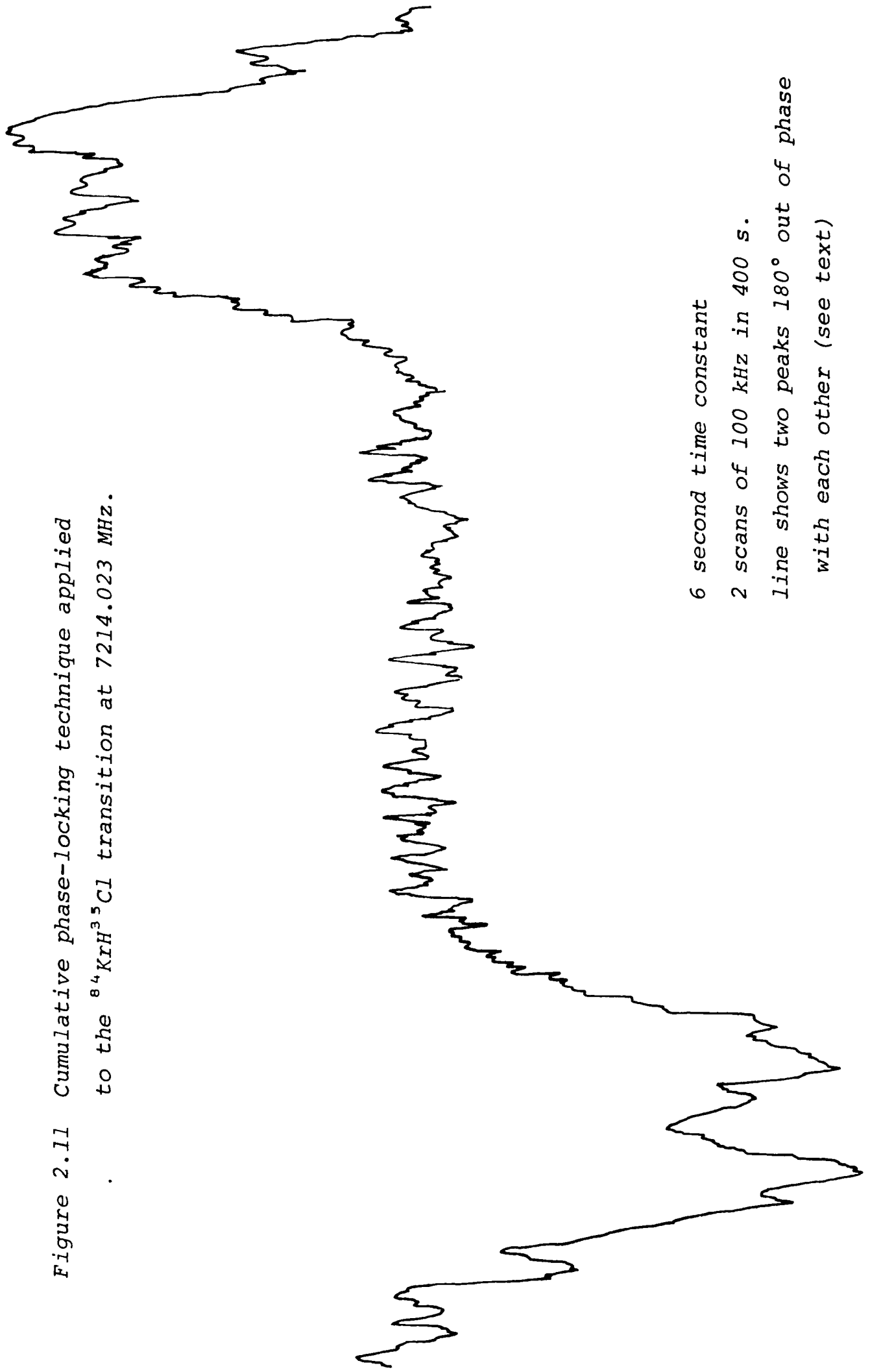

Figure 2.11 Cumulative phase-locking technique applied to the $^{84}KrH^{35}Cl$ transition at 7214.023 MHz.

6 second time constant

2 scans of 100 kHz in 400 s.

line shows two peaks 180° out of phase with each other (see text)

References to Chapter 2

1. I.I. Rabi, Phys. Rev., *51*, 652, (1957); E.W. Kaiser, J. Chem. Phys., *53*, 1686,(1970).

2. J.C. Zorn and T.C. English, in "Advances in Atomic and Molecular Physics", (Academic Press, N.Y., 1973), vol. 9, page 243; in "Methods in Experimental Physics", (Academic Press, N.Y., 1973), vol. 3, part B.

3. P. Kusch and V.W. Hughes, Handbüch der Physik, (Springer-Verlag, Berlin, 1959), vol. 37, page 1.

4. The nozzles were drilled by Harwell engineers, courtesy of D.N. Travis.

5. A.E. Barton, Part II Thesis, (Oxford, 1977); K.C. Jackson, Part II Thesis, (Oxford, 1978).

6. A. Kantrowitz and J. Grey, Rev. Sci. Instrum., *22*, 328, (1951).

7. G.B. Kistiakowsky and W.P. Slichter, Rev. Sci. Instrum., *22*, 333, (1951).

8. N.F. Ramsey, Molecular Beams, (OUP, Oxford, 1956), chapter 2.

9. P.L. Owen and C.K. Thornhill, Aeronautical Research Council, R&M No. 2616, (1948); W.L. Fite, Extranuclear Laboratories Report # 1, (Pennsylvania, January, 1971).

10. J.B. Fenn and J. Deckers, in Rarified Gas Dynamics (Academic Press, N.Y., 1963), vol. 1, page 516; J.B. Anderson and J.B. Fenn, Phys. Fluids, *8*, 780, (1965).

11. W.L. Meerts, G. Ter Horst, J.M.L.J. Reinartz and A. Dymanus, Chem. Phys., *35*, 253, (1978).

12. G.M. McClelland, K.L. Saenger, J.J. Valenti and D.R. Herschbach, J. Phys. Chem., *83*, 947, (1979); T.D. Russell, B. DeKoven, J.A. Blazy and D.H. Levy, J. Chem. Phys., *72*, 3001, (1980).

13. D.N. Travis, J.C. McGurk, D. McKeown and R.G. Denning, Chem. Phys. Lett., *45*, 287, (1977).

14. A.A. Frost and R.G. Pearson, Kinetics and Mechanism, (Wiley, N.Y., 1963), page 63.

15. H. Ashkenas and F.S. Sherman, in Rarified Gas Dynamics, (Academic Press, N.Y., 1966), vol. II, page 84; J.B. Anderson, R.P. Andres, J.B. Fenn and G. Maise, *ibid.*, page 106; Adv. Chem. Phys., *10*, 275, (1966).

16. T.A. Milne, T.A. Vandegrift and F.T. Greene, J. Chem. Phys., *52*, 1552, (1970); D. Golomb, R.E. Good and R.F. Brown, J. Chem. Phys., *52*, 1545, (1970); K. Bier and O. Hagena, Proc. 4th Symp. Rarified Gas Dynamics, *2*, 260, (1966); the disagreement in results is discussed by B.J. Howard in MTP International Review of Science, (Butterworths, London, 1975), vol. 2, chapter 3.

17. W.E. Falconer, A. Büchler, J.L. Stauffer and W. Klemperer, J. Chem. Phys., *48*, 312, (1968).

18. E.W. Kaiser, Ph.D. Thesis, (Harvard, 1969), chapter 3.

19. I.E. Dayton, F.C. Shoemaker and R.F. Mozley, Rev. Sci. Instrum., *25*, 485, (1954); W.C. Elmore and M.W. Garrett, Rev. Sci. Instrum., *25*, 480, (1954).

20. H.G. Bennewitz, W. Paul and C. Schlier, Z. Phys., *141*, 6, (1955).

21. E. Majorana, Nuovo Cimento, *9*, 43, (1932); R.C. Luce and J.W. Trishka, J. Chem. Phys., *21*, 105, (1955).

22. R.W. Wood, Physical Optics, (Macmillan, N.Y., 1934), page 207.

23. R. Weiss, Phys. Rev., *131*, 659, (1963).

24. C.H. Townes and A. Schawlow, Microwave Spectroscopy, (Dover, N.Y., 1975), page 382.

25. A.L. Lance, Introduction to Microwave Theory and Measurement, (McGraw-Hill, N.Y., 1964), chapter 2.

26. B. Fabricant, D. Krieger and J.S. Muenter, J. Chem. Phys., *67*, 1576, (1977).

27. A.H. Kwon, Microwave J., *19*, 61, (1976); D.D. Greig and H.F. Englemann, Proc. Inst. Radio Eng., *40*, 1644, (1952); F. Assadourian, and E. Rimai, Proc. Inst. Radio Eng., *40*, 1651, (1952).

28. R.M. Neumann, Astrophys. J., *161*, 779, (1970).

29. W.L. Meerts and A. Dymanus, J. Mol. Spectrosc., *44*, 320, (1972).

30. K.C. Jackson, P.R.R. Langridge-Smith and B.J. Howard, Mol. Phys., *39*, 817, (1980).

31. T.R. Dyke, G.R. Thomasevich, W. Klemperer and W.E. Falconer, J. Chem. Phys., *57*, 2277, (1972).

32. B.G. Wicke, J. Chem. Phys., *63*, 1035, (1975).

33. J.S. Muenter, J. Chem. Phys., *48*, 4544, (1968). Fields were reversed to check on any offset potentials due to electrostatic effects but these were always < 50 mV.

34. R. Weiss, Rev. Sci. Instrum., *32*, 397, (1961).

35. M. Kaufmann, Ph.D. Thesis, (Harvard, 1969).

36. The tubes deteriorate with use, and a lifetime of around a year is typical before the gain reduces to unacceptable limits (< 500).

37. B.J. Howard, private communication.

38. Hewlett-Packard electronic instruments and systems manual,1978.

39. This second oscillator was kindly loaned by Dr. R. Freeman.

CHAPTER 3: MOLECULAR BEAM ELECTRIC DEFLECTION STUDIES

In addition to the spectroscopic studies that have been done on simple molecular complexes, molecular beam deflection experiments can indicate whether larger polyatomic species are polar or not. This places constraints upon the allowed molecular symmetry and hence the possible molecular structures. With this structural information it is possible to infer the nature of the intermolecular forces that dominate in the complex. It is then interesting to compare similar information about these forces derived from other data. At present this comes mainly from molecular crystal structures. This chapter describes electric deflection studies of the carbon dioxide dimer. A structure for the dimer is proposed and evidence from other experiments and derived structures are compared. A series of deflection studies on other dimers is also described and the validity of structural assumptions commonly made from deflection studies is discussed.

3.1 The carbon dioxide dimer

The structure of the carbon dioxide dimer has been the subject of several theoretical and experimental studies in recent years[1]. Mannik *et. al.*[2] studied the infrared spectrum of the dimer in the region of the CO_2 $(\nu_1, 2\nu_2)$ Fermi doublet at 1300 cm^{-1}. Several sharp peaks about 5 cm^{-1} wide were seen on top of the pressure-induced spectrum. After subtracting a computed profile two sets of peaks were left each about 60 cm^{-1} in total width and of similar shape. They assigned these to ν_1 stretching P, Q, R branches of the dimer, and combination bands $(\nu_1 \pm \nu_5)$ for the dimer in a locked 'T-shape' configuation. ν_1 is the in-phase vibration of the two CO_2 molecules and ν_5 is an out-of-phase libration. From the P,R maxima splitting they obtained a distance of 4.1 $\mathring{A}$ for a T-shaped structure. Novick appeared to confirm this structural prediction by reporting a 1% refocussing of $(CO_2)_2$ in a MBER

spectrometer deflection experiment[3], the polarity being ascribed to quadrupole-induced dipole moments and a slight distortion of the sub-molecule that forms the top of the T. Furthermore, Fredin *et. al.*[4] studied CO_2 trapped in nitrogen and argon matrices at 20 K, and assigned several features to CO_2 dimers in the argon matrix. In solid nitrogen, however, the analysis was less clear, but they concluded from their results that the dimer did not appear to have a centre of symmetry.

Recent theoretical calculations by both Koide and Kihara[5] and Walmsley[6] led to the re-investigation of the polarity of CO_2 dimer by the author, since they both failed to predict the most stable structure for the dimer as T-shaped. The deflection studies presented here are in disagreement with the work of Novick[3]. It is shown that a lack of re-focussing is incompatible with the T-shaped geometry for which a dipole moment of a few tenths of a Debye is expected. It is also shown that a simple quadrupole-quadrupole interaction between molecules would favour a parallel non-polar configuration for the dimerisation of long rod-shaped molecules like carbon dioxide.

(a) Experimental

For these deflection studies the focussing rods described in chapter 2 are used. Mixtures of carbon dioxide (BDH, 99.995%) and argon were expanded through a 35 μm nozzle. Several mixtures were used consisting of various proportions of carbon dioxide from 100% down to less than 5%. The nozzle temperature was varied between 20°C and -78°C with a stagnation pressure of ~ 500 torr. The experiment consists of shadowing the detector by introducing a small stopwire (~ 700 μm diameter) and attempting to deflect the molecules around it by applying a voltage to the focussing fields. A typical composition of an expansion, together with the refocussing characteristics of each oligomer are listed in table 3.1.

Table 3.1 Typical mass spectrum of a carbon dioxide expansion

Mass (m/e)	Ion	Relative Intensity[1]	Refocussing[2] A[3]	Refocussing[2] B[4]
44	CO_2^+	1000	0%[3]	+11.8%
88	$(CO_2)_2^+$	44	-0.9%	+1.5%
132	$(CO_2)_3^+$	6.8	-0.7%	+2.5%
176	$(CO_2)_4^+$	3.8	-1.0%	—

[1]Expanding a 5% CO_2/Ar mixture at -76°C.
[2]Percentage refocussing as a function of the unstopped beam, with a potential of 25 kV applied to the A field and about 20 kV to the B field.
[3]Conditions as for note 1. Using pure CO_2 leads to a defocussing of m/e = 44 of 0.7%.
[4]Expanding a 2% CO_2/Ar mixture at -100°C.

(b) Results

With all mixtures at most temperatures there is no observable refocussing of the $(CO_2)_2$ mass peak (m/e = 88). On decreasing the temperature and percentage of CO_2 in the beam considerably, slight refocussing of $(CO_2)_2$ is seen. Since it seems unlikely that these slight temperature changes can alter the polarity of $(CO_2)_2$ it is believed that the refocussing is caused by the fragmentation of higher polar polymers in the mass spectrometer. As partial verification of this a weak polar peak at m/e = 128 assigned to $Ar(CO_2)_2^+$ is observed under these forcing conditions. Also the trimer peak is observed to be slightly polar. The temperature dependence of the m/e = 44 peak is even more marked. The peak is found to be essentially non-polar above -80°C but further cooling and decreasing the concentration of the CO_2 (to avoid nozzle blocking) causes the peak to become polar. The polarity is due to significant portions of the polar species $ArCO_2$ being formed in the expansion and breaking up in the ionizing gun, to produce CO_2^+ (m/e = 44).

Microwave and radiofrequency spectra have been observed for this complex[7] and using A,B fields of 25,20 kV it is easy to observe two asymmetry doublets at 6 and 32 MHz. It appears likely then that the slight polarity observed by Novick[3] was a result of these higher polar polymers.

Any molecule with an electric dipole moment should possess rotational states with positive Stark effects. In $(CO_2)_2$ contributions from polarisibility terms are about two orders of magnitude lower and so make no contribution.

In reference 1 it was assumed that the percentage refocussing was given by

$$\% \text{ refocussing} \propto \sum_i^+ \frac{(\text{Stark effect})\exp(-\varepsilon_i/kT)}{(\text{partition function})} \qquad (3.1)$$

where the summation is over those states with a positive Stark shift, and applies to a first approximation to underfocussed molecules. This linear dependence on the Stark effect is found experimentally to be approximately true for first-order Stark states, but for states with a second-order effect the onset of refocussing occurs at a particular critical field and is fairly independent of field above and below this value. Using the maximum voltage applied to the A field rods (30 kV) a calculation of the lowest detectable second-order dipole moment is given in appendix A.

A T-shaped $(CO_2)_2$ is a near-prolate symmetric top with an asymmetry parameter, κ, of -0.978, and an estimated rotational constant of 1160 MHz ($\frac{1}{2}(B+C)$). Any induced dipole moment will be along the *a* inertial axis. In appendix A minimum second-order moment is calculated to be 0.075 Debyes for the fastest Stark state. For the $J,M_J = 2,0$ state the reduction of the Stark effect increases this to 0.154 Debyes. However, the focussing of these states will only be seen if around 1% of the beam molecules are in this state. The partition function for a

near-prolate rotor is given approximately by[10]

$$Q_{rot} \simeq \frac{1}{\sigma}\left[\frac{\pi}{A\bar{B}^2}\left(\frac{kT}{hc}\right)^3\right]^{\frac{1}{2}} \tag{3.2}$$

and estimating the A rotational constant as that of CO_2 (11.7 GHz)[11], gives a value of ~ 250 for the dimer at 5 K. This suggests that around ½% refocussing may be seen if the dipole moment is of the order of 0.1 Debye or more, but the refocussing will be difficult to observe.

Not only K = 0 states are populated, but any even value of K is allowed (K odd is forbidden by symmetry and hence $\sigma \sim 2$). In states with $K \neq 0$ the complex produces closely spaced doublets. Their splitting is given by Wang[12] as

$$\Delta W = \frac{b^K (J+K)!}{8^{K-1}(J-K)![(K-1)!]^2}\left[A - \frac{(B+C)}{2}\right] \tag{3.3}$$

where b = (B-C)/(2A-B-C). This splitting decreases rapidly with K but increases relatively slowly with J. As a consequence, interaction between two of these asymmetry doublets will lead to a first-order Stark effect when $\Delta W < \mu EMK/J(J+1)$, but a second-order effect when $\Delta W > \mu EMK/J(J+1)$. The focussing characteristics of a molecule in a first-order Stark state are different from the harmonic force felt by a molecule in a second-order Stark state. The molecule with a first-order moment experiences a force given by[13]

$$F = -\nabla W = \left(\frac{\mu MK}{J(J+1)}\right)\cdot\frac{V}{R^2}\cdot\frac{r}{r} \tag{3.4}$$

The focal length of the quadrupole lens now depends on the entrance angle θ of the molecule into the electric field. To obtain an approximate value for the lowest detectable first-order moment it is necessary to compare the focussing characteristics of $(CO_2)_2$ with that of a symmetric top, for example CH_3Cl. If the dipole moment is of the order of 10^{-2} Debyes first-order states are expected for almost all the rotational levels with K > 2 that are significantly populated. Such states provide

the dominant contribution to the sum in equation 3.1. If an unfavourable case of the pure CO_2 expansion is taken where $T_{rot} \sim 30$ K [14] the evaluation of expression 3.1 gives a refocussing proportional to 0.060 μE (see appendix A) where E is some effective field seen by the molecules in the A and B fields. Comparing with methyl chloride for which all first-order Stark states may be refocussed by A,B = 2,2 kV, this suggests that a refocussing of 1% should be expected for a dipole moment of 0.005 Debyes. A better comparison can be made with $ArCO_2$ [7] which is very similar in its values of rotational constants: A = 11914(80) MHz, B = 1979.87(25) MHz, and C = 1682.75(70) MHz. Corresponding asymmetry splittings are therefore very similar. Under conditions that favour $ArCO_2$ formation a 12% refocussing is seen. A dipole moment from low-field second-order Stark tracking is 0.06793(20) Debyes, with optimised A,B fields of 25,20 kV. Therefore a 1% refocussing would suggest a dipole moment of 0.0057 Debyes, in good agreement with the value above. It is also possible to detect refocussing of CH_3D which is a symmetric top with a dipole moment of 5×10^{-3} Debyes[15]. A lower bound to the dipole of $(CO_2)_2$ of 10^{-2} Debyes therefore seems reasonable.

(c) Dipole moment of T-shaped $(CO_2)_2$

A major contribution to the dipole moment of the T-shaped dimer is that dipole induced in each monomer by the electric field from the electrostatic moments of the other. If only fields due to the quadrupole moment are considered (the first non-vanishing multipole moment) then the induced dipole is given by

$$\mu_{ind} = 3\alpha_{\perp}\frac{Q}{R^4} + \frac{3}{2}\alpha_{\parallel}\frac{Q}{R^4} = 0.182 \text{ Debyes} \qquad (3.5)$$

where $\alpha_{\parallel} = 4.05$ Å^3 and $\alpha_{\perp} = 1.95$ Å^3 [5], are the parallel and perpendicular components of the molecular polarisability, $Q = -4.32 \times 10^{-26}$ esu cm^2 [16] and R = 4.1 Å [2]. If proper account is taken of the total charge distribution in carbon dioxide and if HOMO-LUMO charge transfer is allowed

between the two molecules an even larger dipole moment is expected. This result was checked by performing three SCF calculations on the dimer with a Slater double zeta, a 4-31G, and a 6-31G basis set, using the value of R given above[17]. These gave values of 0.25, 0.37, and 0.32 Debyes respectively. The first two basis sets usually give poor estimates of dipole moments of monomers (30 - 50% error) but 6-31G usually provides better estimates (10 - 30%), the latter usually too high[18]. Although the calculated moments are small they are the result of interaction of two identical non-polar closed shell molecules and therefore the errors suggested by calculations on monomers may be more appropriate than those for dimers. With such a large moment (~ 0.25 D), the T-shaped dimer should be easily refocussed in the spectrometer, especially in view of the refocussing that is easily achieved for the $ArCO_2$ complex.

(d) Discussion

Koide and Kihara[5] and Walmsley[6], both using model potentials predicted a parallel structure for the dimer. The first study utilised second virial coefficient data to fit a Kihara potential (a modified Lennard-Jones potential)[19], with an additional long range multipole expansion for the attractive part. The latter study fitted an exp-6 with additional multipole attractive terms to crystalline carbon dioxide data, as well as attempting CNDO and 4-31G calculations on the dimer. The derived equilibrium structures and well depths are given in table 3.2. The *ab initio* calculations are almost certainly subject to the dimerisation energy errors indicated in chapter 1. The stability of the dimer may be understood in terms of the long range quadrupole-quadrupole interaction[16]. This takes the form

$$V_{QQ} = \frac{3}{4}Q^2R^{-5}(1 - 5\cos^2\theta_1 - 5\cos^2\theta_2 + 17\cos^2\theta_1\cos^2\theta_2 + 2\sin^2\theta_1\sin^2\theta_2\cos^2\phi - 16\sin\theta_1\cos\theta_1\sin\theta_2\cos\theta_2\cos\phi) \qquad (3.6)$$

where θ_1, θ_2 is the angle that each molecule makes with the C-C axis, and R is the C-C separation. Although a multipolar series is not fully convergent at small values of R (R ≃ 2 or 3 times the C-O bond length) a large fraction of the attractive part of the well is due to this interaction (see table 3.2).

Table 3.2 Calculated stability of parallel and T-shaped configurations

Method	R/Å	θ/degrees	$U_{parallel}$ /kJ mol^{-1}	U_{par}/U_T
Kihara	3.8	55	5.65	1.50
Walmsley empirical	3.47	60	5.44	1.37
4-31G	3.5	55	9.76	1.66[1]
Simple hard core/ quadrupole	3.44	57	4.85	1.66

[1]For 6-31G the value is 1.11.

At fixed intermolecular distance R, equation 3.6 leads to a minimum energy of $-3Q^2/R^5$ for the T-shaped structure. However there is a second minimum of $-2.3Q^2/R^5$ at the staggered parallel geometry; $\theta_1 = \theta_2 = \cos^{-1}(3^{-\frac{1}{2}}) = 54.7°$. In this second configuration the monomers can approach closer to each other before they experience strong repulsion. As a result the parallel staggered form can become the most stable structure, according to this model.

To test this suggestion further a simple potential surface for the carbon dioxide dimer was constructed, treating each molecule as a hard core capsule of radius one half of the sum of the van der Waals radii of carbon and oxygen, and using only the quadrupole-quadrupole attractive force. Minimisation of the energy of equation 3.6 subject to the

condition of closest approach leads to a minimum energy configuration of -4.85 kJ mol^{-1} at $R = 3.44$ Å, $\theta_1 = \theta_2 = 57.4°$.

In crystalline CO_2 the orientations are such that the quadrupole-quadrupole energy is a minimum[20,5]. This is such that nearest neighbours are orientated in a severely distorted T-structure and second nearest neighbours are in the parallel staggered arrangement[21]. This also suggests that a hard sphere repulsive/quadrupole attractive potential should represent the CO_2-CO_2 interaction well.

Subsequent to the completion of these deflection studies[1] Guasti *et. al.*[22] published a study of the geometry of CO_2 dimer trapped in Ar, Kr, and Xe rare gas solids. They showed that some of the peaks attributed to $(CO_2)_2$ by Fredin[4] in the argon matrix were due to impurities of water, and that two substitutional sites exist for CO_2 in the argon matrix. For the heavier inert gases, simpler spectra were obtained which showed that in the ν_3 (antisymmetric stretching) region of CO_2, a single dimer peak is observed to higher frequency of the monomer, and in the ν_2 (bending) region peaks occurred either side of the monomer peak. Selection rules and semi-quantitative calculations using a resonant dipole-dipole interaction model indicated that for the T-shaped dimer and for a dimer in a twisted configuration, peaks should be observed only to lower frequency of the CO_2 monomer in the ν_2 region. For the parallel staggered arrangement, however, transitions to higher frequency should also be observed. They concluded that the latter structure occurs in matrix isolation studies.

This appears to discredit the assignment by Mannik *et. al.*[2] of their infrared spectra. The collisional line broadening width Γ (see chapter 1) in their experiment is ~ 6000 MHz and so no rotational fine structure could be determined. A re-analysis of the spectra in this region would be helpful, especially at higher resolution *e.g.* molecular beam diode laser measurements, (see chapter 1). At present then, a parallel

staggered arrangement of monomers appears to be the structure of $(CO_2)_2$.

3.2 Bonding in van der Waals dimers

The success of such a simple hard sphere model as outlined above leads one to ask whether other anisotropic potentials may be similarly characterised. Other deflection studies (see table 3.3) have led to the establishment of two theories as to the dominant effects that determine dimer structures. Klemperer[23,24] has proposed that the equilibrium structures of complexes can be understood using the HOMO-LUMO approach of Mulliken[25]. This donor-acceptor view of bonding clearly emphasises the role of charge transfer in the complex. This theory was proposed for two main reasons: (a) Most hydrogen bonded species, for example $(HF)_2$, HFHCl, HFClF[26] exhibit a ground state geometry of approximately the tetrahedral angle for the external hydrogen (*i.e.* $\angle$HF-HCl ~ 110°) and this corresponds to the overlap of tetrahedrally oriented lone pairs on HF with orbitals on the acceptor molecule. (b) Dipole-induced dipole forces appear to favour a linear structure for ArOCS, whereas a T-shaped structure was found experimentally[27]. Electron donation by argon into the lowest unfilled molecular orbital on OCS, which is predominantly on carbon, predicted the correct result.

The bond in the polar $(Cl_2)_2$, for which an L-shaped structure was suggested[23] could then be described as a π donor $\rightarrow \sigma^*$ acceptor. From the initial supposition of a T-shaped structure for $(CO_2)_2$, it was described as a $\pi \rightarrow \pi^*$ interaction.

The second main theory was the use of a classical electrostatic picture and *ab initio* studies. For these complexes the results of the SCF energy decomposition of Morokuma[28] indicated that the electrostatic term in the total SCF binding energy determines the equilibrium geometries. The total energy is decomposed into electrostatic, charge transfer, exchange repulsion, polarisation and smaller coupling terms. Although initially used for describing hydrogen bonded systems,

Kollman[29] extended the study to other van der Waals species at the 4-31G level. For both these types of systems it was found that effects due to exchange repulsion terms and charge transfer terms tended to cancel each other out approximately, leaving the anisotropy of the electrostatic terms to determine the equilibrium geometry. Pauling explained the effect by suggesting that since any charge transfer is to a species with filled valence orbitals, charge transfer and exchange repulsion terms should largely cancel[30]. Kollman found that by describing the electron distribution as a series of point charges (at lone pair positions, for example) from *ab initio* charge distributions or multipole moments, one was able to predict the correct equilibrium structure of many complexes.

Table 3.3 Electric deflection data for van der Waals molecules

Polar	Very weakly polar (< 1% refocussing)	Non-polar
$(Cl_2)_2$, $(Br_2)_2$, $(I_2)_2$ [1]	$(F_2)_2$ [1]	$(ClCN)_2$ [4]
$(benzene)_2$ [2]	$(BrCN)_2$ [4]	$(SO_2)_2$
$(hexafluorobenzene)_2$ [2]		$(CS_2)_2$
benzene-hexafluorobenzene[2]		$(HNO_3)_2$ [7]
$(OCS)_2$, $(N_2O)_2$ [3]		most trimers etc.
$(ClF)_2$ [1]		
$(ICN)_2$ [4]		
$(ICl)_2$, $(ICl)_3$ [1]		
$(NH_3)_2$ [5], $(H_2O)_2$ [6]		

[1]ref[31]; [2]ref[32]; [3]ref[33]; [4]ref[34]; [5]ref[35]; [6]ref[36]; [7]ref[37].

In a similar manner to $(CO_2)_2$, a hard sphere electrostatic potential energy surface does appear to predict correct equilibrium

geometries for many complexes. For example, in ArOCS the dipole-induced dipole attraction due to the OCS dipole moment is proportional to $4\mu^{OCS}\alpha^{Ar}R^{-6}$ in the linear configurations, and $\mu^{OCS}\alpha^{Ar}R^{-6}$ in the T-shaped configuration. A linear structure might at first sight be predicted, but in the T-shaped complex the argon and OCS molecule can approach more closely than for the linear configurations. If this distance factor is greater than $4^{\frac{1}{6}} \simeq 1.26$ then the T-shaped structure is preferred. For ArOCS the ratio is 1.33, and for ArSCO it is 1.28 using van der Waals radii and experimental bond lengths. So in a similar manner to $(CO_2)_2$ the correct structure is predicted for ArOCS. A similar structural prediction is given for ArMeCl which is experimentally observed to be an asymmetric top[38], and for ArO_3[39]. The equilibrium structures of benzene dimer and hexafluorobenzene dimer are T-shaped[32]. The dominant quadrupole moment may again suggest a parallel staggered (and hence non-polar) arrangement as favoured over a T-shaped structure. However since the molecular dimensions are of the order of the monomer separations, more complex charge distributions may be required. For the mixed dimer however, since the quadrupoles have opposite signs[40], a parallel plate oblate rotor is predicted, and is found experimentally[32]. HOMO-LUMO theory appears unable to predict such structures.

Molecular crystal structures are often described using the same two theories[41]. The crystal structures of complexes which form a 'molecular' type of crystal (for example, chains of monomer units) often have structures which correlate with deflection structures. One form of ICl[21] has an assemblage in which pairs of ICl molecules form an L-shaped structure. A polar dimer is found[31]. Similar structures with chains of these L-shaped units are found for the heavier halogens. Whilst a simple hard sphere repulsive/electrostatic model is unable to predict such structures, Kollman was able to predict such structures using his point charge model. Fluorine has a different crystal structure to the

other halogens, being a layered structure. Nearest neighbours approximately form a square arrangement. The $(F_2)_2$ is correspondingly barely refocussable[31]. Non-polar equilibrium structures are predicted by both Kihara[5] and Morokuma[28].

The structures of halogen cyanides consist of chains of monomer units head to tail. The units overlap at their van der Waals radii. The chains are separated by distances similar to the van der Waals radii. In ClCN[42] the chains are antiparallel, and a non-polar dimer is formed[34]. In the crystal structure of ICN[43], the chains are parallel and a polar dimer should result, which is found[34]. For BrCN the chains are antiparallel again[44], but a slightly polar complex is found. Similarly for OCS which has a related crystal structure with parallel chains[45], a polar dimer is found and a staggered parallel structure predicted. HOMO-LUMO theory is unable to predict these results, and SCF energy decompositions indicate that as the dipole moment of the molecule increases a greater likelihood of a non-polar centrosymmetric complex exists[29], whereas the opposite is true for the cyanogen halides[46].

Some similarities also exist with the nearest neighbour liquid phase orientations. In liquid benzene the distribution function indicates a favoured T-shaped arrangement[47], while a similar study in liquid CS_2 indicated a preferable parallel arrangement[48], as in solid CS_2[49]. A non-polar CS_2 dimer was seen in deflection studies[50].

In conclusion then, it appears that each model is only partially successful in predicting dimer structures. The problems associated with determining dimerisation energies at the 4-31G level may account for some of the failures of the electrostatic theory[28,29]. An example of this is the stability of HF..ClF versus ClF..HF. Including polarisation functions (to the 4-31G** level) reverses the predicted relative stability and the lowest energy is predicted for the HFClF form which is found experimentally[26]. Larger basis sets including correlation

effects would be useful but expensive.

The theories may be unified to a certain extent by observing that models based on electron distributions produce the lowest energies when the monomers approach each other at orientations such that the regions of excess electronic charge on one monomer approach regions deficient in electronic charge on the other. These positions will often correspond to the positions of occupied and unoccupied molecular orbitals respectively on the monomer.

It should also be mentioned that the results of beam deflection studies may not always give the identity of the equilibrium structure for the complex. Although a non-polar dimer formed from non-polar monomers excludes a polar dimer ground state, the observation of polar dimers from polar or non-polar monomers does not exclude non-polar structures for the potential minima. This may be the case for $(F_2)_2$ and $(BrCN)_2$ where only weak focussing is seen. The beam expansion may well contain a more stable non-polar species, since the expansion freezes out thermodynamic parameters and is not at equilibrium. On a multidimensional potential surface several wells may occur and a corresponding mixture of structures may be present in the expansion. An example of this non-equilibrium effect is for the expansions of 1,2-difluoroethane and methyl nitrite[52]. In methyl nitrite the high conformational barrier (2 kcal mol^{-1}) inhibited a significant cooling of the conformer distribution, but for 1,2-difluroethane with a smaller barrier (0.6 kcal mol^{-1}) significant cooling occurred. Large barriers to interconversion of van der Waals dimer 'conformations' may lead to the freezing out of less stable polar species, and an incorrect assignment of equilibrium structures.

References to chapter 3

1. A.E. Barton, A. Chablo and B.J. Howard, Chem. Phys. Lett., *60*, 414, (1979).

2. L. Mannik, J.C. Stryland and H.L. Welsh, Can. J. Phys., *49*, 3056, (1971).

3. S.E. Novick, P.B. Davies, T.R. Dyke and W. Klemperer, J. Am. Chem. Soc., *95*, 8547, (1973).

4. L. Fredin, B. Nelander and G. Ribbegård, J. Mol. Spectrosc., *53*, 410, (1974).

5. A. Koide and T. Kihara, Chem. Phys., *5*, 34, (1974).

6. N. Brigot, S. Odiot, S.H. Walmsley and J.L. Whitten, Chem. Phys. Lett., *49*, 157, (1977).

7. J.M. Steed, T.A. Dixon and W. Klemperer, J. Chem. Phys., *70*, 4095, (1979).

8. T.R. Dyke, B.J. Howard and W. Klemperer, J. Chem. Phys., in the press; B.J. Howard, private communication.

9. G.M. McClelland, K.L. Saenger, J.J. Valenti and D.R. Herschbach, J. Phys. Chem., *83*, 947, (1979); T.R. Dyke, G.R. Thomasevich, W. Klemperer and W.E. Falconer, J. Chem. Phys., *57*, 2277, (1972).

10. G. Allen and H.O. Pritchard, Statistical mechanics and Spectroscopy, (Butterworths, London, 1974).

11. B.P. Stoicheff, Adv. Spectrosc., *1*, 91, (1959).

12. S.C. Wang, Phys. Rev., *34*, 243, (1929).

13. R.A. Berg, L. Wharton, W. Klemperer, A. Büchler and J.L. Stauffer, J. Chem. Phys., *43*, 2416, (1965).

14. D.N. Travis, J.C. McGurk, D. McKeown and R.G. Denning, Chem. Phys. Lett., *45*, 287, (1977).

15. S.C. Wofsy, J.S. Muenter and W. Klemperer, J. Chem. Phys., *53*, 132, (1970).

16. A.D. Buckingham, Adv. Chem. Phys., *12*, 132, (1967); J.A. Pople, Proc. Roy. Soc. A, *221*, 508, (1954).

17. A. Chablo, Part II Thesis, (Oxford, 1978).

18. J.D. Dill, L.C. Allen, W.C. Topp and J.A. Pople, J. Am. Chem. Soc., *97*, 7220, (1975).

19. T. Kihara, Adv. Chem. Phys., *5*, 147, (1963).

20. A.D. Buckingham, Quart. Rev. Chem. Soc., *13*, 183, (1959).

21. R.W.G. Wyckoff, Crystal Structures, (Interscience, N.Y., 1963), vol. I, page 368.

22. R. Guasti, V. Schettino and N. Brigot, Chem. Phys., *34*, 391, (1978).

23. S.J. Harris, S.E. Novick, J.S. Winn and W. Klemperer, J. Chem. Phys., *61*, 3866, (1974).

24. K.C. Janda, J.M. Steed, S.E. Novick and W. Klemperer, J. Chem. Phys., *67*, 5162, (1977).

25. R.S. Mulliken and W.B. Person, Molecular Complexes, (Wiley, N.Y., 1969).

26. T.R. Dyke, B.J. Howard and W. Klemperer, J. Chem. Phys., *56*, 2442, (1972); K.C. Janda, J.M. Steed, S.E. Novick and W. Klemperer, J. Chem. Phys., *67*, 5162, (1977); S.E. Novick, K.C. Janda and W. Klemperer, J. Chem. Phys., *65*, 5115, (1976).

27. S.J. Harris, K.C. Janda, S.E. Novick and W. Klemperer, J. Chem. Phys., *63*, 881, (1975).

28. K. Morokuma, J. Chem. Phys., *55*, 1236, (1971); H. Umeyama and K. Morokuma, J. Am. Chem. Soc., *99*, 330, (1977); *ibid.*, *99*, 1316, (1977).

29. P. Kollman, J. Am. Chem. Soc., *99*, 4875, (1977).

30. L. Pauling, in Hydrogen Bonding, ed. D. Hadzi, (Pergamon, N.Y., 1959).

31. K.V. Chance, K.H. Bowen, J.S. Winn and W. Klemperer, J. Chem. Phys., *72*, 791, (1980).

32. J.M. Steed, T.A. Dixon and W. Klemperer, J. Chem. Phys., *70*, 4940, (1979).

33. A.E. Barton, Part II Thesis, (Oxford, 1977); Subsequent studies at low r.f. frequencies have shown first-order Stark effects for either ℓ-doublets (linear structure) or asymmetry doublets (asymmetric top). No microwave frequencies have been found at present.

34. P.R.R. Langridge-Smith, unpublished results.

35. J.A. Odutola, T.R. Dyke, B.J. Howard and J.S. Muenter, J. Chem. Phys., *70*, 4884, (1979).

36. T.R. Dyke and J.S. Muenter, J. Chem. Phys., *57*, 5011, (1972).

37. J.A. Odutola and T.R. Dyke, J. Chem. Phys., *68*, 5663, (1978).

38. J.M. Steed, L.S. Berstein, T.A. Dixon, K.C. Janda and W. Klemperer, J. Chem. Phys., *71*, 4189, (1979).

39. R.L. DeLeon, K.M. Mack and J.S. Muenter, J. Chem. Phys., *71*, 4487, (1979).

40. J.S. Brennan, N.M.D. Brown and F.L. Swinton, J.C.S. Faraday I, *70*, 1965, (1974); F.L. Swinton, private communication.

41. H.A. Bent, Chem. Rev., *68*, 587, (1968).

42. R.B. Heiart and G.B. Carpenter, Acta. Cryst., *9*, 889, (1956).

43. J.A.A. Ketelaar and J.W. Zwartsenberg, Rec. Trav. Chim., *58*, 449, (1939).

44. S. Geller and A.L. Schawlow, J. Chem. Phys., *23*, 779, (1955).

45. L. Vegard, Z. Physik, *58*, 497, (1929).

46. C.H. Townes and A.L. Schawlow, Microwave Spectroscopy, (Dover Press, N.Y., 1975), page 30.

47. L.L. Lowden and D. Chandler, J. Chem. Phys., *61*, 5228, (1974); A.H. Narten, J. Chem. Phys., *48*, 1630, (1968).

48. K. Suzuki and P.A. Engelstaff, Can. J. Phys., *52*, 241, (1974).

49. N.C. Baenzeger and W.L. Duax, J. Chem. Phys., *48*, 2974, (1968).

50. A 10% mixture of the study gas in argon was prepared, and expanded at various temperatures, in a similar manner to $(CO_2)_2$.

51. H. Lischka, J. Am. Chem. Soc., *96*, 4761, (1974).

52. P. Felder and Hs.H. Günthard, Chem. Phys. Lett., *66*, 283, (1979).

CHAPTER 4: THE KRYPTON-HYDROGEN CHLORIDE SYSTEM

4.1 KrHCl isotopes

(a) Introduction

The work that is presented in this chapter arises from a desire to obtain as much information about the structure and dynamics of van der Waals molecules as possible from MBER spectroscopy[1]. Following Klemperer's pioneering investigation of ArHCl[2,3], it seemed appropriate to attempt to study KrHCl since krypton itself has a wealth of isotopes, and hence the effects of isotopic substitution of all three atoms could be found. Also, during the course of this work, in an attempt to explain all the information contained in the experimental results (to the level of the 1 kHz resolution) several new molecular parameters were obtained. These subsequently led to a deeper understanding of the dynamics of atom-diatom systems than Klemperer had been able to achieve with his early work.

The earliest studies on the subject of atom-diatomic molecule interactions were limited to the perturbation effects of the inert gas atom upon properties of HCl. These included the rotation and rotation-vibration spectra of HCl and DCl in inert gas matrices[4], as well as the broadening effects and frequency shifts of pure rotation and rotation-vibration lines of gaseous HCl[5]. This early work gave little direct information on the inert gas-HCl interaction. More recently work has been done on rotational energy transfer in inert gas-HCl collisions[6], the cross-sections being compared with trajectory calculations over several simple potential surfaces.

Van der Elsken and co-workers have been studying the KrHCl interaction in the far infrared by measuring the line broadening and frequency shifts of the HCl low-J monomer transitions in the presence of the inert gas using FT IR spectroscopy[7]. This readily provided

cross-sections for line broadening; these were used to fit parameters for trial model potentials using semiclassical line broadening theories[8]. The authors fitted the limited KrHCl data to a Lennard-Jones (12-6) pseudodiatomic radial potential and a truncated Legendre expansion for the angular potential. It will be shown in a later chapter that the potentials derived in this way are generally far too anisotropic in the attractive region of the potential and not nearly anisotropic enough at the repulsive wall to reproduce MBER data, as well as giving the wrong sign for the angular-radial coupling effect. The group have also given a preliminary understanding to the far infrared spectra of X..HCl in terms of an angular potential alone[9], which predicts angular barrier heights to free internal rotation for X..HCl (X = Ar, Kr, Xe) which agree remarkably well with barriers estimated from fitting the MBER data, (see chapter 7).

Few other krypton systems have been studied that warrant inclusion as studies of van der Waals forces. KrClF has been studied by MBER spectroscopy[10]. In this molecule with its massive diatomic molecule, angular motion is very much more restricted than in KrHCl, and the molecule can be analysed as a linear triatomic molecule with a weak bending vibration frequency (see, for example, table 6 of reference 10). Welsh has studied the infrared spectrum of KrH_2 and KrD_2[11], and Kr..NH and OH interactions have been studied by resonance fluorescence spectroscopy of the trapped radicals in rare gas matrices[12]. In this study non-pairwise additive effects that are seen are indicative of specific Kr-radical interactions, but as in most cases the effects of the matrices are not clear and assignment of effects due to these single Kr..HX interactions are somewhat tentative.

Subsequent to the completion of our work on KrHCl, Flygare and co-workers published an elegant study of the J = 3$\leftrightarrow$4 and 4$\leftrightarrow$5 microwave transitions of KrHCl (12 isotopes were studied in all) by pulsed

molecular beam/pulsed FT microwave spectroscopy[13]. His transitions at 9 and 11 GHz have half width at half maximum (HWHM) of 5 - 10 kHz. Although HWHMs at 9 GHz are about 10 - 30 kHz for our MBER machine, linewidths of 5 kHz are readily achieved at lower frequencies. The lack of resolution in his apparatus (for example, no discrete deuterium quadrupole structure was observed in the spectra) led him to ignore the effects that are described in this chapter. His data has been included, however, in some fitting, to de-correlate B and D_J values (section 4.5).

(b) Experimental

KrHCl was produced by expansion of 4% of HCl (BDH, 99.0%), and 25% krypton (B.O.C., C.P. grade), and neon (B.O.C., C.P. grade) through a 50 μm diameter Monel nozzle cooled by liquid N_2. The temperature of the source was kept around 150 K, with no skimmer being used as usual. An increase in the amount of HCl in the mixture led to increases in HCl polymer formation which cut down the KrHCl formation at these low temperatures. With an estimated stagnation pressure of 500 torr behind the nozzle the optimum temperature was about 30 K above that at which extreme condensation and consequent nozzle blocking occurs. Neon was chosen as the major carrier gas in order to facilitate rotational cooling during the isentropic expansion and to prevent formation of krypton clusters. Also initial refocussing studies on this system using argon as the carrier gas[14] led to interference of the mass spectra of KrHCl at around m/e = 120 by ArKr dimers (and polymers, $Ar_n Kr_m^{r+}$). The range of temperatures over which the spectra could be taken with adequate signal/noise ratios was only about ±20 K.

All spectra were recorded on the parent ion mass peaks ($KrHCl^+$) which are shown for the major isotopes in table 4.1. A typical mass spectrum is shown in figure 4.1. The absolute magnitudes of the ion currents varied by a factor of 10 over the period taken to obtain the spectra, but typical values for ion currents and refocussing

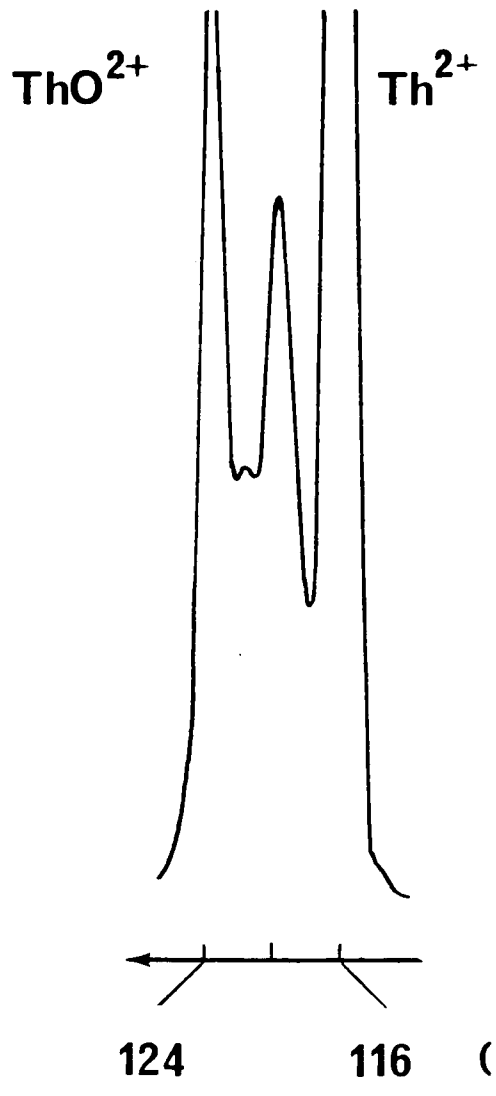

Figure 4.1 Mass spectrum of KrHCl isotopes

characteristics are given in table 4.2. Maximum refocussing, at about A and B fields of 20 and 15 kV respectively, could vary from 80 - 110% of the straight through beam, and reflects slight changes in the expansion conditions from day to day. The intensities of the peaks for krypton, neon and HCl provided a good check on the composition of the mixture.

(c) Results

If a similar structure is postulated for KrHCl to that found for ArHCl then a similar inert gas-HCl centre of mass separation yields a B value of 1.25 GHz while using half the separation difference of the interatomic distances in Ar_2 and Kr_2, 0.125 Å,[15] gives a value of 1.19 GHz. The $J = 0 \rightarrow 1$ transition at 2B was searched for by Henderson[14]

Table 4.1 Isotopic abundances in KrHCl (abundance > 5% of total)

Complex	Mass no.	% of total
$^{82}KrH^{35}Cl$	118	8.7
$^{83}KrH^{35}Cl$	119	8.7
$^{84}KrH^{35}Cl$	120	43.0
$^{86}KrH^{35}Cl$	122	13.1
$^{84}KrH^{37}Cl$	122	13.2

and a feature at ~ 2.41 GHz (noise broadened to ~ 10 MHz line width) was identified, with a signal/noise ratio of little more than 1:1. In view of the poor signal/noise ratios (improved by a factor of ~ 30 principally because of improvement of rotational cooling in the present generation of nozzles) and the author's observations of the difficulty of obtaining the $0 \rightarrow 1$ transition on KrHCl which required exact beam alignment due to aperture effects, the agreement with the line position quoted here is

Table 4.2 Ion currents and refocussing characteristics of KrHCl (at m/e = 120).

		Ion current (Amps)[1]	% refocussing
'straight through' beam		0.0066×10^{-7}	
'stopped' beam		0.0010×10^{-7}	
refocussed beam	A,B = 5,3 kV	0.0021×10^{-7}	20
	10,6	0.0036×10^{-7}	46
maximum refocussing	21,14	0.0064×10^{-7}	96

[1]Currents measured with electron multiplier tube voltage of 1.6 kV.

probably fortuitous.

The first transitions conclusively found were the $J = 2 \rightarrow 1$ transitions at 4.8 GHz, using 3 MHz noise broadened scans with the Hewlett-Packard sweep oscillators and the Varian V71 minicomputer for on-line signal averaging. Transitions found in this way were then recorded with ~ 1 MHz noise broadening and the line centre estimated. This provided a much needed good estimate of the line centre since scanning 1 MHz phase-locked (using the crystal harmonic generator method) with a time constant of 10 s would require ~ ½ hr. The method employed usually determined the line centre to < 100 kHz.

The zero-field microwave frequencies for the KrHCl species studied are shown in table 4.3. Despite the large off-axis motion of the hydrogen atom (see section 4.3) the rotational spectrum of the complex is that of a linear triatomic molecule (or a symmetric top in the $K = 0$ states) with one hyperfine nucleus, similar to that of ArHCl[2,3]. There is no evidence for any significant population of excited vibrational states in the beam (equivalent to excited K_a states if the complex is considered as a near-prolate symmetric top). This is probably due to population effects since a typical vibration/bending frequency is about 40 cm^{-1} and as the rotational temperature of the beam is about 5 K [16], a factor of $e^{-(40 \times 0.69)/5} = 3.9 \times 10^{-3}$ is involved in population statistics.

Power broadening of the lines was a constant source of problems and the phase-locked line usually had to be scanned many times and reducing the power until a minimum linewidth was found; on reducing the power below this minimum the signal/noise ratio would simply decrease. Unoptimised power levels can lead to peculiar line shapes characteristic of a two level system in a time dependent field[17]. Typical spectra obtained are shown in figures 4.2 and 4.3 and an unoptimised power broadened transition in figure 4.4, (*cf.* figure 5 of reference[17]).

Table 4.3 Observed microwave transition frequencies at zero electric field for KrHCl isotopes

Complex	Transition[1]	Frequency /MHz	Obs - calc /kHz [2]	Uncertainty (HWHM)/MHz
$^{84}KrH^{35}Cl$	$1\frac{1}{2} \rightarrow 0\frac{3}{2}$	2408.5350	0.0	0.003
	$2\frac{1}{2} \leftrightarrow 1\frac{1}{2}$	4802.2587	-1.8	0.008
	$2\frac{7}{2} \rightarrow 1\frac{5}{2}$	4802.8882	-0.1	0.004
	$2\frac{1}{2} \rightarrow 1\frac{3}{2}$	4815.4199	0.5	0.004
	$3\frac{9}{2} \leftarrow 2\frac{7}{2}$	7203.2986	-0.2	0.006
	$3\frac{3}{2} \rightarrow 2\frac{3}{2}$	7208.7927	0.2	0.012
	$3\frac{3}{2} \rightarrow 2\frac{5}{2}$	7214.0231	0.2	0.006
	$4\frac{5}{2} \rightarrow 3\frac{3}{2}$	9602.4842	-0.1	0.023
$^{84}KrH^{37}Cl$	$1\frac{1}{2} \rightarrow 0\frac{3}{2}$	2317.8682	0.1	0.008
	$2\frac{1}{2} \rightarrow 1\frac{1}{2}$	4624.0201	0.0	0.008
	$2\frac{1}{2} \rightarrow 1\frac{3}{2}$	4634.4115	-0.1	0.006
	$3\frac{3}{2} \rightarrow 2\frac{3}{2}$	6940.237[3]	-0.5	0.02
	$3\frac{3}{2} \rightarrow 2\frac{5}{2}$	6944.3681	0.1	0.012
$^{86}KrH^{35}Cl$	$1\frac{1}{2} \rightarrow 0\frac{3}{2}$	2391.9605	-1.8	0.006

Table 4.3 continued

Complex	Transition	Frequency /MHz	Obs - calc /kHz	Uncertainty (HWHM)/MHz
$^{86}KrH^{35}Cl$	$2\frac{1}{2} \rightarrow 1\frac{1}{2}$	4769.1147	-1.4	0.008
	$2\frac{1}{2} \rightarrow 1\frac{3}{2}$	4782.2810	2.7	0.006
	$3\frac{3}{2} \rightarrow 2\frac{5}{2}$	7164.3193	-1.3	0.012
$^{82}KrH^{35}Cl$	$2\frac{1}{2} \rightarrow 1\frac{1}{2}$	4837.02 [4]	(27.8)	0.20
	$2\frac{7}{2} \rightarrow 1\frac{5}{2}$	4837.65	(29.5)	0.20

[1] J,F → J',F', focussing state is at start of arrow; double arrows indicate either state could be focussed.
[2] Least-squares fit with radiofrequency data also.
[3] Weak transition; not included in the fit.
[4] Lines as yet not phase-locked; Obs - calc is from a fitting with Flygare's data.

Typical power requirements for optimisation are shown in the last set of transitions in table 4.4. These powers represent attenuation of a 2V peak/peak r.f. output of the Schlumberger frequency synthesiser. This is fed into 50Ω cable to the C field. The transitions showed a marked electric field versus power dependence, the transition becoming much more strongly allowed as the field strength increases[18].

For all the spectra time constants of 10 or 30 seconds were employed. All the figures have scales which correct for the corresponding frequency lag. All frequency measurements were referred to the timebase of the Hewlett-Packard 5345A counter (accuracy > 1 part in 10^8 in frequency), and measurements of the d.c. field applied across the C field plates were, as usual, measured using the Fluke 895A

Figure 4.2 *Noise broadened low resolution microwave spectrum of $^{84}KrH^{35}Cl$. The transitions are $J = 2 \rightarrow 1$, $F = 1/2 \rightarrow 1/2$, $F = 7/2 \rightarrow 5/2$ and $F = 1/2 \rightarrow 3/2$. The spectrum was recorded with a 30 second time constant.*

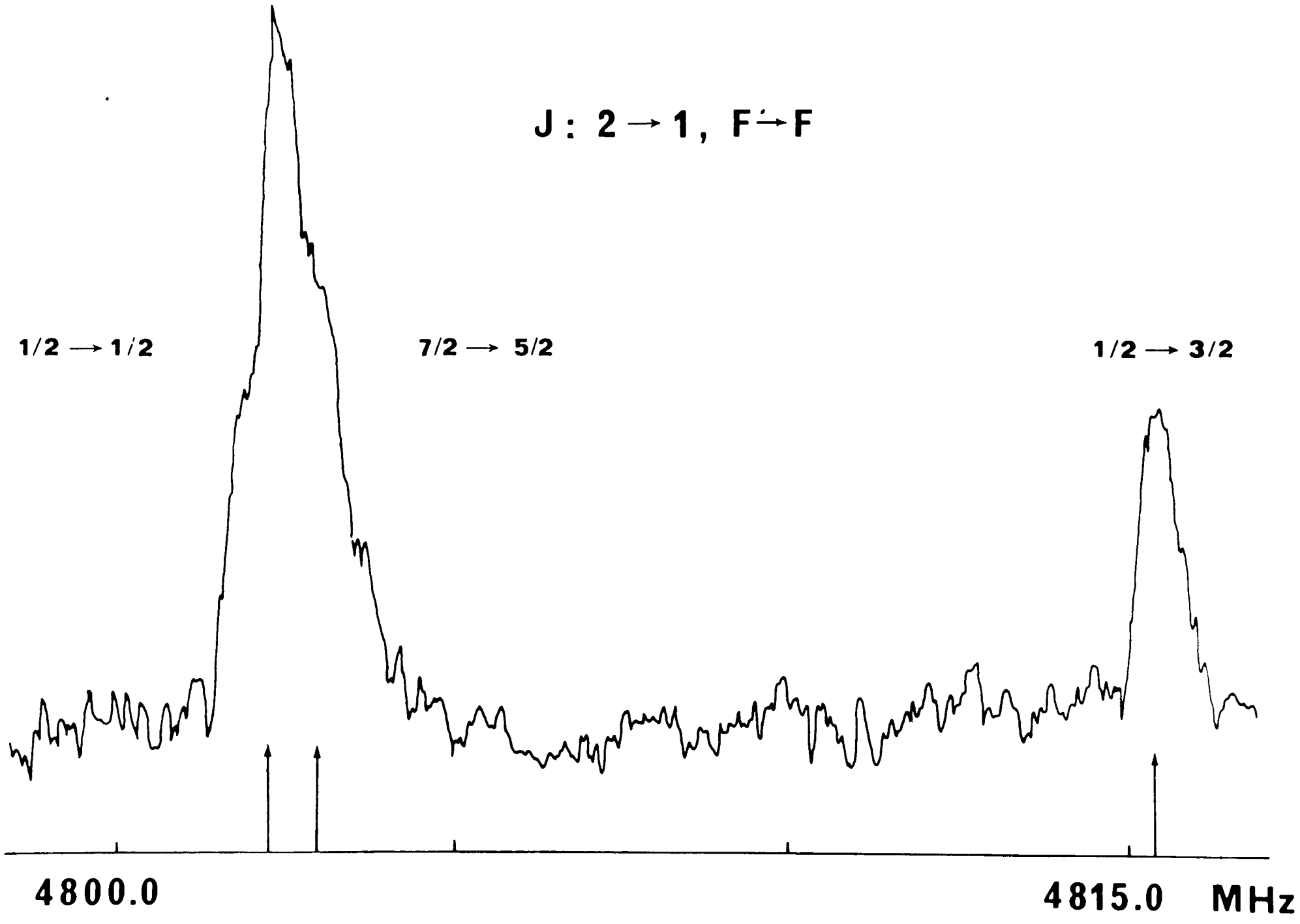
J : 2 → 1, F → F
1/2 → 1/2
7/2 → 5/2
1/2 → 3/2
4800.0
4815.0 MHz

Figure 4.3 Radiofrequency spectrum of KrHCl isotopes showing structure due to the spin-spin interaction. The transitions are:
(a) $^{84}KrH^{35}Cl$, $J = 2$, $F, |M_F| = 1/2,\ 1/2 \rightarrow 5/2,\ 3/2$
(b) $^{86}KrH^{35}Cl$, $J = 3$, $F, |M_F| = 3/2,\ 3/2 \rightarrow 7/2,\ 5/2$
The splittings are discussed in the text, and in Appendix B.

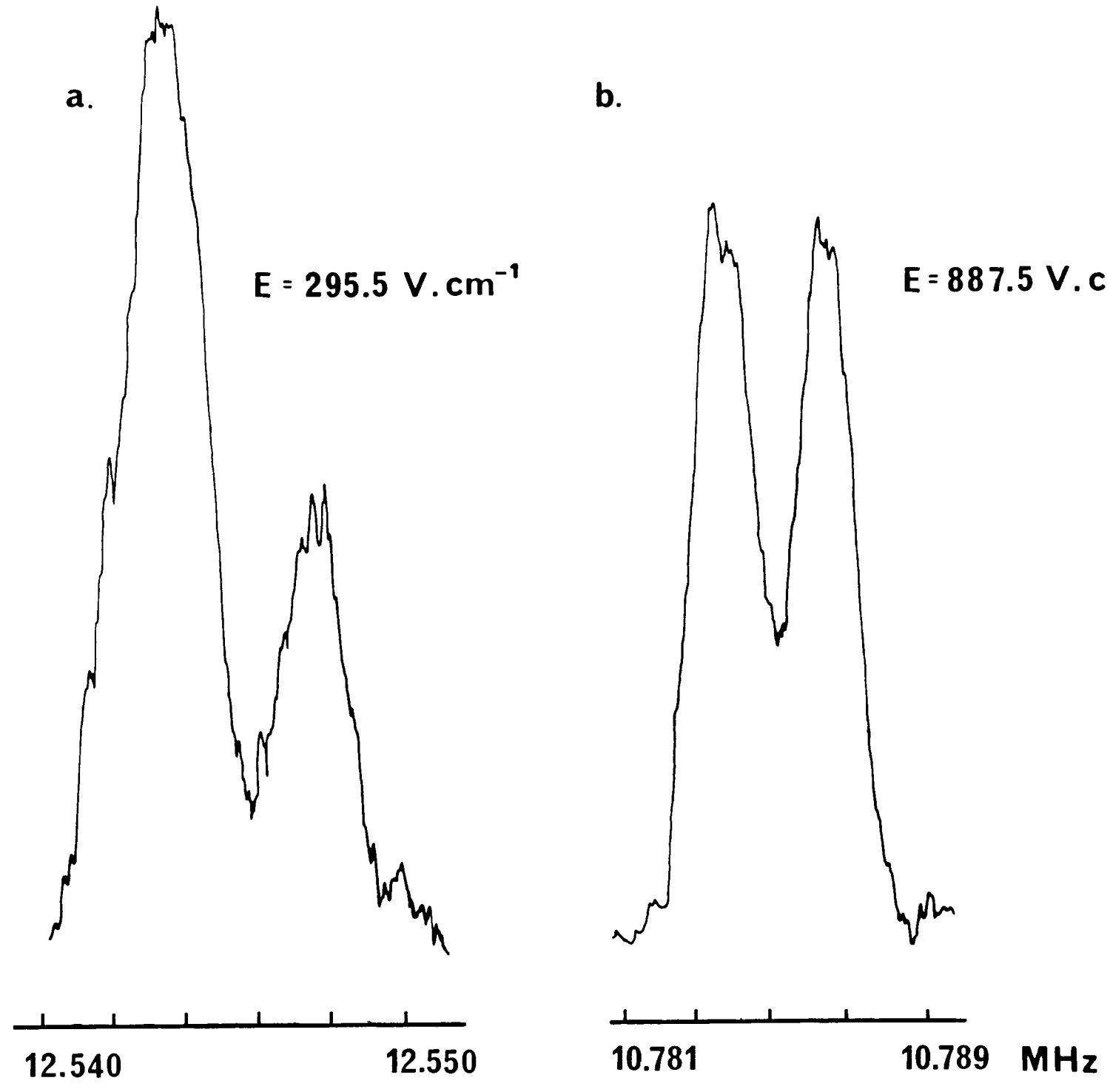
a.
E = 295.5 V.cm⁻¹
b.
E = 887.5 V.cm⁻¹
12.540
12.550
10.781
10.789
MHz

differential voltmeter (accuracy > 1 part in 10^4). In the case of the radiofrequency transitions two points should be made. Firstly transitions around 7 MHz were identified as $\Delta F = 1$ transitions, using the notation $J + I_{Cl} = F$, and a series of 12 MHz type of transitions corresponding to $\Delta F = 2$. The latter set were as strong as the $\Delta F = 1$ set and required similar optimum powers. However they were easily observed,

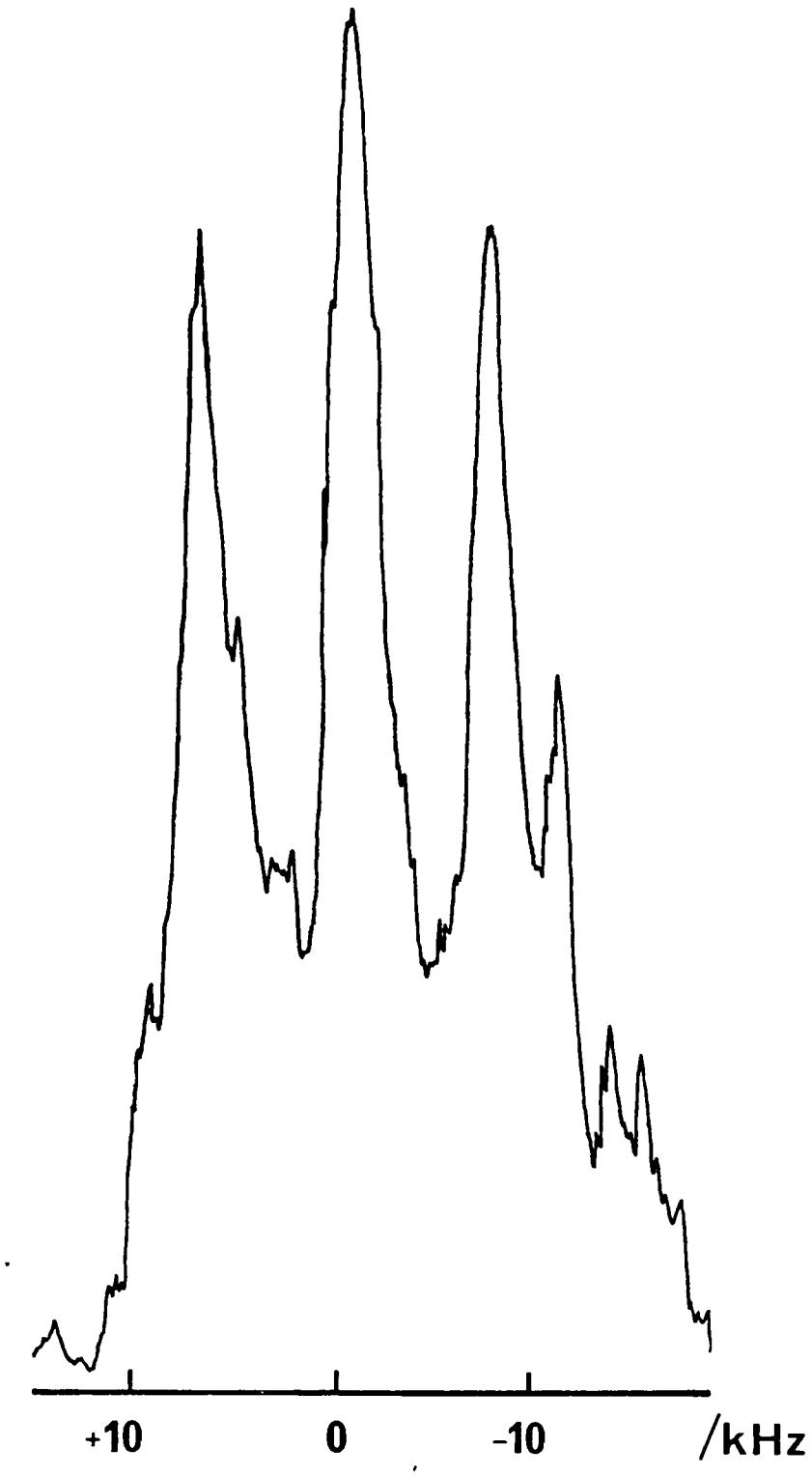

Figure 4.4 $^{84}KrH^{35}Cl$ *transition at 7203.299 MHz, showing power broadening effects*

Table 4.4 Radiofrequency transitions in KrHCl isotopes

C field voltage /volts [3]	Centre frequency /MHz	Δ [1] /kHz	Obs - calc /kHz	Uncertainty (HWHM)/MHz	P [5] /dB
Transition					
$^{84}KrH^{35}Cl$					
$J = 1;\ F = 3/2 \rightarrow 1/2;\ M_F = 1/2 \rightarrow 1/2$					
299.806	14.116_9		0.1	0.007	
399.758	15.252_8		-1.7	0.006	
499.707	17.098_7		0.6	0.006	
599.630	19.688_5		-3.0	0.012	
699.587	22.980_2		1.7	0.008	
799.497	26.920_9		-2.8	0.010	
899.446	31.467_6		0.1	0.006	
999.361	36.586_2		0.2	0.007	
1098.971	42.239_8		-2.5	0.005	
$J = 2;\ F = 7/2 \rightarrow 5/2;\ M_F = 3/2 \rightarrow 3/2$					
199.395	7.3806_6		0.0_8	0.0020	
299.286	7.4903_5		0.1_1	0.0015	
399.213	7.6809_8		0.3_3	0.0017	
499.107	7.9837_6		-0.0_5	0.0016	
599.029	8.4334_3		-0.2_1	0.0015	
698.972	9.0593_7		-0.2_1	0.0016	
798.841	9.8810_9		-0.2_4	0.0014	
898.768	10.9109_0		0.4_0	0.0012	
998.664	12.1539_7		0.4_0	0.0018	
1098.260	13.6094_9		-0.5_3	0.0018	
$J = 2;\ F = 7/2 \rightarrow 5/2;\ M_F = 3/2 \rightarrow 5/2$					
199.395	7.4538_2	2.6_9	0.1_1	0.0014	
299.298	7.6465_5	2.6_3	-0.0_5	0.0016	
399.231	7.9373_0	2.6_9	0.0_8	0.0016	

Table 4.4 continued

C field voltage / volts	Centre frequency /MHz	Δ /kHz	Obs - calc /kHz	Uncertainty (HWHM)/MHz	P /dB
Transition					
499.132	8.3426_4	2.6_5	0.2_6	0.0018	
599.060	8.8800_2	u [2]	-0.2_1	0.0019	
698.971	9.5668_1	u	0.1_8	0.0018	
698.991	9.5671_5	u	0.3_7	0.0020	
798.882	10.4192_4	2.8_4	-0.1_5	0.0022	
998.701	12.6780_4	2.5_3	0.2_5	0.0014	
1098.281	14.1043_0	2.7_8	0.5_4	0.0012	
$J = 2;\ F = 1/2 \rightarrow 5/2;\ M_F = 1/2 \rightarrow 1/2$					
199.395	12.4861_8		0.0_7	0.0023	
299.277	12.4386_1		-0.0_4	0.0018	
399.194	12.3945_0		0.1_4	0.0019	
499.062	12.3765_7		0.0_4	0.0018	
598.975	12.4165_1		-0.0_7	0.0017	
698.979	12.5554_7		-0.0_7	0.0019	
798.881	12.8437_1		-0.0_9	0.0016	
898.811	13.3388_1		-0.2_2	0.0014	
998.711	14.0953_3		0.1_7	0.0016	
1098.297	15.1476_2		-0.3_3	0.0018	
$J = 2;\ F = 1/2 \rightarrow 5/2;\ M_F = 1/2 \rightarrow 3/2$					
199.395	12.5282_6		0.1_7	0.0018	
299.291	12.5443_1		0.1_0	0.0014	
399.220	12.6086_9		-0.0_5	0.0017	
499.117	12.7612_0		0.0_9	0.0012	
599.033	13.0455_1		0.0_3	0.0014	
698.991	13.5033_2		-0.2_2	0.0019	
798.864	14.1672_4		-0.1_4	0.0022	
898.794	15.0602_5		-0.2_1	0.0024	
998.694	16.1966_0		-0.2_9	0.0030	

Table 4.4 continued

C field voltage /volts	Centre frequency /MHz	Δ /kHz	Obs - calc /kHz	Uncertainty (HWHM)/MHz	P /dB
Transition					
$J = 3;\ F = 3/2 \rightarrow 7/2;\ M_F = 3/2 \rightarrow 5/2$					
199.866	10.6873_1	2.9_1	-0.0_4	0.0006	
299.809	10.6450_2	2.8_8	0.0_5	0.0006	
399.761	10.5965_5	2.9_8	-0.1_1	0.0005	
499.706	10.5539_2	2.9_6	-0.0_5	0.0005	
599.628	10.5321_2	2.5_0	0.0_7	0.0005	
699.582	10.5489_8	2.9_0	-0.0_7	0.0005	
799.495	10.6246_3	2.8_6	-0.0_9	0.0005	
899.452	10.7784_4	2.5_4	0.1_4	0.0005	
999.375	11.0276_7	2.5_2	0.0_7	0.0005	
1098.988	11.3884_4	2.5_1	0.0_0	0.0005	
$J = 3;\ F = 3/2 \rightarrow 5/2;\ M_F = 1/2 \rightarrow 3/2$					
299.789	7.3994_4		-0.3_0	0.0012	
399.736	7.4706_6		-0.3_0	0.0010	
499.675	7.5625_3		-0.0_5	0.0010	
599.590	7.6742_6		0.1_2	0.0007	
699.538	7.8047_1		-0.1_2	0.0010	
799.442	7.9533_5		0.0_5	0.0010	
899.383	8.1185_6		0.0_7	0.0007	
999.307	8.2999_8		-0.0_2	0.0010	
1098.920	8.4988_5		0.1_4	0.0007	
$^{84}KrH^{37}Cl$					
$J = 2;\ F = 7/2 \rightarrow 5/2;\ M_F = 3/2 \rightarrow 5/2$					
299.749	6.1305_0	u	0.0_0	0.0022	
399.680	6.4463_0	u	0.0_0	0.0015	

Table 4.4 continued

Transition C field voltage /volts	Centre frequency /MHz	Δ /kHz	Obs - calc /kHz	Uncertainty (HWHM)/MHz	P /dB
499.605	6.8921_2	u	-0.1_0	0.0017	
599.504	7.4888_2	u	-0.1_7	0.0016	
699.436	8.2564_6	u	-0.1_5	0.0015	
799.334	9.2124_8	u	0.4_1	0.0016	
889.249	10.2460_0	u	0.3_8	0.0020	
999.160	11.7473_2	u	0.0_0	0.0017	
1098.747	13.3456_9	u	-0.2_2	0.0016	
$J = 3;\ F = 3/2 \rightarrow 7/2;\ M_F = 3/2 \rightarrow 5/2$					
299.749	8.3891_1	2.1_7	-0.0_1	0.0015	
399.681	8.3466_3	2.2_5	-0.0_4	0.0015	
499.605	8.3190_6	2.2_2	0.0_5	0.0013	
599.493	8.3266_9	2.1_7	0.0_0	0.0014	
699.421	8.3929_3	2.4_1	-0.0_4	0.0014	
799.325	8.5409_2	2.0_9	0.0_1	0.0014	
899.272	8.7917_6	2.0_0	0.0_5	0.0013	
999.164	9.1665_0	2.0_9	-0.0_4	0.0018	
$^{86}KrH^{35}Cl$					
$J = 2;\ F = 7/2 \rightarrow 5/2;\ M_F = 3/2 \rightarrow 5/2$					
199.392	7.4561_6	2.6_0	-0.1_1	0.0012	
299.293	7.6506_0	2.6_6	0.0_1	0.0011	
399.225	7.9437_5	2.4_7	0.0_2	0.0011	
499.141	8.3525_9	u	0.1_2	0.0016	
599.052	8.8945_8	u	-0.0_5	0.0014	
698.985	9.5877_2	u	-0.1_6	0.0015	
798.883	10.4480_3	u	-0.1_0	0.0017	
998.703	12.7280_6	u	0.1_6	0.0021	
1098.287	14.1672_7	u	0.0_2	0.0018	

Table 4.4 continued

Transition C field voltage /volts	Centre frequency /MHz	Δ /kHz	Obs - calc /kHz	Uncertainty (HWHM) /MHz	P /dB
$J = 3;\ F = 3/2 \rightarrow 7/2;\ M_F = 3/2 \rightarrow 5/2$					
199.389	10.6888_4	2.8_3	-0.0_3	0.0015	-25
299.288	10.6464_0	2.8_5	0.0_9	0.0013	-28
399.218	10.5978_1	2.7_5	-0.0_2	0.0011	-32
499.141	10.5550_8	2.8_0	-0.0_3	0.0011	-32
599.057	10.5335_2	2.8_6	0.0_0	0.0011	-33
698.981	10.5514_7	2.9_4	0.0_5	0.0012	-35
798.881	10.6285_5	2.7_0	-0.1_7	0.0017	-38
898.807 [4]	10.7850_3	2.7_4	0.0_7	0.0011	-41
998.709	11.0379_8	2.6_6	0.0_1	0.0011	-42
1098.292	11.4037_3	2.4_2	-0.0_3	0.0012	-44

[1] Δ refers to the splitting in the $M_F \neq 1/2$ levels, and is the spin-spin splitting due to the H...Cl interaction. For states connecting $M_F = 1/2$ states the splitting is more complicated and is discussed in the text. For the case of the $J = 2;\ F = 7/2 \rightarrow 5/2;\ M_F = 3/2 \rightarrow 3/2$, the expected splitting is 2.0 kHz, which was only seen as an unresolved broadening consistent with this value in the spectra.

[2] u = unresolved splitting.

[3] C field applied voltage measured by the Fluke 895A differential voltmeter; the C field spacing is 1.01270(2) cm using the $J = 1;\ M_J = 1 \leftarrow 0$ transition in OCS.

[4] This transition frequency is drawn correctly in fig.3 of ref[1], but the scale is incorrect owing to a temporary fault with the Schlumberger frequency sweep which was losing ~ 16.5 kHz. The spectrum was subsequently re-taken, and the correct frequencies have been used for the parameter determinations of table 4.5.

[5] Optimum power broadening requirements (see text). The output also passes through the 40dB power amplifier.

even down to 200 V cm^{-1}, where F would be expected to be a good quantum number (see figure 4.5). This effect is probably due to the nature of the electric resonance experiment, but is not fully understood at present.

Figure 4.5 The energy levels and observed microwave and radiofrequency transitions in $^{84}KrH^{35}Cl$ from the spectroscopic constants.

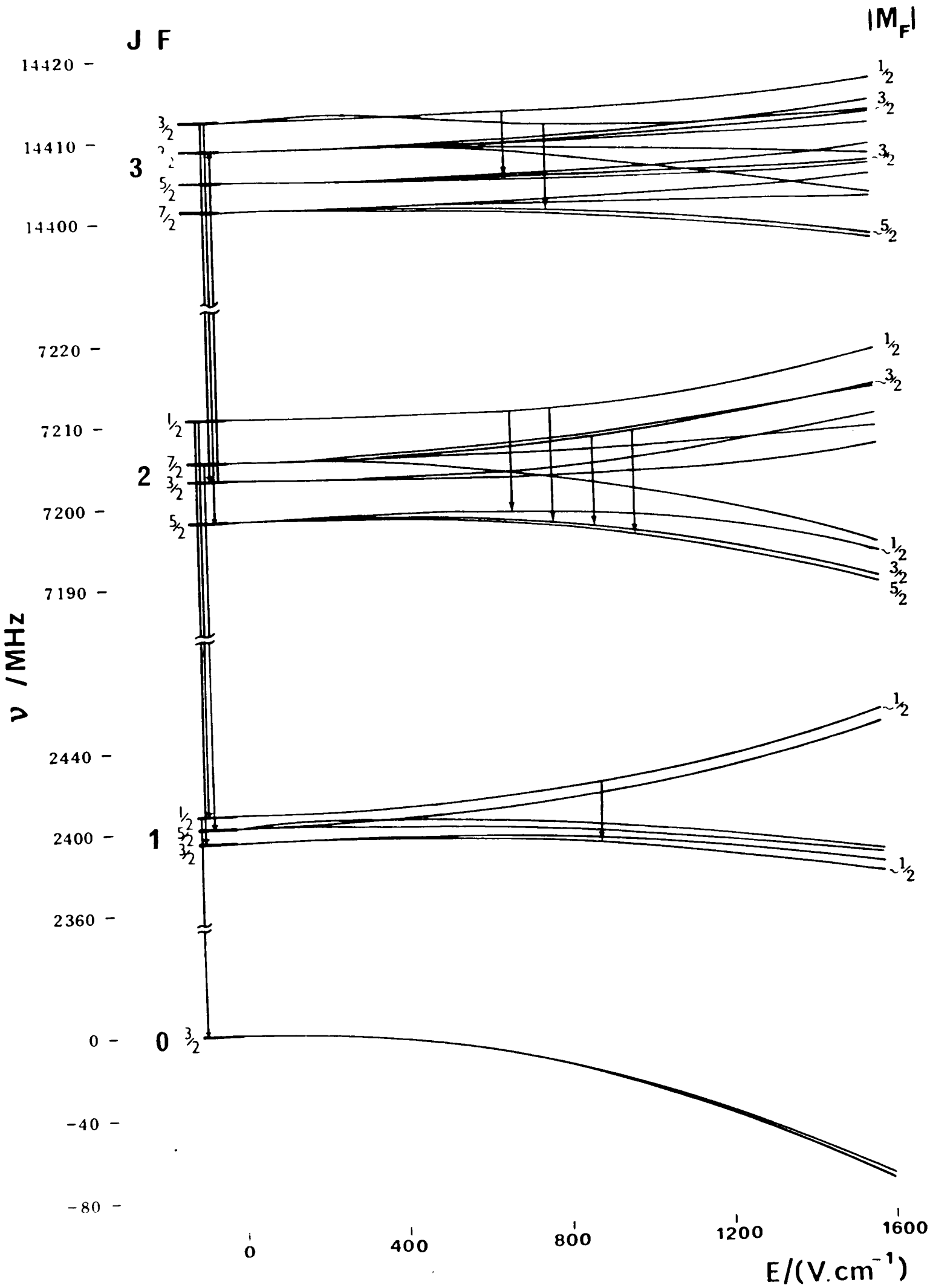
J F
|M_F|
ν /MHz
14420
14410
14400
7220
7210
7200
7190
2440
2400
2360
0
-40
-80
3
2
1
0
3/2
5/2
7/2
1/2
0
400
800
1200
1600
E/(V.cm⁻¹)

(d) Theory

For the KrHCl isotopes the microwave and radiofrequency transitions were fitted to the following Hamiltonian:

$$H = \bar{B}_o J^2 - D_J J^4 - \mu_J . E + Q_{Cl} : \nabla E + c_b^{Cl} I_{Cl} . J$$

$$+ \frac{2d_a}{(2J-1)(2J+3)} \{3(I_{Cl} . J)(I_H . J) - (I_{Cl} . I_H) J^2\} \qquad (4.1)$$

in a low basis set, $|JKI; FM_F>$, where $J + I = F$. The matrix elements have been given for a symmetric top by Benz[19]. The resulting matrix was diagonalised to give eigenstates and the corresponding eigenvalues[20]. All matrix elements up to and including those linking J to J + 2 states have been included. Additional matrix elements will be discussed below. The molecular parameters were adjusted by a non-linear least - squares fit to the data[21], and the derivatives of the energy with respect to various molecular parameters were found using the Hellman-Feynman theorem, $\partial U/\partial p_i = <\phi|\partial H/\partial p_i|\phi>$, where ϕ is the eigenvector for the particular eigenstate under consideration. Convergence is considered complete when the corrections to each parameter in the new iteration are each less than one fifth of the parameter standard deviation (the square root of the variance-covariance matrix). Usually only two or three iterations are required for convergence using initial guess parameters from first-order Stark-quadrupole theory[22].

The Hamiltonian consists of a rotational part, suitable for K = 0 rotational levels, and a part due to the nuclear quadrupole coupling due to the chlorine nucleus ($I = \frac{3}{2}$). On initial fits to the J = 3 and 2 r.f. data separately, it was found that the calculated dipole moment $\mu_a^{J=3}$, and quadrupole coupling constant $(eQq)_a^{J=3}$, differed from those of J = 2 by many standard deviations. Similar results were obtained by Langridge-Smith for ArHBr[23], who found that the fitting procedure above gave poor fits for the usual four parameter Hamiltonian[2]. Also the ratio of D_J

for the two isotopes $ArH^{79}Br$ and $ArH^{81}Br$ did not scale as μ^{-2}, where μ is the reduced mass of the complex, if the complex is treated as a pseudo-diatomic; in $ArHCl$[2], such a scaling is found to be well followed by the system.

To explain these phenomena a centrifugal distortion (J-dependence) of $(eQq)_a$ for bromine and chlorine, and the dipole moment were introduced; these are DQ and Dμ respectively. Thus, for all matrix elements diagonal in J the effective quadrupole Hamiltonian becomes

$$H^{QUAD}_{diagonal} = [\,(eQq)_a + DQJ^2] \times \left[\frac{3(I.J)^2 + \frac{3}{2}I.J - I^2J^2}{2I(2I-1)(2J+3)(2J-1)}\right] \qquad (4.2)$$

and for the Stark effect becomes

$$H^{STARK} = -\mu_J.E = -(\mu + D\mu J^2).E \qquad (4.3)$$

The credibility of including these terms is shown by the J-dependence of $(eQq)_a$ and μ_a values for separate rotational levels in figure 4.6.

Two other terms for inclusion in the Hamiltonian have also been identified, principally from the KrHCl r.f. spectra. These are included in equation 4.1, as the fifth and sixth terms. They are respectively, the chlorine spin-rotation interaction and the hydrogen/chlorine spin-spin interaction. No effects due to the hydrogen spin-rotation interaction were resolved. The two terms were treated differently in the spectral analysis. For the chlorine spin-rotation interaction only the diagonal matrix elements were included. For the low field basis set, $c_b^{Cl}I_{Cl}.J$ may be rewritten as

$$c_b^{Cl}(F - J).J = c_b^{Cl}[F.J - J(J+1)] \qquad (4.4)$$

since $I_{Cl} + J = F$

and $F.J = \frac{1}{2}\{F(F+1) + J(J+1) - I_{Cl}(I_{Cl}+1)\}$

so $\langle J0I;F|c_b^{Cl}I.J|J0I;F\rangle$

$$= \tfrac{1}{2}c_b^{Cl}\{F(F+1) - I_{Cl}(I_{Cl}+1) - J(J+1)\} \qquad (4.5)$$

The major effect of this term is to cause significant shifts in the extrapolated zero field values of r.f. transitions, (see Appendix B).

For the spin-spin term the derivation of the necessary matrix elements are given in Appendix B. For states not involving $M_F = \pm\frac{1}{2}$ a symmetric doublet results. For states involving $M_F = \pm\frac{1}{2}$, matrix elements

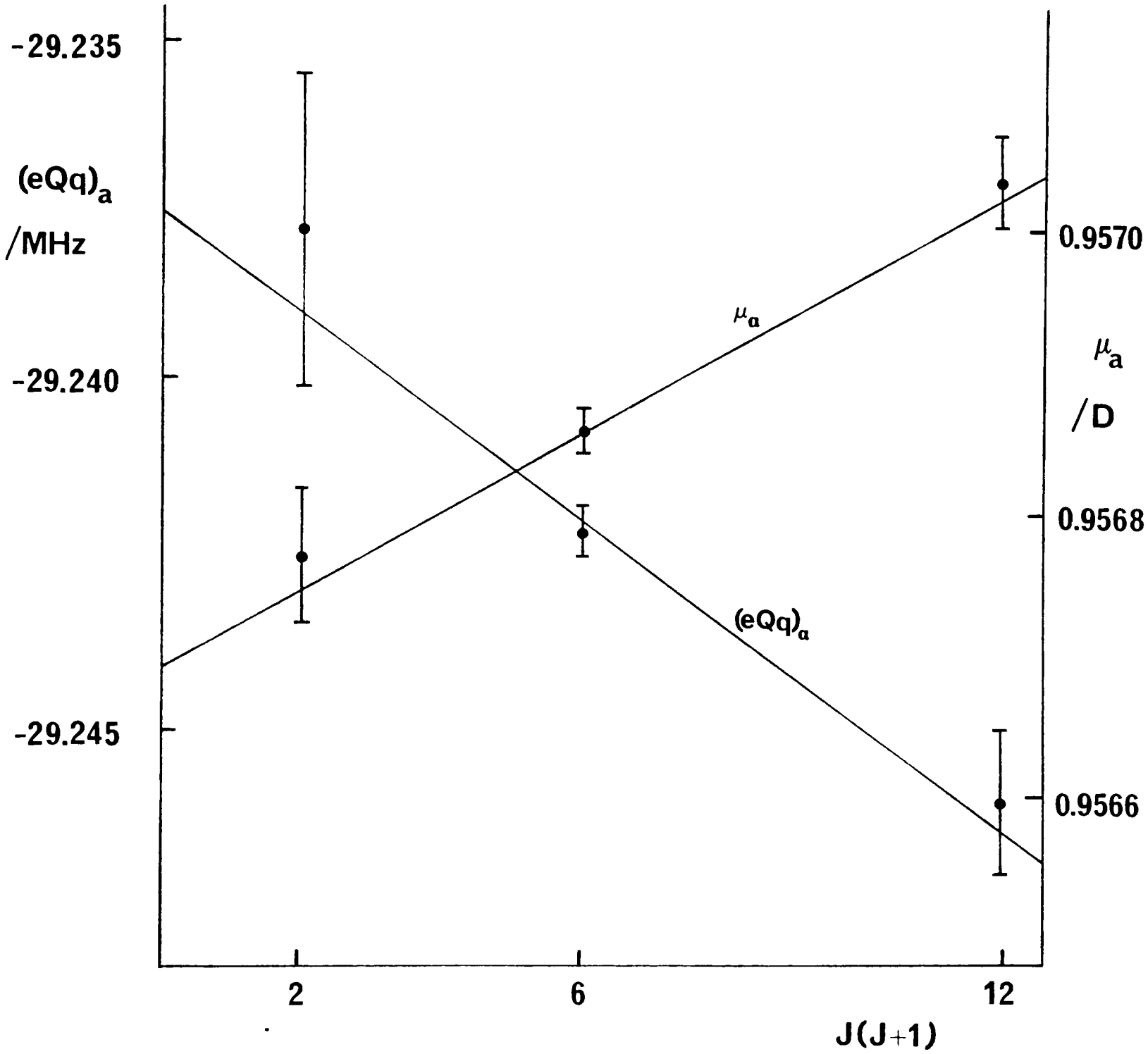

Figure 4.6 Least-squares fits to individual J Stark data shown against J(J+1). Error bars are 2σ; lines represent fit to all data

of the spin-spin interaction exist linking $M_F = \pm\frac{1}{2}$, $M_{I_2} = \mp\frac{1}{2}$ states (I_2 is $\frac{1}{2}$ for hydrogen). This causes a splitting of one or both components of the above doublet, and the transition usually looks like a

doublet with a 3:1 intensity ratio. From the pattern splittings and the doublet splittings a value for d_a is readily obtained and the centres of the line patterns determined. Two such patterns are shown in Appendix B.

These line centres form the input for the fitting program, and the resulting spectroscopic constants are given in Table 4.5.

4.2 KrDCl

(a) Experimental

Deuterium chloride from Merck Co. (25 litre atmos, 98%) was used in these experiments. It has been found by other workers[24] that it was necessary to 'season' the gas inlet system after use of HCl to prevent isotopic exchange. The author has found that the best way of achieving this seasoning quickly is to pass pure DCl through the nozzle into the source chamber for an hour followed by vigorous degassing of the pumping system. This yields good beams of DCl consistent with the DCl content of the gas mixture. A typical mass spectrometer scan for the deuterated system is shown in figure 4.7. The optimum focussing fields for KrDCl were found to be less than that required for KrHCl indicating a significantly larger dipole moment (see table 4.6) Typical microwave and radiofrequency transitions are shown in figures 4.8 and 4.10.

Compared with the KrHCl spectra, the KrDCl spectra are further complicated by the presence of deuterium quadrupole structure. For the radiofrequency spectra the splittings were found to be field dependent, due to the fact that although at low fields the deuterium spin is coupled to F_1, (where $I_{Cl} + J = F_1$), on increasing the field strength I_{Cl} becomes decoupled from J and F_1 becomes a less good quantum number. Also no spin-spin structure was resolved in the r.f. spectra since the value of the spin-spin constant in DCl is only one sixth of that in HCl.

(b) Theory

For KrDCl it was found easier to diagonalise a high field basis set

Table 4.5 Spectroscopic constants for KrHCl isotopes

	$^{84}KrH^{37}Cl$	$^{86}KrH^{35}Cl$	$^{84}KrH^{35}Cl$	$^{82}KrH^{35}Cl$
$\bar{B}$/MHz	1156.05904(64) [1]	1192.33612(64)	1200.62374(31)	1209.3074(11)
D_J/kHz	6.762(46)	7.143(58)	7.343(22)	7.427(28)
$(eQq)_a^{Cl}$/MHz	-23.0892(25)	-29.2451(15)	-29.23757(61)	-29.254(14)
DQ/kHz	-0.51(29)	-0.46(13)	-0.730(70)	-0.7 [2,3]
μ_a/Debye	0.957922(74)	0.956958(84)	0.956692(11)	—
Dμ/Debye	0.000016(11)	0.000019(12)	0.0000294(25)	—
c_b^{Cl}/kHz	0.124(59)	0.13 [2]	0.132(24)	0.13 [2]
d_a/kHz	1.95(11)	2.40(11)	2.43(29)	—

[1]Values in parentheses are 2 standard deviations from least-squares fitting program.

[2]Value fixed in fitting.

[3]Flygare's high J data included to determine D_J; *cf.* table 4 of our paper. $\bar{B}$ and eQq are, of course, also determined more accurately.

matrix, $|JKM_J;I_1M_{I_1};I_2M_{I_2}>$, the matrix elements of which have been calculated[26]. $Q:\nabla E$ for deuterium was also included in the Hamiltonian. Because $M_{I_2} = \pm 1$ splitting was only seen on a few lines the program was written excluding matrix elements in $(eQq)^D$ which linked $M_{I_2} = 0$ to ± 1 and $M_{I_2} = \pm 1$ to ∓ 1, which are given in Appendix C. Remaining matrix elements depended only on $M_{I_2}^2$, and so the size of matrix to be diagonalised was reduced by a factor of three. For the transitions in which $M_{I_2} = \pm 1$ splitting was seen, the hypothetical centre was calculated

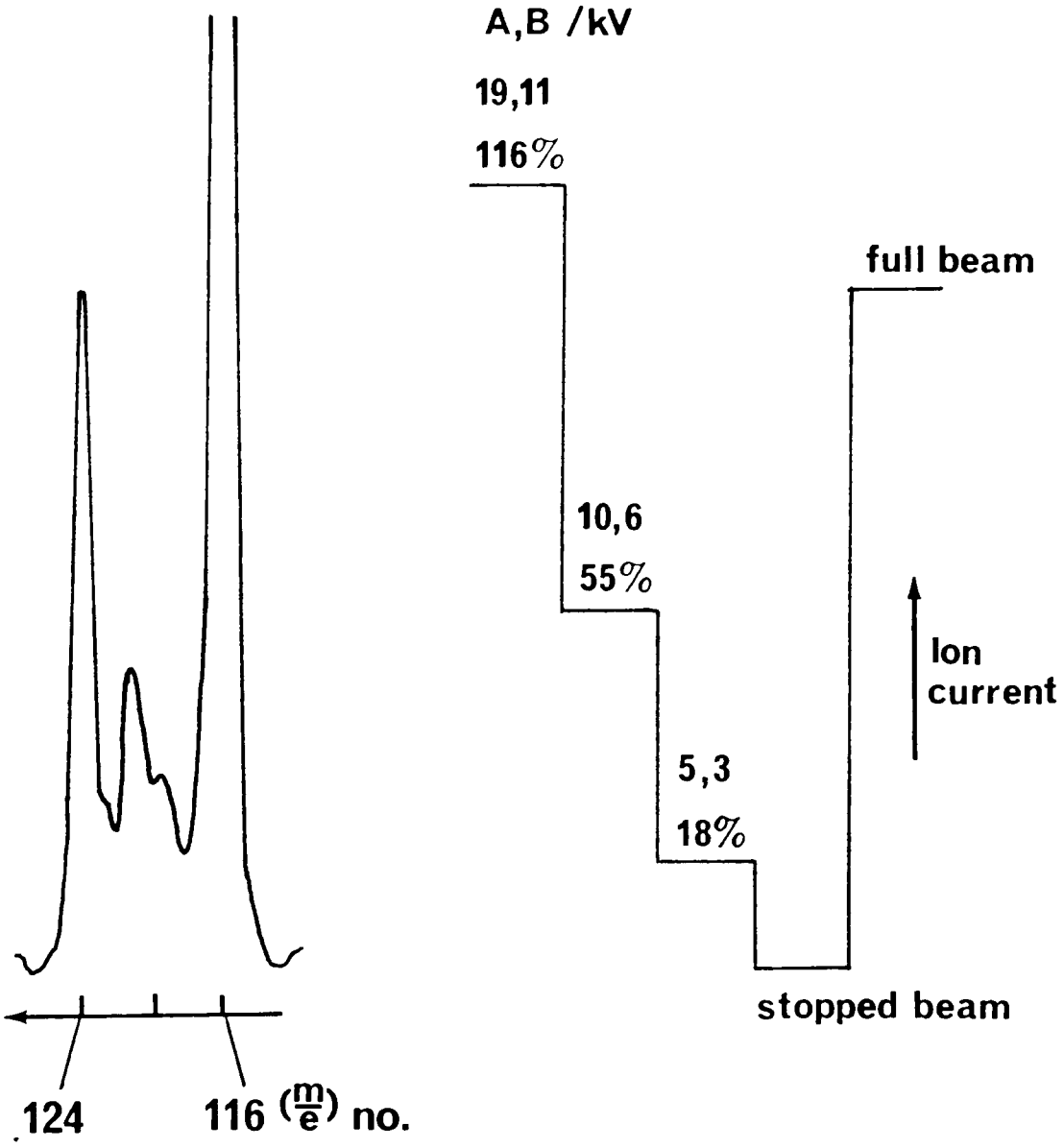

Figure 4.7 KrDCl mass spectrum and refocussing characteristics (shown by % refocussing)

as if the transition were high field by diagonalising a large matrix including off-diagonal interactions using molecular parameters from a fitting using the unsplit lines only. The extra transition frequencies

Figure 4.8 a. Radiofrequency spectrum of $^{84}KrD^{35}Cl$ showing deuterium quadrupole splitting, which varies with field. The electric field is 887.7 V cm^{-1}, and at this field the deuterium spin is decoupled from the molecular rotation while the chlorine is in an intermediate coupling region. The transition is $J = 3$, $F_1 = 3/2 \rightarrow 7/2$, $M_{F_1} = 3/2 \rightarrow 5/2$.

b. Phase-locked spectrum of $^{84}KrD^{35}Cl$ showing the splitting caused by the deuterium quadrupole coupling constant. The transition is $J,F_1 = 2,1/2 \rightarrow 1,3/2$, F being the total quantum number.

a.

(x 2)

M_{I_2} = 0

±1

14.990 15.000 15.010 MHz

b.

F → F

3/2 → 5/2

3/2 → 3/2
1/2 → 3/2

3/2 → 1/2
1/2 → 1/2

4753.220 4753.280 MHz

Table 4.6 Optimum focussing field voltages for KrHCl isotopes

J	$H^{35}Cl$		$D^{35}Cl$	
	A [1]	B	A	B
1	5	3	4.2_5	2.5
2	6.5	4.5	5.5	3.7_5
3	8.5	5.5	7	4.5
4	10	6	8.2_5	5

[1]Voltages given in kV, applied to the rods (see chapter 2).

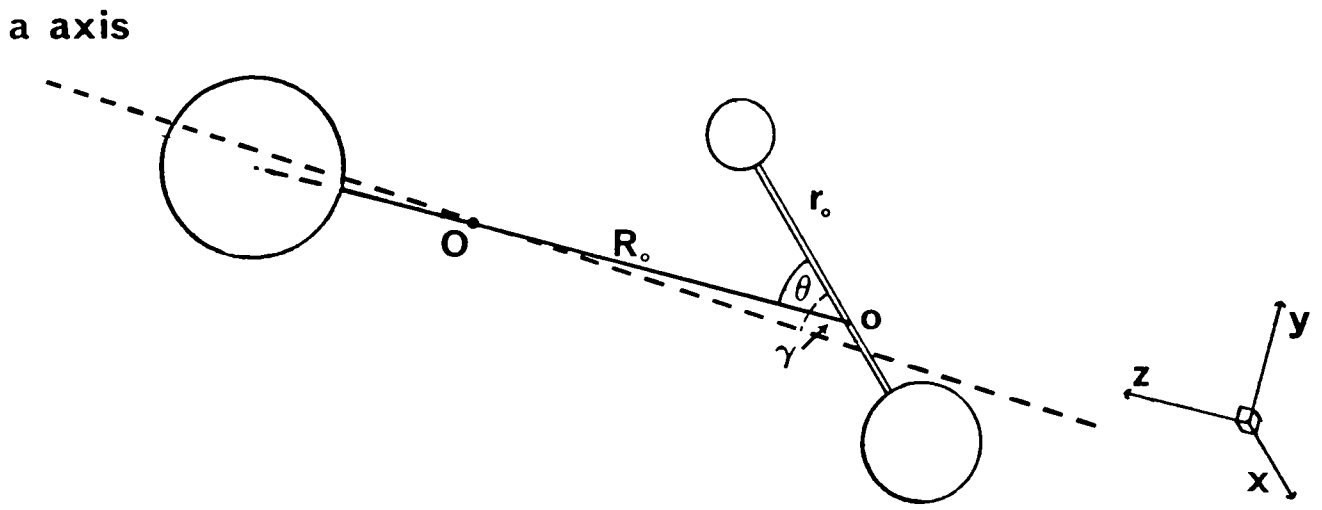

Figure 4.9 Coordinate system for atom-diatomic molecule complexes. O is the centre of mass of the complex, and o is the centre of mass of the diatomic molecule. The origin of the molecule fixed axis system is at O. x is out of the plane of the paper.

were then included in a further fitting. A separate estimate of $(eQq)_a^D$ can be obtained from the zero-field microwave spectrum. The D-Cl spin-spin interaction also contributes to the splitting of the lines. The dependence of the line patterns on $(eQq)_a^D$ and d_a are given in Appendix C.2 for a selection of transitions. $(eQq)_a^D$ and d_a were obtained from a least-squares fit to the splittings in these transitions. It was also found that $(eQq)_a^{Cl}$ was a great deal more accurately determined by r.f.

Table 4.7 Observed microwave transitions at zero electric field for $^{84}KrD^{35}Cl$

Transition [1] $J,F_1 \rightarrow J',F_1'$	Frequency /MHz	Centre Frequency [2] /MHz	Obs - calc /kHz	Uncertainty (HWHM) /MHz
$1\frac{1}{2} \rightarrow 0\frac{3}{2}$	2377.7353	2377.7353	0.0	0.0013
$2\frac{1}{2} \rightarrow 1\frac{1}{2}$	4734.8820	4734.8820	-1.4	0.0081
$2\frac{1}{2} \rightarrow 1\frac{3}{2}$	4753.2259			0.0027
	4753.2444	4753.2489	0.1	0.0023
	4753.2669			0.0028
$2\frac{7}{2} \leftarrow 3\frac{7}{2}$	7092.2548			0.0024
	7092.2451			0.0024
	7092.2222 [3]			0.0057
	7092.2145	7092.2193	0.0	0.0038
	7092.1898			0.0020
	7092.1832			0.0020
$2\frac{1}{2} \rightarrow 3\frac{1}{2}$	7099.8663			0.0046
	7099.8834	7099.8882	1.3	0.0030
	7099.9066			0.0030
$3\frac{3}{2} \rightarrow 2\frac{3}{2}$	7110.0619			0.0024
	7110.0787	7110.0839	-0.6	0.0024
	7110.9066			0.0024
$4\frac{9}{2} \rightarrow 3\frac{9}{2}$	9458.619 [4]	9458.619	-3.4	0.035
$3\frac{3}{2} \rightarrow 4\frac{5}{2}$	9467.647 [4]	9467.647	4.8	0.028

[1] The various transitions are further characterised by a total quantum number F, where $I_D + F_1 = F$, and are all readily assigned. An assignment is shown in figure 4.10.

[2] Centre frequency is the hypothetical centre correcting for deuterium hyperfine structure and spin-spin splitting.

[3] Unresolved doublet

[4] Unresolved multiplet

Table 4.8 Observed radiofrequency transitions in $^{84}KrD^{35}Cl$

Transition C field voltage /volts	Frequency [1] /MHz	D-splitting [2] /kHz	Obs - calc /kHz	Uncertainty (HWHM)/MHz
$J = 2,\ F_1 = 7/2 \rightarrow 5/2,\ M_{F_1} = 3/2 \rightarrow 3/2,\ M_{I_2} = 0$				
99.457	10.2159_3	—[3]	-0.12	0.0025
199.492	10.2894_5	8.7_9	0.43	0.0015
299.393	10.4349_5	12.4_8	0.03	0.0015
399.323	10.6879_4	15.7_5	-0.08	0.0013
499.253	11.0909_3	19.5_4	-0.18	0.0012
599.158	11.6890_5	23.8_9	-0.43	0.0012
699.083	12.5236_8	27.5_4	0.00	0.0012
798.987	13.6224_3	31.1_5	0.26	0.0015
898.927	15.0024_8	33.5_4	0.35	0.0011
		$\lvert M_{I_2}\rvert = 1$		
199.492	10.2982_4	$10.2955_1 \lvert+1\rangle$[4] $10.3009_6 \lvert-1\rangle$	1.50	0.0013 0.0013
299.393	10.4474_3	$10.4461_6 \lvert+1\rangle$ $10.4487_5 \lvert-1\rangle$	-0.62	0.0012 0.0012
399.323	10.7036_8		-0.66	0.0020
499.253	11.1104_7		-0.68	0.0016
599.158	11.7129_4		-0.56	0.0015
699.083	12.5512_2		-0.32	0.0012
798.987	13.6535_8		0.11	0.0014
898.927	15.0360_2		-0.33	0.0018
$J = 2,\ F_1 = 1/2 \rightarrow 5/2,\ M_{F_1} = 1/2 \rightarrow 1/2,\ M_{I_2} = 0$				
199.472	17.4314_3	-6.2_5	0.06	0.0012
299.373	17.3650_5	-4.2_0	-0.17	0.0008
399.304	17.3020_2	-2.2_9	0.17	0.0020
499.231	17.2723_4	0.0	0.43	0.0015
599.129	17.3168_0	3.5_5	0.08	0.0009
699.077	17.4900_3	7.5_4	0.10	0.0010
798.974	17.8579_1	12.5_4	-0.09	0.0010

Table 4.8 continued

Transition C field voltage /volts	Frequency /MHz	D-splitting /kHz	Obs - calc /kHz	Uncertainty (HWHM)/MHz
898.908	18.4976_4	18.0_9	-0.09	0.0015
998.496	19.4801_2	23.7_5	0.18	0.0016
		$\|M_{I_2}\|=1$		
199.472	17.4251_8		-0.26	0.0015
299.373	17.3608_5		0.17	0.0013
399.304	17.2997_9		0.43	0.0020
499.231	17.2723_4		0.34	0.0015
599.129	17.3203_5		0.21	0.0013
699.077	17.4975_7		0.10	0.0013
798.974	17.8704_5		0.00	0.0013
898.908	18.5156_7		-0.08	0.0016
998.496	19.5038_7		0.11	0.0018
$J=3,\ F_1=3/2\rightarrow 7/2,\ M_{F_1}=3/2\rightarrow 5/2,\ M_{I_2}=0$				
199.462	14.9236_4	-10.2_1	-0.29	0.0009
299.362	14.8649_8	-8.6_0	-0.13	0.0009
399.295	14.7970_4	-6.6_8	-0.07	0.0010
499.230	14.7348_7	-3.8_6	-0.24	0.0008
599.139	14.6984_6	0.0	-0.59	0.0016
699.083	14.7130_2	2.6_7	0.04	0.0010
798.989	14.8031_0	6.9_7	-0.16	0.0010
898.930	14.9957_8	11.1_3	0.37	0.0010
998.831	15.3152_9	15.8_4	-0.34	0.0010
1098.423	15.7825_4	20.2_9	0.31	0.0010
		$\|M_{I_2}\|=1$		
199.462	14.9134_4	$14.9119_0\|-1\rangle$ $14.9149_7\|+1\rangle$	-0.24	0.0011 0.0011
299.362	14.8563_8	$14.8556_5\|-1\rangle$ $14.8571_1\|+1\rangle$	0.24	0.0022

Table 4.8 continued

Transition C field voltage /volts	Frequency /MHz	D-splitting /kHz	Obs - calc /kHz	Uncertainty (HWHM)/MHz
399.295	14.7903_7		-0.11	0.0020
499.230	14.7310_2		-0.06	0.0016
599.139	14.6984_6		0.21	0.0016
699.083	14.7156_9		-0.26	0.0013
798.989	14.8100_7		-0.33	0.0013
898.930	15.0069_0		0.76	0.0013
998.831	15.3311_3		-0.43	0.0013
1098.423	15.8028_3		-0.43	0.0013
$J = 3,\ F_1 = 3/2 \rightarrow 5/2,\ M_{F_1} = 1/2 \rightarrow 3/2,\ M_{I_2} = 0$				
199.386	10.2455_5	— [3]	0.81	0.0017
299.264	10.3136_4	— [3]	0.27	0.0019
399.211	10.4097_4	11.1_0	-0.12	0.0010
499.098	10.5341_3	11.4_7	0.11	0.0009
599.030	10.6853_0	11.5_4	-0.15	0.0009
698.975	10.8629_7	11.2_8	-0.06	0.0009
798.870	11.0648_7	11.1_9	-0.14	0.0009
898.795	11.2899_7	10.8_0	0.07	0.0008
998.689	11.5370_0	10.7_7	0.11	0.0008
1098.273	11.8070_5	10.6_8	0.33	0.0009
$\lvert M_{I_2} \rvert = 1$				
399.211	10.4218_4		0.86	0.0014
499.098	10.5456_0		0.47	0.0011
599.030	10.6968_4		-0.34	0.0010
698.975	10.8742_5		0.29	0.0010
798.870	11.0760_6		0.30	0.0010
898.795	11.3007_7		-0.32	0.0009
998.689	11.5477_7		0.49	0.0008
1098.273	11.8177_3		0.63	0.0010

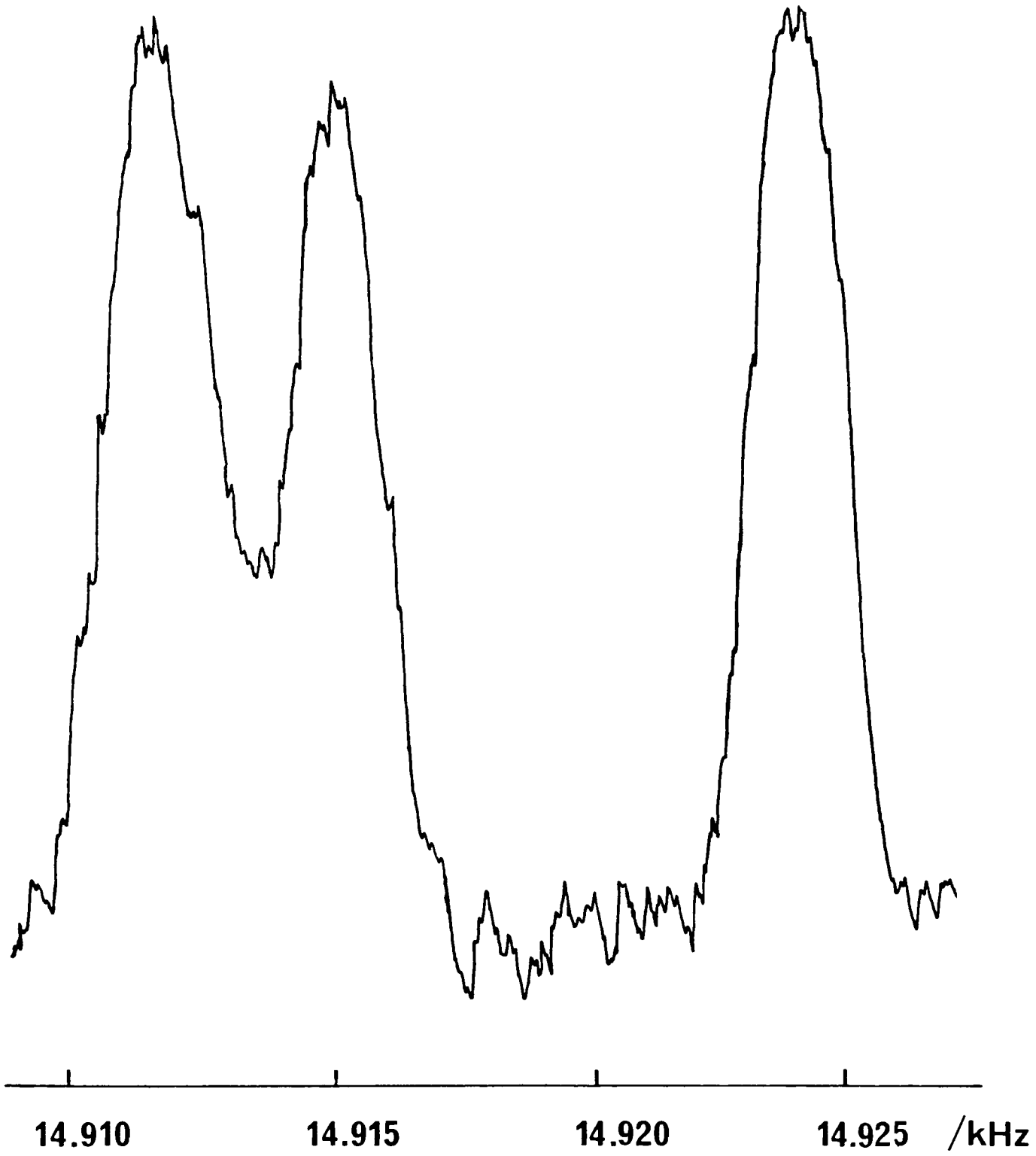

Figure 4.10 Radiofrequency spectrum of $^{84}KrD^{35}Cl$ showing deuterium quadrupole splitting at low field. The transition is $J = 3$, $F_1 = 3/2 \rightarrow 7/2$, $M_{F_1} = 3/2 \rightarrow 5/2$, at a C field of 196.961 volts cm^{-1}.

Footnotes to Table 4.8

[1]No spin-spin structure is resolvable.
[2]The $M_{I_2} = 0, \pm 1$ separation is given in the $M_{I_2} = 0$ set.
[3]Several overlapping and interfering lines prevented assignment with certainty.
[4]$M_{I_2} = \pm 1$ transitions are degenerate at high field but split at low field. Assignment as $|\pm 1\rangle$ is the M_{I_2} quantum number of the largest component of the wavefunction (see text).

than by microwave, and so the microwave data were only used to determine $\bar{B}$ and D_J. Optimum molecular parameters are given in table 4.9.

Table 4.9 Spectroscopic constants for $^{84}KrD^{35}Cl$

$\bar{B}$/MHz	1183.77283(25) [1]
D_J/kHz	6.510(16)
$^2(eQq)_a^{Cl}$/MHz	-40.80445(97)
$^3(eQq)_a^{Cl}$/MHz	-40.8037(40)
DQ/kHz	-0.72(12)
μ_a/Debye	1.106371(95)
Dμ/Debye	0.000043(13)
$^2(eQq)_a^{D}$/kHz	114.3(1.3)
$^3(eQq)_a^{D}$/kHz	113.0(0.8)
$^4(eQq)_a^{D}$/kHz	113.5(1.1)
c_b^{Cl}/kHz	0.193(43)
d_a/kHz	0.43(13)

[1]Errors quoted to two standard deviations from least-squares fit.
[2]From r.f. data.
[3]From microwave data only.
[4]Composite value for distributions. See ref[27]. The value given in Table 5 of ref[1] is in error.

4.3 Analysis of results

(a) Structural analysis

In order to obtain structural parameters from the spectroscopic constants it is necessary to formulate a model for the complex. In this model it is assumed as in earlier work[2] that since the binding energy is small (around 1 kcal mol^{-1}, or ~ 1% of normal chemical bonds), it is valid to consider the molecular constants of the HCl subunit as being essentially unchanged from that of the isolated free molecule. Small

or negligible effects on the electron distribution of the krypton should also be felt (see section 4.4). Also certain molecular constants sample different regions of electron distribution in the HCl subunit, so some confirmation of the validity of the model may be obtained. This is discussed below for the individual molecular parameters.

Since the spectra obtained are only those of the ground vibrational state of the complex this model will produce vibrationally averaged structural information. Estimates of equilibrium structures in the more classical chemical sense may be obtained from a further analysis of isotopic species.

The coordinate system chosen is shown in figure 4.9. R_o represents the vibrationally averaged distance from the inert gas atom to the centre of mass of HCl, and θ is the corresponding Kr-Cl-H angle. Treating the complex as near rigid and bent, the angle that HCl makes with the instantaneous *a* inertial axis is defined as γ. Since the two heavy atoms describe the inertial axis system the difference between θ and γ is very small (about 5′) and the distinction is rather academic since polarisation effects affect the model at this level. θ can best be calculated by what will be called a semi-rigid model for the complex.

The vibrationally averaged angle γ may be obtained from the quadrupole coupling constants for chlorine and deuterium and the spin-spin coupling if any charge rearrangement may be neglected. It is then the tensor component along the *a* inertial axis that is measured in the experiment. Since both (eQq) and d are second rank tensors they are related to the free molecule values by the equations:

$$(eQq)_a^X = (eQq)^X_{diatom}[\,3\langle\cos^2\gamma\rangle - 1]/2 \qquad (4.6)$$

$$d_a = d^{HCl}[\,3\langle\cos^2\gamma\rangle - 1]/2 \qquad (4.7)$$

where X is Cl or D.

The finite value of the quadrupole coupling constant is due to the

non-zero field gradient(∇E) at the nucleus. Since it is proportional to the inverse cube of the electron nuclear distance[25], it is only the electrons near to this nucleus that contribute significantly to this field gradient. In the case of the spin-spin interaction the major component is the direct spin-spin tensor interaction (see Appendix B.1). Excellent agreement is seen between the angles obtained in all cases (see table 4.11), and the model seems to be working reasonably well in the case of the inner shell electrons which might be affected differently at chlorine and deuterium by any significant charge transfer or polarisation. The HCl and DCl monomer values are given in table 4.10. The ^{83}Kr data given in section 4.4 indicates that these angles are accurate to within 1%.

In chapter 7 the coordinate system of the atom-diatom complex is described in terms of R_o and θ. If θ is determined from an equation of the form of equation 4.6 then additional effects occur by mixing in of excited bending states ($K \neq 0$). $K = \pm 1$ states can be mixed in by off-diagonal terms in the field gradient tensor which have $\sin\theta\cos\theta e^{\pm i\phi}$ angular parts (where ϕ is the corresponding azimuthal angle) and magnitude of order B/b_o[31].

The measured dipole moments also provide in theory, angular information about the complexes. The observed value in this model can be interpreted as the projection of the HCl dipole along the *a* axis together with induced moments in the krypton atom.

$$\mu_a = \mu^{HCl}\langle P_1(\cos\gamma)\rangle[1 + 2\alpha_{Kr}/R_o{}^3] \qquad (4.8)$$
$$+ \alpha_{Kr}[3\theta^{HCl}\langle P_2(\cos\gamma)\rangle/R_o{}^4 + 4\Omega^{HCl}\langle P_3(\cos\gamma)\rangle/R_o{}^5] + \ldots$$

where $\langle P_x(\cos\gamma)\rangle$ are the Legendre polynomials in $\cos\gamma$ averaged over the wide amplitude motion, and θ^{HCl} and Ω^{HCl} are the quadrupole and octupole moments of HCl. Several errors arise in the determination of $\langle P_1(\cos\gamma)\rangle$. The multipole expansion is only slowly convergent, the dipole and quadrupole terms giving contributions of 0.062 D and 0.043 D respectively.

Table 4.10 Spectroscopic constants for HCl isotopes

	$H^{35}Cl$ [2]	$H^{37}Cl$	$D^{35}Cl$	$D^{37}Cl$
b_o/MHz [1]	312989.297	312519.121	161656.238	161183.122
$(eQq)^{Cl}$/MHz [2]	-67.61881(15) [4]	-53.436(95)	-67.39338(9)	-53.073(113)
$(eQq)^{D}$/kHz	—	—	187.36(30)	
μ/Debye	1.1086(3)		1.1033(5)	
c^{Cl}/kHz	53.841(18)	56(10)	27.426(7)	24(13)
d/kHz	5.59(9)	4.65(10)	0.85	
r_o/Å [3]	1.28387	1.28386	1.28124	1.28123

[1] ref[28]; H isotopes ± 20 kHz, D isotopes ± 15 kHz.
[2] $H^{35}Cl$ value from ref[29]; otherwise data from ref[30].
[3] Conversion factor b/MHz = 505379.04(±0.3)/I_b(amu Å^2); ref[27].
[4] Errors quoted at 3 standard deviations.

Table 4.11 Structural parameters for KrHCl complexes

Complex	$\gamma^{o}_{P_2}$	$\gamma^{o}_{P_1}$	R(Kr-Cl) /Å	∠KrClH /deg	k_s /mdyne.Å^{-1}	k_b /mdyne.Å
$^{84}KrH^{35}Cl$	37.9628(5) [1]	39.8_2 [5]	4.1117(5)	37.6947(6)	0.0156	0.0013
	37.8(2) [2]					
$^{84}KrH^{37}Cl$	37.97(3) [4,1]	39.7_3	4.1110(5)	37.785(32)	0.0157	0.0013
	38.5(1.3) [2]					
$^{86}KrH^{35}Cl$	37.9584(7) [1]	39.8_0	4.1115(5)	37.7195(9)	0.0158	0.0013
	38.1(6) [2]					
$^{84}KrD^{35}Cl$	30.8543(6) [1]	28.1_0	4.1258(10)	30.5387(13)	0.0172	0.0015
	30.8(4) [3]					
	35(6) [2]					

[1] from $(eQq)_a^{Cl}$; γ_{P_2} = arc cos[(<cos$^2\gamma$>)$^{\frac{1}{2}}$]
[2] from d_a
[3] from $(eQq)_a^{D}$
[4] error mostly due to uncertainty in $(eQq)^{Cl}$ in $H^{37}Cl$
[5] γ_{P_1} = arc cos(<cosγ>)

Higher terms have not been determined experimentally, but may well contribute another 0.04 D or more. The arc cos $(\langle P_1(\cos\gamma)\rangle) = \gamma_{P_1}$ value of 39.8° is derived from dipole and quadrupole polarisation terms only. Neglect of charge transfer in this model also contributes error to the value of $\langle P_1(\cos\gamma)\rangle$. It is shown in a later section that this is less than ~ 0.15 D, although because of this small electron redistribution the multipole moments in the HCl subunit will be slightly different from the values in free HCl, reducing γ_{P_1}. The value of γ_{P_1} given is therefore probably a lower bound and up to 10% may be the associated uncertainty in its value. Obviously then, its usefulness in structure prediction is limited in this case.

The same angular structure from different hyperfine data confirms that inner shell electrons are negligibly perturbed in the complex compared to the free atoms, but small charge transfer and polarisation effects do alter the valence molecular orbitals slightly. Consequently, a reasonable model for predicting the binding energy and structure of the complex is unlikely to include significant amounts of charge transfer.

An estimate of the value of the second structural parameter R_o may be obtained by treating the complex as a pseudodiatomic molecule. R_o is then related to the measured rotational constant by the equation $\bar{B}_o = \hbar^2/2\mu R_o^2$, where μ is the reduced mass of the complex:

$$\mu = \frac{m_{Kr} m_{HCl}}{m_{Kr} + m_{HCl}} \tag{4.9}$$

The semi-rigid model[1], based on figure 4.9 and described below provides another estimate of R_o. Considering figure 4.9, as $\theta \simeq \gamma$ to a good approximation then the instantaneous moments of inertia about the three axes are given by

$$\begin{aligned} I_{xx} &= \mu R_o^2 + \mu^{HCl} r_o^2 \cos^2\theta \\ I_{yy} &= \mu R_o^2 + \mu^{HCl} r_o^2 \end{aligned} \tag{4.10}$$

$$I_{zz} = \mu^{HCl} r_o^2 \sin^2\theta$$

where μ^{HCl} is the reduced mass of HCl similar to equation 4.9. A small term I_{xz} also exists since the molecular axis system used is not quite the principal axis system. (However since $\theta \simeq \gamma$ this neglected term is insignificant within the level of assumptions implicit in the model.) The experimental value of the rotational constant $\bar{B}_o$ can then be equated with $\frac{1}{2}(B+C)$ which is proportional to $(I_{xx} + I_{yy})^{-1}$. Expanding the I^{-1} terms as Taylor series and truncating at the second term leads to the equation

$$\bar{B}_o = B_{diatomic} - B^2_{diatomic}(1 + \langle\cos^2\theta\rangle)/2b_o^{HCl} \qquad (4.11)$$

where $B_{diatomic} = \hbar^2/2\mu R_o^2$ and $b_o^{HCl} = \hbar^2/2\mu^{HCl} r_o^2$.

Terms of the next highest order contribute a correction of about 10 kHz. The semi-rigid model is therefore assuming a rigidly bent complex, with the vibrational average of $\cos^2\theta$ being included to allow for averaging over slow, large amplitude bending motions.

The virtual equality of θ and γ may be shown by the relationship between them[20],

$$\frac{\cos^2\gamma}{\cos^2\theta} = 1 + \frac{2(\alpha+\beta)\sin^2\theta}{(\alpha-1)(\alpha-1+\beta) + 2(2\alpha+\beta)\cos^2\theta} \qquad (4.12)$$

where $\beta = [(\alpha+1)^2 - 4\alpha\sin^2\theta]^{\frac{1}{2}}$ and $\alpha = \mu R_o^2 (\mu^{HCl})^{-1}$, by considering the interrelation of the axis systems. For KrHCl $\gamma = 37.96°$ and $\theta = 38.00°$. Employing equations 4.11 and 4.12 iteratively yields values for R and θ. Usually the values are converged after two iterations. The values obtained for the main hydrogen and deuterium isotopes are shown in table 4.12.

The semi-rigid model, however is incorrect. In the limit of free rotation of the HCl subunit (zero bending anisotropy of the angular potential) $\bar{B}_o$ should equal $B_{diatomic}$ but equation 4.11 reduces to $B_{diatomic}[1 - 2B_{diatomic}/3b_o]$, since then $\langle\cos^2\theta\rangle = 1/3$. As the

Table 4.12 Model structural parameters for $KrH^{35}Cl$ and $KrD^{35}Cl$

	$^{84}KrH^{35}Cl$	$^{84}KrD^{35}Cl$
γ_{P_2}/degrees	37.9628	30.8543
θ (from corrected semi-rigid theory)	38.0031	31.0377
R_o (from corrected semi-rigid theory)/Å	4.0833	4.065 [1]
R_o (semi-rigid)/Å	4.0822	4.0653
R_o (pseudodiatomic)/Å	4.0886	4.0782
$f(\langle\cos^2\theta\rangle)$	0.79(14)	1.11(24) [1]

[1]The value of f should go smoothly to 1 as $\langle\cos^2\theta\rangle$ increases. There is a large uncertainty in the experimental value of C_b^{Cl} for KrDCl; the optimised KrHCl potential energy surface in chapter 7 yields values of 0.83(H) and 0.95(D) well within the error limit.

anisotropy increases and $\langle\cos^2\theta\rangle$ increases the equation will more nearly be obeyed, and in order to model this deviation it is assumed that a function f exists which multiplies the correction to the rotational constant, and is a single valued function of $\langle\cos^2\theta\rangle$. Thus equation 4.11 becomes

$$\bar{B}_o = B_{diatomic} - B^2_{diatomic}[1 + \langle\cos^2\theta\rangle] \times f(\langle\cos^2\theta\rangle)/2b_o^{HCl} \qquad (4.13)$$

This is given the title of the 'corrected semi-rigid equation'.

The contribution to the rotational constant from the structure of the diatomic molecule can more accurately be described using perturbation theory. The correction may then be formulated as a mixing in of excited bending vibrational states with the ground state via Coriolis terms in the Hamiltonian of the form $-B\mathbf{J}.\mathbf{j}$, where $\mathbf{J}$ is the total angular momentum operator and $\mathbf{j}$ is the angular momentum operator for the HCl subunit. In chapter 7 this theory will be directly applied to zeroth-order

eigenstates of the complex obtained from a solution of the Hamiltonian using the Born-Oppenheimer separation. The perturbation solution leads to a rotational constant of the form

$$\bar{B}_o = B_{diatomic} - 4B^2_{diatomic} \sum_n \frac{|\langle 0|j_x|n\rangle|^2}{E_n - E_o} \qquad (4.14)$$

where $B_{diatomic} = \langle 0|\hbar^2/2\mu R^2|0\rangle$, n labelling the excited bending states. So the difference between the corrected semi-rigid and the 'dynamic' theory is the replacement of $(1 + \langle\cos^2\theta\rangle)f(\langle\cos^2\theta\rangle)$ by $8\sum_n |\langle 0|j_x|n\rangle|^2/(E_n - E_o)$. The semi-rigid correction is 3.73 MHz in KrHCl and so this value will provide the major uncertainty in the value of R, unless an independent value of $f(\langle\cos^2\theta\rangle)$ is available. Happily this is possible from spin-rotation constant data.

The spin-rotation interaction is written as[32]

$$H_{SR} = c^{Cl}\, \mathbf{I}.\mathbf{J} \qquad (4.15)$$

which represents the interaction of the chlorine nuclear magnetic moment with the magnetic fields set up by the rotating nuclear framework and electrons (see Appendix B.2). The electronic term dominates in HCl (~ 104%). For the spin-rotation constant it is the b component of the spin-rotation tensor that is determined[33]. Using the semi-rigid model the value is predicted to be

$$c_b^{Cl} = c^{HCl} B_{diatomic} [\, 1 + \langle\cos^2\theta\rangle]/2b_o \qquad (4.16)$$

and following through the argument for the rotational correction again, the corrected semi-rigid theory would add $f(\langle\cos^2\theta\rangle)$ to equation 4.16. In the dynamic model **I.J** terms arise between terms of the form $-2B\mathbf{J}.\mathbf{j}$ and $c^{HCl}\mathbf{I}.\mathbf{j}$. In perturbation theory this leads to an operator of the form[31]

$$H_{SR} = 4c^{HCl} B_{diatomic} \sum_n |\langle 0|j_x|n\rangle|^2/(E_n - E_o) \qquad (4.17)$$

This is exactly the same form of correction as applied to the

rotational constant. Therefore, the observation of the spin-rotation constants provides a value for $f(\langle\cos^2\theta\rangle)$, which in turn provides a correction to the rotational constant. The corresponding values of R are given in table 4.12.

The choice of an acute angle for γ (and θ) in KrHCl follows this assignment for ArHCl. Klemperer[2] used an uncorrected semi-rigid analysis to obtain Ar...Cl distances. He then assigned an acute structure because a decrease in Ar...Cl distance was seen upon heavy atom substitution, similar to trends seen for more chemically bound chlorine species. For the obtuse assignment an increase in distance was seen. The corresponding values for the KrHCl system are shown in table 4.13, where a similar trend is found.

Table 4.13 Kr-Cl internuclear separation and isotope effects

γ	acute		obtuse	
	R(Kr-Cl)/Å	Difference/Å	R(Kr-Cl)/Å	Difference/Å
$^{84}KrH^{35}Cl$	4.1117		4.0574	
		0.0007		-0.0020
$^{84}KrH^{37}Cl$	4.1110		4.0594	
$^{84}KrD^{35}Cl$	4.1258		4.0103	
		0.0006		-0.0010
$^{84}KrD^{37}Cl$ [1]	4.1252		4.0113	

[1] $\bar{B}_0$ and $(eQq)_a^{Cl}$ value from ref[13].

However in view of the weakness of the bond and large zero-point motion of the van der Waals vibration the validity of the method must be open to question in view of the small changes in the value of R upon isotopic substitution. A further argument supporting the acute assignment using

the sign of DQ will be given in the next section.

(b) Distortion and force constant analysis

The structural analysis gives little indication of the extent of bending and vibrational motion in the complexes. Usually a linear ($\theta = 0°$) structure is assumed for the complex with the hydrogen or deuterium undergoing large amplitude motion about this linear configuration. The main confirmation of this assumption is provided by a comparison of the average angles derived from the quadrupole data for the hydrogen and deuterium species (see table 4.12). For a linear geometry and a harmonic bending potential the ratio of the fourth power of the angles should be 2 ($\simeq m_D/m_H \simeq$ ratio of bending moments); it is 2.3. Although such large amplitude bending motion is unlikely to be described adequately by a harmonic force field potential it also provides an indication of the force constants involved. The potential surface around the minimum can be written as:

$$V(R,\theta) = V_{min} + \tfrac{1}{2}k_s(R-R_e)^2 + \bar{k}_s(R-R_e)^3 + \ldots$$

$$+ \tfrac{1}{2}k_b\theta^2 + \bar{k}_b\theta^4 + \ldots$$

$$+ k'(R-R_e)\theta^2 + \bar{k}'(R-R_e)^2\theta^2 + \ldots$$

If we neglect the coupling of bending and stretching motion and assume a harmonic stretching potential ($V_{eff}(R) = \tfrac{1}{2}k_s(R-R_e)^2$), then it can be readily shown (*e.g.* ref[33], page 249) that the k_s is related to the centrifugal distortion constant, (treating the complex as a pseudo-diatomic molecule) by the Kratzer equation:

$$D_J = \frac{4\bar{B}_o^3}{\omega_s^2} \qquad (4.18)$$

where $k_s = 4\pi^2\omega_s^2\mu$. The values of ω_s are given in table 4.14 and k_s for each of the isotopes in table 4.11. These force constants are seen to be isotope dependent, demonstrating that the radial and angular vibrational motions are not independent.

Table 4.14 Distortion parameters for KrHCl complexes

Complex	ω_s /cm^{-1}	f(<cos$^2\gamma$>)	D_{P_2} (× 10^6) [1]
$^{84}KrH^{35}Cl$	32.39(5)	0.79(14)	10.8(1.0)
$^{84}KrH^{37}Cl$	31.89(11)	0.74(34)	9.5(5.5)
$^{86}KrH^{35}Cl$	32.50(13)	—	6.8(2.0)
$^{84}KrD^{35}Cl$	33.68(4)	1.11(24)	10.6(1.8)

[1] $D_{P_2} = DQ/(eQq)^{Cl}_{diatom}$

An effective harmonic bending force constant, k_b, may also be obtained from the equation

$$k_b = \frac{\hbar^2}{I_b \langle\theta^2\rangle^2} \qquad (4.19)$$

where I_b is the bending moment of inertia, and is essentially that of the hydrogen chloride about its centre of mass. The values of k_b are shown in table 4.11, and are also seen to be isotope dependent.

An indication of the magnitude of the bend-stretch coupling term $k'(R-R_e)\theta^2$ is given by the size of DQ. As the complex rotates faster (J quantum number increases), the centrifugal forces will increase the effective R separation, as indicated by the sign of D_J. This is seen to lead to an increase in the value of $(eQq)^{Cl}_a$ at the level of several parts per million (ppm) of $(eQq)^{HCl}$ and hence a smaller effective angle γ_{P_2}. Alternatively, the sign of DQ indicates that the effective bending force constant increases as the van der Waals bond length increases. This sign of DQ can also be rationalised by the potential energy surface in figure 4.11. As the molecule rotates the zero-point amplitude of

Figure 4.11 Schematic diagram illustrating the origin of the centrifugal distortion of the quadrupole coupling constant in a van der Waals atom-diatom complex. The contours for the potential surface on the left hand side are at 10 cm^{-1} intervals referred to the minimum. The two effective bending potentials on the right hand side of the diagram refer to those of a non-rotating (A) and rotating (B) complex. The classical amplitude of motion associated with zero-point energy for these two potentials can be seen to be markedly different. This leads to a J-dependent value of $\langle P_2(\cos\theta)\rangle$.

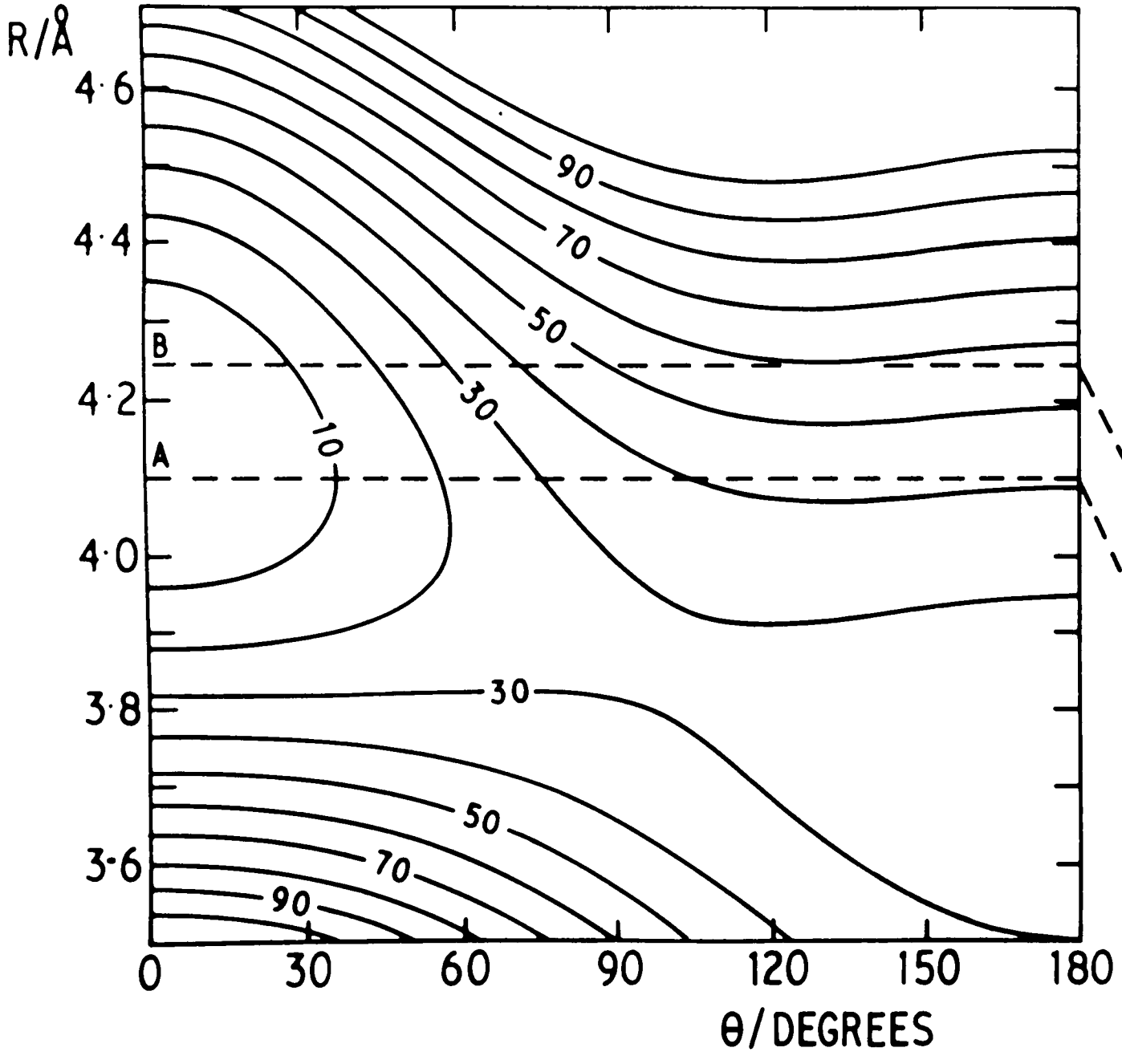
R/Å
4·6
4·4
4·2
4·0
3·8
3·6
B
A
10
30
50
70
90
30
50
70
90
0
30
60
90
120
150
180
θ/DEGREES

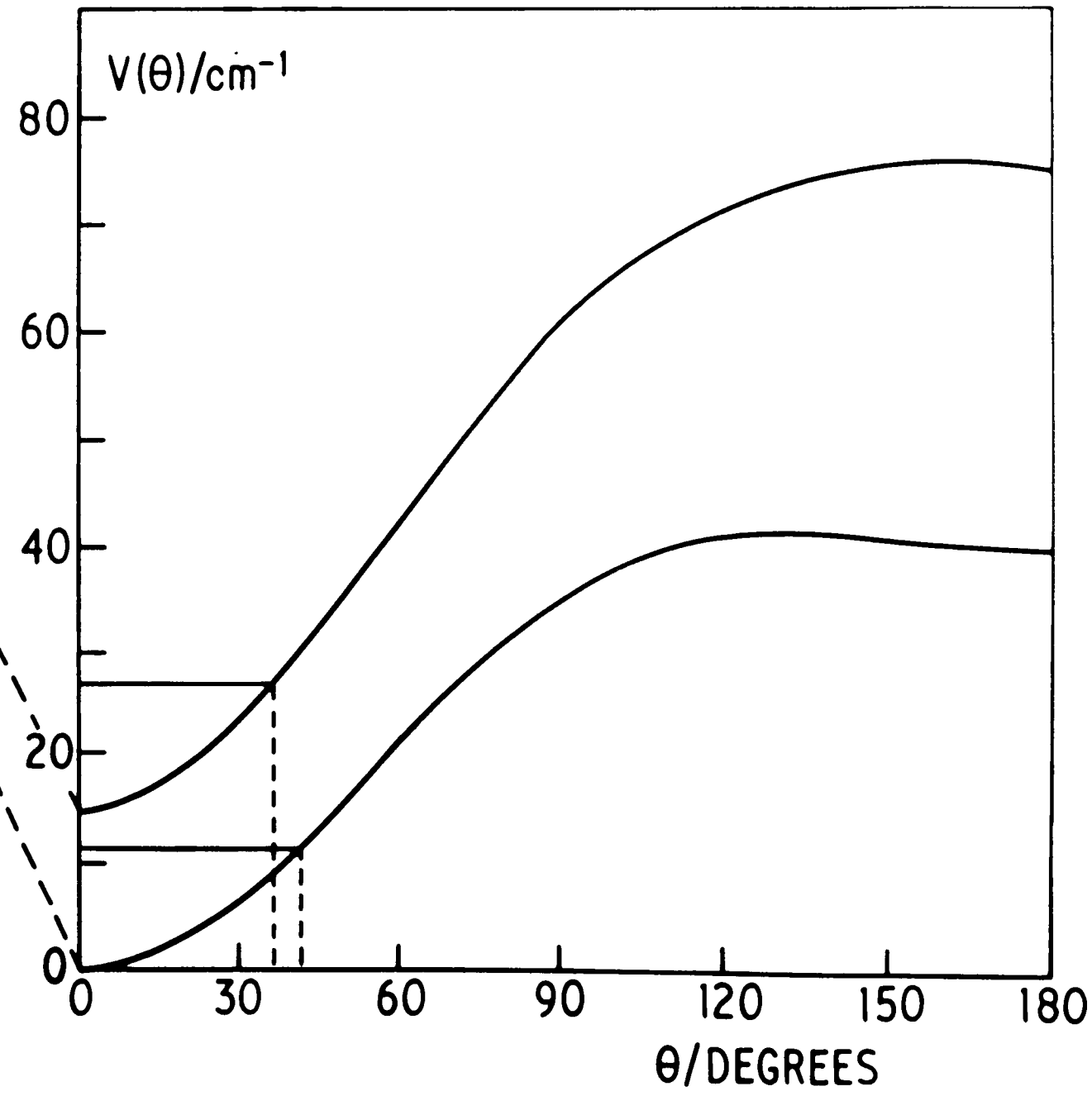
V(θ)/cm⁻¹
80
60
40
20
0
0
30
60
90
120
150
180
θ/DEGREES

motion decreases for bending if the surface has the R/θ curvature shown. Such results can be understood in terms of the angular effects of intermolecular repulsion due to electron exchange. As the hydrogen atom is bent away from the linear axis, the repulsive forces are reduced (due to the anisotropy of the electron distribution in HCl) and the krypton and hydrogen chloride can approach more closely. The assumption of an acute value for γ is also strengthened by consideration of the sign of DQ. For the acute choice the Kr-Cl distance is seen to increase in going from H to D (see table 4.13), whereas θ decreases, this agreeing with the sign of DQ (the R_o value however decreases due to a c.o.m. shift from HCl to DCl). The opposite is true for the obtuse case.

Flygare[33] assumed a rigid structure and minimised his data according to

$$f = \sum_{i=1}^{6} (\bar{B}_{oi} - \bar{B}_{ci})^2 \qquad (4.20)$$

for the H and D isotopes separately. He also found an acute assignment for both series.

It should perhaps be emphasised again that in view of the large amplitudes of zero-point motion in these complexes, (to be discussed quantitatively in chapter 7), any small changes in 'equilibrium' separations are unlikely to fix absolutely the acute or obtuse assignment, but a consideration of the sign of DQ provides the best evidence that an acute assignment is correct.

The centrifugal distortion of the dipole moment has also been measured for these complexes (see tables 4.5 and 4.9) and is of the order of 3×10^{-5} Debyes. The Stark effect for these complexes is second-order, the diagonal contribution in a decoupled basis being

$$\Delta W^{(2)} = - \frac{\mu_{eff}^2 E^2}{2\bar{B}_o} \left[\frac{3M^2 - J(J+1)}{(2J-1)(2J+3)} \right] \frac{1}{J(J+1)} \qquad (4.21)$$

from which is measured a $\mu_{eff}^2 = \mu_o^2 + \mu_o D\mu J(J+1) + O(D\mu^2)$, the $D\mu^2$ term

being neglected. μ_o can be considered as arising from a permanent moment and several induced moment contributions. $\mu_o D\mu$ has several contributors to its magnitude also, which vary in sign. These terms are: (a) The centrifugal change in the projection of the dipole of the diatom along the intermolecular axis resulting from the change in γ_{P_1} as R increases; this is equivalent to the DQ term, and provides a positive contribution to DQ. (b) A contribution due to the polarisability anisotropy of the complex ($\equiv(\alpha_{\parallel} - \alpha_{\perp})^{HCl}$). From Mizushima[25], (4-5-17) this is given by

$$\Delta W^{(2)} = \frac{E^2}{3}(\alpha_{\parallel} - \alpha_{\perp})^{HCl} \cdot \frac{3M^2 - J(J+1)}{(2J-1)(2J+3)} \cdot \langle P_2(\cos\gamma)\rangle \qquad (4.22)$$

since the polarisibility anisotropy transforms as a second rank tensor. This provides a negative contribution to $D\mu$. (c) The second-order mixing in of excited bending states via the perpendicular dipole moment. This has been shown to provide a contribution of the form[34]

$$\Delta W^{(2)} = -\frac{E^2}{3\bar{\omega}} \mu_{\perp}^2 \left[1 + \frac{3M^2 - J(J+1)}{(2J-1)(2J+3)}\right] \qquad (4.23)$$

where $\bar{\omega}$ is an effective bending excitation energy from the closure approximation and $\mu_{\perp}^2 \simeq \sum_b |\langle 00|\mu^{HCl}\sin\theta|\nu_b K=1\rangle|^2$. This gives a negative contribution to $D\mu$ of the form

$$D\mu = -\frac{\mu_{\perp}^2}{\mu_{\parallel}} \frac{\bar{B}_o}{3\bar{\omega}} \qquad (4.24)$$

The magnitude of these terms and the dramatic change in the third contribution on going from Kr to Ne as the inert gas is changed will be discussed in the next chapter.

4.4 Charge transfer in KrHCl

One method of estimating the extent of charge transfer in van der Waals molecules is by the measurement of the induced nuclear quadrupole coupling constant of ^{83}Kr in $^{83}KrHCl$. ^{83}Kr, with an isotopic abundance of 11.6%, has a nuclear spin of 9/2. In the isolated spherical atom

the electric field gradient at the nucleus is zero, and so $(eQq)^{^{83}Kr} = 0$. Any charge transfer (which is neglected in our semi-rigid model) gives rise to an effective field gradient, and hence to a non-zero value for $(eQq)_a^{Kr}$. Induced effects due to the HCl subunit electrostatic moments can also contribute to this field gradient.

The J,F = $3,\frac{3}{2} \rightarrow 2,\frac{3}{2}$ transition of $^{83}KrH^{35}Cl$ was obtained by cumulative computer scanning using < 1 MHz white noise modulation, at 7234.4_5 MHz. The signal/noise ratio was very poor and significant signal/noise ratios using the phase-lock technique could not be achieved to distinguish ^{83}Kr hyperfine structure. However as shown in figure 4.12 a consistent splitting was seen on long time averaging of the transition of about 0.95 MHz. The pattern of hyperfine structure on this transition should be a quartet of lines at 0.073, 0.040, -0.033, -0.073 [35], and fitting the average of the separation of the two doublets gives an upper bound to the magnitude of $(eQq)_a^{Kr}$ as 9.1 MHz.

This value in turn gives an upper limit to the field gradient. Faust[36] has measured the nuclear quadrupole moment of ^{83}Kr as 0.270(13) barns (1 barn = 10^{-24} cm^2) which produces a field gradient of

$$|q| = 1.4_0 \times 10^{21} \text{ V m}^{-2} \qquad (4.25)$$

Flygare and co-workers have very recently published $(eQq)_a^{^{83}Kr}$ as + 10.227(71) MHz in KrHF[37]. Partition functions in that case favour improved signal/noise ratios due to the lack of a fluorine quadrupole coupling constant. It will be assumed here that the sign is the same for KrHCl as for KrHF.

The presence of the charge distribution of HCl produces a contribution to the field gradient made up of two terms for each multipole effect[38],

$$q_{dipole} = \frac{-3\mu^{HCl}}{2\mu_o\varepsilon_o R_o^4} \langle P_1(\cos\gamma)\rangle (1 - \gamma^{Kr}) \qquad (4.26)$$

$$q_{quadrupole} = \frac{-3\theta^{HCl}}{\mu_o \varepsilon_o R_o{}^5} \langle P_2(\cos\gamma)\rangle (1 - \gamma^{Kr}) \qquad (4.27)$$

where the first term in brackets represents the electrostatically induced gradient due to a Kr...$\overset{\delta+}{H} - \overset{\delta-}{Cl}$ charge distribution (for the dipole term). The second term (γ^{Kr}) is the Sternheimer antishielding correction for krypton. Sternheimer and co-workers have shown[39] that extranuclear charges can produce enhanced electric field gradients by perturbing the core electrons and these create quadrupole polarisability in the atom which enhances the field gradient (antishielding). γ^{Kr} has been calculated from a Hartree-Fock basis set as -41.0 [40]. This gives $q_{induced} = -0.23 \times 10^{21}$ V m^{-2} for the dipole term. Other multipole terms contribute to a lesser extent and yield approximately a further -0.18×10^{21} V m^{-2}. The difference of -1.0×10^{21} V m^{-2} is then assumed to be caused by charge transfer from the outer Kr (4p) orbital on to the HCl.

An estimate of the amount of charge transfer can be made as follows. On the loss of one electron the electronic configuration is that of Br, with a slight contraction of orbital radius due to increase of nuclear charge. The resultant field gradient can be estimated either from the measured value of eQq for atomic bromine from spectra, which yields -0.98×10^{23} V m^{-2} [41], or an estimate of the radius of the $4p^5$ shell in Br from spin-orbit data which yields -1.23×10^{23} V m^{-2} [42]. These suggest that only about $\leq 0.9\%$ of an electron of charge transfer is occurring. Induced field gradient effects due to this charge transfer, and the decrease of an induced $4p \rightarrow np$ contribution to γ^{Kr} [40] are not significant. An upper limit to the amount of charge transfer is then

$$\begin{aligned} \mu^{CT} &\leq 0.009 \times 1.602 \times 10^{-19} \times 4.08 \times 10^{-10} \\ &= 0.59 \times 10^{-30} \text{ C m} \\ &= 0.18 \text{ Debyes} \end{aligned} \qquad (4.28)$$

or ~ 0.13 Debyes if it is assumed that the charge is transferred mainly on to the H. This leads to the uncertainty in γ_{P_1} as already discussed.

The estimation of the effect of charge transfer in other van der Waals and weak hydrogen bonding complexes is difficult. Janda[43] reported that in HFDCl, the expected value for $(eQq)_a^D$ was +154 kHz from

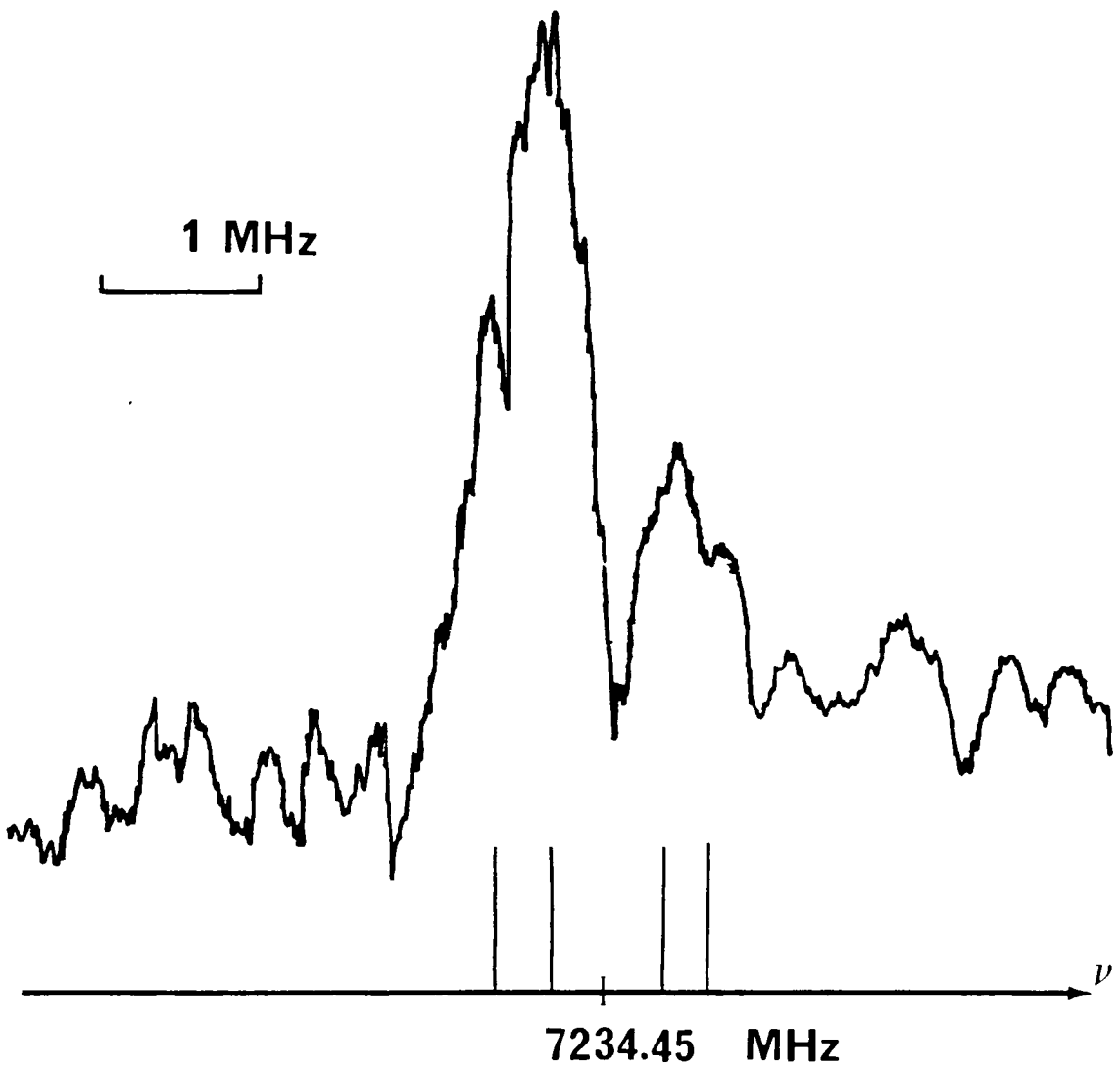

Figure 4.12 Noise broadened microwave spectrum of $^{83}KrH^{35}Cl$

γ_{P_2} for chlorine whereas a value of 145 ± 5 kHz was found. This indicates a net increase of electronic charge at the deuterium nucleus contributing to the field gradient[44]. This trend is not seen in general in *ab initio* calculations which suggest a resultant loss of charge on the proton on complex formation[45]. The latter effect can be further decomposed to a charge transfer type term and induced moment terms which counteract each other as far as the hydrogen atom charge is concerned[46]. Although it is the induced terms which seem to dominate in these

ab initio calculations it is difficult to define the charge shell of an atom in a molecule and to give any precise meaning to 'population changes' upon complex formation[47]. In this molecule then the effects on the field gradient by charge transfer and induced moment effects appear to almost cancel. From this it is possible to estimate a contribution to the dipole moment of about 0.4 Debyes, which is reasonable. A further consideration of the role of charge transfer is made for $(HF)_2$ in chapter 7.

4.5 Conclusion

The extent to which correlation affects the absolute values of the derived spectroscopic constants in KrHCl should also be mentioned. The correlation matrix for the spectroscopic parameters of $^{84}KrH^{35}Cl$ is shown in table 4.15.

Table 4.15 Correlation matrix for $^{84}KrH^{35}Cl$ spectroscopic parameters

	$\bar{B}_o$	D_J	$(eQq)_a^{Cl}$	DQ	μ_a	Dμ	c_b
$\bar{B}_o$	1.0						
D_J	0.891	1.0					
$(eQq)_a^{Cl}$	0.144	0.111	1.0				
DQ	-0.134	-0.109	-0.872	1.0			
μ_a	0.042	0.034	0.329	-0.214	1.0		
Dμ	-0.029	-0.027	-0.242	0.253	-0.919	1.0	
c_b	0.051	0.047	0.201	-0.619	0.207	0.034	1.0

$\bar{B}_o$ and D_J are largely determined by the microwave data (8 values) and the quadrupole and distortion data by the r.f. data (67 values). The largest correlations occur between $\bar{B}_o$ and D_J, $(eQq)_a^{Cl}$ and DQ, and μ_a and Dμ. $\bar{B}_o$ and D_J are separately determined within 95% confidence limits[48]. A significant correlation also exists between DQ and c_b and

in the fitting programs in chapter 7 large error limits have been placed upon DQ data. The DCl data is poor because of the unresolvable spin-spin structure and the deuterium quadrupole splittings.

The result of including Flygare's data for KrHCl is shown in table 4.16. Only $\bar{B}_o$ and D_J are found to have smaller standard deviations associated with them, and the standard deviations for the other quantities actually increase because of poorer quality data. In no case do the combined fit parameters differ by more than one standard deviation from the results quoted in this chapter.

Table 4.16 Comparison of $\bar{B}_o$ and D_J experimental values

	This work	Combined data
$^{84}KrH^{35}Cl$		
$\bar{B}_o$/MHz	1200.62374(31) [1]	1200.62392(23)
D_J/kHz	7.343(22)	$7.350_5(7_4)$
$^{84}KrD^{35}Cl$		
$\bar{B}_o$/MHz	1183.77283(25)	1183.77297(24) [2]
D_J/kHz	6.510(16)	6.517(11)

[1] Errors at 2σ

[2] The smaller reduction in 2σ is due to unresolved deuterium quadrupole hyperfine structure in the experiment[13].

For the KrHCl system then, all experimental features have been explained and appropriate parameters derived. New distortion constants have been obtained which relate directly to the coupling of vibrational modes in the complex. A semi-rigid model which provides a simple analysis of the data has been given; it describes the atom-diatom

complex as an acute, large-amplitude bender, with very little charge reorganisation of the individual monomer species.

References to chapter 4

1. A.E. Barton, T.J. Henderson, P.R.R. Langridge-Smith and B.J. Howard, Chem. Phys., *45*, 429, (1980).

2. S.E. Novick, P.B. Davies, S.J. Harris and W. Klemperer, J. Chem. Phys., *59*, 2273, (1973).

3. S.E. Novick, K.C. Janda, S.L. Holmgren, M. Waldman and W. Klemperer, J. Chem. Phys., *65*, 1114, (1976).

4. L.F. Keyser and G.W. Robinson, J. Chem. Phys., *44*, 3225, (1966); H. Friedman and S. Kimel, J. Chem. Phys., *44*, 4359, (1966); B. Katz, A. Ron and O. Schnepp, J. Chem. Phys., *46*, 1926, (1967); W.G. Holle and D.W. Robinson, J. Chem. Phys., *53*, 3768, (1970).

5. H.A. Gebbie and N.W.B. Stone, Proc. Phys. Soc. (London), *82*, 309, (1963).; A. Ben-Reuven, S. Kimel, M.A. Hirschfeld and J.H. Jaffe, J. Chem. Phys., *35*, 955, (1961); D.H. Rank, D.P. Eastman, B.S. Rao and T.A. Wiggins, J. Mol. Spectrosc., *10*, 34, (1963).

6. A.M. Ding and J.C. Polanyi, Chem. Phys., *10*, 39, (1975).

7. R.M. van Aalst, J.A. Schuurman and J. van der Elsken, Chem. Phys. Lett., *35*, 558, (1975).

8. J.G. Kircz, G.J.Q. van der Peyl and J. van der Elsken, J. Chem. Phys., *69*, 4606, (1978); J.G. Kircz, Ph.D. Thesis, (Amsterdam, 1979).

9. E.W. Boom, D. Frenkel and J. van der Elsken, J. Chem. Phys., *66*, 1826, (1977); E.W. Boom and J. van der Elsken, private communication, to be published; E.W. Boom and J. van der Elsken, J. Mol. Struct., *45*, 113, (1978).

10. S.E. Novick, S.J. Harris, K.C. Janda and W. Klemperer, Can. J. Phys., *53*, 2007, (1975).

11. A. Kudian and H.L. Welsh, Can. J. Phys., *49*, 230, (1968).

12. J. Goodman and L.E. Brus, J. Chem. Phys., *65*, 3146, (1976); *ibid.*, *67*, 4858, (1977).

13. T.J. Balle, E.J. Campbell, M.R. Keenan and W.H. Flygare, J. Chem. Phys., *71*, 2723, (1979); *ibid.*, *72*, 922, (1980).

14. T.J. Henderson, Part II Thesis, (Oxford, 1977).

15. J.M. Parson, P.E. Siska and Y.T. Lee, J. Chem. Phys., *56*, 1511, (1972); J.A. Barker, R.O. Watts, J.K. Lee, T.P. Schafer and Y.T. Lee, J. Chem. Phys., *61*, 3081, (1974).

16. G.M. McClelland, K.L. Saenger, J.J. Valenti and D.R. Herschbach, J. Phys. Chem., *83*, 947, (1979).

17. T.R. Dyke, G.R. Thomasevich and W. Klemperer, J. Chem. Phys., *57*, 2277, (1972).

18. H.W. Kroto, Molecular Rotation Spectra, (Wiley-Interscience, London, 1975), chapter 8.

19. H.P. Benz, A. Bauder and Hs.H. Günthard, J. Mol. Spectrosc., *21*, 156, (1966).

20. J.M. Hutson, Part II Thesis, (Oxford, 1979).

21. W.C. Hamilton, Statistics in Physical Science, (Ronald Press, N.Y., 1965), chapters 4 and 5.

22. See, for example, W. Gordy and R.L. Cook, Microwave Molecular Spectra, (Wiley-Interscience, London, 1970).

23. K.C. Jackson, P.R.R. Langridge-Smith and B.J. Howard, Mol. Phys., *39*, 817, (1980).

24. K.C. Janda, Ph.D. Thesis, (Harvard, 1977), page 19.

25. M. Mizushima, The Theory of Rotating Diatomic Molecules, (Wiley-Interscience, N.Y., 1975), table 4-4.

26. K. Kawaguchi, C. Yamada, T. Tanaka and E. Hirota, J. Mol. Spectrosc., *64*, 125, (1977).

27. G.W. Kaye and T.H. Laby (compilers), Tables of Physical and Chemical Constants, (Longman, London, 1979), 14th edition, chapter 4.

28. F.C. de Lucia, P. Helminger and W. Gordy, Phys. Rev. A, *3*, 1849, (1971).

29. F.H. de Leeuw and A. Dymanus, J. Mol. Spectrosc., *48*, 427, (1973).

30. E.W. Kaiser, J. Chem. Phys., *53*, 1686, (1970).

31. B.J. Howard, private communication.

32. J.M.B. Kellog, I.I. Rabi, N.R. Ramsey and J.P. Zacharius, Phys. Rev., *56*, 728, (1939).

33. W.H. Flygare, Molecular Structure and Dynamics, (Prentice-Hall, N.J., 1978), chapter 6.9.

34. T.R. Dyke, B.J. Howard and W. Klemperer, J. Chem. Phys., to be published.

35. C.H. Townes and A.L. Schawlow, Microwave Spectroscopy, (Dover, N.Y., 1975), chapter 6.

36. W.L. Faust and L.Y. Chow Chin, Phys. Rev., *129*, 1214, (1963).

37. E.J. Campbell, M.R. Keenan, L.W. Buxton, T.J. Balle, P.D. Soper, A.C. Legon and W.H. Flygare, Chem. Phys. Lett., *70*, 420, (1980).

38. A.D. Buckingham, Quart. Rev. Chem. Soc., *13*, 183, (1959).

39. R. Sternheimer, Phys. Rev., *86*, 244, (1952); H.M. Foley, R. Sternheimer and D. Tycko, Phys. Rev., *93*, 734, (1954); R. Sternheimer and H.M. Foley, Phys. Rev., *102*, 731, (1956).

40. G. Burns and E.G. Winkler, Phys. Rev., *121*, 155, (1961).

41. Reference[35], chapter 9.

42. R.G. Barnes and W.V. Smith, Phys. Rev., *93*, 95, (1954).

43. K.C. Janda, J.M. Steed, S.E. Novick and W. Klemperer, J. Chem. Phys., *67*, 5162, (1977).

44. M. Dixon and J.A.S. Smith, Trans. Faraday Soc., *64*, 1, (1968).

45. H. Umeyama, K. Morokuma and S. Yamabe, J. Am. Chem. Soc., *99*, 330, (1977); *ibid.*, *99*, 1316, (1977).

46. P. Kollman, J. Am. Chem. Soc., *99*, 4875, (1977).

47. T.P. Groen and F.B. van Duijneveldt, unpublished results.

48. P.R. Bevington, Data Reduction and Error Analysis in the Physical Sciences, (McGraw-Hill, N.Y., 1969).

CHAPTER 5: THE NEON-DEUTERIUM CHLORIDE SYSTEM

5.1 Introduction

It seemed reasonable, in view of the success of the KrHCl system to attempt to obtain the microwave and radiofrequency spectra of NeHCl and its deuterium analogue, to investigate the effect of changing the inert gas atom[1].

Few previous investigations of neon complexes appear to have taken place although a large number of helium and heavy inert gas - diatomic molecules have been studied[2]. McKellar and Welsh[3] obtained the spectra of NeH_2 and NeD_2 as discrete lines accompanying the collision-induced and quadrupole-induced spectra of H_2 and D_2 in the near infrared. The discrete (rotation-vibration) spectra yielded B and D_J values for the complexes. An equilibrium distance of 3.99 Å for NeH_2 was obtained. The weakness of the neon complexes was demonstrated by the fact that only three bound (and one quasibound) rotational levels were seen, and only four bound (and two quasibound) levels were seen for NeD_2. A Lennard-Jones potential with a well depth of 25 cm^{-1} reproduced these results. Also little or no effect due to anisotropic parts of the potential was seen in contrast to the heavier inert gas complexes[4]. Levy and co-workers have used fluorescence excitation spectroscopy and dispersed fluorescence spectroscopy to study complexes of Ne atoms with I_2[5]. The formation of Ne_7I_2 required forcing conditions (~ 95 atmospheres) for its formation. It also showed anomalous binding from its fluorescence excitation spectral shift over pure I_2 suggesting some sort of coordination shell of 6 for Ne atoms around I_2[5]. The dispersed fluorescence spectrum yielded product state distributions which were used to bracket the binding energy of NeI_2 at 72.4 - 74.7 cm^{-1}[6], again, a very weak complex. Brus has shown that there is little interaction of diatomic molecules in neon matrices compared with the heavier inert

gases, by studying OH and OD ($A^2\Sigma^+$) vibrational relaxation[7], and NH and ND relaxation[8].

The particular interaction between neon and hydrogen chloride has been studied by the perturbing effect of the rare gas atom on vibrational and rotational transitions of the hydrogen halide. Among these are matrix isolation studies[9] and pressure-induced shifts of vibration-rotation lines of HCl[10]. Little or no direct information on the complex was obtained from these experiments, however.

A number of *ab initio* calculations have also been undertaken. NeH_2O[11] and NeHF[12] have been studied at the Hartree-Fock level. For NeHF the lowest energy was found for a linear complex of 82 cm^{-1}, with a neon to centre of mass of HF distance of 3.73 Å. In view of all these results it is expected that the binding energy of NeHCl will be much lower than that of KrHCl.

NeHCl and NeDCl were first formed in a supersonic expansion by Novick and co-workers[13]. A few percent of HCl (DCl) was expanded through a 30 μm nozzle at 298 K stagnation temperature. They observed a refocussing of 5% of straight-through beam intensity for NeDCl, using 25 kV applied to shorter quadrupole rods than those in the Oxford spectrometer. NeHCl was observed to be defocussed. Novick ascribed this behaviour to the effects of severe non-rigidity. Assuming that NeHCl is structurally similar to ArHCl, a non-polar species would result from unhindered rotation of the HCl subunit in the complex, (zero angular anisotropy in the potential). The first possible polar state would then correspond to the $J = 1$ state of HCl, 21 cm^{-1} above the ground state. The polarity of NeDCl was ascribed to either a net DCl dipole along the *a* inertial axis or population of this first excited state, for NeDCl now only 10.8 cm^{-1} above the ground state.

In this chapter the radiofrequency and microwave spectra of $NeD^{35}Cl$ and $NeD^{37}Cl$ are presented. It is shown that the ground state is polar

and is responsible for the refocussing, no excited states being detectable in the cold beam. NeHCl is still apparently non-polar in the beam and this is also accounted for.

5.2 Experimental

The microwave and radiofrequency spectra of $NeD^{35}Cl$ and $NeD^{37}Cl$ were taken in the same way as KrDCl. The complex was formed by expanding a mixture of 2% DCl (HCl) in neon, with a backing pressure of ~ 500 torr, through a 35 μm stainless steel nozzle at around 140 - 150 K. Again, no skimmer was used. Ion currents for $NeD^{35}Cl$ at m/e = 57 were much reduced over KrHCl; a typical value being 2.3×10^{-11} A (electrometer current) of straight-through beam, about 5% of the KrHCl signal. Background signal existed at m/e = 57 (of unknown origin) and was about the same intensity as the beam signal, but at m/e = 59, for $NeD^{37}Cl$, the mass spectrum of the ion chamber was free from significant background. (In between at m/e = 58 ($^{232}Th^{4+}$) the background signal was about 30 times larger than the $NeD^{35}Cl$ signal.) Most spectroscopic transitions were monitored at these parent mass peaks, although they could also be observed at the DCl daughter peaks (Cl^+, DCl^+, m/e = 35, 37 and 39). The refocussed signal was around one order of magnitude larger for the J = 1 states of NeDCl at these daughter peaks, but long run times increased the background of DCl at these peaks, and this significantly reduced the signal/noise ratios[14].

The focussing characteristics of NeDCl suggested a much smaller dipole moment and hence smaller bending anisotropy for the complex than for KrDCl. J = 1 was found to be focussed by A,B = 11,6 kV, and J = 2 by A,B = 26,16 kV (~ 20 - 30% refocussing). These fields are about three to five times larger than those for KrDCl (see table 4.6). Since to a first approximation the field required to focus a given J state is proportional to $\mu_a^{-1}\bar{B}_o^{\frac{1}{2}}$ (see Appendix A), then using van der Waals radii for the inert gas atoms suggests a μ_a of ~ 0.4_5 Debyes.

Unfortunately, since A and B potentials up to 30 kV only may be applied to the rods (due to discharging), it did not prove possible to focus any $J = 3$ states.

The resulting microwave spectral transitions are shown in table 5.1 and the radiofrequency spectrum in table 5.2. Representative transitions are shown in figures 5.1 and 5.2.

Table 5.1 Microwave transition frequencies at zero electric field

Transition		$NeD^{35}Cl$		$NeD^{37}Cl$	
Final state $J'F'$	Initial state[1] $J\ F$	Frequency /MHz	Obs - calc /kHz	Frequency /MHz	Obs - calc /kHz
$0\ \frac{3}{2}$	$1\ \frac{5}{2}$	5396.206(13)[2]	-2	5297.712(8)	-2
$0\ \frac{3}{2}$	$1\ \frac{1}{2}$	5398.8659(22)	0	5299.8196(18)	0
$2\ \frac{3}{2}$	$1\ \frac{1}{2}$	10783.370(20)	-1	10587.502(10)	5
$2\ \frac{1}{2}$	$1\ \frac{1}{2}$	10786.698(20)	2	10590.140(17)	4
$1\ \frac{3}{2}$	$2\ \frac{1}{2}$	10792.679(12)	2	10594.877(14)	3
$3\ \frac{3}{2}$	$2\ \frac{1}{2}$	16168.390(20)	-2	15874.05(3)[3]	-18

[1] Initial state is focussing state. The $2\frac{1}{2} \leftrightarrow 1\frac{1}{2}$ transition could be obtained focussing $J = 1$ or 2.
[2] Values in parentheses are HWHM.
[3] Broad weak transition. All line positions quoted are expected line centres corrected for deuterium quadrupole hyperfine structure.

NeHCl was formed by the same method as for NeDCl. To date little or no refocussing has been seen on $m/e = 56$ ($NeH^{35}Cl$). An explanation of this is given in the next section.

Figure 5.1 *The $J,F_1 = 1,1/2 \rightarrow 0,3/2$ microwave transition in $NeD^{37}Cl$ at zero electric field. No deuterium hyperfine structure should be present in this transition.*

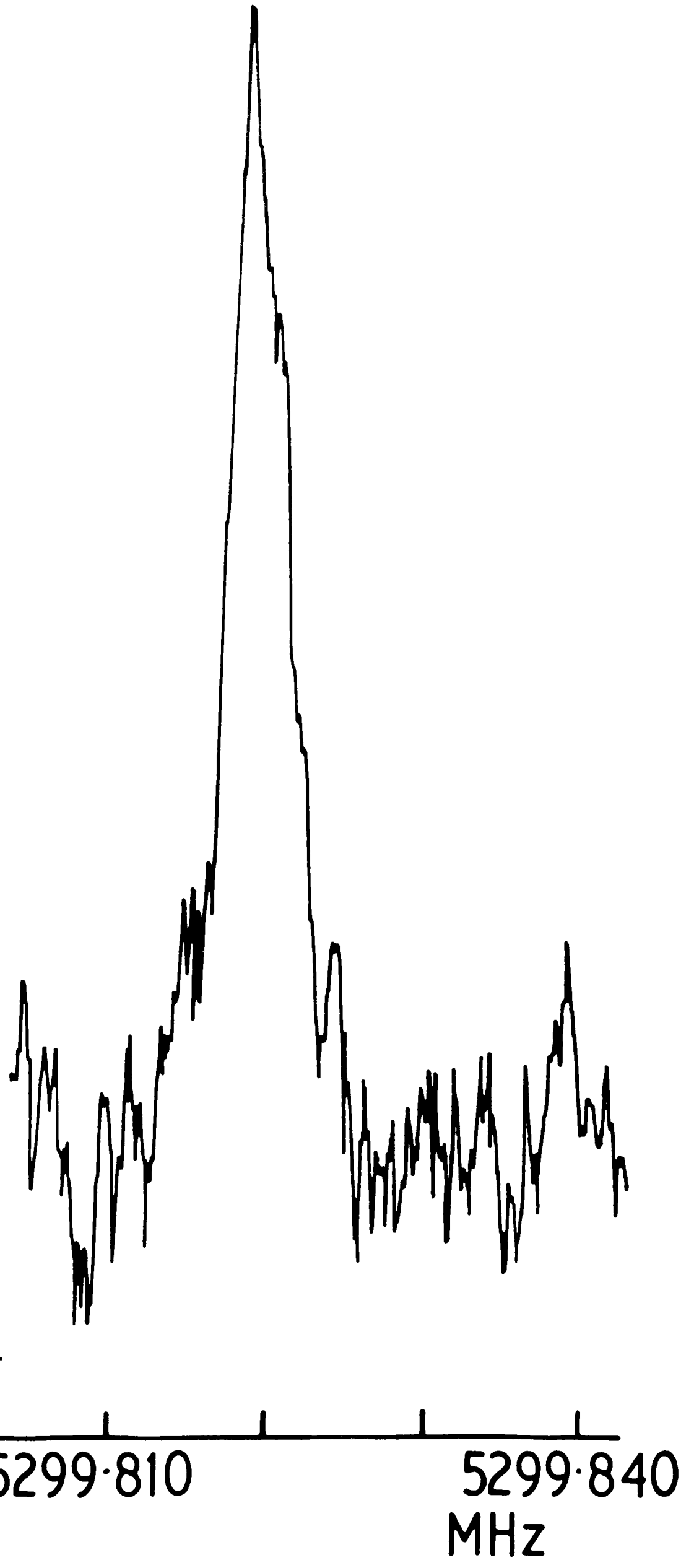
5299·810
5299·840
MHz

Figure 5.2 *Radiofrequency spectrum of $NeD^{35}Cl$ at an electric field of 1084.87 V cm^{-1}. The transition is $J = 1$, $F_1 = 1/2 \rightarrow 3/2$, $M_{F_1} = 1/2 \rightarrow 1/2$. The splitting is due to deuterium nuclear quadrupole hyperfine effects, the components being $M_{I_2} = 0$ at lower frequency than $M_{I_2} = \pm 1$.*

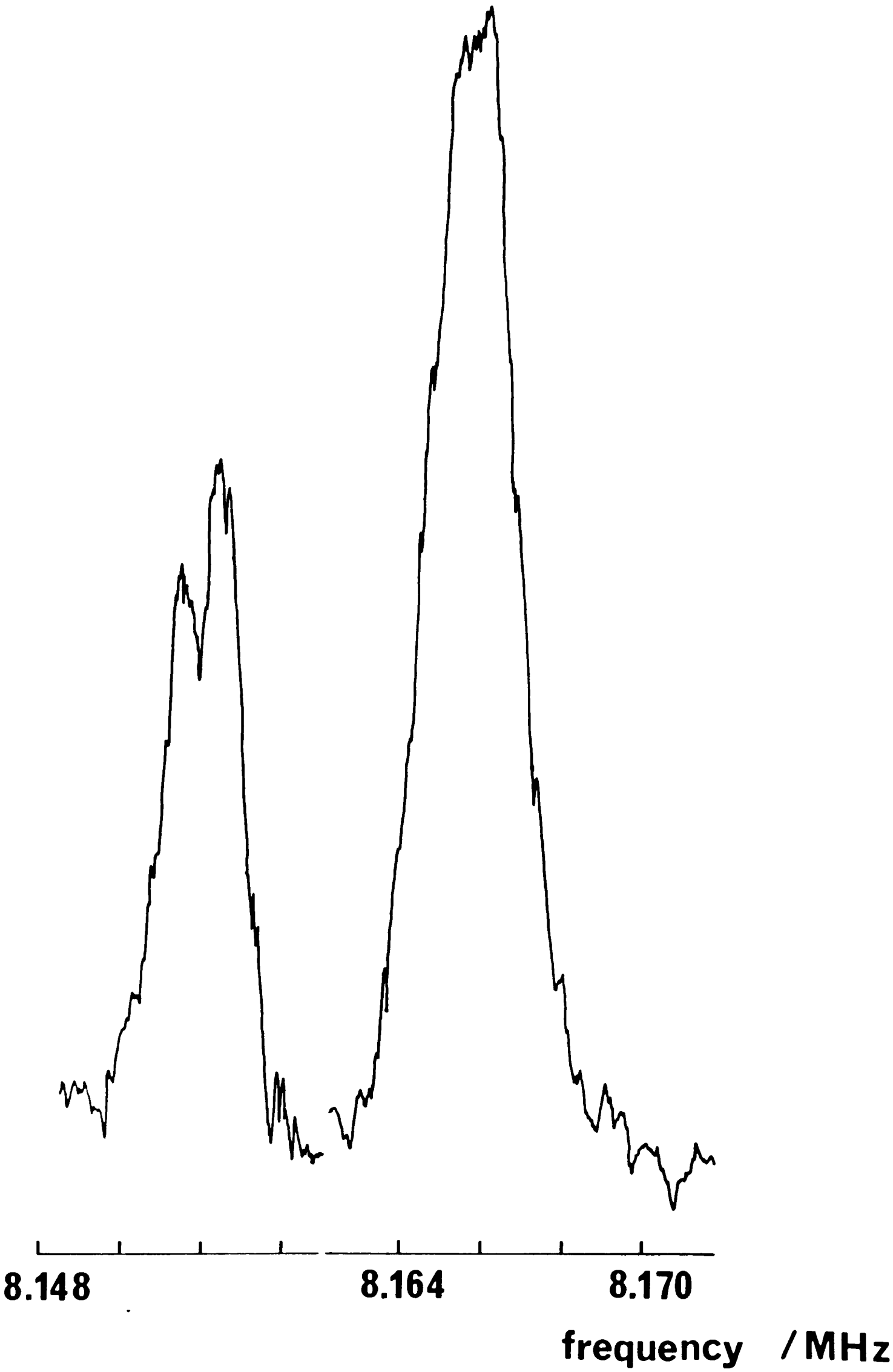
8.148
8.164
8.170
frequency /MHz

Table 5.2 Radiofrequency transition frequencies of NeDCl

Transition C field voltage /volts	Transition frequency /MHz	Obs - calc /kHz	Δ /kHz
$NeD^{35}Cl$			
$J = 1,\ F_1 = 1/2 \rightarrow 3/2,\ M_{F_1} = 1/2 \rightarrow 1/2,\ M_{I_2} = 0$			
299.712	$6.0598_7(9)$ [1]	0.1_3	5.3_3
399.626	$6.1316_4(12)$	0.2_9	5.8_8
499.551	$6.2363_0(15)$	-0.4_7	7.0_0
699.366	$6.5912_0(12)$	-0.0_9	9.1_3
899.173	$7.2116_0(12)$	-0.5_1	12.3_5
1098.643	$8.1521_5(10)$	0.2_1	13.5_3
	$M_{I_2} = \pm 1$		
299.712	$6.0652_0(10)$	0.2_1	
399.626	$6.1375_2(16)$	0.2_2	
499.551	$6.2433_0(15)$	-0.3_3	
699.366	$6.6003_3(10)$	-0.1_9	
899.173	$7.2239_7(10)$	0.0_7	
1098.643	$8.1656_8(12)$	0.0_5	
$J = 2,\ F_1 = 1/2 \rightarrow 5/2,\ M_{F_1} = 1/2 \rightarrow 3/2,\ M_{I_2} = 0$			
299.710	$5.7048_7(14)$	-0.1_4	(0) [2]
499.540	$5.7058_4(13)$	0.1_7	(0)
699.347	$5.7185_8(14)$	0.6_4	(0)
899.149	$5.7553_3(12)$	0.3_3	2.2_6
1098.592	$5.8327_5(14)$	-0.2_1	4.3_3
	$M_{I_2} = \pm 1$		
299.710	$5.7048_7(14)$	0.0_8	
499.540	$5.7058_4(13)$	0.2_6	

Table 5.2 continued

Transition C field voltage /volts	Transition frequency /MHz	Obs - calc /kHz	Δ /kHz
699.347	$5.7185_8(14)$	-0.7_4	
899.149	$5.7575_9(12)$	-0.0_3	
1098.592	$5.8370_8(14)$	0.0_5	
$NeD^{37}Cl$			
$J = 1,\ F_1 = 1/2 \rightarrow 3/2,\ M_F = 1/2 \rightarrow 1/2,\ M_{I_2} = 0$			
299.716	$4.8185_0(10)$	-0.1_6	5.6_6
499.550	$5.0160_0(9)$	0.1_7	7.8_3
699.360	$5.4276_5(9)$	0.1_3	10.3_1
899.152	$6.1463_8(12)$	0.1_7	13.2_9
1098.607	$7.1966_0(10)$	-0.2_7	15.5_0
$M_{I_2} = \pm 1$			
299.716	$4.8241_6(15)$	-0.1_6	
499.550	$5.0238_3(12)$	0.1_7	
699.360	$5.4379_6(10)$	-0.3_6	
899.152	$6.1596_7(10)$	0.0_3	
1098.607	$7.2121_0(10)$	0.2_1	

[1]HWHM of transition
[2]No splittings discernable for these transitions. For voltages of 299 and 499 V the predicted splitting is < 1 kHz, but about 1.4 kHz on the 699 V line.

5.3 Interpretation of results

(a) Spectral analysis

The microwave and radiofrequency spectra obtained were again characteristic of a linear triatomic molecule or symmetric top in the

K = 0 state. It is assumed that the complex possesses a linear acute geometry like KrHCl. The spectra were least-squares fitted to the Hamiltonian given in chapter 4 for KrDCl, and the results are presented in table 5.3.

Table 5.3 Spectroscopic constants for NeDCl

	$NeD^{35}Cl$	$NeD^{37}Cl$
$\bar{B}_o$/MHz	2698.1373(12) [1]	2648.9471(9)
D_J/kHz	183.07(10)	176.77(19)
$(eQq)_a^{Cl}$/MHz	-13.28692(94)	-10.522(2) [3]
DQ/kHz	-4.93(22)	-3.8 [2]
$(eQq)_a^D$/kHz	36.6(1.3)	37.6(1.2)
μ_a/Debye	0.47507(26)	—
Dμ/Debye	-0.00253(12)	—
c_b/kHz [2]	0.085	0.08
d_a/kHz [2]	0.168	0.14
$(eQq)_a^{J=1}$/MHz	-13.2968(5)	-10.5296(5)
$\mu_a^{J=1}$/Debye	0.47002(3)	0.47213(3)

[1]Errors in brackets quoted to 2 standard deviations.
[2]Values fixed in fitting procedures.
[3]Uncertainty estimated due to estimated value of DQ.

The signal/noise ratios on the J = 2 r.f. transitions were much poorer than for J = 1, to such an extent that although some evidence of J = 2 r.f. transitions for $NeD^{37}Cl$ was obtained, the transitions were too weak to be recorded without extensive power broadening. Consequently DQ and Dμ were undetermined for $NeD^{37}Cl$.

Deuerium hyperfine structure could be resolved in the radiofrequency

spectra of both isotopes. The $M_{I_2} = 0 \leftrightarrow M_{I_2} = \pm 1$ splitting was again found to be field dependent. The resultant values of $(eQq)_a^D$ are shown in table 5.3. In the microwave region no deuterium quadrupole hyperfine structure was obtainable. The signal/noise ratios on the transitions were so poor that it was necessary to apply a good deal of power broadening to obtain good lineshapes. This obscures the deuterium splittings. The $1_{\frac{1}{2}} \rightarrow 0_{\frac{3}{2}}$ transitions, however, have no such structure associated with them, allowing the power requirements to be cut down so that the theoretical linewidth could be reached (see table 5.1 and figure 5.1).

The spin-spin and spin-rotation constants were not determined from the spectra, but the values were found according to the procedure outlined in chapter 4 and are further discussed in the next section.

(b) Structural analysis

The corrected semi-rigid theory was then used to derive the structural constants in table 5.4. For the angular data similar effects are seen for NeDCl as were noted for KrDCl. The γ_{P_2} angles from deuterium and chlorine nuclear quadrupole coupling constants again agree well within the error limits for the major isotope. In the case of $D^{37}Cl$ no value of $(eQq)^D$ appears to have been published (though a value of 189.6(6.1) kHz is estimated from γ_{P_2} and $(eQq)_a^D$). The two isotopic forms have γ_{P_2} values that differ by more than 2 standard deviations. $NeD^{37}Cl$ is seen to have a slightly smaller angle than $NeD^{35}Cl$. This is explained in a harmonic approximation by the increased bending moment of the heavier complex, which leads to smaller amplitude bending vibration. The bending moment of inertia, I_b, is related to the amplitude of motion by the equation

$$\langle\theta^2\rangle = \frac{\hbar}{k_b^{\frac{1}{2}} I_b^{\frac{1}{2}}} \qquad (5.1)$$

where $$I_b^{-1} = \frac{1}{m_D}\left[\left(\frac{1}{r_{Ne\text{-}D}} + \frac{1}{r_{DCl}}\right)^2 + \frac{1}{m_{Ne} r_{Ne\text{-}D}^2} + \frac{1}{m_{Cl} r_{DCl}^2}\right]$$

Table 5.4 Structural constants for NeDCl

	$NeD^{35}Cl$	$NeD^{37}Cl$
μ/amu Å^2 (reduced mass)	12.97717	13.21474
I_b/amu Å^2 (bending m. of inertia)	1.37142	1.40276
$\langle P_2(\cos\gamma)\rangle$ [1]	0.19715(2)	0.1983(5)
arc cos$\sqrt{\langle\cos^2\gamma\rangle}$/deg	47.0202(6)	46.976(19)
$\langle P_2(\cos\gamma)\rangle$ [2]	0.1953(69)	0.2007(64)
arc cos$\sqrt{\langle\cos^2\gamma\rangle}$/deg [2]	47.09(26)	46.88(24)
$\langle P_1(\cos\gamma)\rangle$ [3]	0.422(5)	0.424(5) [4]
arc cos $\langle\cos\gamma\rangle$/deg	65.0(8)	64.9(8)
R/Å (pseudodiatomic)	3.7992	3.7996
R_o/Å (corrected semi-rigid)	3.7906(19)	3.7913(19)
R(Ne...Cl)/Å	3.8382(19)	3.8364(19)
α(∠NeClD)/Å	46.244(2)	46.189(20)

[1] From $(eQq)_a^{Cl}$ data.

[2] From $(eQq)_a^{D}$ data; $(eQq)^D$ for $D^{37}Cl$ set equal to $(eQq)^D$ for $D^{35}Cl$.

[3] Assuming 2 ± 1% moment.

[4] Assuming $D\mu(NeD^{37}Cl) = D\mu(NeD^{35}Cl)$.

and $$r_{Ne-D} \simeq R_o - r_{DCl}$$

The proportionate increase in I_b, however, is larger than the increase in $\langle\theta^2\rangle$, hence the smaller value of k_b for the heavier isotope in table 5.5. The harmonic approximation is unlikely to provide an accurate description of large amplitude motion. The differences then are probably not quantitatively meaningful although qualitatively predictive.

Table 5.5 Force constant and distortion analysis for NeDCl

	$NeD^{35}Cl$	$NeD^{37}Cl$
ω_s/cm^{-1} [1]	21.85	21.63
k_s/mdyne Å^{-1}	0.0036_5	0.0036_4
k_b/mdyne Å	0.0076	0.0074_5
$D_{P_2} \times 10^6$	73.2(3.2)	—

[1] From $D_J = 4\bar{B}_o^3/\omega_s^2$

[2] Defined as $DQ/(eQq)^{DCl}$

The dipole moment of each complex may again be represented as comprising an oriented molecular dipole plus induced moments. The polarisability of neon however, is much less than that of krypton (0.395 Å^3 and 2.479 Å^3, respectively[15]), and this lowers the induced moment contribution to about 2 - 3% of the dipole moment. A smaller amount of charge transfer might also be expected in view of the 50% increase of ionization potential for the inert gas atom. These two facts suggest that the derived value of $\langle P_1(\cos\gamma)\rangle$ is more reliable than for other atom-diatom complexes. An isotopic dependence of the dipole moment is also observed ($\sim$0.4% increase) for the complexes, the heavier complex again exhibiting the smaller amplitude motion.

The most striking feature of the data presented in table 5.4 is the differences between the γ_{P_1} and γ_{P_2} angles for both isotopes. This is caused by the much smaller anisotropic bending potential in this complex than for the heavier inert gas HCl (DCl) complexes. The motion of the DCl subunit is now that of a slightly hindered rotor. In the limit of free rotation the average values of $(eQq)_a$ and μ_a will be zero, implying that $\langle P_1(\cos\gamma)\rangle$ and $\langle P_2(\cos\gamma)\rangle$ equal zero, *i.e.* $\gamma_{P_1} = 90°$ and $\gamma_{P_2} = 54.7°$, the semitetrahedral angle (since then $\cos^2\gamma = 1/3$). The

angle differences indicate therefore that the amplitude of motion is far greater for NeDCl than for heavier complexes. It is only for strongly hindered rotors that γ_{P_1} and γ_{P_2} acquire approximately the same value (for example, in $^{132}XeH^{35}Cl$ $\gamma_{P_2} = 34.765(12)°$ and $\gamma_{P_1} = 33.8°$ [16]). It is shown in chapter 7 that the motion of the DCl is so large that the complex spends a significant amount of time in the obtuse configuration.

Several values of R may also be obtained from the spectral data in a similar manner to KrHCl. These are presented in table 5.4. The value of R_o is determined from the corrected semi-rigid theory[17]:

$$\bar{B}_o = B_{diatomic} - B^2_{diatomic}\,[\,1 + \langle\cos^2\theta\rangle]\frac{f(\langle\cos^2\theta\rangle)}{2b_o} \qquad (5.2)$$

and $$B_{diatomic} = \frac{\hbar^2}{2\mu R_o{}^2}$$

Since no spin-rotation constants could be determined, it was assumed that $f(\langle\cos^2\theta\rangle)$ could be estimated by extrapolation of a curve using ArHCl, KrHCl and ArHBr data (see next section). The potential surfaces derived from fitting the molecular beam data also each provide an f versus $P_2(\cos\theta)$ curve. A value of $0.4_5(1)$ for NeDCl was predicted and this uncertainty provides the estimated errors for intermolecular distances in table 5.4 (see figure 5.3 for the curve and the text for an explanation).

Considering the effects of isotopic substitution, Klemperer's theory[18] indicates the decrease in R(Ne...Cl) that is indeed seen, but the difference is inside the error limits and probably not meaningful. The sign of DQ again indicates that the shape of the potential is such that as θ decreases R should increase, and so the data gives no indication of whether the complex has an acute of obtuse structure. The spectra and structure of NeHCl are required for such a test.

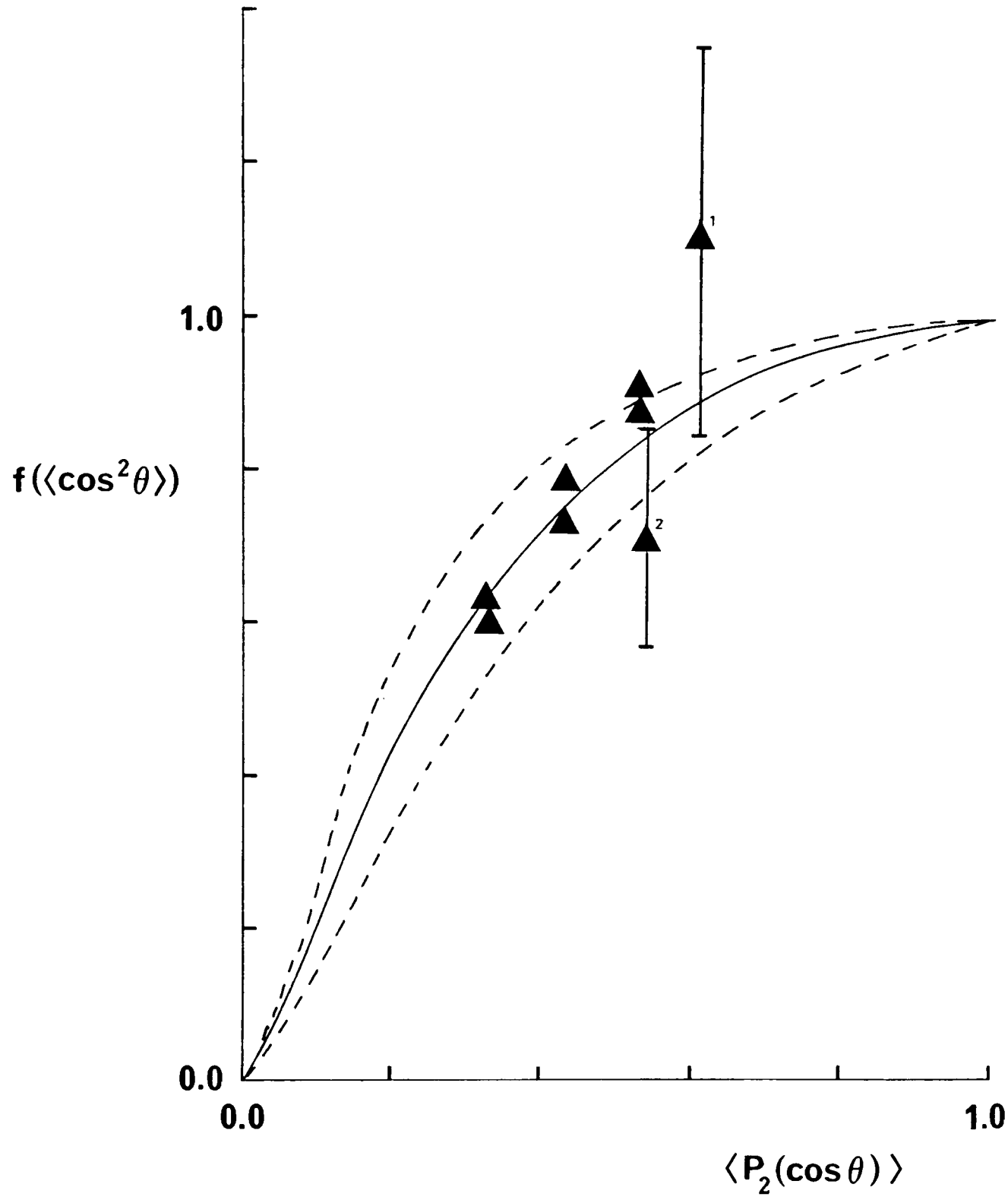

Figure 5.3 Diagram showing the variation of the correction function f, with <$P_2(\cos\theta)$>. The triangles show experimental values with error limits (2σ). The dotted lines show the approximate limits for curves calculated from fitted potentials (chapter 7). 1 represents KrDCl, and 2 represents ArDCl.

(c) NeHCl

We can estimate whether it is possible to refocus NeHCl in the molecular beam spectrometer. Considering the near free rotor limit the effect of a coupling potential and an electric field on the HCl can be written in a Hamiltonian as follows (see chapter 7):

$$H = B_0(J - j)^2 + b_0 j^2 + V_1\cos\theta + \mu^{HCl}.E \qquad (5.3)$$

where J - j represents the end-over-end rotation of the complex and $V_1\cos\theta$ is the term coupling the HCl to the *a* inertial axis. This V_1 term yields a net dipole along the *a* axis by mixing in excited j states of the HCl. The wavefunction for mixing in of the j = 1 state using perturbation theory becomes:

$$|0'\rangle = |0\rangle + \frac{V_1}{2b_o} \langle 0|\cos\theta|1\rangle . |1\rangle \qquad (5.4)$$

where $|x\rangle$ labels the j quantum state of HCl. This leads to a second-order Stark effect on turning on an electric field because of the resultant dipole moment, μ_a of

$$\mu_a = \langle 0'|\mu_{HCl}\cos\theta|0'\rangle = \left(\frac{V_1}{3b_o}\right)\mu_{HCl}$$

hence
$$W^{(2)} = \frac{\mu_a^2 E^2}{10B_o} = \left(\frac{\mu_{HCl}V_1}{3b_o}\right)^2 \frac{E^2}{10B_o} \qquad (5.5)$$

ignoring quadrupole hyperfine effects. Also in the free rotor limit there is a negative Stark effect caused by the freely rotating HCl in the j = 0 state which takes the form $-\mu_{HCl}^2 E^2/6b_o$. This effect is decreased on coupling and correlates with a perpendicular moment effect in a coupled representation, as has been discussed elsewhere[19]. In view of the near free rotation of the complex the second-order Stark effect consists mainly of two terms

$$W^{(2)} = -\frac{\mu_{HCl}^2 E^2}{6b_o} + \left(\frac{\mu_{HCl}V_1}{3b_o}\right)^2 \frac{E^2}{10B_o}$$

$$= \frac{\mu_{HCl}^2 E^2}{b_o}\left[-\frac{1}{6} + \frac{V_1^2}{90B_o b_o}\right] \qquad (5.6)$$

V_1 can be estimated by applying equation 5.5 to $NeD^{35}Cl$, and the rotational constant of $NeH^{35}Cl$ will be about 2.7_3 GHz. This gives a value for V_1 of 210 GHz. The second term in brackets is then equal to 3.4/6 and dominates the other effect. For DCl where the rotational constant is only about half the size of that for HCl the term is 6.7/6. Thus

both molecules will be polar, but the dipole moment μ_a of NeHCl will be $\sim b_o^{DCl}/b_o^{HCl}$ of that of NeDCl *i.e.* $\sim 0.24_5$ Debyes. Terms of the V_2 type are also non-negligible[20]. They will tend to decrease the value of μ_a, *cf.* figure 6 of reference[21]. Fitting a potential surface to the NeDCl data (see chapter 7), provided an estimate of μ_a as 0.20_0 Debyes, suggesting a fall-off of $\sim$ 0.4 D, due to the V_2 term. The contribution to the Stark effect from $\mu_\perp$ means that μ_a for NeDCl is actually 7% larger than measured. This value is about 0.035 Debyes, and will cancel with the value of the induced and charge transfer moment approximately. $\langle P_1(\cos\gamma)\rangle$ may still then provide good quality information for a potential surface fitting. For NeHCl the same arguments apply approximately and the estimate above is probably accurate to within ±0.05 Debyes.

The focussing voltages required for the J = 1 state of NeHCl are thus estimated to be A,B ≃ 27,15 kV, and in view of the assumptions, any underestimation of this could put refocussing out of range of our spectrometer, as appears to be the case. A longer set of A field focussing rods will be built in the future to focus NeHCl.

5.4 Comparison of inert gas-HCl (DCl) series

These results for NeDCl and the KrHCl system complete the study of inert gas...HCl (DCl) interactions. Several interesting trends occur on going down the series (Ne → Xe) and these will be discussed below. The data for comparison are given in tables 5.6 and 5.7 for the hydrogen and deuterium complexes respectively. Data for ArHCl is taken from the spectroscopic constants in reference[22], and for XeHCl from reference[23]. The R(X...Cl) distances are calculated from R_o values from the corrected semi-rigid theory and trigonometry. These distances require an estimation of $f(\langle\cos^2\theta\rangle)$ in the case of Xe and Ne complexes and the curve for this is shown in figure 5.3 together with experimental points for ArHCl[22], KrHCl, and ArHBr[24]. The dotted lines give representative limits of curves calculated from fitted potential surfaces (chapter 7).

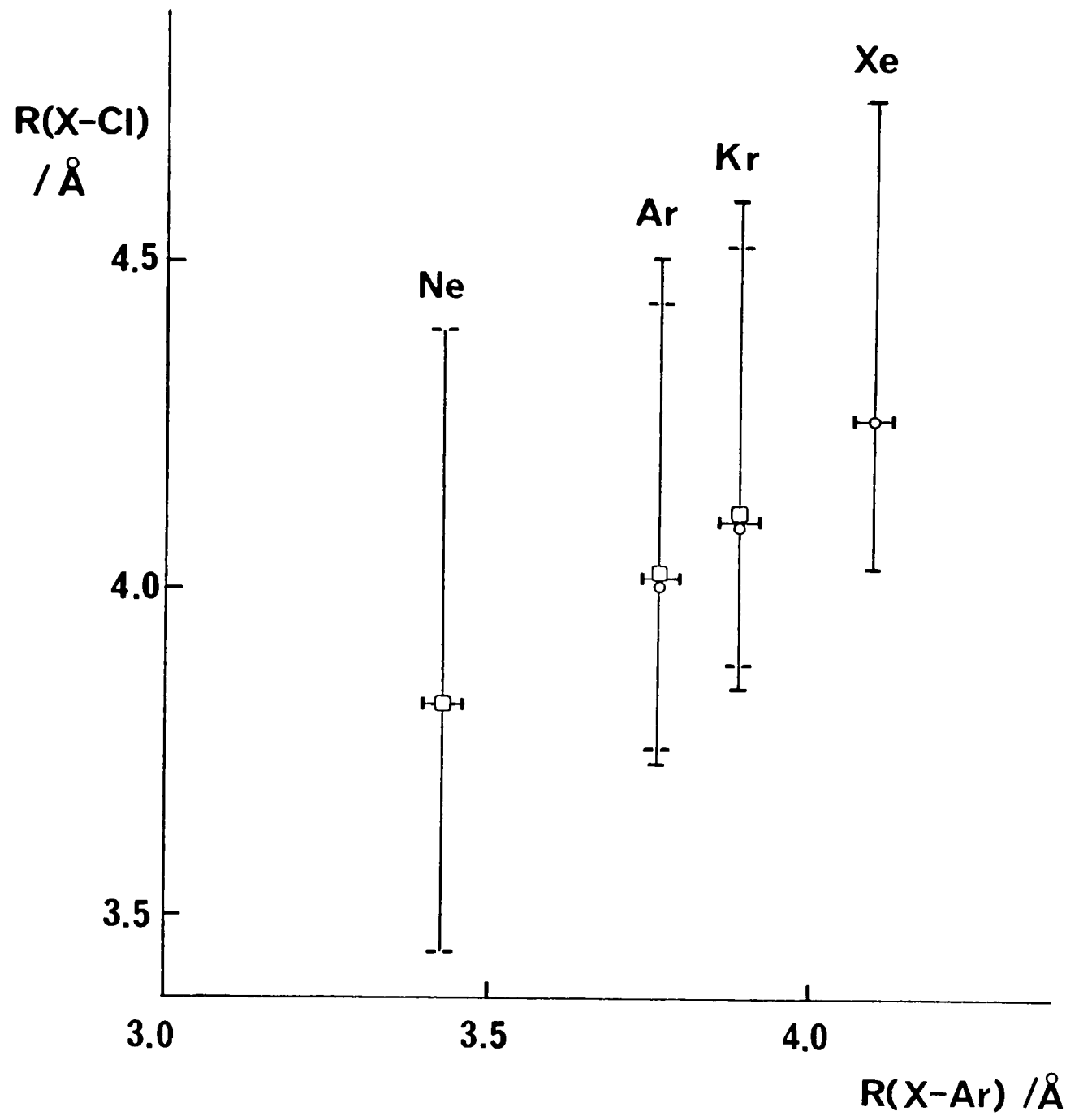

Figure 5.4 Diagram showing the correlation of the intermolecular separation in the van der Waals species XHCl (O) and XDCl (□) where X is an inert gas atom, with the interatomic distance in XAr. Zero-point bending amplitudes of XHCl (XDCl) are indicated from fitted potentials in chapter 7.

As might be expected the values of R increase on going down the series, following the increase in size of the inert gas atom. They are plotted in figure 5.4 against the equilibrium distances of the series of inert gas dimers XAr where X = Ne, Ar, Kr, Xe.[25]. The error bars for the XHCl complexes give the classical amplitudes of motion from the fitted

Table 5.6 Comparison of inert gas - HCl series

Complex [1]	R(X...Cl) /Å	∠XClH /deg	γ_{P_2} /deg	γ_{P_1} /deg	% induced μ_a/D	ω_s /cm^{-1}	k_s /mdyne Å^{-1}	k_b /mdyne Å	U' [3] /cm^{-1}	$\frac{C_X}{C_{Ar}}$ [2]
ArHCl	4.0088	41.342	41.5316	47.6	8	32.4	0.0117	0.0009	96	1.00
KrHCl	4.1117	37.695	37.9627	39.8	11	32.4$_5$	0.0156	0.0013	118	0.90
XeHCl	4.2757	34.574	34.765	33.8	15	33.6	0.0188	0.0017	141	0.82

[1] References are given in the text.

[2] $C_X = \alpha_X \theta_X^4 / R_o^6$.

[3] U' for Ne is 36 cm^{-1}.

Table 5.7 Comparison of various molecular parameters for X...DCl complexes

Complex [1]	R(X...Cl) /Å	∠XClD /deg	γ_{P_2} /deg	γ_{P_1} /deg	ω_s /cm^{-1}	k_{bend} /mdyne Å	$\frac{k'_{r\theta}}{k'^{Ne}_{r\theta}}$ [3]	Dμ × 10^4 /Debyes
^{20}NeD^{35}Cl	3.838	46.24	47.0202(6)	65.0	21.9	0.0003_6	1.0	-25.3(1.2)
^{40}ArD^{35}Cl	4.030	33.75	33.7502(5)	32.5	33.0	0.0010	4.8	1.13(18) [4]
								{-0.21(5)} [5]
^{84}KrD^{35}Cl	4.130	30.54	30.8543(6)	28.1	33.7	0.0015	6.3	0.43(13)
								{0.29(3)}
^{132}XeD^{35}Cl [2]	4.283	27.6	28.2	25	35	0.002	—	

[1] References given in the text.
[2] Values estimated from fitting to XeHCl data.
[3] Where $k'_{r\theta} = k_{r\theta}/(k_s k_b)^{\frac{1}{2}}$
[4] Ref[22].
[5] The values for the hydrogen isotopes are given in brackets.

potentials; similar magnitudes will be expected for the inert gas dimers for which the minima uncertainties are illustrated. It can be seen from figure 5.4 that the X...Cl distance increases more slowly than the X...Ar distance suggesting that the overlap of orbitals increases on going from the neon complex to the xenon complex, and this in turn implies that the validity of an undistorted HCl subunit in the complex will therefore decrease down the series. This change is due to an increase in the attractive forces which reduce the X...Cl distance despite the fact that the hydrogen is forced into a more acute orientation on going down the series. The attractive part of the binding energy of the complex can be estimated by considering the dipole-induced dipole and dispersion contributions. If the potential energy is written in the form:

$$V = Ae^{-b(R-R_e)} - \frac{C}{R^6} \qquad (5.7)$$

Then $$\left\{\frac{dV}{dR}\right\}_{R_e} = 0 = -Ab + \frac{6C}{R^7}$$

so $$V_e = U'\left[\frac{6}{bR_e} - 1\right] \qquad (5.8)$$

where $U' = C.R_e^{-6}$; changes in the attractive part of the potential will then reflect changes on going down the series. This attractive part has been given by Buckingham[26] for the X..HCl complexes as

$$\frac{C}{R^6} = \frac{\alpha_X \mu_{HCl}^2}{8\pi\varepsilon_o R^6}.(3\cos^2\theta + 1) + \frac{3I_X I_{HCl}\alpha_X}{2(I_X + I_{HCl})R^6} \times \left[\alpha_{HCl} + \frac{1}{3}(\alpha_{\parallel} - \alpha_{\perp})(\frac{3}{2}\cos^2\theta - \frac{1}{2})\right] \qquad (5.9)$$

where I_X, I_{HCl} are the ionization potentials[27]. The first contribution (dipole-induced dipole) is only ~ 5 cm^{-1} for KrHCl, and the major contribution is the dispersion interaction. The multipole expansion may not be fully convergent at the equilibrium distance but the trends are likely to be qualitatively significant. The binding energy falls

dramatically on going from Ar to Ne and a similar fall-off is also seen in the decrease in the stretching force constants.

The amplitude of bending motion decreases from Ne to Xe (γ_{P_1} and γ_{P_2} data) and can be explained in terms of the increased polarisability of the inert gas atom. On a multipole model the angle dependence of the polarisability term (5.9), the polarisability anisotropy and smaller terms contribute to the bending potential. The ratios of the polarisability contributions are shown in table 5.6, with θ^4 as a measure of the anisotropy. The ratios are seen to be reasonably constant.

An estimation of the magnitude and the variation in the magnitude of R/θ coupling can be obtained from an analysis of the DQ quantity. The interaction potential is first written as an expansion around the minimum

$$V(R,\theta) - V_{min}(R_e,\theta_e) = \tfrac{1}{2}k_b\theta^2 + \tfrac{1}{2}k_{r\theta}(R-R_e)\theta^2 + \tfrac{1}{2}k_s(R-R_e)^2 \qquad (5.10)$$

then $$k_b^{eff} = \left(\frac{\partial^2 V}{\partial\theta^2}\right) = k_b + k_{r\theta}(R-R_e) \qquad (5.11)$$

and $$k_{r\theta} = \left(\frac{\partial^3 V}{\partial R\partial\theta^2}\right)$$

Any change in the measured value of $(eQq)_a$ can be related to a change in θ by the equation

$$d\langle P_2\rangle = -3\langle\cos\theta\sin\theta d\theta\rangle \qquad (5.12)$$

and its distance variation will be

$$\frac{d\langle P_2\rangle}{dR} = -3\left\langle\cos\theta\sin\theta\,\frac{d\theta}{dR}\right\rangle$$

$$= -3\left\langle\cos\theta\sin\theta\,\frac{d\theta}{dk_b}\right\rangle\cdot\frac{dk_b}{dR} \qquad (5.13)$$

Now $\langle\theta\rangle$ can be related to k_b through equation 5.1, and therefore for a small change of $\langle\theta\rangle$

$$d\langle\theta\rangle \simeq -\frac{1}{4} I_b\hbar^{-2}\langle\theta\rangle^5 dk_b$$

and $$\frac{dk_b^{eff}}{dR} = k_{r\theta}$$ from equation 5.11

Therefore

$$dP_2 \simeq \frac{3}{4\hbar^2} I_b k_{r\theta} \langle \theta^5 \cos\theta \sin\theta \rangle dR \qquad (5.14)$$

Now dR can be related to the centrifugal distortion constant by the equation

$$dR \simeq \frac{R_o D_J}{B_o} J(J+1) \qquad (5.15)$$

since $$dB = d\left(\frac{\hbar^2}{2\mu} R_o^{-2}\right) = -2D_J J(J+1)$$

and so $$D_{P_2} \cong dP_2' \simeq \frac{3 I_b R_o D_J k_{r\theta}}{4\hbar^2 B_o} \langle \theta^5 \cos\theta \sin\theta \rangle \qquad (5.16)$$

which is the form of the equation referred to in section 6.1 of reference 1 given in chapter 4. If $k_{r\theta}$ is estimated by the angle change and X...Cl distance change in going from KrHCl to KrDCl *i.e.* $k_{r\theta} \simeq \Delta k_b / \Delta R$ and $\theta \simeq \gamma_{P_2}$, then a value of 14.7 ppm is calculated for the KrHCl system. Compared with the experimental values of around 11 ppm, the agreement is very good. Similarly for ArHCl, the calculated value for the system is 27.3 ppm, compared with the experimental values of 23.7 and 19.0 ppm [22] for the H and D isotope forms. This suggests that the value of DQ will be useful in fitting the amount of R/θ coupling when modelling potential energy surfaces; other effects such as Coriolis contributions also make small contributions.

The trend of R/θ coupling is shown in table 5.7 which shows a relative increase in coupling. However the absolute values of the ratios are probably not meaningful in view of the assumptions made for the harmonic approximation, especially for neon complexes.

The centrifugal distortion of the dipole moment is represented by Dμ. Strictly speaking, the centrifugal distortion of the Stark effect is measured and takes the form μ.Dμ, and so on going up the series from Xe to Ne the decrease in μ (as the bending force constant decreases) requires a concomitant increase in Dμ. However, the products μ.Dμ for the deuterium complexes have the values -120.2, +11.0, +3.89 ($\times 10^{-5}$

Debye^2) for NeDCl, ArDCl and KrDCl respectively. For ArHCl and KrHCl they are -1.70 and +2.82 ($\times 10^{-5}$ Debye^2). In the case of ArHBr, the values of $D\mu$ were less well determined and the values for the ^{81}Br isotope are -25(11)[H], and -16(9)[D] ($\times 10^{-5}$ Debye^2)[21].

Thus as the value of γ_{P_2} increases a negative contribution is seen to swamp the other contributors to $D\mu$. The various contributors to $D\mu$ have been listed in chapter 4. In any analysis of these values it should be appreciated that the terms are difficult to separate. Briefly again, they are: (a) the centrifugal change in DCl (HCl) projection along the *a* inertial axis resulting in a change in $\langle\cos\gamma\rangle$ as the van der Waals bond stretches; (b) the polarisability anisotropy contribution, $(\alpha_{||} - \alpha_{\perp})_{XDCl}$ which is $\simeq (\alpha_{||} - \alpha_{\perp})_{DCl} \langle P_2(\cos\gamma)\rangle$; (c) the second-order mixing in of excited bending vibrational states via the perpendicular dipole moment. The first two terms give rise to values of $\mu D\mu$ of the order of 10^{-5} (Debye)^2 and would not be expected to change dramatically down the DCl series, and they are both positive. The large change is then almost certainly due to a large increase in the contribution of (c). The value of $\mu D\mu$ has been shown in chapter 4 to be

$$\mu D\mu \simeq - \mu_{\perp}^2 \frac{\bar{B}_o}{3\Delta\nu_{eff}} \qquad (5.17)$$

where $\mu_{\perp}^2 \simeq \sum_b |\langle 0, K=0|\mu_{DCl}\sin\theta e^{\pm i\phi}|b, K=\pm 1\rangle|^2 \simeq \mu_{DCl}^2\langle\sin^2\theta\rangle$, the perpendicular dipole moment. For a freely rotating diatom, $\Delta\nu_{eff} \simeq 2b_o^{DCl}$, and it is expected to be only slightly larger here ($\Delta\nu \simeq 10 - 20$ cm^{-1}). This gives rise to a contribution to $\mu D\mu$ of -130×10^{-5} (Debye)^2 for NeDCl (for $\Delta\nu_{eff}$ = 15 cm^{-1}). In ArDCl and KrDCl, $\Delta\nu_{eff}$ is likely to be a factor of two or more larger, the bending frequencies being 45.3 and 52.9 cm^{-1} respectively from the harmonic analysis. These give values of -15 and -8 ($\times 10^{-5}$ Debye^2) respectively. This suggests that the terms (a) and (b) contribute about + 10 to 20 ($\times 10^{-5}$ Debye^2) to the value of $\mu D\mu$. Using this value suggests that the value of $D\mu$ is readily

accounted for in NeDCl. The value of ν_b for Ne from the harmonic analysis suggests a value for $\mu D\mu$ of -63×10^{-5} Debye^2, which highlights the errors linked with using a harmonic approximation for a van der Waals molecule with very wide amplitude bending and vibrational motions. This same underestimation is also reflected in the values for ArHBr and ArDBr from equation 5.17 of -12 and -11 ($\times 10^{-5}$ Debye^2) respectively. Clearly however, the negative values of $D\mu$ are accounted for very satisfactorily by this increase in size of the perpendicular moment contribution.

In conclusion, qualitative and semi-quantitative methods have been shown to reproduce experimentally determined trends in structure and dynamics of the series of inert gas - HCl (DCl) complexes. The amplitude of motion in these complexes is obviously very large from a simple force constant analysis culminating in near free rotation of DCl (HCl) in the neon complexes. To put these semi-quantitative features on a more firm basis requires the fitting of potential energy surfaces to the data.

References to chapter 5

1. A.E. Barton, D.J.B. Howlett and B.J. Howard, Mol. Phys., to be published.

2. B.L. Blaney and G.E. Ewing, Ann. Rev. Phys. Chem., *27*, 553, (1976).

3. A.R.W. McKellar and H.L. Welsh, Can. J. Phys., *50*, 1458, (1972).

4. H.L. Welsh, in MTP International Review of Science, Physical Chemistry Series 1, Volume 3, ed. A.D. Buckingham, (Butterworths, London, 1972), chapter 2, and references therein.

5. J.E. Kenny, K.E. Johnson, W. Sharfin and D.H. Levy, J. Chem. Phys., *72*, 1109, (1980).

6. J.A. Blazy, B.M. DeKoven, T.D. Russell and D.H. Levy, J. Chem. Phys., *72*, 2439, (1980).

7. L.E. Brus and V.E. Bondybey, J. Chem. Phys., *63*, 786, (1975).

8. L.E. Brus and V.E. Bondybey, J. Chem. Phys., *63*, 794, (1975); J. Goodman and L.E. Brus, J. Chem. Phys., *67*, 4858, (1977).

9. W.G. von Holle and D.W. Robinson, J. Chem. Phys., *53*, 3768, (1970).

10. A. Ben-Reuven, S. Kimel, M.A. Hirschfeld and J.H. Jaffe, J. Chem. Phys., *35*, 955, (1961).

11. M. Losonczy, J.W. Moskowitz and F.H. Stillinger, J. Chem. Phys., *59*, 3264, (1973); M. van Hemert and A. van der Avoird, J. Chem. Phys., *71*, 531, (1979).

12. M. Losonczy, J.W. Moskowitz and F.H. Stillinger, J. Chem. Phys., *61*, 2438, (1974).

13. S.E. Novick, P.B. Davies, T.R. Dyke and W. Klemperer, J. Am. Chem. Soc., *95*, 8547, (1973).

14. E.B. Wilson, J.C. Decius and P. Cross, Molecular Vibrations, (McGraw-Hill, N.Y., 1955).

15. N.J. Bridge and A.D. Buckingham, Proc. Roy. Soc. A, *295*, 334, (1966).

16. K.V. Chance, K.H. Bowen, J.S. Winn and W. Klemperer, J. Chem. Phys., *70*, 5157, (1979).

17. In equation 5.2 it makes negligible difference if $\bar{B}_o^2$ or $B^2_{diatomic}$ is used in the equation.

18. See chapter 4, reference[2].

19. T.R. Dyke, B.J. Howard and W. Klemperer, J. Chem. Phys., *56*, 2442, (1972); J. Chem. Phys., (1980), submitted for publication.

20. S.L. Holmgren, M. Waldman and W. Klemperer, J. Chem. Phys., *69*, 1661, (1978).

21. K.C. Jackson, P.R.R. Langridge-Smith and B.J. Howard, Mol. Phys., *39*, 817, (1980).

22. S.E. Novick, P. Davies, S.J. Harris and W. Klemperer, J. Chem. Phys., *59*, 2273, (1973); S.E. Novick, K.C. Janda, S.L. Holmgren, M. Waldman and W. Klemperer, J. Chem. Phys., *65*, 1114, (1976); J.M. Hutson and B.J. Howard, J. Chem. Phys., submitted for publication.

23. K.V. Chance, K.H. Bowen, J.S. Winn and W. Klemperer, J. Chem. Phys., *70*, 5157, (1979).

24. M.R. Keenan, E.J. Campbell, T.J. Balle, L.W. Buxton, T.K. Minton, P.D. Soper and W.H. Flygare, J. Chem. Phys., *72*, 3070, (1980).

25. M. Waldman and R.G. Gordon, J. Chem. Phys., *71*, 1325, (1979), and references therein.

26. A.D. Buckingham, Adv. Chem. Phys., *12*, 107, (1967), equation (59).

27. J.A. Pryde, The Liquid State, (Hutchinson, London, 1966), chapter 4.

CHAPTER 6: THE RARE GAS...HX SERIES

This short chapter is concerned with a refocussing study on the ArHI complex, with a re-analysis of the spectra of ArHF, together with suggestions for future work. A comparison with the derived structural data for two series is made, viz., ArHX and KrHX, where X = F, Cl, Br, I, and the trends in the series are explained. As in the case of the X...Cl comparison, a determination of potential energy surfaces from experimental data is required to give the amplitudes of motion in these complexes, but a simple harmonic analysis does illustrate the trends.

The spectroscopic data from which the structural data are derived, by the corrected semi-rigid theory, are from the following references: ArHF[1], ArHCl[2], ArHBr[3], KrHF[4], KrHCl[5], KrHBr[6], XeHF[7], and XeHCl[8]. All are MBER studies with the exception of XeHF; this was studied by a crossed beam experiment, a reliable spherically symmetric potential being derived from the angular scattering data by standard semiclassical techniques. An MMSV (Morse-Morse-spline-van der Waals) potential form was used to fit the data. A well depth of 129(6) cm^{-1} at a distance (r_m) of 3.77(11) Å is observed.

6.1 Comparison of Ar, Kr...HX series

The data for this comparison is shown in tables 6.1 and 6.2 for the argon and krypton complexes, respectively.

From the angular data the expected increase in bending anisotropy is seen on going from the argon to the krypton series but the values of γ_{P_1} and γ_{P_2} are seen to be fairly constant across the HX series, with only a slight increase in angle. In a harmonic analysis the value of γ_{P_2} depends inversely on the product of bending moment of inertia and bending force constant. The value of I_b^{-1} decreases from HF to HI in the same way as the rotational constant of the diatom (HF 20.56 cm^{-1} [9] to HI 6.43 cm^{-1} [10]). Thus, in order to maintain a constant value of γ,

Table 6.1 Comparison of Ar...HX structural and harmonic force constants

	$ArH^{19}F$	$ArH^{35}Cl$	$ArH^{79}Br$	ArHI
R(Ar...X)/Å	3.5468	4.0088	4.1483	(4.35) [1]
R_o/Å	3.5118(7)	3.9818	4.1331	
γ_{P_2}/deg	41.3(5) [1]	41.53	42.11	
γ_{P_1}/deg	48.4	47.6	50.4	51.2(5.5) [1]
k_s/mdyne Å^{-1}	0.0140	0.0117	0.0076	
ω_s/cm^{-1}	42.2	32.4	22.0	
k_b/mdyne Å	0.00156	0.00091	0.00075	
ω_b/cm^{-1}	76.1	45.3	38.1	
$\left(\frac{k'_{ArHX}}{k'_{ArHCl}}\right)^2$ [2]	—	1.00	1.61	
U'/cm^{-1} [5]	55	96	103	108
Δr_i/Å [3]	-0.49	-0.39	-0.39	(-0.38)
Δr/Å [4]	0.29	0.30	0.29	(0.29)

[1] From value of rotational constant estimated in text.
[2] $k' = k_{r\theta}(k_b k_s)^{-\frac{1}{2}}$
[3] Overlap radius, see table 6.2 for details; the values for NeHCl (est.) and XeHCl are -0.28 and -0.41 respectively.
[4] See table 6.2 for details.
[5] U' is the dispersion term of Buckingham[13].

the bending force constant or anisotropy of the interaction must decrease down the series (F to I). This trend follows both the expected decrease in the dipole-induced dipole interaction, the dipole moments of the hydrogen halides decreasing from 1.826178(3) D in HF[11] to 0.4477(5) D in HI[12], and the major term, the anisotropic dispersion term. This takes

Table 6.2 Comparison of Kr...HX structural and harmonic force constants

	$^{84}KrH^{19}F$	$^{84}KrH^{35}Cl$	$^{84}KrH^{79}Br$
R(Kr...X)/Å	3.6486	4.1117	4.2583
R_o/Å [2]	3.6118(6)	4.0836	4.2441(5)
γ_{P_2}/deg	(37.9) [1]	37.96	38.10
γ_{P_1}/deg	—	39.8	—
k_s/mdyne Å^{-1}	0.0181	0.0156	0.0132
ω_s/cm^{-1}	43.60	32.4	23.4
k_b/mdyne Å	0.00214	0.00128	0.00109
ω_b/cm^{-1}	88.0	52.9	45.2
$\left(\frac{k'_{KrHX}}{k'_{KrHCl}}\right)$	—	1.00	1.97
Δr_i/Å [3]	-0.48	-0.37	-0.36
Δr/Å [4]	0.30	0.31	0.31

[1]Value estimated.
[2]Using corrected semi-rigid theory.
[3]Overlap distance of van der Waals radii $\Delta r_i = R - r_{HX} - r'_H - r'_{Kr}$; where where r' are the van der Waals radii of ref.15.
[4]$\Delta r = R - r'_{Kr} - r'_X$.

the form[13]

$$- \frac{3U_A U_{HX} \alpha_A}{4(U_A + U_{HX}) R_o^6} (\alpha_{\parallel} - \alpha_{\perp})^{HX} \cos^2\theta \qquad (6.1)$$

and although no consistent set of polarisability anisotropy values is available[14], the value of the rest of the formula decreases from ~ 78 to ~ 20 cm^{-1}/Å^3 from ArHF to ArHI. Even the most unfavourable set of data (MBER: HF, 0.22 Å^3; HCl, 0.29 Å^3; HBr 0.37 Å^3) still suggest a decrease in expression 6.1 of 4.9, 3.0, and 2.9 cm^{-1} respectively.

The radial information suggests that the amount of overlap of van der Waals radii is approximately constant across both series. Using the value of 1.20 Å for the van der Waals radius of hydrogen and van der Waals radii for the halogens and rare gases[15], yields the values in tables 6.1 and 6.2. (The negative values indicate that the distances are all shorter than the van der Waals radii would predict indicating some overlap of outer charge clouds.) The distances are also shown in figure 6.1 plotted against the corresponding inert gas dimer distance[16]. It can be seen that there is a smooth progression for both the argon and krypton series.

The value of k′, the scaled bend-stretch coupling constant, is seen to increase from the HCl to the HBr complex for the argon and krypton series, whereas the values for ArHCl and KrHCl are virtually identical. An increase in value of k′ suggests that the potential surface for the bromine complex shows a more pronounced fall-off in the average inert gas atom - halogen distance as the angle θ is increased than for the chlorine complex. This effect is seen in the fitted potentials (see chapter 7), but is small compared with the amplitudes of radial motion (~0.1 to 0.2 Å fall-off in <R> from θ = 0° to 60°) and may well not be significant. The overestimation in this analysis is probably due to a failure of the harmonic analysis.

The estimation of well depths (ε) and equilibrium bond lengths (R_e) has been undertaken by several workers for their respective van der Waals complexes. These include ArHF and ArHCl[1], KrHCl[5b], and ArHBr and KrHBr[3,4]. Briefly by assuming that the radial interaction, assuming an angle averaged potential, can be estimated by a Lennard-Jones (12-6) potential of the form

$$V(R) = \varepsilon \left[\left(\frac{R_e}{R} \right)^{12} - 2 \left(\frac{R_e}{R} \right)^{6} \right] \qquad (6.2)$$

it is possible to use k_s and $\bar{B}_o$ to estimate ε and R_e. Expanding

equation 6.2 about $R = R_e$ in a Taylor series yields[4]:

$$V(R) = -\varepsilon + \frac{36\varepsilon}{R_e^2}(R - R_e)^2 - \frac{252\varepsilon}{R_e^3}(R - R_e)^3 + \ldots \qquad (6.3)$$

So for this potential in the harmonic limit $\varepsilon = k_s R_e^2/72$. B_e is related to the experimental value B_o by $B_o = B_e - \frac{1}{2}\alpha$, where α is the vibration-rotation interaction constant. For a Lennard-Jones potential this then becomes[17]

$$B_o = B_e - 18\frac{B_e^2}{\omega_s} \qquad (6.4)$$

The resulting values are shown for a selection of atom - diatom complexes in table 6.3.

Table 6.3 Lennard-Jones (12-6) parameters for van der Waals complexes

		Ar	Kr
HF	ε [1]	116	
	R_e [1]	3.458	
HCl	ε	126	179
	R_e	3.940	4.064
HBr	ε	91	165
	R_e	4.081	4.219

[1]units: ε in cm^{-1}, R_e in Å.

Shin has calculated the vibrational spacings of Lennard-Jones potentials for these atom - diatom complexes, and derived thermodynamic functions for the van der Waals bond[18]. This analysis is at best only qualitatively predictive for well depths, and may well be meaningless for predicting or comparing the HX series. Several reasons can be given for this and are as follows: a. Lennard-Jones or Morse potentials do not provide a good simple representation of the interactions of even rare

gas species, let alone pseudo-diatomic species. This has been apparent from early studies on rare gas interactions using combined data, such as molecular beam and viscosity data[19]. Lennard-Jones potentials typically underestimate the well depth, and overestimate by factors of around two the magnitudes of long range attractive forces. Le Roy[20] has argued

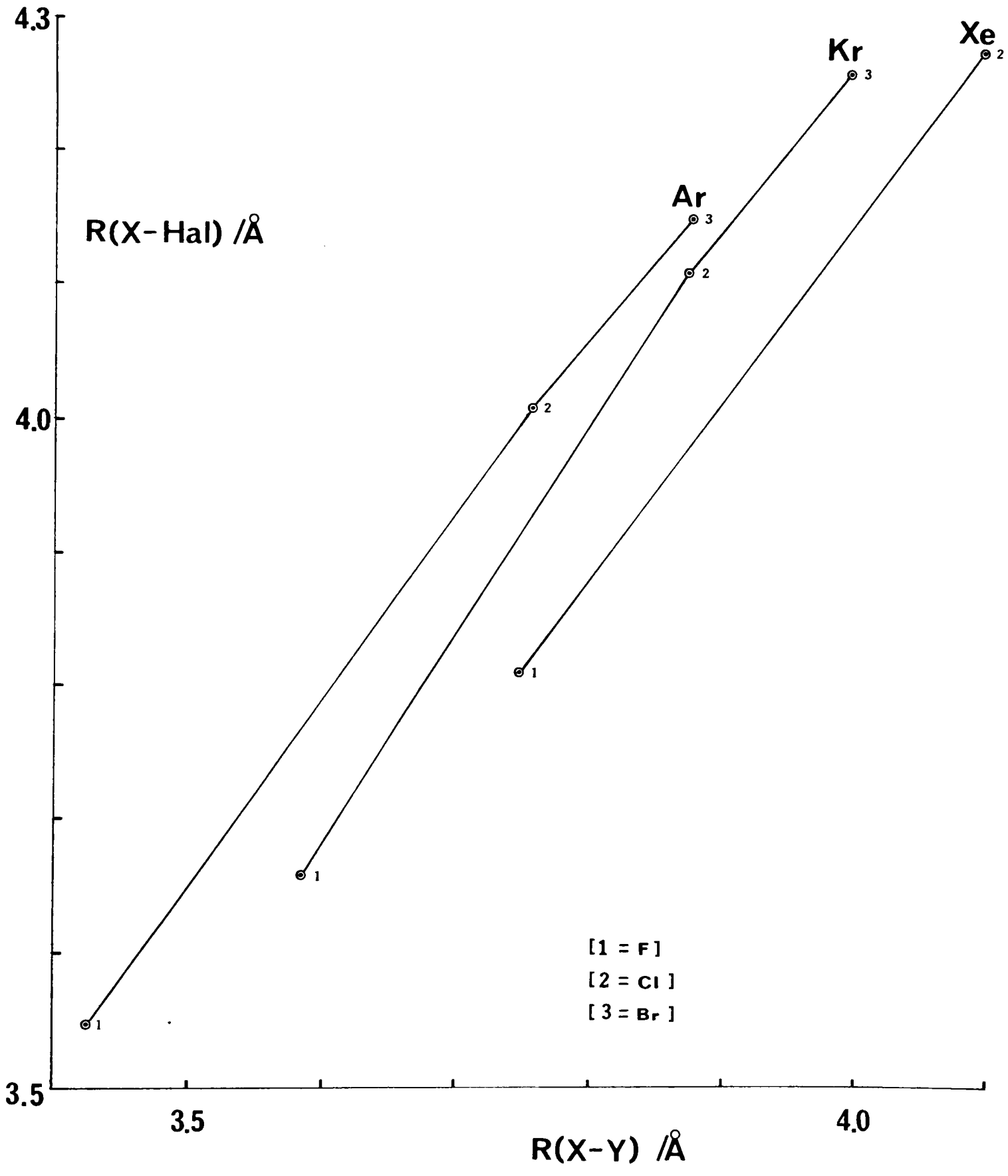

Figure 6.1 Plot of equilibrium separation of inert gas dimer (X,Y = Ne,...Xe) against the corresponding X-halogen distance.

convincingly against the use of Lennard-Jones (12-6) potentials and has discussed the inadequacy of deriving thermodynamic properties and predicting the number of vibrational levels in the well. An example of this is also by Shin[21] for Ar_2, Kr_2 and Xe_2. Using known well depths, he altered R_e to obtain reasonable agreement with vibrational spacings from UV spectra, but the values of R_e obtained were consistently ~ 8% below even slightly more flexible potentials, which were all within 1% of each other. b. An effective stretching force constant (or frequency) must be used and the finite coupling of R and θ motions makes this impossible.

The derivation of ε and R_e can be done for each isotopic form of each van der Waals complex *e.g.*table VII of reference[5b]. A large difference is always seen between R_e and ε values for the hydrogen and deuterium isotopes *e.g.* for KrDCl, $\varepsilon = 199$ cm^{-1} and $R_e = 4.081$ Å; compare the values for KrHCl in table 6.3.

When the values are compared with other complexes expected trends in ε are not found. Both Flygare[4] and Langridge-Smith[5] expected the well depths to increase from ArHCl to ArHBr presumably as shown by the trend in the dispersion terms in table 6.1, but as shown in table 6.3 a decrease was found. Both sets of workers attempted to overcome this in a similar manner. Langridge-Smith extrapolated the value of k_s to infinite bending mass using the bending reduced mass and k_s for the H and D complex. Flygare wrote $k_s = k_s^\circ + 2k\langle\theta^2\rangle$, and found k_s at 0° *i.e.* at infinite bending reduced mass. Both then found that these extrapolations yielded a deeper well for ArHBr than for ArHCl. A proper consideration of the motions of both the hydrogen and deuterium isotopes on a single potential energy surface would be preferable, the difference in the rather meaningless values of ε and R_e for the isotopes being due to the difference in zero-point energy between the two complexes. The extrapolated potentials for hypothetical linear complexes, however, do

seem to be quantitatively very similar to the potential curves characterising the $\theta = 0°$ part of the 4-angle surfaces (see chapter 7).

The number of bound states in these wells is also incorrect[18], as argued by Le Roy[20]. Shin's value of ω_s of 27.6 cm^{-1} for ArHBr is incorrect, the measured harmonic value being 22.0 cm^{-1}. Thus the numbers of vibrational levels supported for ArHBr and ArHI are incorrect.

The two following sections describe refocussing work on ArHI, and a simple re-analysis of ArHF spectra. Derived molecular constants from these two sections are given in table 6.1.

6.2 ArHI studies

(a) Experimental

Refocussing studies were carried out on the ArHI complex. The complex was formed by expanding ~ 1% of HI (Matheson Gas, 98%) with argon (B.O.C., CP grade) through a 35 μm nozzle at 195 K. These conditions were chosen to maximise both the formation of ArHI at m/e = 168 and the % refocussing. The formation of stable beams of HI was very difficult and the stainless steel inlet and nozzle system generally required about 1 week to begin to 'mature' and so produce reasonable beams of HI. ArHI was found to be more readily formed than either KrHCl or NeDCl, about 7 - 10% of the HI peak (as I^+) appearing as ArHI (see figure 6.2). The refocussing was reasonably good and the maximum could not be reached at A,B = 30,20 kV, the refocussing still showing signs of increasing beyond that point. Several attempts to obtain the spectra were made in both the r.f. and microwave regions but with no success. The author wishes to include this as a reminder of the difficulty of the experimental flop-out technique despite the amount of data in the preceding two chapters. Further studies are planned for this complex.

(b) Analysis

The refocussing characteristics of ArHI do allow an estimation of either the rotational constant or the dipole moment of the complex using

the equations of Appendix A. An estimate of the rotational constant can be made either from van der Waals radii[15], or from an extrapolation of figure 6.1, by comparing the value with that of ArXe[16]. Both methods produce an estimate of $\bar{B}_0$ of about 860 MHz (± ~ 20 MHz). In order to

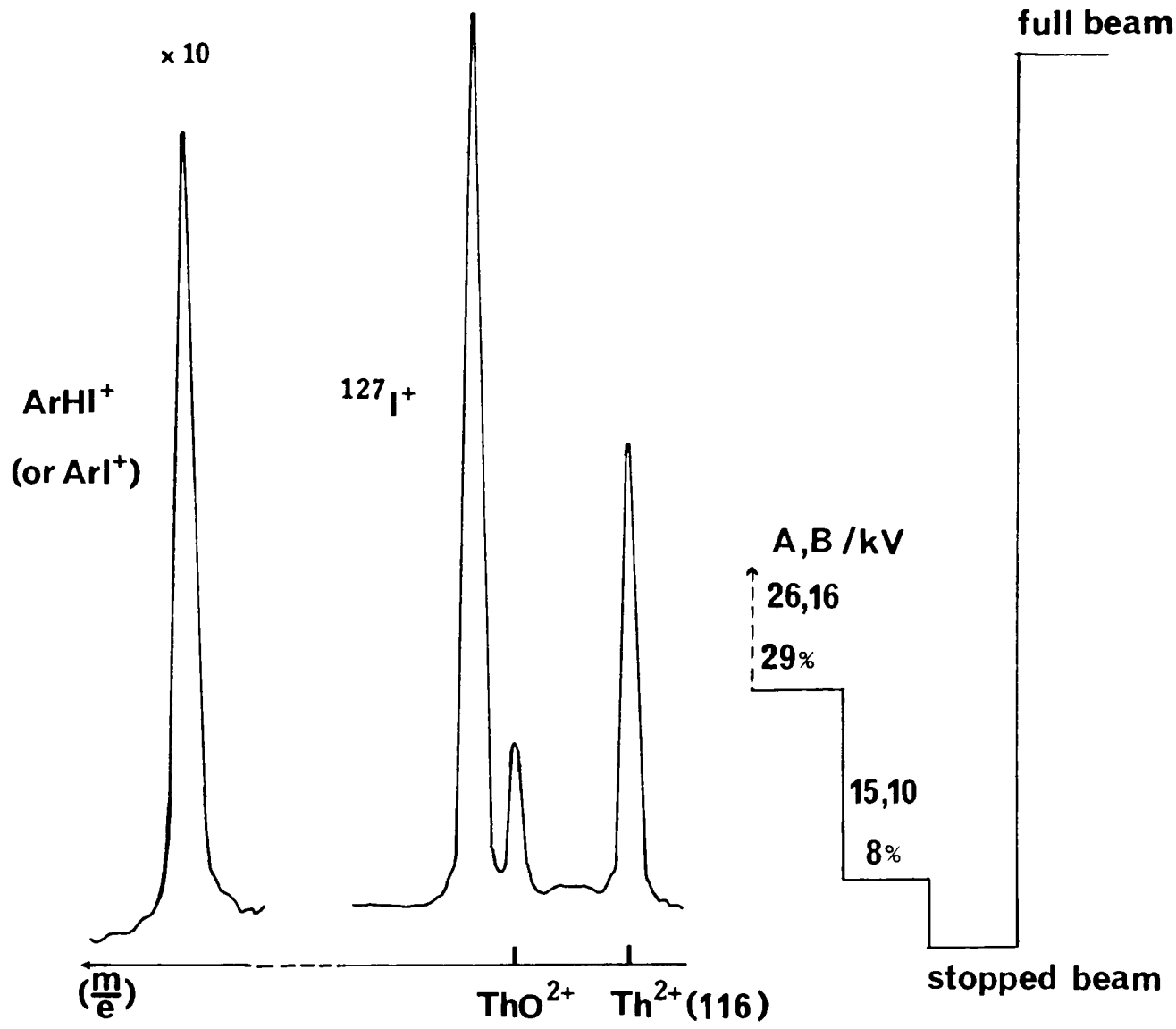

Figure 6.2 Mass spectrum and refocussing of ArHI. The identification of the mass peak (167 or 168) is not possible because of the lack of background calibrants and the low mass resolution of the apparatus.

estimate the dipole moment of the complex compare the refocussing characteristics of KrHCl in the spectrometer. The focussing fields for J = 4 of KrHCl are A,B = 10,6(±1) kV and this focusses ~ 43(4)% of the straight-through beam intensity. If a similar rotational temperature is assumed for the complex, as seems likely[22], then a similar percentage refocussing, corrected for the change in partition function, will give a similar J state refocussing. For the ArHI complex this is found for

A,B fields of 26(2),16(2) kV. The dipole moment of the complex can then be estimated as

$$\mu_a \simeq \frac{0.9567}{2.6} \times \left(\frac{860}{1200.624}\right)^{\frac{1}{2}} = 0.311(33) \text{ Debye} \qquad (6.5)$$

If an induced moment of 10% is assumed, then a value for γ_{P_1} of 51.2° (5.5) is estimated, using the calculated dipole moment of HI of 0.4477(5) D [12]. This value of γ_{P_1} indicates that the value of γ_{P_2} is not likely to be vastly different from the value of ~43° obtained from the extrapolation of the values of γ_{P_2} for the other ArHX complexes. The value of $(eQq)^I$ for $H^{127}I$ (spin 5/2) is however -1828.286(9) MHz [10], much larger than the nuclear hyperfine data for Cl or Br, and $(eQq)^I_a$ is estimated at ~ -553 MHz, of the same order of magnitude as the rotational constant, so the nuclear hyperfine splittings will be a large perturbation on the rotational spacings, making searching for new lines more difficult.

6.3 ArHF studies

In their initial paper on ArHF, Harris *et. al.*[1] obtained $J = 0 \rightarrow 1$ and $1 \rightarrow 2$ transitions and apparently observed splittings due to the H..F spin-spin interaction. They give a value of d_{HF} ($\equiv S_{HF}$ in their nomenclature) for free HF of 28.675(5) kHz in the $\nu = 0$, $J = 0$ state from previous measurements[23]. This however neglected the $[(2J+3)(2J-1)]^{-1}$ factor[24], present in their initial analysis and d_{HF} should equal $5S_{HF}$ = 143.375(25) kHz. Signal/noise ratios were very poor (~ 1/1 [24]) for the published transition frequencies. The $0 \rightarrow 1$ transitions at 6131 MHz were subsequently re-taken by Janda using a 1 hour computer averaged scan[25]. He found a doublet only at 6131.185_0 MHz and 6131.138_5 MHz, the HWHM of the lines being ~ 7 - 10 kHz. A splitting of 45.5 kHz was estimated with a probable error of ~ ±2 kHz since generally sum of squares fitting indicated that about one tenth of the linewidth was equal to the final uncertainty in the least-squares analysis. Janda

failed to realise that the spin-spin interaction constant is a second rank tensor quantity and so the measured value of d will be related to the free molecular value by the equation

$$d_a = d^{HF}\langle P_2(\cos\gamma)\rangle \tag{6.6}$$

The spectra may then be analysed as follows. The two nuclei, H and F, each have nuclear spins = ½, and a simple coupling scheme couples the two nuclei together, and the resultant to the rotational angular momentum

$$I_R = I_1 + I_2 \text{ and } F = J + I_R \tag{6.7}$$

The spin-spin Hamiltonian then takes the form[23]:

$$H_{SS} = \frac{d_a}{(2J-1)(2J+3)}\left\{\frac{I_R(I_R+1) + 4I_1(I_1+1)}{(2I_R-1)(2I_R+3)}\right\} \times \left[3(I_R.J)^2 + \frac{3}{2}(I_R.J) - (I_R{}^2J^2)\right] \tag{6.8}$$

and the diagonal matrix element

$$\langle J,I_R;F|\hat{H}_{SS}|J,I_R;F\rangle = \frac{d_a}{(2J-1)(2J+3)}\left\{\frac{I_R(I_R+1) + 4I(I+1)}{(2I_R-1)(2I_R+3)}\right\} \times \left[\frac{3}{4}\{F(F+1) - J(J+1) - I_R(I_R+1)\}^2 + \frac{3}{4}\{F(F+1) - J(J+1) - I_R(I_R+1)\} - J(J+1)I_R(I_R+1)\right]$$

where $I = I_1 = I_2 = \frac{1}{2}$ (6.9)

This tensor spin-spin coupling constant contains the direct spin-spin interaction and the tensor component of the electron coupled spin-spin interaction; the first term is just $g_H g_F \mu_N{}^2/\langle R^3\rangle_o$ [24], and agrees within experimental error with the value found, indicating that the second term is negligible in HF. A further term is the electron coupled scalar spin-spin interaction of the form

$$\delta I_1.I_2 = \tfrac{1}{2}\delta[I_R - I_1{}^2 - I_2{}^2] = \tfrac{1}{2}\delta[I_R(I_R+1) - I_1(I_1+1) - I_2(I_2+1)] \tag{6.10}$$

in this basis set. δ has been measured at +0.529(23) kHz [23].

The spin-rotation interaction Hamiltonian takes the form

$$H_{SR} = c_b^F I_F.J + c_b^H I_H.J \qquad (6.11)$$

Matrix elements may be similarly expanded to those in Appendix B and C, and the diagonal elements take the form

$$\langle J, I_R; F | \hat{H}_{SR} | J, I_R; F \rangle = \frac{c_F}{4} \{F(F+1) - J(J+1) - I_R(I_R+1)\} + \text{a similar term for } c_H \qquad (6.12)$$

Focussing states for $J = 1$ are $F = 0,2$. A transition to the $J = 0$, $F = 1,0$ state will yield two doublets, the separations of which are given by $0.9d_a + \frac{3}{2}(c_b^H + c_b^F)$ and $0.9d_a + \frac{3}{2}(c_b^H + c_b^F) + \delta$. The splitting due to δ is not resolved in the spectra. Ignoring the values of c_b suggests a value of $d_a \sim 50.6$ kHz *i.e.* $\langle P_2 \rangle$ of ~ 0.35. The values of c_b^F and c_b^H can then be estimated from corrected semi-rigid theory, using a value of 0.6 for $f(\langle \cos^2\theta \rangle)$, and measured value for HF[23]. This yields values of $c_b^F = 0.517$ kHz and $c_b^H = -0.119$ kHz. d_a is therefore estimated to be 49.6 ± 2 kHz and $\langle P_2 \rangle = 0.346(14)$. γ_{P_2} is then $41.3(5)°$, and $B - 2D_J = 3065.567(1)$ MHz. Clearly the $J = 1 \rightarrow 2$ transitions need to be re-examined to fix D_J precisely but the observation of transitions around 12260.5 MHz in the original paper yields a value for D_J of around 74 kHz. A study on ArDF would also be informative for potential energy surface calculations. A similar problem is also found to ArHI in seasoning the system to HF (DF)[26], and observation of ArHF in the Oxford spectrometer has proved very difficult.

The previous chapters have shown that a wealth of spectroscopic information may be obtained for the ground state of these complexes. The next chapter discusses the use of this data in determining potential energy surfaces.

References to chapter 6

1. S.J. Harris, S.E. Novick and W. Klemperer, J. Chem. Phys., *60*, 3208, (1974).

2. S.E. Novick, P. Davies, S.J. Harris and W. Klemperer, J. Chem. Phys., *59*, 2273, (1973); J.M. Hutson and B.J. Howard, J. Chem. Phys., submitted for publication.

3. K.C. Jackson, P.R.R. Langridge-Smith and B.J. Howard, Mol. Phys., *39*, 817, (1980); see also reference 6.

4. E.J. Campbell, M.R. Keenan, L.W. Buxton, T.J. Balle, P.D. Soper, A.C. Legon and W.H. Flygare, Chem. Phys. Lett., *70*, 420, (1980).

5. A.E. Barton, T.J. Henderson, P.R.R. Langridge-Smith and B.J. Howard, Chem. Phys., *45*, 429, (1980); T.J. Balle, E.J. Campbell, M.R. Keenan and W.H. Flygare, J. Chem. Phys., *72*, 922, (1980).

6. M.R. Keenan, E.J. Campbell, T.J. Balle, L.W. Buxton, T.K. Minton, P.D. Soper and W.H. Flygare, J. Chem. Phys., *72*, 3070, (1980).

7. C.H. Becker, P.W. Tiedemann, J.J. Valenti and Y.T. Lee, J. Chem. Phys., *71*, 481, (1979).

8. K.V. Chance, K.H. Bowen, J.S. Winn and W. Klemperer, J. Chem. Phys., *70*, 5157, (1979).

9. D.U. Webb and K.N. Rao, J. Mol. Spectrosc., *28*, 12, (1968).

10. F.A. van Dijk and A. Dymanus, Chem. Phys. Lett., *2*, 235, (1968).

11. J.S. Muenter, J. Chem. Phys., *56*, 5409, (1972).

12. F.A. van Dijk and A. Dymanus, Chem. Phys. Lett., *5*, 387, (1970).

13. A.D. Buckingham, Adv. Chem. Phys., *12*, 107, (1967).

14. By the Kerr effect: Landolt-Börnstein tables (Springer-Verlag, Berlin, 1951), vol.1, part 3; N.J. Bridge and A.D. Buckingham, Proc. Roy. Soc. A, *295*, 334, (1966). From molecular beam studies of dipole moments: E.W. Kaiser, J. Chem. Phys., *53*, 1686, (1970); D.W. Johnson and N.F. Ramsey, J. Chem. Phys., *67*, 941, (1977); see also references 11 and 12.

15. L. Pauling, The Nature of the Chemical Bond, (Cornell, Ithaca, 1940), page 187.

16. Values from: M. Waldman and R.G. Gordon, J. Chem. Phys., *71*, 1325, (1979).

17. G.W. King, Spectroscopy and Molecular Structure, (Holt, Reinhart, Winston, N.Y., 1964), page 171.

18. H.K. Shin, Chem. Phys. Lett., *49*, 193, (1977).

19. J.A. Barker and A. Pompe, Aust. J. Chem., *21*, 1683, (1968).

20. R.J. Le Roy, Chem. Phys. Lett., *67*, 207, (1979).

21. H.K. Shin, Chem. Phys. Lett., *47*, 225, (1977).

22. G.M. McClelland, K.L. Saenger, J.J. Valenti and D.R. Herschbach, J. Phys. Chem., *83*, 947, (1979).

23. J.S. Muenter and W. Klemperer, J. Chem. Phys., *52*, 6033, (1970).

24. N.F. Ramsey, Molecular Beams, (OUP, Oxford, 1956), chapter 8, equation 11.

25. K.C. Janda, Ph.D. Thesis, (Harvard, 1977).

26. W. Klemperer, private communication.

CHAPTER 7: THE BORN-OPPENHEIMER APPROXIMATION APPLIED TO VAN DER WAALS COMPLEXES

In this final chapter the Born-Oppenheimer angular-radial separation method (BOARS) developed by Holmgren *et. al.*[1] and extended by Hutson[2] (CBO) will be used to gain a quantitative idea of the extent of radial and angular motion that exists in these complexes, and the trends that occur on changing the identity of the constituents of the complex. The limitations of the form of the intermolecular surface will be discussed, and the information content of the molecular beam data realised. The method is then extended to diatom-diatom complexes, and applied to the tunnelling species $(HF)_2$. Potential surfaces that are available for this molecule will be compared and contrasted. Other approaches that have been undertaken for the solution of the dynamics of these complexes will also be mentioned briefly.

A. Atom - diatom complexes

7.1 Zeroth-order solution (BOARS level)

The choice of an axis system in which to describe the motions and derive the Hamiltonian of the complex is arbitrary to a certain extent, but the choice of the use of a space-fixed or body-fixed frame is somewhat governed by the anisotropy of the intermolecular potential. Bratoz and Martin[3] divided van der Waals complexes into three types depending on the anisotropy of the complex: Case *a* coupling is appropriate where the anisotropy of the interaction is weak compared with the rotational constant of the complex ($V_{anis} < B$); it is then advisable to quantise the constituent angula momenta in a space-fixed axis system (for example, ArH_2). Case *b* coupling occurs when the magnitude of the anisotropic potential is greater than the rotational constant (B) of the complex, and less than the rotational constant of the diatom subunit (b_o, following Holmgren *et. al.*[1]). The angular momentum of the diatomic molecule

is then coupled to the major (z) axis of the complex, and hence a body-fixed axis system (rotating with the complex) is preferable. For case *c* complexes, the anisotropy dominates over both rotational constants, and the bending motions eventually correlate with the vibrations of a rigid triatomic molecule[4]. A van der Waals molecule which approaches this case is ArOCS[5].

As illustrated for NeDCl and NeHCl the anisotropy is of approximately the same magnitude as the diatom rotational constant. For the other rare gas hydrogen halide complexes the anisotropy of the potential increases but not to such an extent that a conventional force field analysis is likely to provide a good description of the system.

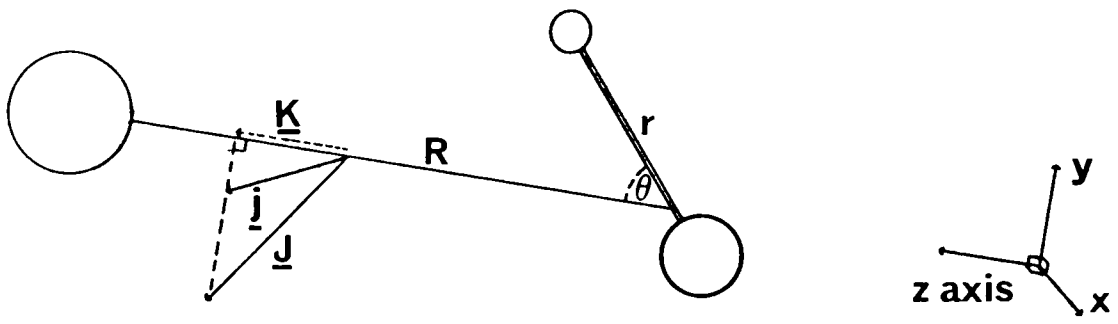

Figure 7.1 Atom - diatom coordinate system

The coordinate system is the usual one chosen for atom - diatom complexes (figure 7.1). R is the distance from the diatom centre-of-mass to the atom, and r is the length of the diatom. θ is related to the corresponding vectors by the equation

$$\theta = \cos^{-1}\left(\frac{\mathbf{R}.\mathbf{r}}{|\mathbf{R}||\mathbf{r}|}\right) \qquad (7.1)$$

The axis system chosen, {x,y,z}, is then defined such that the z axis is parallel to R and forms a right-handed axis system. In the body-fixed coordinate system the Hamiltonian (excluding the centre of mass motion) is given by[1,3]

$$H = \frac{\hbar^2}{2\mu}\left(-\frac{\partial^2}{\partial R^2} + \frac{(J-j)^2}{R^2}\right) + V(R,r,\theta) - \frac{\hbar^2}{2\mu_d}\cdot\frac{\partial^2}{\partial r^2} + b(r)j^2 \qquad (7.2)$$

and the individual terms are discussed below. μ is the reduced mass of the system, J is the total angular momentum operator for the complex, and j is the angular momentum operator for the diatom measured with respect to the rotating axis system. μ_d is the reduced mass of the diatom ($\mu_d = m_H m_X/(m_H + m_X)$), and b(r) its rotational constant.

The total angular momentum is conserved in any axis system, but the vector $\underline{J} - \underline{j}$ represents the motion due to end-over-end rotation of the complex. The diatomic angular momentum, $\underline{j}$, which is conserved in the free rotor limit is coupled to the molecular axis via the angle dependent terms in the intermolecular potential, $V(R,r,\theta)$. Its projection on the z axis is approximately a constant of the motion. By conservation of angular momentum, this value is equal to the projection of the total angular momentum vector on the z axis.

In the molecular beam experiment described here there is little or no information about the r dependence of the potential from the data. The potential is then written as a function dependent on R and θ only. The functional form to describe $V(R,\theta)$ is then written as a sum over Legendre polynomials each multiplied by a radial function

$$V(R,\theta) = \sum_n P_n(\cos\theta) V_n(R) \qquad (7.3)$$

These terms are each averaged over r. The choice of radial functions will be given below. The term $-\hbar^2/2\mu_d(\partial^2/\partial r^2)$ is therefore also excluded from the equation, since the diatom is assumed to be a rigid rotor. For the b(r) term representing the rotation of the diatom the free molecular value, b_o, is assumed. This assumption was also made in the semi-rigid analysis. If any dependence on the diatom vibrational motion is suggested, (such as for rotational constant anomalies - see later) then Le Roy[3] has suggested a simple extension to the equation 7.3 of the form

$$V(R,r,\theta) = \sum_n \sum_k \xi^k P_n(\cos\theta) V_{nk}(R) \qquad (7.4)$$

where ξ (= $(r/r_o) - 1$, for example) represents the amount of diatom stretching.

For a zeroth-order solution to the problem the stretching and bending wavefunctions are separated by a method similar to the Born-Oppenheimer or adiabatic separation of electronic and vibrational motions in a molecule[6]. Although the bending and stretching frequencies are comparable in the complexes (see chapters 4 and 5 for harmonic estimates), this does not invalidate the separation, the success of which depends on the strength of non-adiabatic coupling terms[7]. It will be shown that the separation for $(HF)_2$ is more exact than for the atom-diatom complexes. The wavefunction is then assumed to take the form

$$\Psi = \psi_{bs}(\theta,R) D^{J*}_{MK}(\alpha\beta\gamma) \tag{7.5}$$

and

$$\psi_{bs}(\theta,R) = \phi_b(\theta;R)\chi_{bs}(R) \tag{7.6}$$

where b,s label the bending and stretching quantum numbers respectively and the azimuthal angle dependence of ϕ_b has been dropped. The total wavefunction for the system also contains a symmetric top wavefunction, D^{J*}_{MK}, which represents rotation of the complex. $(\alpha\beta\gamma)$ are the Euler angles linking the body-fixed axis to the space-fixed axis[8].

The wavefunction in equation 7.6 shows a parametric R dependence for the bending wavefunction. The dynamics of the zeroth-order solution then pictures the bending wavefunction as relaxing instantaneously as the van der Waals bond is stretched. It therefore takes the place of electronic motion in the original Born-Oppenheimer paper. The method consists of solving the angular part of the Hamiltonian at a number of values of R, and then solving for the stretching motion. It is convenient to separate out the J-dependence of the parts of the Hamiltonian and solve for them later. The J-independent equation to be solved is

$$H_b\phi^K_b(\theta;R) = \left[\left(b_o + \frac{\hbar^2}{2\mu R^2}\right) j^2 - \frac{\hbar^2 K^2}{\mu R^2} + V(R,\theta)\right] \phi^K_b(\theta;R) = U^K_b(R)\phi^K_b(\theta;R) \tag{7.7}$$

where the K dependence (the angular momentum quantum number along the z axis) of ϕ and U has been included. A suitable expansion of the bending wavefunction is given in terms of

$$\phi_b^K(\theta;R) = \sum_j^N c_{bj}^K(R) Y_j^K(\theta) \qquad (7.8)$$

Diagonalisation of the matrix gives the coefficients $c_{bj}^K(R)$. The extent of variations in these with R indicates the validity of the Born-Oppenheimer separation. The expansion in equation 7.8 is truncated at that value of j when the required convergence of all calculated observables is attained. The solution of the matrix diagonalisation yields a series of bending potentials within the adiabatic approximation.

The action of the Hamiltonian of equation 7.2 (for a rigid rotor diatom and a rotationless complex) on the zeroth-order wavefunction is then

$$H\psi_{bs}(\theta,R) = U_b^K(R)\psi_{bs}(\theta,R) - \frac{\hbar^2}{2\mu}\left\{\frac{\partial^2}{\partial R^2}\phi_b^K(\theta;R)\right\}\chi_{bs}^K(R) \qquad (7.9)$$

$$- \frac{\hbar^2}{2\mu}\left\{\frac{\partial^2}{\partial R^2}\chi_{bs}^K(R)\right\}\phi_b^K(\theta;R) - \frac{\hbar^2}{\mu}\left\{\frac{\partial}{\partial R}\phi_b^K(\theta;R)\cdot\frac{\partial}{\partial R}\chi_{bs}^K(R)\right\}$$

The second and fourth terms are coupling terms which are zero in the Born-Oppenheimer approximation[6c]. Neglecting these terms therefore leads to a Schrödinger equation for the stretching motion

$$\left[-\frac{\hbar^2}{2\mu}\frac{\partial^2}{\partial R^2} + U(R)\right]\chi(R) = E_1^{(0)}\chi(R) \qquad (7.10)$$

where (0) represents a zeroth-order solution and this may be solved by the Cooley method[9]. Epstein has showed that this solution is necessarily a lower bound to the ground state energy[10]. The non-adiabatic terms diagonal in bending may also be added at this stage. The contribution to this from the last term is zero since $\int\phi_b^*(\partial/\partial R)\phi_b d\Omega = \frac{1}{2}(\partial/\partial R)\int\phi_b^2 d\Omega = \frac{1}{2}(\partial/\partial R)\{1\} = 0$, hence the penultimate term is left to give the correction as

$$\tau(R) = \int\phi_b^*\frac{\partial^2}{\partial R^2}\phi_b d\Omega \qquad (7.11)$$

then equation 7.10 becomes

$$\left[-\frac{\hbar^2}{2\mu}\frac{\partial^2}{\partial R^2} + U(R) + \tau(R) \right] \chi(R) = E_u \chi(R) \qquad (7.12)$$

E_u is an upper bound of the true energy since inclusion of non-adiabatic terms lowers the ground state energy[1], although this statement has been challenged[7]. In the results in this chapter, the energies including non-adiabatic terms (see below) do fall between the two extremes, however. From the solution of equations 7.7 and 7.12 a zeroth-order wavefunction, $\psi^{(0)}$ is produced.

7.2 Non-adiabatic corrections (CBO level)

The remainder of the Hamiltonian may be added by perturbation theory[2]. The effect of $\psi^{(0)}$ on equation 7.2 (excluding diatomic vibration) is then

$$H\psi^{(0)} = \left[E_u + \frac{\hbar^2}{2\mu R^2}(J^2 - J_+ j_+ - J_- j_-) + H_{NA} \right] \psi^{(0)} \qquad (7.13)$$

where $J.j = J_z j_z + J_+ j_+ + J_- j_-$, and $\{J_\pm, j_\pm\}$ are the ladder operators in body-fixed axes[11]. The z components are already included in equation 7.7.

The matrix elements for H_{NA} and H_{ROT} where

$$H_{ROT} = \frac{\hbar^2}{2\mu R^2} J^2 \qquad (7.14)$$

are diagonal in the K quantum number. The form of the matrix elements for these is given in Appendix D.1. H_{NA} only has matrix elements off-diagonal in the bending states to be included. The step up/down operators provide a Coriolis part

$$H_{COR} = -\frac{\hbar^2}{2\mu R^2}(J_+ j_+ + J_- j_-) \qquad (7.15)$$

and this connects states with $\Delta K = \pm 1$. The matrix element of H_{COR} over the bending states (at each R) is then

$$\int \phi_b^{K'*} H_{COR} \phi_b^K d\Omega = - \frac{\hbar^2}{2\mu R^2} \sum_j c_b^{K'}(R) c_b^K(R) [j(j+1) - K'K]^{\frac{1}{2}} \times [J(J+1) - K'K]^{\frac{1}{2}} (\delta_{K+1,K'} + \delta_{K-1,K'}) \quad (7.16)$$

Note the $[J(J+1) - K'K]^{\frac{1}{2}}$ dependence of equation 7.16. The Hamiltonian in equation 7.13 can therefore be written as

$$H = H^{(0)} + H_{NA} + H_{ROT} + H_{COR} \quad (7.17)$$

The spectral constants are then calculated by perturbation theory, using the zeroth-order wavefunction as the zeroth-order perturbation wavefunction.

The expectation values are quite straightforward to calculate in the perturbation analysis. As an example consider the rotational constant, $\langle P_2 \rangle$, and the centrifugal distortion constant of the quadrupole coupling constant, D_{P_2}.

The zeroth-order rotational constant is simply $\langle \psi^{(0)} | H_{ROT} | \psi^{(0)} \rangle$, and obviously has a $J(J+1)$ dependence. Two types of additional terms contribute to B; the required dependence may be met by terms first-order in H_{ROT} and n^{th} order in H_{NA}, where $n = 1,2\ldots$, or by terms second-order in H_{COR} (with a $[J(J+1)]^{\frac{1}{2}}$ dependence) and m^{th} order in H_{NA}, where $m = 0,1,2\ldots$. The rotational constant then becomes for the ground ($K = 0$) state, where $|vbK\rangle$ labels the vibrational, bending and K quantum numbers of the product wavefunction (suppressing appropriate $J(J+1)$ dependence)

$$B = \frac{\hbar^2}{2\mu} \langle 000 | \frac{1}{R^2} | 000 \rangle - \sum_{v,b} \frac{|\langle 000 | \hat{H}_{COR} | vb\pm 1 \rangle|^2}{(\varepsilon_{vb\pm 1} - \varepsilon_{000})}$$

$$+ \frac{\hbar^2}{2\mu} \sum_{v,b}' \sum_{v',b'}' \frac{\langle vb0 | \hat{H}_{NA} | 000 \rangle \langle 000 | \hat{H}_{NA} | v'b'0 \rangle}{(\varepsilon_{vb0} - \varepsilon_{000})(\varepsilon_{v'b'0} - \varepsilon_{000})} \times \{ \langle v'b'0 | \frac{1}{R^2} | vb0 \rangle - \langle 000 | \frac{1}{R^2} | 000 \rangle \}$$

$$+ \frac{\hbar^2}{\mu} \sum_{v,b}' \sum_{v',b'}' \frac{\langle v'b'0 | \hat{H}_{NA} | 000 \rangle \langle 000 | R^{-2} | vb0 \rangle}{(\varepsilon_{v'b'0} - \varepsilon_{000})(\varepsilon_{vb0} - \varepsilon_{000})} \langle v'b'0 | \hat{H}_{NA} | vb0 \rangle$$

$$+\sum_{v\,b}\sum_{v'b'}\frac{\langle vb\pm1|\hat{H}_{COR}|000\rangle\langle 000|\hat{H}_{COR}|v'b'\pm1\rangle}{(\varepsilon_{vb\pm1}-\varepsilon_{000})(\varepsilon_{v'b'\pm1}-\varepsilon_{000})}\langle vb\pm1|\hat{H}_{NA}|v'b'\pm1\rangle$$

$$-\sum_{v\,b}\sum_{v'b'}{}'\sum_{v''b''}{}'\frac{\langle v'b'0|\hat{H}_{COR}|vb\pm1\rangle\langle vb\pm1|\hat{H}_{COR}|000\rangle\langle 000|\hat{H}_{NA}|v''b''0\rangle}{(\varepsilon_{vb\pm1}-\varepsilon_{000})(\varepsilon_{vb\pm1}-\varepsilon_{v'b'0})(\varepsilon_{v''b''0}-\varepsilon_{000})}$$

$$\times\langle v'b'0|\hat{H}_{NA}|v''b''0\rangle$$

$$-\sum_{v\,b}\sum_{v'b'}{}'\frac{|\langle vb\pm1|\hat{H}_{COR}|000\rangle|^2|\langle v'b'0|\hat{H}_{NA}|000\rangle|^2}{(\varepsilon_{vb\pm1}-\varepsilon_{000})\ (\varepsilon_{v'b'0}-\varepsilon_{000})^2} \qquad (7.18)$$

The second term is the Coriolis correction to the rotational constant. The third and fourth terms are the direct first-order non-adiabatic corrections to the rotational constant, and the last two terms are the non-adiabatic Coriolis contribution. Only part of the third-order non-adiabatic contribution was found to give a significant effect as well (~ 150 kHz, see appendix D.2). Σ' excludes v,b = 0,0 from the summation.

For the expectation value of P_2 and its centrifugal distortion constant D_{P_2}, integrals such as $\langle 000|P_2|000\rangle$ have to be evaluated. Only terms involving H_{NA} can provide perturbation contributions to $\langle P_2(\cos\theta)\rangle$. These have been included in the results given here for the potentials calculated, but affect $\langle P_2(\cos\theta)\rangle$ *in toto* by about ½%, which is probably at the level of accuracy of the assumption of zero molecular distortion of the subunit diatomic orbitals.

In a earlier chapter it was noted that the value of $\langle P_2(\cos\gamma)\rangle$ is a projection along the *a* inertial axis but for this coordinate system the atom to centre-of-mass of the diatom axis is used. This effect will appear in the value of $\langle P_2(\cos\theta)\rangle$ as a correction of the form

$$\Delta\langle P_2(\cos\theta)\rangle = \frac{1}{\sqrt{3}}\sum_{v,b}{}'\frac{\langle 000|\hat{H}_{NA}|vb0\rangle}{(\varepsilon_{vb0}-\varepsilon_{000})}\langle vb0|C_{21}+C_{2-1}|000\rangle \qquad (7.19)$$

where C_{kq} are the reduced spherical harmonics ($=[4\pi/2k+1]^{\frac{1}{2}}Y_{kq}$). For

KrHCl this has the value of 0.00026 and increases the value of P_2.

For D_{P_2} a similar summation to B is required to obtain the J(J+1) dependence, along with the matrix elements $\langle v'b'K|P_2|vbK\rangle$. The non-adiabatic and Coriolis effects are not insignificant however (see Appendix D.2).

7.3 Convergence and isotope effects

For these studies a set of eight spherical harmonics is used in the matrix diagonalisation to obtain U. This converges the energy to 10^{-3} cm^{-1} and B to ~ 30 kHz. The effective bending potential U(R) is characterised by a grid of 35 values in the range 3 - 6 Å, interpolated to 300 equally spaced points by cubic spline interpolation.

For the atom-diatom complexes the adiabatic and non-adiabatic terms are often quite sharply peaked functions of R. This can arise if the angular minimum at $\theta = 0°$ moves to $\theta = 180°$ as R is reduced (for example, in the HWK type surfaces derived later). This is identified by large sudden changes in the values of the c bending coefficients. For $(HF)_2$ no such sharp peaking occurs.

The convergence over stretching states in the perturbation sums was found to be slow, and so the sum over zeroth-order stretching states was replaced by a direct solution by rewriting the nth order wavefunction corrections $\psi^{(n)}$ as explicit functions of R, instead of expanding them in terms of the $\chi^{(0)}_{vb}$, *i.e.*

$$\psi^{(n)} = \sum_b \chi_b^{(n)} \phi_b \qquad (7.20)$$

and this causes the collapse of the summation over stretching states[13]. Convergence of the appropriate observables (B to 1 kHz, P_2 to 10^{-5}) can be obtained with four bending states typically.

The assumption is made in this chapter that different isotopic forms of an atom-diatom complex have the same intermolecular potential at the same geometry, *i.e.* that the consequences of the r dependence of

the intermolecular potential in equation 7.4 can be neglected. Comparing $^{84}KrH^{35}Cl$ and $^{84}KrD^{35}Cl$ then, it assumes that the effective bond lengths of HCl and DCl are the same. The DCl bond length is however shorter due to slightly different vibrational averaging[14] and an error in the B value of ~ 3 MHz is predicted. The main contribution of the change of the potential parameters in the deuterium complex is caused by the centre of mass shift from HCl to DCl (as well as the reduced mass effects). This effect has been discussed by Le Roy who has developed an efficient method for calculating centre-of-mass corrections terms using Gauss-Legendre quadrature[15].

7.4 Intermolecular potential surfaces from molecular beam data

Exponential - 6 potentials have been used for the $V_n(R)$ functions[1], and the form of the summation over Legendre polynomials given in equation 7.3 will be referred to as the HWK parameterisation. If the summation over n is unrestricted this parameterisation is quite general; however because of the limited amount of experimental data from MBER experiments the summation is often truncated at $n = 2$, which makes the parameterisation much less flexible. It is also not a particularly good parameterisation for fitting the data. In chapters 4 to 6 it has been shown that the configuration of the complex is acute, with large amplitude motion. The fitting of the ArHCl potential with the adiabatic method indicated that the amplitude of the motion was such that the hydrogen reached around $\theta = 80°$ in its classical amplitude. The molecular beam data consequently samples little of the large angle regions of the potential surface ($\theta > 90°$) and uncertainty in this region will be reflected in the uncertainty of all the Legendre coefficients. In an effort to obtain the maximum amount of information from the data an alternative parameterisation was tried. The radial potential is specified at several angles, for instance at $\theta = 0°$, 60°, 120°, and 180°, and then interpolated between these angles using an expansion $P_0(\cos\theta)$ to $P_3(\cos\theta)$

at given R by matrix inversion methods. The principal minimum in $V(R,\theta)$ for these atom-diatom potentials is at $\theta = 0°$, and so the data contains considerable information for this angle, and also for $\theta = 60°$, and this is reflected in well determined parameters. The behaviour at larger angles scarcely affects the spectrum, and it is convenient in the least-squares fitting of the data to fix the 120° and 180° potentials at some physically reasonable value.

An appropriate form for the V(R) potentials is the simple Maitland-Smith potential[16]. This proved to be a very much more accurate and flexible potential for describing inert gas dimer potentials than Lennard-Jones or exponential - 6 functions. Transport data were reproduced more accurately than by even more flexible potentials[17], and recently the glory structure in the total cross-sections of inert gas pairs has been successfully modelled[18]. The potential has the form

$$V(R) = \varepsilon \left[\left(\frac{6}{n-6} \right) x^{-n} - \left(\frac{n}{n-6} \right) x^{-6} \right] \qquad (7.21)$$

where $x = R/R_e$, R_e is the equilibrium separation, ε is the well depth, and n is allowed to vary with R as

$$n = M + \gamma(x - 1) \qquad (7.22)$$

where n and M are constants. γ is typically 10 for the heavier rare gas pair potentials[18a], but is smaller for neon and helium. γ has been fixed at 10 for the Ar, Kr, and Xe potentials below. The radial curvature at the minimum is independent of γ and so it is undetermined by the rotational spectrum. γ was determined for the inert gas species largely from high temperature gas transport data. For the $P_1(\cos\theta)$ term in the HWK parameterisation the radial potential has 6 replaced by 7 to match the leading term in the multipole expansion. However, long range C_n coefficients are poorly estimated in Holmgren's fits[1], because of the lack of long range information in MBER data. This modification has no great effect on the rotational spectra, and was ignored for the

four-angle parameterisation.

The spectroscopic constants available for fitting the data consist of rotational constants, centrifugal distortion constants, $\langle P_2(\cos\theta)\rangle$ and D_{P_2} quantities, and $\langle P_1(\cos\theta)\rangle$ values from dipole moment data. As seen in chapters 4 and 5, the H and D isotopic forms of a complex give complementary data (similar R and θ values are derived), and most information comes from the large change of geometry on deuteration. However, because of the different sizes of HCl and DCl, and the consequent anomalously large rotational constant (from a shift of the $\theta = 0°$ radial minimum, principally) that would result, the rotational constants of the deuterium isotopic forms were omitted when possible. The results for KrHCl and other complexes indicate some discrepancy in rotational constants due to the shortening effect, but not conclusively.

D_J is sensitive to the radial curvature near the minimum, but no other pieces of data provide information on the well depth. It is therefore necessary to fix the isotropic well depths for these complexes. Farrar and Lee have determined the value for ArHCl at 133 ± 7 cm^{-1} [19], but no other XHCl systems have been studied. The values for the HCl series are estimated by considering the empirical combining rule which works well for inert gas pairs

$$\varepsilon_{ij} = \frac{2\varepsilon_{ii}\varepsilon_{jj}}{(\varepsilon_{ii} + \varepsilon_{jj})} \qquad (7.23)$$

Using Farrar and Lee's value of ε_{ij} for ArHCl and ε_{ii} for Ar_2 to obtain ε_{jj}, an estimate of the $(HCl)_2$ isotropic potential (~ 200 cm^{-1}) is obtained. Values for ε_{ij} of X...HCl (X = Ne, Kr, Xe) could then be calculated. A further estimate is obtained from the difference in well depth of ArX (where X = Ne, Kr, Xe) and Ar_2 [20]. Values of 52 (Ne), 133 (Ar), 155 (Kr), and 190 (Xe) cm^{-1} were used. These are only rough estimates. Values for ArHBr (145 cm^{-1}) and other complexes can be made by consideration of dipole moment and polarisability changes. Generally,

an inverse correlation between the well depth and the repulsive wall parameter, M, would be expected such that the radial curvature at the minimum is maintained, and hence D_J fitted (see Appendix D.3).

The number of parameters that are floated for each surface is described for each complex. In general there are too many parameters to be fitted to the small amount of data (8 or 9 pieces of significant information at best)[21]. The Maitland-Smith potential has three parameters (ε, R_e, M; γ is undetermined), and using $\theta = 0°$ and 60° potentials gives a 6-parameter surface. A further linking of these parameters is also carried out.

Multiparameter fitting was achieved with a Marquadt algorithm[20] which involves the input of a Jacobian matrix, and hence the partial derivatives of the observables with respect to the parameters. These are obtained by divided differences. A sum of weighted squares of residuals is also calculated at each iteration[22]. This requires estimates of the errors involved in the calculated values of observables[1], which is difficult. For the distortion quantities, the experimental errors outweigh the calculation errors. In the case of dipole moment data, the dipole moment is corrected for polarisation terms, and included in the fits with large uncertainty limits (about 10 × those of $\langle P_2(\cos\theta)\rangle$ data).

(a) KrHCl

A least-squares fit to the data for $^{84}KrH^{35}Cl$, $^{84}KrH^{37}Cl$, $^{86}KrH^{35}Cl$ and $^{84}KrD^{35}Cl$ using both HWK and 4-angle parameterisations has been performed. The calculated and observed spectroscopic constants are given in table 7.1 and the resultant potential parameters in table 7.2.

For the HWK parameterisation the isotropic well depth (ε_0) was set at 155 cm^{-1}, and the hydrogen potential was truncated at the $P_2(\cos\theta)$ term; for deuterium the centre of mass shift results in a small $P_3(\cos\theta)$ correction term. The values of R_e for the $P_1(\cos\theta)$ and $P_2(\cos\theta)$ terms

Table 7.1 Comparison of experimental and calculated spectroscopic properties.

	B/MHz	D_J/kHz	$\langle P_1(\cos\theta)\rangle$ [1]	$\langle P_2(\cos\theta)\rangle$	D_{P_2}/ppm
$^{84}KrH^{35}Cl$					
Experimental	1200.624	7.34	0.768	0.4324	10.8
HWK	1200.69	7.34	0.716	0.4334	11.0
4 - angle	1200.62	7.32	0.731	0.4321	11.1
Uncertainty	1.00	0.30	0.040	0.0040	1.5
$^{84}KrD^{35}Cl$					
Experimental	1183.773	6.51	0.882	0.6055	10.7
HWK	1183.55	6.42	0.839	0.6015	6.7
4 - angle	1182.51	6.54	0.840	0.6045	8.7
Uncertainty	—	0.30	0.050	0.0040	3.0
$ArH^{79}Br$					
Experimental	1106.671	12.46	0.638	0.3254	34.1
HWK	1106.74	12.79	0.595	0.3184	34.7
4 - angle	1106.76	11.37	0.646	0.3245	34.2
Uncertainty	1.0	0.6	0.030	0.0040	1.5
$ArD^{79}Br$					
Experimental	1087.509	8.52	0.837	0.5206	29.1
HWK	1084.38	9.03	0.788	0.5271	19.0
4 - angle	1087.07	9.67	0.792	0.5223	29.6
Uncertainty	—	0.60	0.040	0.0040	2.0
$NeD^{35}Cl$					
Experimental	2698.137	183.04	0.422	0.1972	73.2
4 - angle	2698.17	184.57	0.416	0.1958	70.1
Uncertainty	4.0	3.0	0.020	0.0040	3.0

[1] Correcting for (estimated) multipole effects.

Table 7.2 Parameters of fitted potentials

HWK	KrHCl	ArHBr	4 - angle	KrHCl	ArHBr	NeDCl
ε_0/cm^{-1}	155.0	145.0	$\varepsilon(\theta=0°)/cm^{-1}$	224.22(45)	185.96(46)	71.83(68)
ε_1/cm^{-1}	18.5(3.6) [1]	16.9(4.8)	$\varepsilon(\theta=60°)/cm^{-1}$	160.16(1.18)	151.73(97)	55.19(1.03)
ε_2/cm^{-1}	51.9(2.3)	31.3(3.1)	$\varepsilon(\theta=120°,180°)/cm^{-1}$	142.72	134.47	47.00
$R_{e_0}/Å$	$3.980_6(11)$	$4.019_0(17)$	$R_e(\theta=0°)/Å$	$4.085_9(3)$	$4.200_9(3)$	$3.768_4(7)$
$R_{e_1}, R_{e_2}/Å$	$4.207_3(11)$	$4.446_0(19)$	$R_e(\theta=60°,120°,180°)/Å$	$3.978_6(5)$	$4.005_2(4)$	3.662_9
M	12.97(32)	8.62(71)	M	13.25(21)	9.54(41)	11.0
γ	10.0	10.0	γ	10.0	10.0	8.0

[1] Quantities in brackets are 1 standard deviation.

were constrained to be the same, but are independent of R_e for the isotropic potential. This gives a five parameter surface. A best fit potential with a sum of weighted squares, $\chi^2 = 9.73$ (17 data points) is obtained. Significant correlation is found between R_{e_0} and the anisotropic R_e ($r = -0.935$), and between the $P_1(\cos\theta)$ and $P_2(\cos\theta)$ potential well depths ($r = -0.903$).

In the 4 - angle fit, 5 parameters were again allowed to float. The 0° and 60° well depths were floated, while the 120° and 180° well depths were fixed at the same value, the latter two being determined from the isotropic well depth and the values of $\theta = 0°$ and 60° by the expression

$$18\varepsilon_{iso} = \varepsilon_{0°} + 8\varepsilon_{60°} + 8\varepsilon_{120°} + \varepsilon_{180°} \qquad (7.24)$$

The wall parameter was initially constrained to be the same at all angles, and $R_e(\theta = 120°, 180°)$ was put equal to $R_e(\theta = 60°)$ for the reasons discussed above.

This parameterisation gave a slightly better fit than the HWK parameterisation, with $\chi^2 = 4.08$. The potential parameters are better determined (see table 7.2) and the parameter correlations are somewhat reduced (see table 7.3).

Table 7.3 Correlation matrix for KrHCl 4 - angle fit.

	$\varepsilon(\theta = 0°)$	M	$R_e(\theta = 0°)$	$\varepsilon(\theta \neq 0°)$	$R_e(\theta \neq 0°)$
$\varepsilon(\theta = 0°)$	1,000				
M	-0.046	1.000			
$R_e(\theta = 0°)$	0.540	0.130	1.000		
$\varepsilon(\theta \neq 0°)$	0.790	-0.199	0.492	1.000	
$R_e(\theta \neq 0°)$	-0.513	0.351	-0.921	-0.378	1.000

The values of R_e are strongly correlated but there are no other correlation coefficients greater than 0.8. The standard deviation for the $\theta = 0°$ well depth results from the fit and all ε values are not determined more accurately than the estimate of the isotropic well depth. This is shown in Appendix D.3 where the well depth parameters follow the isotropic well depth. The values of R_e are determined almost completely from the fit to the rotational constants. The inverse correlation of the M values with well depths is also seen. The data is not very sensitive to this wall parameter although a slightly improved χ^2 statistic is seen for ε_{iso} = 155 cm^{-1} than for the other two fits, though if a different V(R) form is adopted, another 'optimised' value for ε_{iso} would probably be obtained. Other data such as elastic cross-section data is required to decorrelate these effects.

It might be assumed that the wall parameters at $\theta = 0°$ and 60°, 120°, 180° should be different corresponding to Kr...H overlap or Kr...Cl overlap. However, floating a second M parameter leads to a χ^2 of 3.80 which is not significant[21], and the parameters overlap at the 1σ level.

Plots of the HWK and 4-angle potential surfaces from table 7.2 are given in figures 7.2 and 7.3. The comparison is striking, and demonstrates their region of validity. Within the classically allowed region around $\theta = 0°$ to 80° the two potentials have a very similar shape and this should be reliable. Beyond these angles they are completely different; the HWK potential has a deep secondary minimum, whereas the 4-angle potential has not. Potential energy surfaces that are derived from MBER data are reliable near the minimum but cannot be extrapolated beyond the classical turning points. It is clear that the spectra contain little information on the potential beyond $\theta = 90°$.

The secondary minimum for the HWK parameterisation occurs because the P_2 coefficient is greater than one third of the P_1 coefficient. In fact the P_2 anisotropy is greater than the P_1 anisotropy which is not as

Figure 7.2 Potential surface for KrHCl using the HWK parameterisation. Contours are at 10 cm^{-1} intervals above the minimum (at $\theta = 0°$, $\varepsilon = -219.152\ cm^{-1}$, $R_e = 4.074$ Å); the dashed curves outline the classically accessible regions for KrHCl and KrDCl.

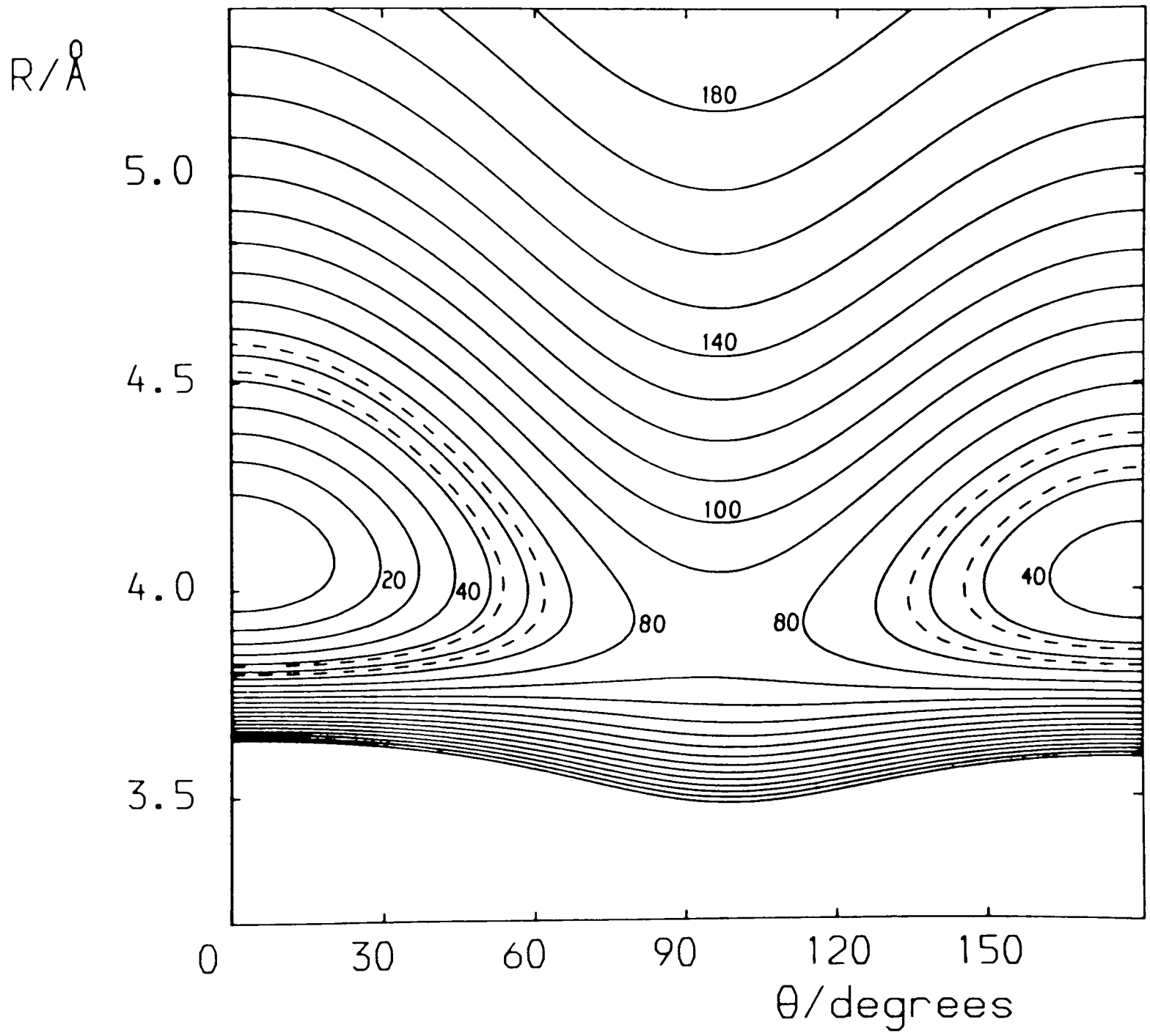
R/Å
5.0
4.5
4.0
3.5
180
140
100
20
40
80
80
40
0
30
60
90
120
150
θ/degrees

Figure 7.3 *4 - angle potential for KrHCl. Contours are at 10 cm^{-1} intervals above the minimum at $\theta = 0°$. The well depth is given by the value of $\varepsilon(\theta = 0°)$. The classically allowed regions for large amplitude motion in KrHCl and KrDCl are shown by the dashed contours, the motion of the deuterium complex being less than that of the hydrogen complex.*

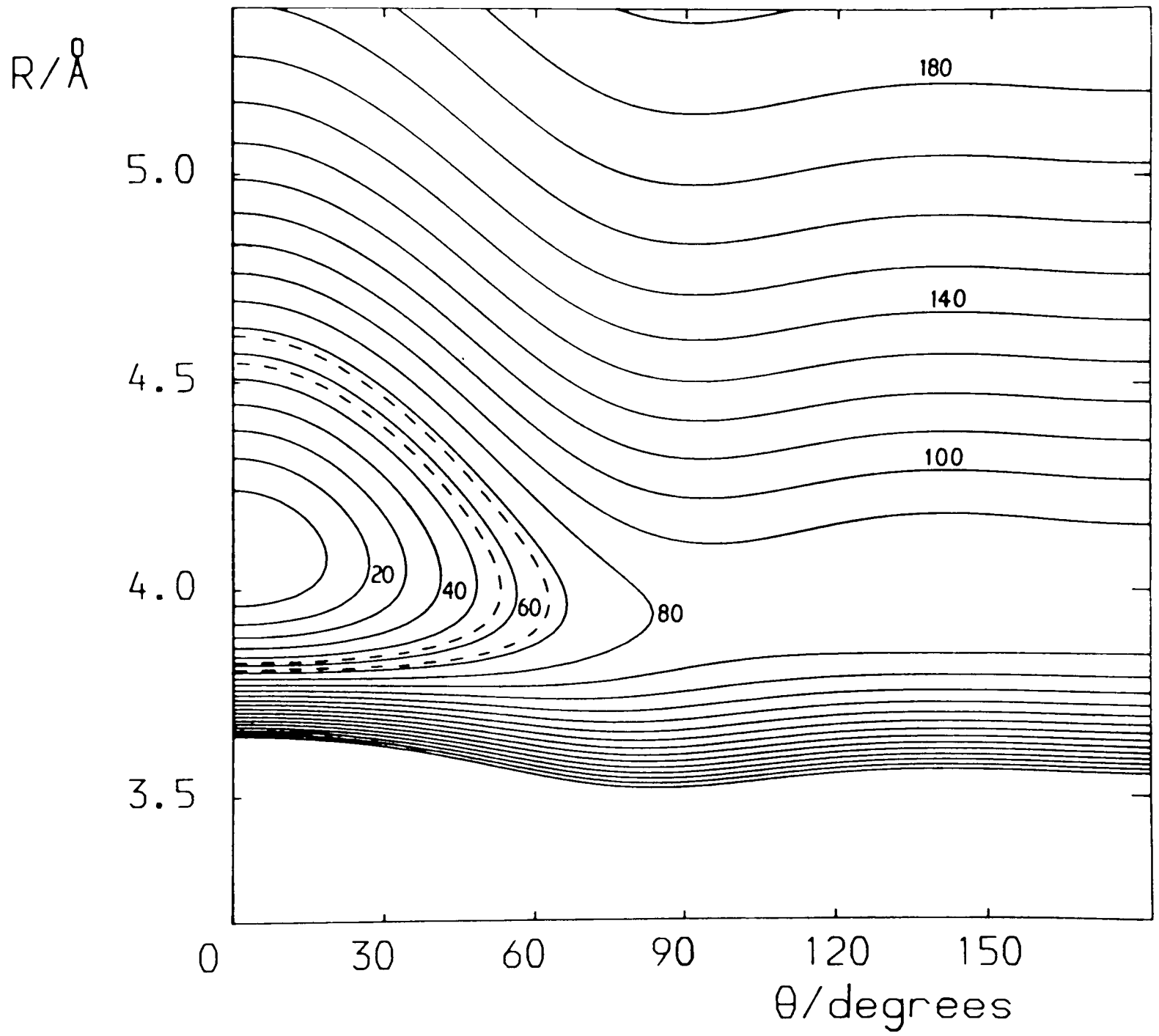
R/Å
5.0
4.5
4.0
3.5
180
140
100
80
60
40
20
0
30
60
90
120
150
θ/degrees

expected from long range behaviour. This is largely an artefact of the parameterisation of the potential. In the well region high P_n anisotropies may well contribute to the curvature, and the large P_2 coefficient is probably an attempt to compensate for these missing higher order terms. Since only about eight pieces of information are characterising the potential, there is insufficient data from the MBER experiments alone to determine these contributions.

(b) ArHBr

A similar set of potential surfaces was derived for the ArHBr data, and the results for the 4 - angle and HWK potentials are shown in tables 7.1 and 7.2. The HWK parameterisation was unable to fit the data successfully and a χ^2 of 74 was obtained with a similar minimum at $\theta = 180°$ to the KrHCl case[23]. Higher order Legendre terms are clearly required for this surface. The 4 - angle potential gave a much better fit, with a χ^2 of 16.84. No correlation coefficient was greater than 0.8, (18 data points). The isotope effect in D_J is not reproduced well suggesting a variation of wall parameter, M, with angle. However, in view of the correlation found between the wall parameters and the isotropic well depth in KrHCl (Appendix D.3), such a variation will require an experimental value of ε_{iso}. Also as the size of the halogen species increases, it might be expected that more Legendre (or angular) terms would be required to model the short range repulsive forces successfully. The 4 - angle surface therefore probably represents the most reasonable surface from the limited data available. It is expected that the shape of the well near the minimum is well determined by the molecular beam data (see figure 7.4). Again, other data are required to obtain information on other regions of the potential surface, and a fit using the 'dimensionless standard deviation' concept of Le Roy[24] is clearly required for both complexes.

Figure 7.4 *4-angle potential for ArHBr. Contours are at 10 cm^{-1}. The ArDBr motion is smaller than that of ArHBr, and the classically accessible regions are shown for them by dashed contours.*

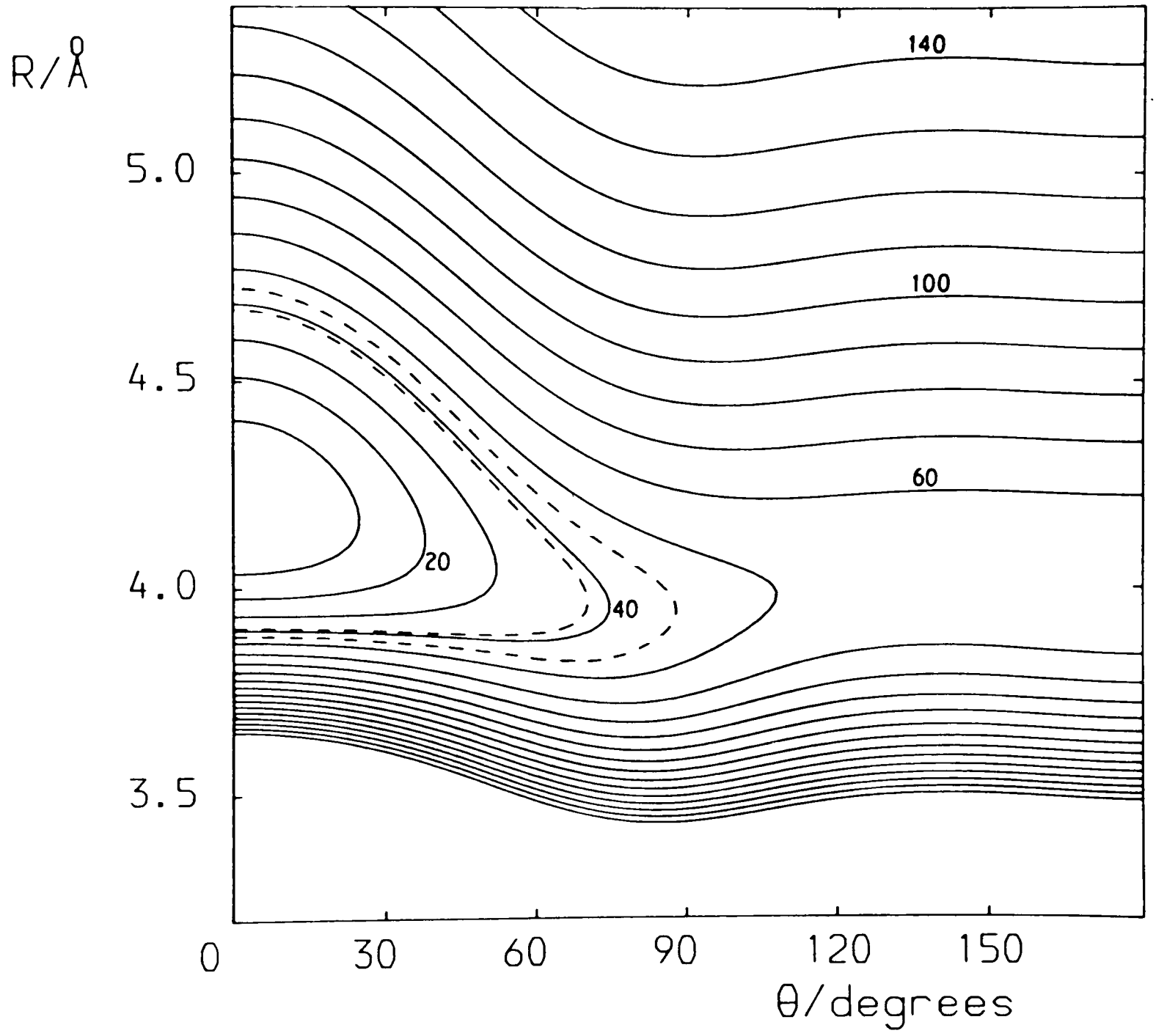
R/Å
5.0
4.5
4.0
3.5
140
100
60
20
40
0
30
60
90
120
150
θ/degrees

(c) The X...HCl series.

The potential parameters resulting from fits to the XHCl series data are shown in table 7.4, and the surfaces illustrated in figure 7.5. The number of variable parameters has been cut down for the surfaces for neon and xenon in view of the lack of data and they should be regarded as less reliable than the krypton and argon surfaces.

The surfaces in figure 7.5 show clearly the decrease in bending amplitude on going from neon to xenon - HCl. The neon surface suggests virtually unhindered rotation of the HCl subunit, but further data (NeHCl) may well restrict this, since the determining feature is the difference in the $P_2(\cos\theta)$ value for the two NeDCl isotopes which is small. The values of R_e follow a similar trend to that discussed in chapter 5 since they are determined by the rotational constant data. $f(<\cos^2\theta>)$ may be obtained from the Coriolis contribution to the rotational constant and provides the curve shown in chapter 5. One interesting feature of the argon and krypton surfaces is that the difference in R_e values for $R_e(\theta = 0°)$ and $R_e(\theta = 60°)$ is virtually the same (the distance for $R_e(\theta = 0°)$ is larger because of the intrusion of the hydrogen). This difference might have been expected to be approximately constant for the series with the same hydrogen halide. This observation has been used in fixing the $R_e(\theta = 60°)$ values in NeDCl and XeHCl potential surface fits.

In fitting the dipole moment data $(<P_1(\cos\theta)>)$, the values obtained from the optimised surfaces are consistently lower than the $<P_1(\cos\theta)>$ value derived from the experimental dipole moment corrected for induced moments (80% of χ^2 for the KrHCl 4 - angle fit comes from the these discrepancies). This suggests that the effects of charge transfer are being observed, but they are not well determined within the errors in the fitting program.

Several workers have attempted to produce an analogue of the law of

Figure 7.5 4-angle potentials for the XHCl series where X = Ne, Ar, Kr, Xe. Contours are at 10 cm^{-1} intervals above the minimum and the parameters for the surfaces are given in table 7.4. The extent of H and D motions are shown by dashed contours.

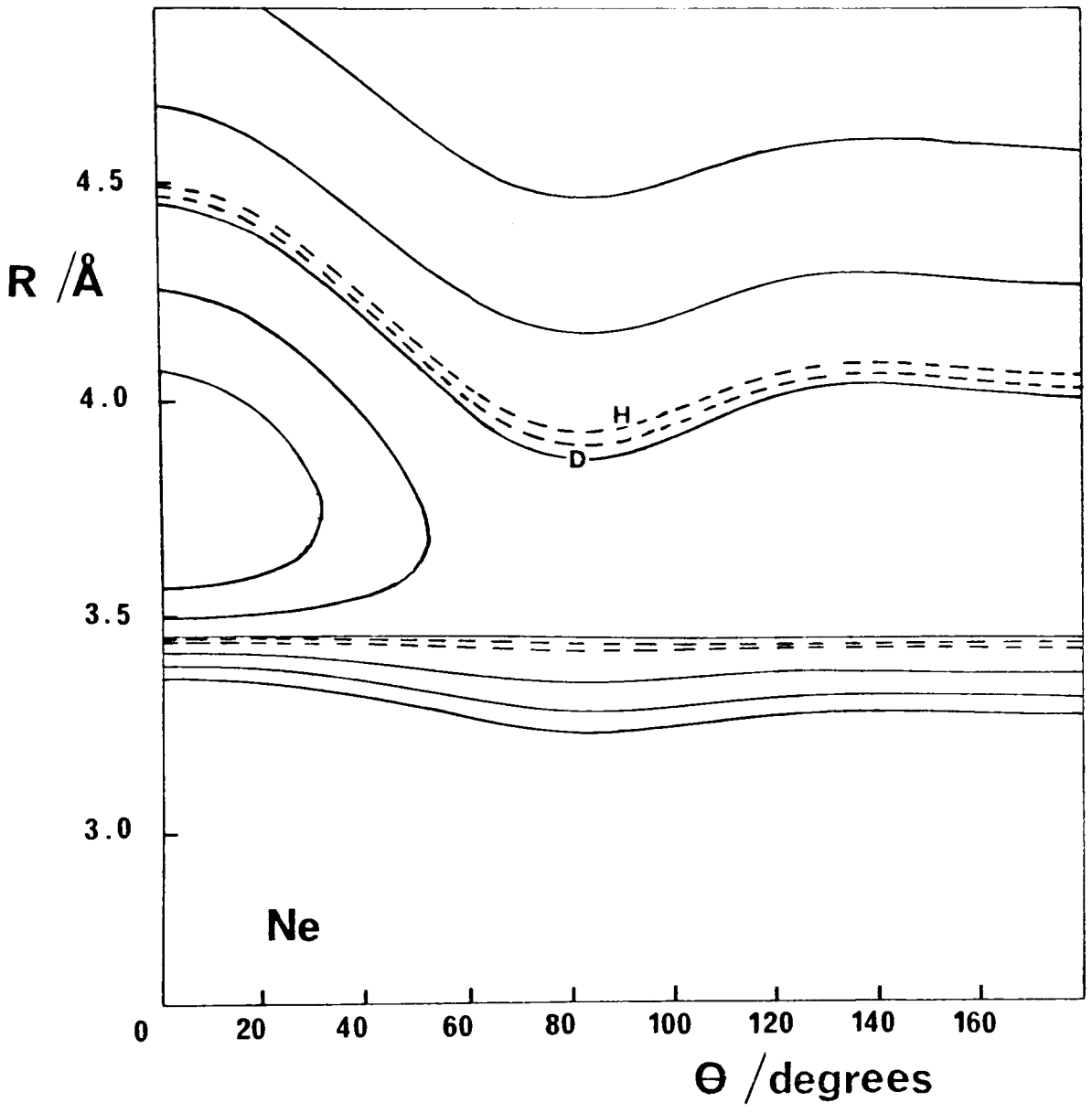
R /Å
4.5
4.0
3.5
3.0
H
D
Ne
0
20
40
60
80
100
120
140
160
Θ /degrees

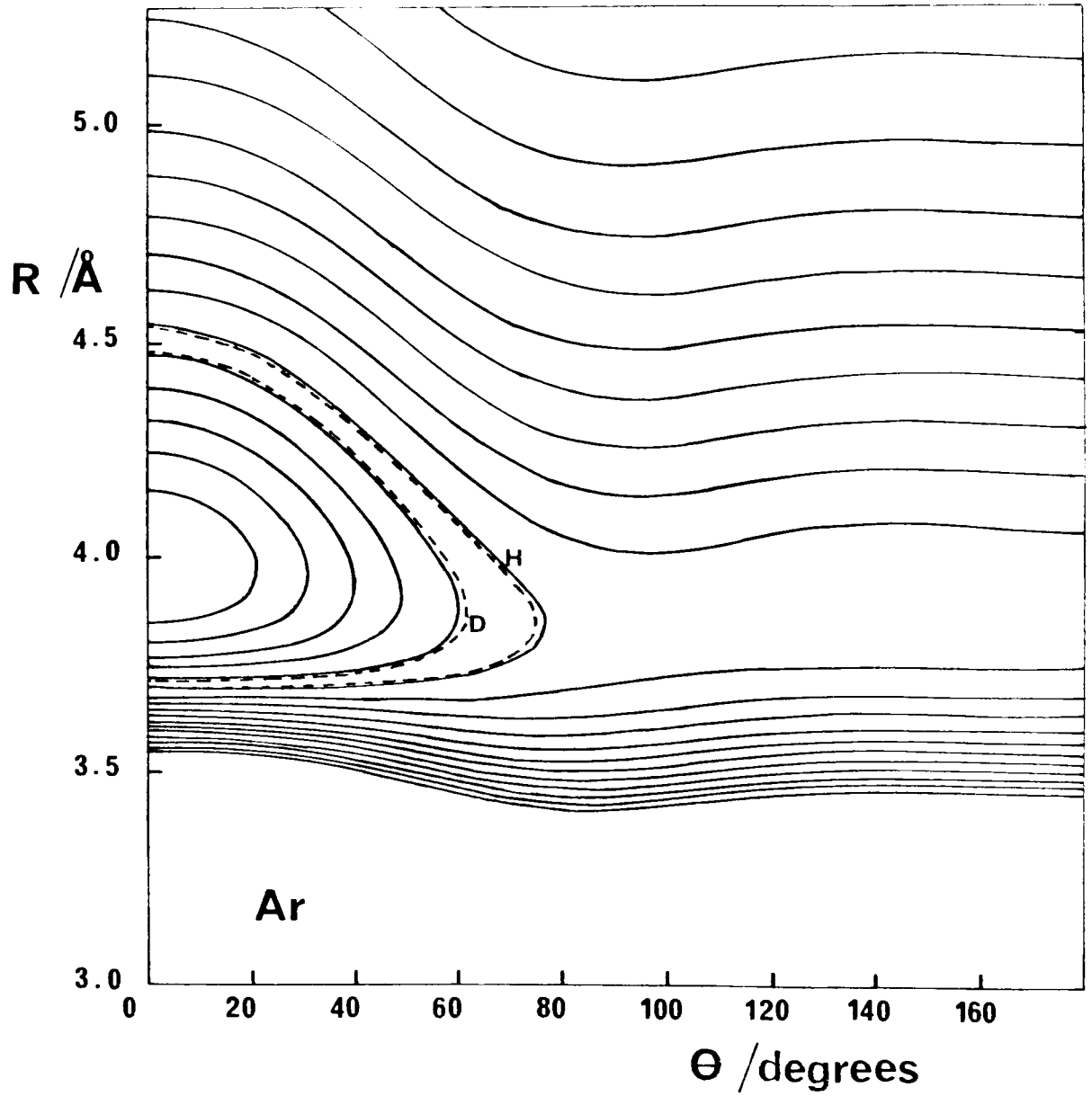
R /Å
5.0
4.5
4.0
3.5
3.0
H
D
Ar
0
20
40
60
80
100
120
140
160
Θ /degrees

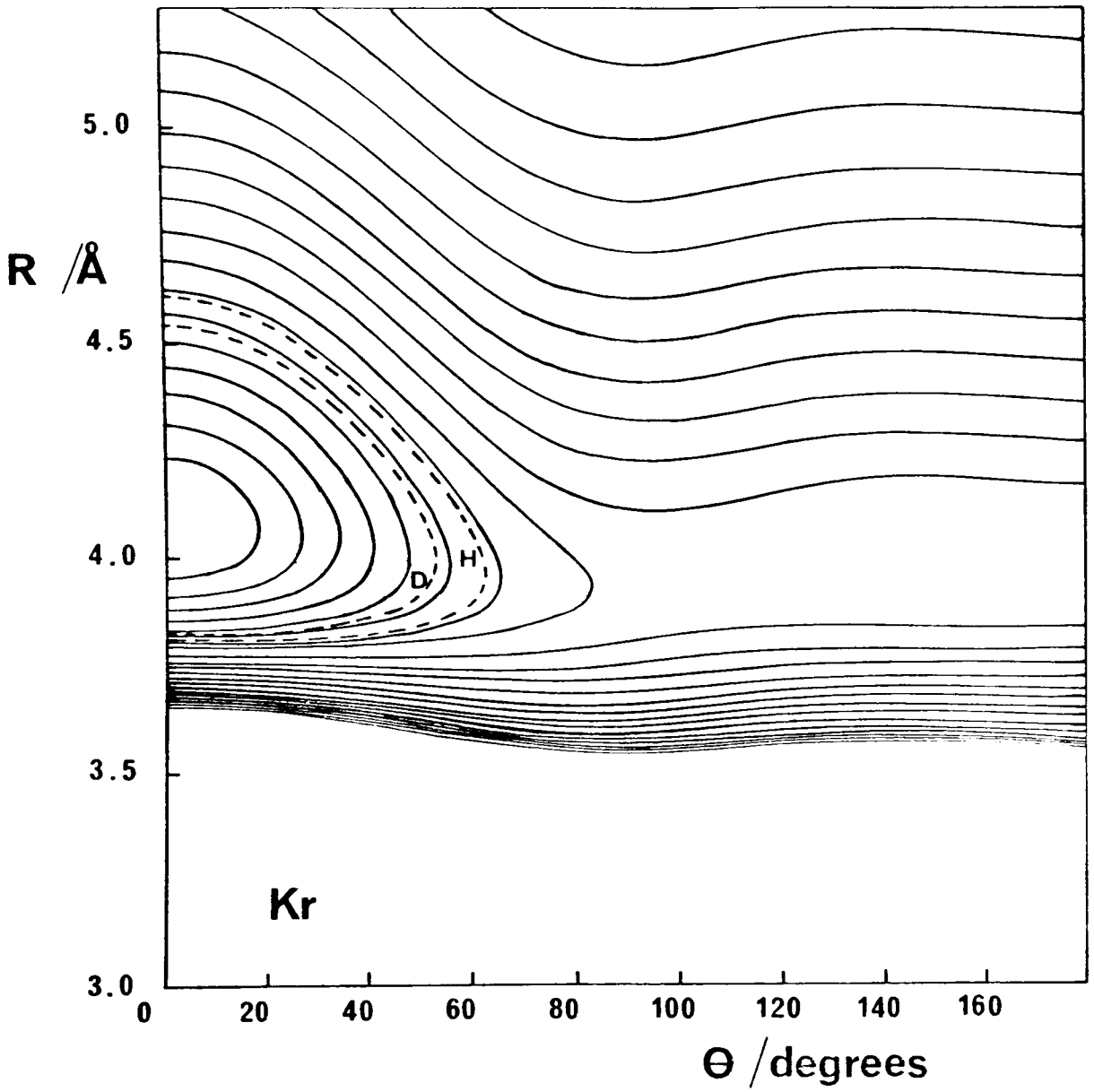
5.0
R /Å
4.5
4.0
3.5
3.0
D
H
Kr
0
20
40
60
80
100
120
140
160
Θ /degrees

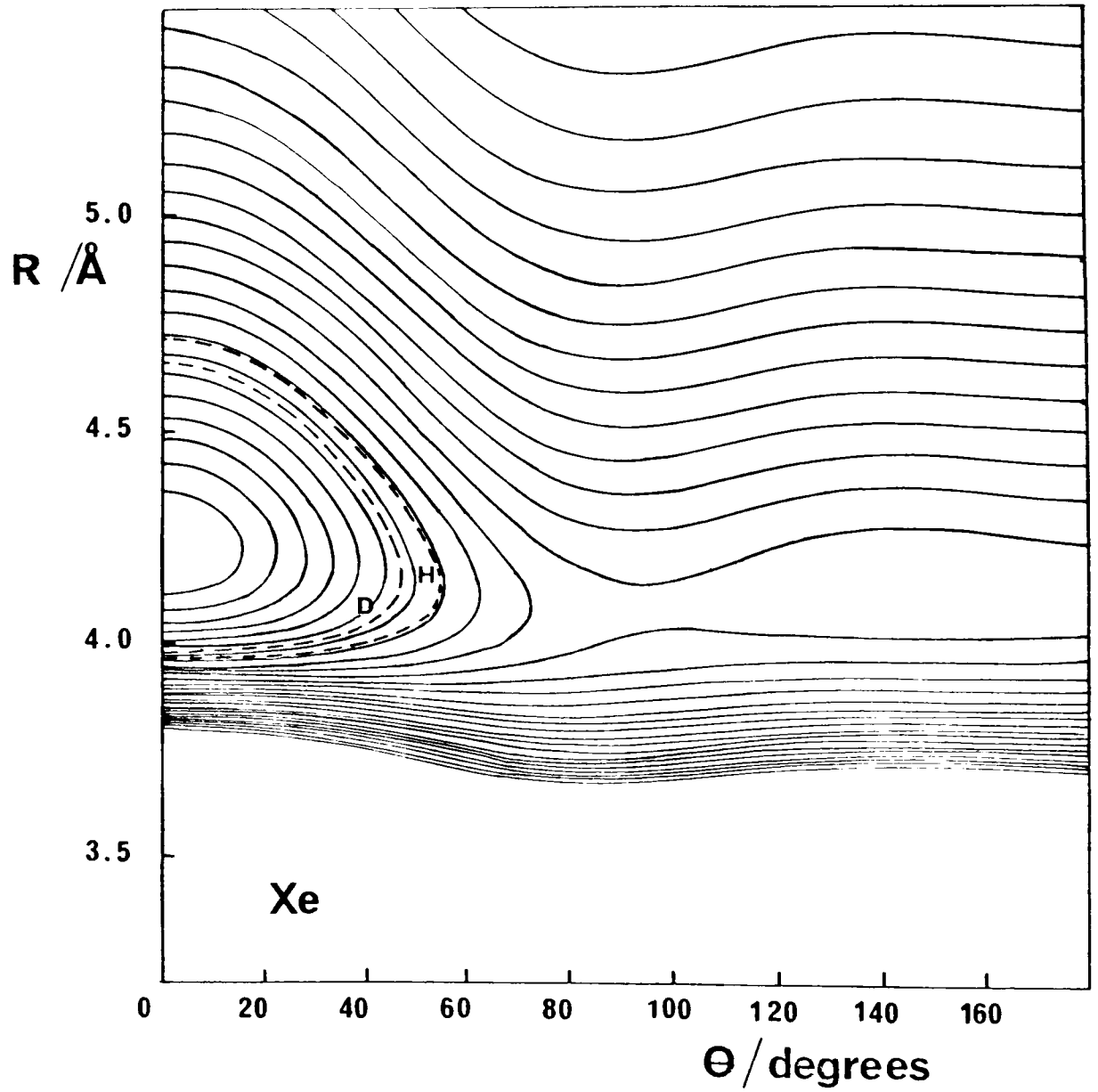
5.0
R /Å
4.5
4.0
3.5
H
D
Xe
0
20
40
60
80
100
120
140
160
Θ/degrees

corresponding states for simple gases[25], for the XHCl series. Kircz[26] and van Aalst[27] both fitted potential surfaces from rotational line broadening data of HCl. Their form of potential was a simple isotropic potential, usually Lennard-Jones (12-6), expanded as a Legendre series

$$V(R;\theta) = V_0^R(r)\left[1 + P_1 R P_1(\cos\theta) + P_2 R P_2(\cos\theta)\right] + V_0^A(r)\left[1 + P_1 A (d/r) P_1(\cos\theta) + P_2 A P_2(\cos\theta)\right] \quad (7.25)$$

where $V_0^R(r) + V_0^A(r)$ is the isotropic potential, $d = r_{min}$, and $P_X A$, $P_X R$ are multipicative strength parameters. Both authors scaled the line broadening data of XHCl to ArHCl by using the relationships

$$\sigma_{ij} = \tfrac{1}{2}(\sigma_{ii} + \sigma_{jj}) \quad (7.26)$$

and

$$\varepsilon_{ij} = (\varepsilon_{ii}\varepsilon_{jj})^{\frac{1}{2}} \quad (7.27)$$

or using equation 7.23 with 7.26. Kircz found that using equation 7.23 gave superior results to equation 7.27, but both were outside error limits for the computed line broadening cross-sections. However the potentials are not very accurate and do not agree with the MBER potentials. Kircz's K potential (a Lennard-Jones form of equation 7.25)[26] predicts a <u>negative</u> value for D_{P_2} for both KrHCl and KrDCl, while van Aalst's modified Neilsen-Gordon potential predicts <u>negative</u> values for $\langle P_2(\cos\theta)\rangle$. This is because the line broadening data is sensitive to the long range part of the potential for the broadening of low j-state transitions, and to the repulsive wall for high j-state transitions. The data appears insensitive to the anisotropy of the well minimum. Le Roy has also shown that an anisotropic potential expansion such as that given in equation 7.25 is to be avoided as large correlations between parameters can occur[24].

In view of the uncertainties in the absolute well depths, and the magnitudes of P_1 and P_2 terms, trends in the fitted potential surfaces may not be quantitatively meaningful. In table 7.4, however, the trends of $V(\theta)/\varepsilon_{iso}$ are shown against R_e/σ, where σ is the ArX interatomic

Table 7.4 X...HCl 4-angle potentials (X = Ne, Ar, Kr, Xe)

X/	Ne	Ar	Kr	Xe
$\varepsilon(\theta=0°)/cm^{-1}$	71.83(68)	186.79(34)	224.22(53)	278.23(1.55)
$\varepsilon(\theta=60°)/cm^{-1}$	55.19(1.03)	136.95(47)	160.16(1.18)	192.00
ε/cm^{-1} [1]	47.00	123.51	142.72	178.42
$R_e(\theta=0°)/Å$	3.768(7)	3.983(2)	4.086(3)	4.247(2)
$R_e/Å$ [2]	3.663	3.877(2)	3.979(6)	4.136
M	11.0	12.34(11)	13.25(32)	14.5
γ	8.0	10.0	10.0	10.0
P_1(calc)	0.416	0.654	0.731	0.785
% ind. moment	2	11	15	20
$\Delta R/Å$	—	0.106(3)	0.107(6)	—
$\varepsilon_{iso}/cm^{-1}$	52.0	133.0	155.0	190.0
R_e/σ	1.10	1.06	1.05	1.04
$\varepsilon(\theta=0°)/\varepsilon_{iso}$	1.38	1.40	1.45	1.42
$\varepsilon(\theta=60°)/\varepsilon_{iso}$	1.06	1.03	1.03	1.01

[1] for θ = 120°, 180°.
[2] for θ = 60°, 120°, 180°.

separation[22]. A smooth variation in the $V(\theta = 60°)$ series is seen but not for the $V(\theta = 0°)$ data. In the R_e/σ values overlap of orbitals is seen to be dominating over the expected increase due to the decreasing value of θ (Ne to Xe), and hence lengthening of the bond due to the intrusion of the hydrogen.

Boom[29] has recently begun to analyse the far infrared spectrum of X...HCl (X = Ar, Kr, Xe) in terms of excitation of the angular bending mode (hindered internal rotations). From a consideration of the $P_1(\cos\theta)$ anisotropic potential he obtained well depths of 60, 80, and 100 cm^{-1} for Ar, Kr, and XeHCl respectively. He also indicated that the V_2 contribution is not sufficiently large to sustain a $\theta = 180°$ minimum. The corresponding well depths from MBER data are respectively ~ 65, 80 and

105 cm^{-1}, in very good agreement with the far infrared data (the potential is plateau-like for $\theta > \sim 80°$ for the MBER potentials). The MBER angular potential surfaces should be considered reliable in view of the extent of angular motion in the complexes.

These two techniques (MBER and line broadening) seem to produce data which is sensitive to complementary parts of the potential surface. A combined fitting of the data is beyond the scope of this thesis, however.

B. Diatom - diatom complexes

In these remaining sections the BOARS/CBO approach[1,2] is extended to diatom-diatom complexes. The number of internal variables is doubled to four, viz., R,θ becomes R,θ_1,θ_2,ϕ, where ϕ is a dihedral angle. It will be shown that the extra degrees of freedom cause a considerable increase in the required computing time. The form of the potential surface that is used is based on previous literature findings on the nature of the interaction, and is discussed below.

7.5 The hydrogen fluoride dimer

Hydrogen bonding is a widely studied interaction both experimentally and theoretically[30]. Much of the information about the nature of the binding is obscured, however, because the majority of studies occur in condensed phases, where solvent and lattice effects also exist. In the gas phase relatively few studies exist, for example work by Klemperer[31], Muenter[32], and Millen[33], but these are largely restricted to structural interpretation and harmonic force constant analyses. More information is available for $(HF)_2$, however.

The microwave and radiofrequency spectrum of $(HF)_2$ was obtained by Dyke *et. al.*[34]. They found that the complex was an asymmetric rotor with a tunnelling motion between the two equivalent hydrogen bonding structures (see figure 7.6). More detailed spectral information on the

$K_a = 0$ and $K_a = 1$ states has recently been obtained[35], and this data will be used to fit a potential energy surface. A non-linear hydrogen bond is also suggested[35] from a crude interpretation of the data.

Smith has obtained an estimate of the dissociation energy of the dimer (6 ± 1 kcal mol^{-1}) from the temperature dependence of the infrared spectrum[36], although this estimate may well be too high, an observation which has been made for atom-diatom complexes[37] from their infrared spectra[38] (see chapter 6). Analysis of rotational structure, however, has not yielded results that agree with the microwave data[39].

Many *ab initio* studies have been undertaken. Most of the early studies concentrated on finding the equilibrium structure of the complex and the binding energy. A list of some of these studies is given by Pople[40]. Many of these studies also assumed a linear hydrogen bond for the complex, for example[41], but full geometry optimisation for even small basis sets showed the presence of a non-linear hydrogen bond[42]. However, the range of equilibrium geometries is high (θ_1: $30 - 80°$; θ_2: $0 - 30°$; $R \sim 2.5 - 2.8$ Å), as is the range of dissociation energies (about $3 - 8$ kcal mol^{-1}). This is the outcome of not using Hartree-Fock quality wavefunctions and this results in basis set superposition errors occurring[43]. Van Duijneveldt has shown that the range of values given above may be reduced significantly by a careful consideration of these errors[44]. The effects of electron correlation are also not insignificant[45].

The binding energy decomposition analysis of Morokuma[46] has found that the multipole (electrostatic) contribution dominates for $(HF)_2$ over exchange and charge transfer effects and is largely responsible for the equilibrium geometry of the complex[47]. Other workers have found similar effects with other high quality basis sets[48].

Several potential energy surfaces have been derived from fits to these *ab initio* calculations. Around fifty points are required on a surface for the simplest characterisation, but the inclusion of more

points is often prohibitively expensive for calculations with larger basis sets. Yarkony and co-workers mapped out a surface for a (9s5p1d/4s1p) basis set, and fitted the points to several simple surfaces[49]. These *ab initio* calculations have subsequently been used by other workers for liquid phase studies[50] and vibrational relaxation studies[51]. Both sets of studies have indicated that calculated quantities from the fitted surfaces agree tolerably well with experiment. Other surfaces have been derived from different sets of calculations[52]. Results of a large basis set calculation have been reported recently by Lischka[53].

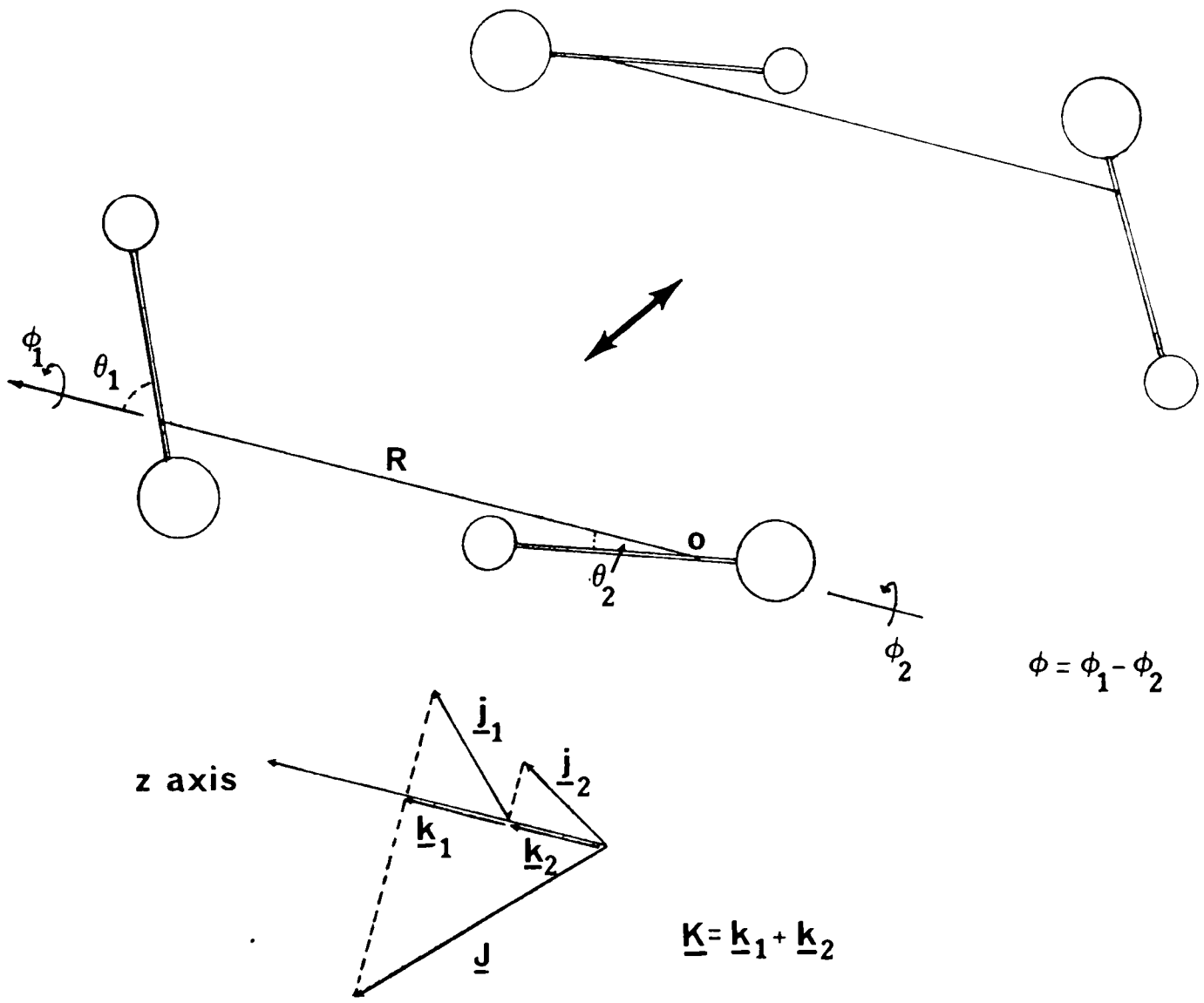

Figure 7.6 Coordinate and vector coupling scheme for $(HF)_2$. Both tunnelling species are shown. $\phi = \phi_1 - \phi_2$ is equal to π for the planar structure shown by definition. o is the centre of mass of the HF diatomic molecule. $\underline{j}_1$ and $\underline{j}_2$ are vectors in the molecule fixed axis system whose origin is at the centre of mass of the complex.

As a starting point for the $(HF)_2$ potential energy surface, the surface of Alexander and DePristo derived from Yarkony's data will be used[54]. Alexander used the potential surface for the study of rotational inelastic scattering[55].

7.6 Method (BOARS level)

The solution of the dynamics of $(HF)_2$ follows a similar path to the atom-diatom case. The Hamiltonian for the diatom-diatom complex is written in body-fixed axes, with the stretching frequency of the diatom factored off. It takes the form:

$$H = -\frac{\hbar^2}{2\mu}\left[\frac{\partial^2}{\partial R^2} + \frac{(J - j_1 - j_2)^2}{R^2}\right] + b_1 j_1^2 + b_2 j_2^2 + V(R,\theta_1,\theta_2,\phi) \qquad (7.28)$$

where $b_1 = b_2 \equiv b_{HF}$, the rotational constant of the ground vibrational state of HF; $J - j_1 - j_2$ represents the end-over-end rotational angular momentum of the complex, j_1 and j_2 representing the angular momentum of the HF subunits with respect to the molecular axis system. The definitions of R, θ_1, and θ_2 are given in figure 7.6; $\phi = \phi_1 - \phi_2$ and is the dihedral angle between the two diatomic molecules. Equation 7.28 may be expanded and rewritten as

$$H = -\frac{\hbar^2}{2\mu R^2}\frac{\partial^2}{\partial R^2} + \frac{\hbar^2}{2\mu R^2}J^2 + b(R)(j_1^2 + j_2^2) + V(R,\theta_1,\theta_2,\phi) - \frac{\hbar^2}{\mu R^2}(J.j_1 + J.j_2) + \frac{\hbar^2}{\mu R^2}j_1.j_2 \qquad (7.29)$$

where $b(R) = b_{HF} + \frac{\hbar^2}{2\mu R^2}$. The only good quantum number is the total angular momentum J, but the projection of J on the *a* axis ($\simeq$ the z axis), K, is also nearly conserved. Again as in the atom-diatom case solutions to the bending potential at fixed R are sought, for a rotationless complex, using a Born-Oppenheimer type product wavefunction. The

Schrödinger equation is then solved for the stretching motion and the remaining non-adiabatic and other terms are added by perturbation theory.

A more complex bending wavefunction is considered in this case than for ArHCl. In order to reduce the size of the bending matrix to be diagonalised the tunnelling motion of the complex is considered. The bending Hamiltonian is given by

$$H_b = b(R)(j_1^2 + j_2^2) + V(\theta_1,\theta_2,\phi;R) + \frac{\hbar^2}{2\mu R^2}\left[2j_{1z}j_{2z} + j_{1+}j_{2-} + j_{1-}j_{2+} - (j_{1z} + j_{2z})^2\right] \quad (7.30)$$

where $J_z = j_{1z} + j_{2z} \equiv$ angular momentum along the z axis. The z component of the Coriolis coupling term has been added to H_b in a similar manner to the atom-diatom case. In a similar manner to section A of this chapter the wavefunction can be written as a product of spherical harmonics

$$\Phi_b^K(\theta_1,\theta_2,\phi;R) = \sum_j c_{bj}^K(R) Y_{j_1k_1}(\theta_1\phi_1) Y_{j_2k_2}(\theta_2\phi_2) D^{J*}_{MK}(\alpha\beta\gamma) \quad (7.31)$$

where $k_1 + k_2 = K$, by conservation of angular momentum. However, the symmetry under the tunnelling motion can be included to reduce the number of basis functions required in the problem. Dyke[34] has shown that a proper consideration of the permutation-inversion group symmetry of $(HF)_2$[56] leads to the approximate identification of the tunnelling motion with P^*_{12}, the permutation-inversion operator. Under this operator

$$Y_{jk}(\theta,\phi) \xrightarrow{P^*_{12}} Y_{jk}(\pi - \theta,\phi) = (-1)^{j-k} Y_{jk}(\theta,\phi) \quad (7.32)$$

and

$$D^{J*}_{MK}(\alpha\beta\gamma) \xrightarrow{P^*_{12}} D^{J*}_{MK}(\alpha\beta,\pi + \gamma) = (-1)^K D^{J*}_{MK}(\alpha\beta\gamma) \quad (7.33)$$

using well-known relationships for spherical harmonics and rotation matrices[8]; so the basis set becomes

$$\Phi_b^{K\pm}(\theta_1,\theta_2,\phi;R) = N\sum_j c_{bj}^K(R)\left\{ Y_{j_1k_1}(\theta_1\phi_1)Y_{j_2k_2}(\theta_2\phi_2) \pm (-1)^{j_1+j_2}Y_{j_2k_2}(\theta_1\phi_1)Y_{j_1k_1}(\theta_2\phi_2)\right\} D^{J*}_{MK}(\alpha\beta\gamma) \qquad (7.34)$$

since $K = k_1 + k_2$. N is a normalisation constant and is set equal to $1/\sqrt{2}$. $D^{J*}_{MK}(\alpha\beta\gamma)$ is the rotation matrix which approximately describes the rotation of $(HF)_2$ which is a near prolate top. The ± signs represent the symmetry of the wavefunction under P^*_{12} and hence under tunnelling in an analogous way to the case of ammonia inversion. The sum over j represents a more complicated summation over j_1, j_2 and k than in the case of ArHCl[12]. The bending Hamiltonian is solved independently for each value of K. For each value of K, $k_1 + k_2 = K$, and k_1 is set to run from K/2 if k_1 is even, K if odd, to infinity, k_2 decreasing from $K - k_1$. For each of these values the corresponding j_1 must be greater than or equal to k_1. If $j_1 = j_2$ and $k_1 = k_2$ then the negative tunnelling state does not exist and the wavefunction for the positive state reverts to a product of spherical harmonics. There are two different states for $j_1 \neq j_2$ and/or $k_1 \neq k_2$. The Hamiltonian matrix is block diagonalised by k_1 values, but off-diagonal elements occur between these blocks because of the functional form of the multipole parameterisation for the attractive potential. The remaining matrix elements are given in Appendix D.4 for the angular momentum operators, $j_{1,2}$, and the potential form used is discussed below.

The method then consists of solving the equation

$$H_b\Phi_b^{K\pm} = U_b^{K\pm}\Phi_b^{K\pm} \qquad (7.35)$$

at several values of R which gives a family of effective potentials for the radial motion $U_b^{K\pm}(R)$. The zeroth-order wavefunction is given by

$$\psi^{(0)\pm}_{vbK} = \Phi_b^{K\pm}(\theta_1,\theta_2,\phi;R)\chi_{vb}^{K\pm}(R) \qquad (7.36)$$

and following the atom-diatom procedure an upper bound to the energy may

be obtained by solving the radial equation[9] for the zeroth-order energy $E^{(0)}$

$$\left[-\frac{\hbar^2}{2\mu}\frac{\partial^2}{\partial R^2} + U(R) + \tau(R) \right] \chi(R) = E^{(0)} \chi(R) \qquad (7.37)$$

dropping all sub- and super-scripts. $\tau(R)$ is again the diagonal adiabatic correction term, and is given by

$$\tau(R) = -\frac{\hbar^2}{2\mu} \int \Phi_b^{K\pm *} \left(\frac{\partial^2}{\partial R^2} \right) \Phi_b^{K\pm} d\Omega = \frac{\hbar^2}{2\mu} \sum_j \left(\dot{c}_{bj}^{K\pm}(R) \right)^2 \qquad (7.38)$$

where Ω represents an integration over θ_1, θ_2 and ϕ. The first radial derivatives of the coefficients are therefore required for $\tau(R)$. The use of a matrix inversion method[1] will be expensive in view of the large number of basis functions required, and numerical differentiation is used. The method of the gradient of the potential is useful for determining the radial derivatives when the form of the potential is simple[2,3].

The effect of the Hamiltonian in equation 7.29 on the ground state zeroth-order wavefunction is then

$$H\psi^{(0)} = \left[E^{(0)} + H_{ROT} - \frac{\hbar^2}{2\mu R^2} \left\{ J_+ (j_{1+} + j_{2+}) + J_- (j_{1-} + j_{2-}) \right\} + H_{NA} \right] \psi^{(0)} \qquad (7.39)$$

where
$$H_{ROT} = \frac{\hbar^2}{2\mu R^2} J^2 \qquad (7.40)$$

and

$$\int \Phi_{b'}^{K',\pm *} H_{NA} \Phi_b^{K\pm} d\Omega = -\frac{\hbar^2}{2\mu} \delta_{KK'} (1 - \delta_{bb'}) \left[\int \Phi_{b'}^{K',\pm *} \frac{\partial^2}{\partial R^2} \Phi_b^{K\pm} d\Omega + \left(2 \int \Phi_{b'}^{K',\pm *} \frac{\partial}{\partial R} \Phi_b^{K\pm} d\Omega \right) \frac{\partial}{\partial R} \right] \qquad (7.41)$$

The Coriolis part of the Hamiltonian is given by

$$H_{COR} = -\frac{\hbar^2}{2\mu R^2} \left[J_+ (j_{1+} + j_{2+}) + J_- (j_{1-} + j_{2-}) \right] \qquad (7.42)$$

H_{ROT} is included in equation 7.37 and provides a centrifugal barrier

$\hbar^2 J(J+1)/2\mu R^2$ for the radial potential. The equation is then solved for various values of J (0 to 10), and B, D_J and $E^{(0)}$ are derived from a least-squares fit to the eigenvalues. This gives a zeroth-order B value. No terms in the perturbation Hamiltonian ($H_{ROT} + H_{NA} + H_{COR}$) mix + and - tunnelling states. The Coriolis Hamiltonian operates on a general wavefunction as follows

$$J_-(j_{1-} + j_{2-}) Y_{j_1 k_1} Y_{j_2 k_2} D^{J*}_{MK} = \left[J(J+1) - K(K-1)\right]^{\frac{1}{2}}$$

$$\times \left\{ \left[j_1(j_1+1) - k_1(k_1-1) \right]^{\frac{1}{2}} Y_{j_1 k_1 - 1} Y_{j_2 k_2} \right.$$

$$\left. + \left[j_2(j_2+1) - k_2(k_2-1) \right]^{\frac{1}{2}} Y_{j_1 k_1} Y_{j_2 k_2 - 1} \right\} D^{J*}_{M(K-1)} \qquad (7.43)$$

where the (θ_1,ϕ_1), (θ_2,ϕ_2), and $(\alpha\beta\gamma)$ dependences have been omitted. Eigenvectors of the two interacting K states must again be stored as in the case of the atom-diatom complex.

Expectation values of $P_n(\cos\theta_1) + P_n(\cos\theta_2)$, where n = 1,2, as a function of R are also calculated when U(R) is calculated and zeroth-order values then obtained by integration over the R coordinate.

It is also necessary to mention the intermolecular potential function here since it must be invariant to the PI (permutation-inversion) group operations. The potential may be expanded as a series of products of spherical harmonics which form a complete set[34]. In a similar manner to the treatment of the tunnelling wavefunction the most general potential $V(\theta_1\theta_2\phi R)$ is given by

$$V = \sum_{l' \le l} \sum_{m} V_{ll'm}(R) \left\{ \left[C_{lm}(\theta_1\phi_1) C_{l'-m}(\theta_2\phi_2) + C_{l-m}(\theta_1\phi_1) C_{l'm}(\theta_2\phi_2) \right] \right.$$

$$\left. + (-1)^{l'-l} \left[C_{l'm}(\theta_1\phi_1) C_{l-m}(\theta_2\phi_2) + C_{l'-m}(\theta_1\phi_1) C_{lm}(\theta_2\phi_2) \right] \right\} \qquad (7.44)$$

where C_{lm} is the reduced spherical harmonic[8]

$$C_{lm}(\theta\phi) = \left(\frac{4\pi}{2l+1}\right)^{\frac{1}{2}} Y_{lm}(\theta\phi) \qquad (7.45)$$

7.7 Spectroscopic parameters

In order to obtain sufficient convergence of the calculated quantities, a brief review of the spectroscopic parameters derivable for $(HF)_2$ must be mentioned, since it is slightly different from the available atom-diatom information.

For $(HF)_2$ information about excited K states has been derived[35]. The energy levels of the K = 0 states are accurately represented by the equation

$$E_o^{\pm} = \left(\frac{B+C}{2}\right)_o J(J+1) - D_J J^2(J+1)^2 \mp \tfrac{1}{2}\left[\nu_o + \delta_o J(J+1)\right] \qquad (7.46)$$

and the excited K states by the expression

$$E_K^{\pm} = \left(\frac{B+C}{2}\right)_K \left[J(J+1) - K^2\right] - D_J\left[J(J+1) - K^2\right]^2 \mp \tfrac{1}{2}\left\{\nu_K + \delta_K\left[J(J+1) - K^2\right]\right\} \qquad (7.47)$$

where ν represents a tunnelling frequency. The δ parameters represent the J dependence of the tunnelling frequencies, or alternatively, the difference in rotational constants in the two tunnelling states. δ is small compared with the tunnelling frequency. $\frac{1}{2}(B+C)$ and D_J represent the observed rotational constant of the near-prolate top and its centrifugal distortion parameter. Separate $\bar{B}$, ν, and D_J values for each K state have been defined since the structural distortion upon changing the angular momentum K about the *a* inertial axis is not negligible[57], see below.

To equation 7.47 must be added the effects of asymmetry doubling which is given by

$$\Delta E^{\pm} = \pm\left[\left(\frac{B-C}{4}\right)^{\pm} J(J+1) + 1J^2(J+1)^2\right] \qquad (7.48)$$

The resultant spectroscopic parameters for $(HF)_2$ are given in table 7.6.

The difference in dipole moments indicates that significant centrifugal distortion does occur: $\mu_a^{K=0} = 2.98863(10)$ D, and $\mu_a^{K=1} = 2.83684(20)$ D. Thus although $P_2(\cos\theta)$ and D_{P_2} data do not exist for $(HF)_2$ because of the absence of analysed nuclear hyperfine structure, significant information on the magnitude of bending and stretching modes exists because of the observation of the K = 1 state. However, in a similar manner to the atom-diatom surfaces the dipole moment data does provide limited information on the geometry of the complex. The contribution to the dipole moment from the induced moment is fairly constant over reasonable estimates for the angles θ_1 and θ_2 (45 - 65°, and 0 - 20° respectively) and is about 0.30 ± 0.05 Debyes. This yields a value for $\langle P_1(\cos\theta_1)+P_1(\cos\theta_2)\rangle$ of ~ 1.47(3). The constancy of $\mu_{induced}$ with respect to angular changes also suggests that $\Delta\mu$ (K=0 - K=1) is due almost entirely to angle changes on excitation. In a semi-rigid model excitation of K produces θ_1 and θ_2 angle increases of ~ 5° and $\Delta\mu_{ind} < 0.01$ Debyes. If this dipole moment data is combined with tunnelling frequencies, the barrier height and tunnelling path for inversion will be determined fairly precisely. The centrifugal distortion of the dipole moment will provide an estimate of the bending force constants, and D_J of stretching effects, and D_{JK} $(\equiv \frac{1}{2}(B+C)^{K=0} - \frac{1}{2}(B+C)^{K=1})$ will provide information on the bend-stretch coupling, in a similar manner to D_{P_2} data for atom-diatom systems. The asymmetry splitting, as measured by $\frac{1}{2}(B-C)^{\pm}$, will also depend on the geometry of the complex and the bending force constant. Thus nine pieces of information ($\bar{B}_0$, $\bar{B}_1$, D_J, $\frac{1}{2}(B-C)^{\pm}$, $\mu^{K=0}$, $\Delta\mu$, ν_0, ν_1) are used for modelling the potential.

7.8 Convergence and correction terms (CBO level)

In comparison with the well depth, the tunnelling frequency is very small, so in order to fit this parameter, a significant number of terms had to be included in the basis set. Convergence to at least 0.01 cm^{-1} was sought. For this, the value of k_1 had to be increased to 7 to

obtain convergence, and the highest corresponding value of j_1 was ~ 12 for $k_1 \simeq K$, diminishing to $j_1 = 8$ (1 'excitation') for $k_1 = 7$ [12]. This produced a matrix of dimension 391×391 to be diagonalised, and this diagonalisation is the major contributor to the computation time required for a surface. Computation of one isotope of an atom-diatom complex takes typically 10 seconds, whereas for $(HF)_2$ it takes 150 minutes of ICL 1906A time. Approximate fitting (convergence to within 0.05 cm^{-1}) using a matrix of dimension 256×256 is therefore initially undertaken (requiring around 100 minutes of time).

In the approximate fits a radial grid of 11 points was used (2.29 to 3.29 Å) and equation 7.37 solved over a smooth radial function obtained by cubic spline interpolation over 1000 points. Extension of the grid to 49 points (2.29 - 3.49 Å) which allowed convergence of B to 0.1 MHz, suggested that the coarse grid estimated $\bar{B}$ values to ~ 1 MHz. A smaller range of radial points is required for $(HF)_2$ than for atom-diatom potentials since the well is an order of magnitude deeper and nearly harmonic over the ground state. The zeroth-order Born-Oppenheimer wavefunction is also a much better approximation to the total wavefunction than for the atom-diatom cases, and this is shown by the absence of peaking in adiabatic and non-adiabatic correction terms as a function of R. For example $\tau(R)$ reaches a minimum of 1.9 cm^{-1}, whereas for ArDCl $\tau(R)$ has a sharp peak of height 40 cm^{-1} for a Neilsen-Gordon surface (ref.[1a], figure 3a). This small value of $\tau(R)$ for $(HF)_2$ is due to the smooth slow changes in the bending coefficients with R. Lagrange n-point interpolation formulae are used to calculate radial derivatives[58]. This provides a rapid way of calculating the many more derivatives required than for the atom-diatom case.

The expectation values of the required spectroscopic parameters and corrections to zeroth-order values are calculated using second-order perturbation theory, using the zeroth-order ground states as the basis

set. The expressions for the observables are the same as in the atom-diatom system except |vbK> is replaced throughout by |vbK±>, where only states of the same tunnelling sign may interact. One interesting term is the Coriolis correction to the ground state (K = 0) rotational constant, $\Delta\bar{B}^{\pm}_{COR}$, which is related to the asymmetry splitting parameter $\frac{1}{2}(B-C)^{\pm}$. $\Delta\bar{B}^{\pm}_{COR}$ is given by the interaction of the ground state with the K = ±1 states:

$$\Delta\bar{B}^{\pm}_{COR} J(J+1) = \sum_{v,b} \frac{|\langle \pm 000 | \hat{H}_{COR} | vb1_{+}\pm \rangle|^2}{(\varepsilon_{vb1_{+}\pm} - \varepsilon_{000\pm})} \qquad (7.49)$$

where $1_{\pm}$ is a hybrid state $2^{-\frac{1}{2}}\{|K=1\rangle \pm |K=-1\rangle\}$, and |vbK±> represents the zeroth-order ground state wavefunctions (equation 7.36). This interaction causes the asymmetry splitting (of 1_+ and 1_-) in the K = 1 stack of energy levels. The $\frac{1}{2}(B-C)^{\pm}$ term is given then by the interaction of the lowest K = 1 state with the K = 0 stack

$$\tfrac{1}{2}(B-C)^{\pm} J(J+1) = \sum_{v,b} \frac{|\langle \pm 001_{+} | \hat{H}_{COR} | vb0\pm \rangle|^2}{(\varepsilon_{001_{+}\pm} - \varepsilon_{vb0\pm})} \qquad (7.50)$$

where the J(J + 1) dependence of both sides can be cancelled. The interaction with the first few excited K = 0 or K = ±1 bending states (notably b = 2 - 4) was found to dominate the sum for both summations. For the latter summation (equation 7.50) the 1_+ state is depressed below the non-interacting state (1_-). The summation over excited bending and vibrational states is computationally expensive and so for Δb > 2, the contributions are added via theory discussed by Epstein[59], for which a general second-order correction is given by

$$E_m^{(2)} = \int \chi_m^{(0)}(R)^* \, E_m^{(2)}(R) \, \chi_m^{(0)}(R) \, dR \qquad (7.51)$$

where $$E_m^{(2)}(R) = \sum_n \frac{P_{mn}(R) P_{nm}(R)}{U_m(R) - U_n(R)}$$

and $$P_{mn}(R) = \int \Phi_m^* P \Phi_n d\Omega$$

The energy denominator is included in the integration. This approximation is obeyed well when the bending separations are large compared with the vibrational spacings. The closure approximation should lead to a slight overestimation of the interaction energy since integrals over a larger energy denominator have been replaced by a smaller (R dependent) denominator. It has been shown that this approach is also valid for slowly varying functions , $P_{nm}(R)$, and this is true for $(HF)_2$. Errors of approximately 5% are suggested[13]. It is also found that the overlap of excited vibrational wavefunctions with the ground state wavefunction is small. Also, in view of the large number of integrals to be calculated the perturbation expansion was truncated at second-order.

7.9 Results and discussion

(a) Results

The molecular beam data was used to determine the parameters for a simplified form of the Alexander potential[54]. The dominant terms in his potential function (see ref.[54], table V) were transformed to a decoupled representation given in equation 7.44 (see Appendix D.4) and used as a starting point for the optimisation. The potential function is given by

$$\begin{aligned} V(\theta_1,\theta_2,\phi,R) = {} & A_0 e^{-B_0(R-2.79)} - A_3 e^{-B_3(R-2.79)} \\ & + A_1 e^{-B_1(R-2.79)}\{\cos\theta_1 - \cos\theta_2\} \\ & + A_2 e^{-B_2(R-2.79)}\{2\cos\theta_1\cos\theta_2\} \\ & + V_{elect}(\text{dipole-dipole, dipole-quadrupole,} \\ & \quad \text{dipole-octupole, quadrupole-quadrupole}) \end{aligned} \tag{7.52}$$

The various terms are discussed below. $V_{electrostatic}$ forms the major part of the attractive portion of the potential surface. A reference distance of 2.79 Å was chosen for the potential, and the experimental values of the multipole moments were used, viz., $\mu = 1.8262$ Debyes [60],

$Q = 2.36(3)$ Buckinghams [61]. No experimental value of the octupole moment exists. Alexander[54] neglected the quadrupole-quadrupole (QDQD) and higher terms.

A single function dipole-dipole (DPDP0) term has also been added to the attractive part to model charge transfer terms. A similar cosine dependence for this term has been suggested by Allen[62]. Both this term and the monopole-dipole term contain contributions from attractive and repulsive forces.

A_3, B_1, B_2, B_3 were fixed near the Alexander potential values. This left five variable parameters: A_0, B_0, A_1, A_2, DPOC (see Appendix D.4) in the least-squares fit. For the optimisation derivatives of the potential with respect to the parameters were determined by divided differences.

The resultant potentials and their calculated spectrscopic parameters are given in tables 7.5 and 7.6. Decomposition of the contributing terms are given for the optimised potential in table 7.7. Contour plots at fixed distances (R_e) are shown in figures 7.7 and 7.8, and decomposition of the radial terms at approximately the equilibrium angles in figures 7.9 and 7.10 for the optimised potential and Alexander's potential respectively.

It may be seen that the repulsive forces are dominated by the isotropic (monopole-monopole) repulsive terms, and this is rationalised physically by the nearly spherical appearance of the HF electron density contours at the interaction distance[63]. The dipole-octupole term was not initially included in the fit, but it proved impossible to reproduce the change in dipole moment $\Delta\mu$, without it. Exclusion gave a typical value of $\Delta\mu$ of 0.06 Debyes, whereas inclusion of the DPOC term reduced the error significantly.

Table 7.5 Potential function and parameters

$$V(\theta_1\theta_2\phi R) = A_0 e^{-B_0(R-2.79)} - A_3 e^{-B_3(R-2.79)}$$
$$+ \left\{A_1 e^{-B_1(R-2.79)} - A_4 e^{-B_4(R-2.79)}\right\}\left\{\cos\theta_1 - \cos\theta_2\right\}$$
$$- \left\{A_2 e^{-B_2(R-2.79)} - A_5 e^{-B_5(R-2.79)}\right\}\left\{2\cos\theta_1\cos\theta_2\right\}^{1}$$
$$+ \left\{\left[A_6(2.79/R) - A_7\right] e^{-B_6(R-2.79)}\right\}\left\{f(\cos\theta_1\cos\theta_2)\right\}^{2}$$
$$+ V_{el}(\text{DPDP, DPQD, QDQD, DPOC})$$

	This work	Alexander		This work	Alexander
A_0	671.7(10.1) [3]	629.6	A_5	0.0	-79.08
B_0	4.04(3)	3.78	B_5	—	0.898
A_3	537.0	535.1	A_6	0.0	35.29
B_3	2.1	2.08	B_6	—	3.855
A_1	-30.0(9.0)	192.3	A_7	0.0	44.3
B_1	3.5	3.59			
A_4	0.0	224.9	DPDP [4]	773.31	767.73
B_4	—	1.49	DPQD	358.13	393.03
A_2	151.00(30)	54.07	QDQD	165.85	0.0
B_2	1.8	1.89	DPOC	79.0(6.3)	0.0

[1] This term takes the form $2\cos\theta_1\cos\theta_2 - \sin\theta_1\sin\theta_2\cos\phi$ for the Alexander potential.
[2] $f(\cos\theta_1\cos\theta_2) = \{\cos\theta_1(3\cos^2\theta_2 - 1) - \cos\theta_2(3\cos^2\theta_1 - 1)\}$; dipole-quadrupole angular dependence.
[3] Uncertainties quoted to one standard deviation.
[4] DPDP0 = DPDP1 ≡ DPDP etc. (see Appendix D.4). All A and multipole values are in cm^{-1}.

Table 7.6 Calculated and observed spectroscopic constants for $(HF)_2$

	This work	Alexander [1]	Experimental [2]
$\left(\frac{B+C}{2}\right)_0$	6494.9	6801.2	6494.963(36)
$\left(\frac{B+C}{2}\right)_1$	6532	6822	6528.907(30)
$-D_{JK}$	37. (±7)	21	33.944(47)
$D_J^{(K=1)}$	0.0595	0.0665	0.0595(1) [3]
$D_J^{(K=0)}$	0.0612	0.0662	—
$(B-C)^+$	96.2	95.5	95.2076(14)
$(B-C)^-$	91.4	94.6	91.1896(18)
l	—	—	0.002393(12)
ν_0/cm^{-1}	0.658 (±0.005)	0.393	0.658697(3)
δ_0	(-3.9)	(-3.2)	-4.033(14)
ν_1/cm^{-1}	1.068	1.362	1.0642868(4)
δ_1	(-2.5)	(-2.1)	-4.5238(10)
μ_0/Debye	2.6173 [5]	3.0472	2.9886(1)
$\Delta\mu$/Debye [6]	0.1516	0.4041	0.1518(2)
μ_{ind}/Debye [4]	0.3714	(-0.059)	—

[1] Ref.54.
[2] Ref.35.
[3] Value assumed for fitting K = 0 data also.
[4] By obs - calc.
[5] Approximately 0.60 D is due to the pseudo C.T. term.
[6] $\mu_{K=0} - \mu_{K=1}$

All values in MHz unless otherwise stated.

Figure 7.7 Contour plot of the fitted potential for $(HF)_2$ showing the tunnelling paths. Contours are at 100 cm^{-1} intervals above the minimum. The centre-of-mass separation is R_e (table 7.8) and $\phi = 180°$ (figure 7.6). The positions of the minima are indicated by dots.

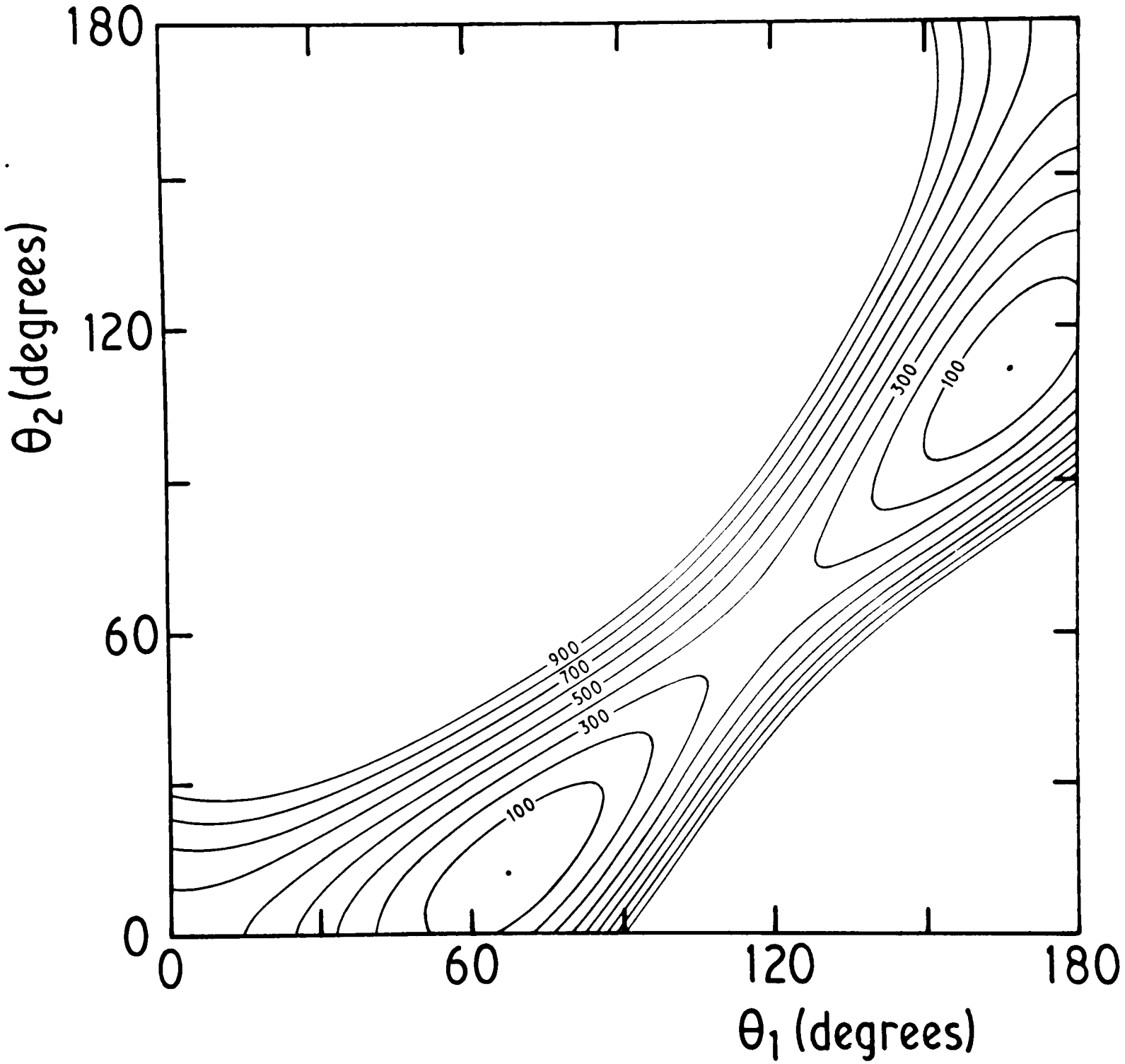
180
120
60
0
0
60
120
180
θ2(degrees)
θ1 (degrees)
300
100
900
700
500
300
100

Figure 7.8 Contour plot of Alexander's potential. Contours are the same as for figure 7.7, and the centre-of-mass separation is again fixed at R_e (table 7.8) and $\phi = 180°$.

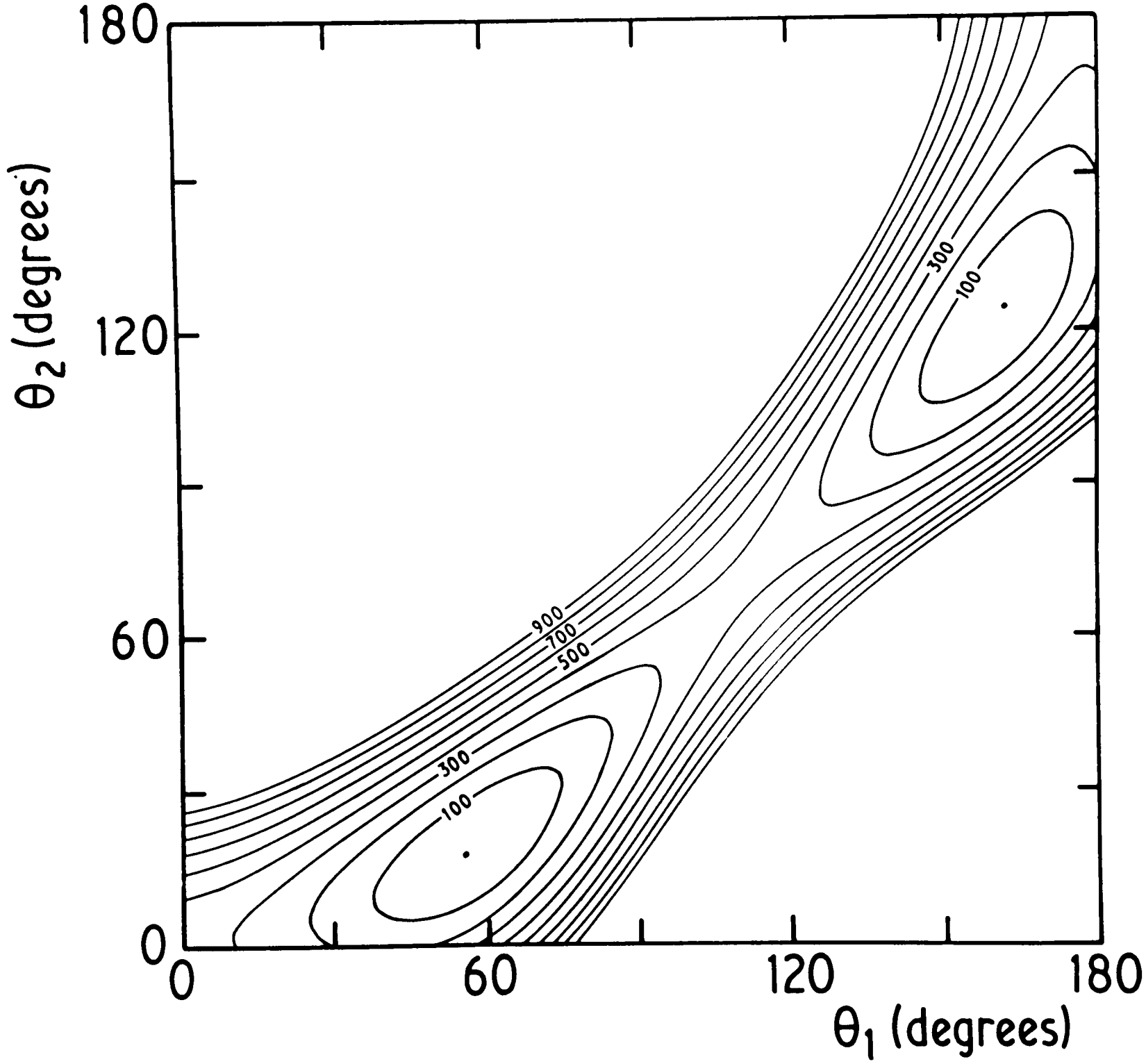
180
120
60
0
θ_2 (degrees)
900
700
500
300
100
300
100
0
60
120
180
θ_1 (degrees)

(b) Discussion

One of the initial observations is the large amount of zero-point energy for the complex, due to the motions of the monomers. This means that the equilibrium distance (R_e) for the potential is greatly different from the ground state distance. For the optimised potential $R_e = 2.675$ Å, $R_e^{bend} = 2.740$ Å, and $\langle R^{-2}\rangle^{-\frac{1}{2}} = 2.767$ Å. Most workers in the *ab initio* field have compared their results with Dyke's pseudodiatomic value for $(HF)_2$ of 2.79 Å, which is the effective distance R_0 in the ground vibrational state.

The equation for the correction to the rotational constant due to the structure of HF by semi-rigid theory is similar to the atom-diatom case and is given by

$$\Delta\bar{B} = \frac{\bar{B}_o^2}{2b_{HF}} \{\langle\cos^2\theta_1 + \cos^2\theta_2\rangle + 2\} \qquad (7.53)$$

for a planar complex, where $b_{HF} = 20.5596$ cm^{-1} [64]. This yields a correction of 115 cm^{-1} using the expectation values from the optimised potential. This is very similar to the value calculated from the Coriolis correction (98 cm^{-1} for the + state). The latter also suggests that the non-adiabatic Coriolis contribution to the rotational constant is about $(100)^2/6500 \simeq 1.5$ MHz, and this will probably provide the largest source of error in the calculation of $\bar{B}$. Error limits of 5 MHz are perhaps generous, but certainly the values of $\delta_{0,1}$ are not well determined. The standard deviations of the fit are given in table 7.5. A_0 and B_0 are strongly correlated as are A_0 and A_1. A correlation coefficient of -0.93 between A_2 and DPOC, the dipole-octupole term also exists. This correlation is caused by their dominance in fitting dipole moment and tunnelling frequency data.

The value of DPOC (79 cm^{-1}) for the fitted potential is equivalent to an octupole moment of 1.45×10^{-34} esu cm^3, which is close to the near Hartree-Fock calculation of Cade and Huo of 1.87×10^{-34} esu cm^3 [65].

This fitted term may well have effects form suppressed higher multipoles contributing to it, however.

From a comparison of figures 7.7 and 7.8 Alexander's potential is seen to be slightly too anisotropic and predicts a dipole moment that is far too high. The smaller values of the angles θ_1 and θ_2 also mean that the tunnelling path is lengthened. Combined with a higher barrier height than the optimised potential, this leads to a smaller tunnelling frequency than is observed experimentally for the K = 0 state, and shows the sensitive dependence of the tunnelling frequencies on the parameters. These changes are reflected in the contour maps for the angular motion at fixed distances. The bending force constants are also slightly smaller than those of the fitted potential, and this leads to an increase in tunnelling frequency on excitation to the K = 1 state, and a large change in dipole moment. Nevertheless, Alexander's potential does provide a good representation of the surface near the minimum.

For a direct comparison with other calculated potentials harmonic force constants ($F_{xy} = \partial^2 F/\partial x \partial y$) are shown in table 7.8. In general the agreement is seen to be remarkably good. The differences in $F_{\phi\phi}$ occur because of the smaller value of θ_2 in Lischka's case. $F_{\phi\phi}$ will tend rapidly to zero as θ_2 tends to zero. The well depths are also given in table 7.8. From an estimate of neglected terms (induced moments, polarisability terms, etc.) the value determined here is probably accurate to 20%, and is then 4.9 ± 1 kcal mol^{-1}. It agrees well with *ab initio* results confirming the suggestion that the superposition errors in basis sets are small for $(HF)_2$ [44]. The evidence for a non-linear hydrogen bond in $(HF)_2$ is also strengthened, though as in the atom-diatom case it is difficult to differentiate between a linear and a slightly non-linear equilibrium geometry for complexes which show such large amplitude motion.

Unfortunately little or no information is available from the

Figure 7.9 *Radial potential for the fitted surface for $(HF)_2$. $\phi = 180°$ and θ_1, θ_2 are fixed at the values given in table 7.8. The contributions to the potential are also shown (m = multipole, d = dipole, etc.).*

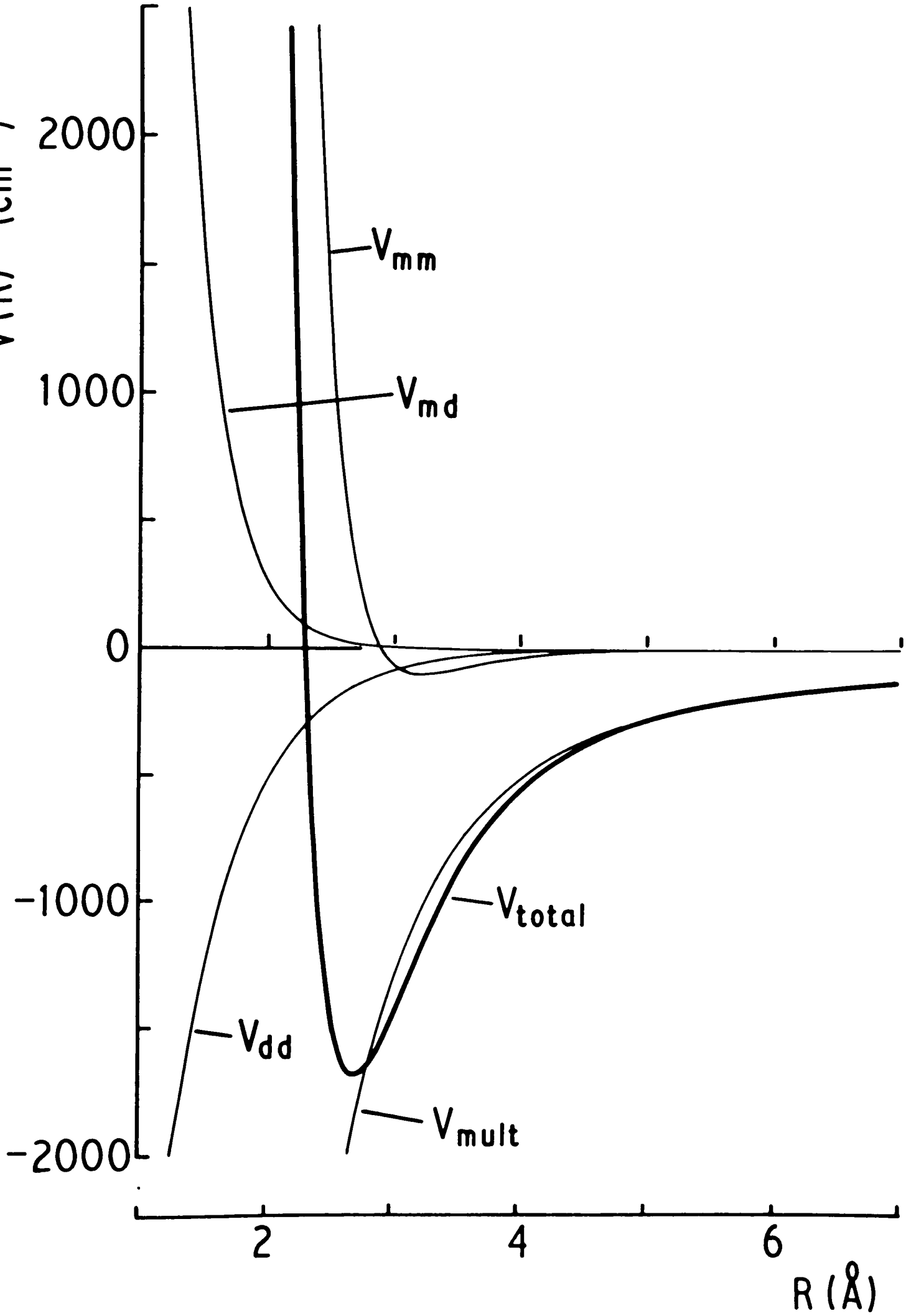
V(R) (cm⁻¹)
2000
1000
0
-1000
-2000
2
4
6
R (Å)
V_mm
V_md
V_total
V_dd
V_mult

Figure 7.10 *Radial potential for Alexander's potential for $(HF)_2$. θ_1 and θ_2 are fixed at 50° and 15° respectively and $\phi = 180°$. The contributions to the curve are labelled in the same way as figure 7.9.*

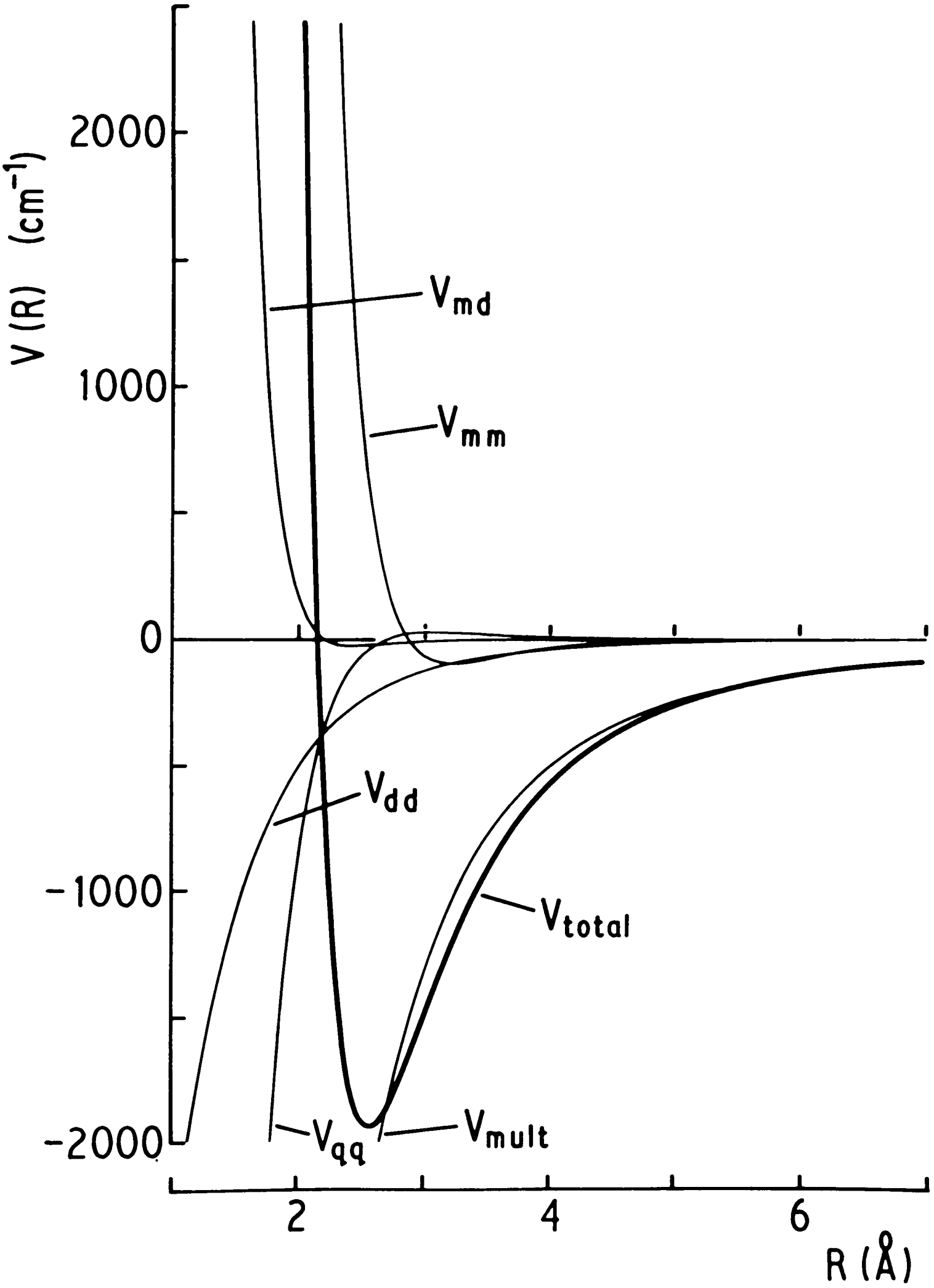
V (R) (cm⁻¹)
2000
1000
0
-1000
-2000
2
4
6
R (Å)
V_{md}
V_{mm}
V_{dd}
V_{total}
V_{qq}
V_{mult}

Table 7.7 Values of spectroscopic parameters (K = 0 states) for $(HF)_2$

	+ state		- state	
Energies/cm^{-1}				
Zeroth-order	-1086.9452		-1086.2871	
Non-adiabatic	-0.0169		-0.0166	
Total	-1086.9621		-1086.3037	
Tunnelling frequency/cm^{-1}		0.6584		(±0.005 cm^{-1})
Rotational constants/MHz				
Zeroth-order	6594.99		6594.39	
Coriolis	-98.31		-101.56	
Non-adiabatic	0.14		0.13	
Total	6496.82		6492.96	(±5 MHz)
P_1: zeroth-order		1.4332 [1]		(±0.001)
P_2: zeroth-order	0.8673		0.8838	
D_J: zeroth-order/kHz	61.2		61.2	(±1 kHz)
(B - C)/MHz				
Excitation (b)				
0 [2]	-8.44		-9.55	
1 - 5	99.61		98.96	
6 - 9	5.02		2.02	
Total	96.19		91.43	(±5 MHz)

[1] P_1 is $\langle 000- | P_1(\cos\theta_1) + P_1(\cos\theta_2) | 000+ \rangle$, see text.
[2] Labels quantum number of excited (K = 0) bending state.

Table 7.8 Harmonic force constants and equilibrium structures for $(HF)_2$

	This work	Alexander	Lischka [1]	Curtiss (6-31G**)
θ_1/deg	67.5	55.5	56	64
θ_2/deg [7]	13	18	7	8
R_e/Å	2.67_5	2.56	2.80	2.78
D_e/cm^{-1}	1705.7 (4.87) [6]	1998.5 (5.71)	1330 (3.8)	1645 (4.7)
F_{RR} [2]	0.188	0.200	0.13	0.20
$F_{\theta_1\theta_1}$ [3]	0.074	0.069	0.048	0.079
$F_{\theta_2\theta_2}$	0.107	0.100	0.15	0.17
$F_{\theta_1\theta_2}$	-0.066	-0.061	-0.054	—
$F_{R\theta_1}$ [4]	0.017	0.027	0.0082	—
$F_{R\theta_2}$	-0.010	-0.010	-0.0084	—
$F_{\phi\phi}$	0.0045	0.0092	0.000015	0.00012
θ_1^{bar}/deg [5]	118.5	110	123	—
R_e^{bar}/Å	2.70	2.56	2.80	—
h^{bar}/cm^{-1} [8]	302 (0.86) [6]	382 (1.09)	~350 (1)	—

[1] 11s7p2d/6s1p SCF calculation; ref.53.
[2] Units of mdyne Å^{-1}.
[3] $F_{\theta\theta}$, $F_{\phi\phi}$; units of mdyne Å.
[4] $F_{R\theta}$; units of mdyne.
[5] $\theta_2^{bar} = 180° - \theta_1^{bar}$; bar = tunnelling barrier geometry.
[6] Values in brackets are kcal mol^{-1}.
[7] This is the angle relative to the centres-of-mass of the HF units. For the angle relative to the F - F axis subtract 0.9° for θ_2 and add 0.9° for θ_1.
[8] h ≡ classical barrier height.

molecular beam data on the changes in average bond length that occur for the HF units on dimer formation. Estimates for these quantities from *ab initio* calculations suggest that they are small, the hydrogen bond HF unit lengthening by ~ 0.004 Å, and the other by ~ 0.002°Å [53]. These values agree with a simple analysis of Smith's infrared spectrum[36].

The data for $(DF)_2$ was not included since the tunnelling frequency is only 0.053 cm^{-1} (K = 0), and a prohibitive amount of computer time would be required to fit both sets of data. Also the $\langle P_2(\cos\theta_1) + P_2(\cos\theta_2)\rangle$ quantity from quadrupole structure is probably less useful than for atom-diatom complexes. In a similar complex HFDCl the $\langle P_2(\cos\theta)\rangle$ values from D and Cl hyperfine structure suggested that some slight unequal distortions of the field gradient occur in this complex.

In conclusion then, the Born-Oppenheimer separation method has been extended to diatom-diatom systems, where a large increase in computer time is noted. The beam data provides information about the potential surface around the well minimum, and provides information sampling a larger portion of the angular surface than for the atom-diatom case because of the tunnelling motion. Lack of hyperfine information prevents determination of θ_2 more precisely, but it appears to be non-zero in agreement with high quality *ab initio* surfaces.

As in the case of atom-diatom complexes, data from different experiments is required to model the $(HF)_2$ surface more exactly. In view of the approximately equal time for potential surface calculations of the CBO[2] and Secular Determinant method[3] for atom-diatom systems, it seems probable that the determination of potential surfaces by the latter method for anisotropic diatom-diatom complexes will be computationally expensive.

References to chapter 7

1. S.L. Holmgren, M. Waldman and W. Klemperer, J. Chem. Phys., *67*, 4414, (1977); *ibid.*, *69*, 1661, (1978).

2. J.M. Hutson and B.J. Howard, Mol. Phys., to be published.

3. S. Bratoz and M.L. Martin, J. Chem. Phys., *42*, 1051, (1965); R.J. Le Roy and J.S. Carley, Adv. Chem. Phys., *42*, 353, (1980).

4. B.J. Howard, in MTP International Review of Science, (Butterworths, London, 1975), volume 2, chapter 3.

5. S.J. Harris, K.C. Janda, S.E. Novick and W. Klemperer, J. Chem. Phys., *63*, 881, (1975).

6. M. Born and R. Oppenheimer, Ann. Physik, *84*, 457, (1927); R.T. Pack and J.O. Hirschfelder, J. Chem. Phys., *52*, 521, (1970); M. Born and K. Huang, Dynamical Theory of Crystal Lattices, (OUP, Oxford, 1954).

7. H. Essén, Int. J. Quantum Chem., *12*, 721, (1977); R.G. Wooley and B.T. Sutcliffe, Chem. Phys. Lett., *45*, 393, (1977).

8. D.M. Brink and G.R. Satchler, Angular Momentum, (OUP, Oxford, 1968), chapter 2; A.R. Edmonds, Angular Momentum in Quantum Mechanics, (Princeton Univ. Press, 1957), chapter 4.

9. J.W. Cooley, Maths. Comp., *13*, 363, (1961).

10. S.T. Epstein, J. Chem. Phys., *44*, 836, (1966).

11. J.M. Brown and B.J. Howard, Mol. Phys., *31*, 1517, (1976); J_+, j_+ are the raising operators for K equivalent to $J_x - iJ_y$, and $j_x + ij_y$.

12. A.E. Barton, Part II Thesis, (Oxford, 1977).

13. J.M. Hutson and B.J. Howard, to be published.

14. E.W. Kaiser, J. Chem. Phys., *53*, 1686, (1970).

15. W.-K. Liu, J.E. Grabenstetter, R.J. Le Roy and F.R. McCourt, J. Chem. Phys., *68*, 5028, (1978); H. Kreek and R.J. Le Roy, J. Chem. Phys., *63*, 338, (1975).

16. G.C. Maitland and E.B. Smith, Chem. Phys. Lett., *22*, 443, (1973).

17. R.A. Aziz and W. Kocay, Mol. Phys., *30*, 857, (1975); V.P.S. Nain and R.A. Aziz, Mol. Phys., *33*, 303, (1977).

18. J.J.H. van Biesen, F.A. Stokvis, E.H. van Veen and C.J.N. van den Meijdenberg, Physica A, *100*, 375, (1980); C.A. Linse, J.J.H. van Biesen, E.H. van Veen, C.J.N. van den Meijdenberg and J.J.M. Beenaker, Physica A, *99*, 145, (1980); *ibid.*, *99*, 166, (1980).

19. J.M. Farrar and Y.T. Lee, Chem. Phys. Lett., *26*, 428, (1974).

20. M. Waldman and R.G. Gordon, J. Chem. Phys., *71*, 1325, (1979).

21. P.R. Bevington, Data Reduction and Error Analysis in the Physical Sciences, (McGraw-Hill, N.Y., 1969), page 310.

22. D.W. Marquadt, J. Soc. Indust. and Appl. Maths., *11*, 431, (1963); Numerical Algorithms group, E04 series (F), volume 2, (1978).

23. J.M. Hutson, A.E. Barton, B.J. Howard and P.R.R. Langridge-Smith, Chem. Phys. Lett., 1980, in the press.

24. R.J. Le Roy, J.S. Carley and J.E. Grabenstetter, Faraday Disc. Chem. Soc., *62*, 169, (1977).

25. J.O. Hirschfelder, C.F. Curtiss and R.B. Bird, Molecular Theory of Gases and Liquids, (Wiley, N.Y., 1954).

26. J.G. Kircz, Ph.D. Thesis, (Amsterdam, 1979).

27. R.M. van Aalst, Ph.D. Thesis, (Amsterdam, 1977).

28. J.G. Kircz, G.J.Q. van der Peyl and J. van der Elsken, J. Chem. Phys., *69*, 4606, (1978).

29. E.W. Boom and J. van der Elsken, to be published; J. Mol. Struct., *45*, 113, (1978).

30. P. Schuster, in The Hydrogen Bond, (North-Holland, Amsterdam, 1976), volume 1; M.D. Joesten and L.J. Schaad, Hydrogen Bonding, (Dekker, N.Y., 1974).

31. K.C. Janda, J.M. Steed, S.E. Novick and W. Klemperer, J. Chem. Phys., *67*, 5162, (1977).

32. T.R. Dyke, K.M. Mack and J.S. Muenter, J. Chem. Phys., *66*, 498, (1977).

33. D.J. Millen, J. Mol. Struct., *45*, 1,(1978); A.C. Legon, D.J. Millen and O. Schrems, Faraday Trans. Chem. Soc. II, *3*, 592, (1979).

34. T.R. Dyke, B.J. Howard and W. Klemperer, J. Chem. Phys., *56*, 2442, (1972).

35. B.J. Howard, T.R. Dyke and W. Klemperer, J. Chem. Phys., submitted for publication.

36. D.F. Smith, J. Mol. Spectrosc., *3*, 473, (1959).

37. W. Klemperer, Ber. Bunsenges. Phys. Chem., *78*, 128, (1974).

38. A.W. Miziolek and G.C. Pimentel, J. Chem. Phys., *65*, 4462, (1976); *ibid.*, *66*, 3840, (1976).

39. G.A. Kuipers, J. Mol. Spectrosc., *2*, 75, (1958); J.L. Himes and T.A. Wiggins, J. Mol. Spectrosc., *40*, 418, (1971).

40. J.D. Dill, L.C. Allen, W.C. Topp and J.A. Pople, J. Am. Chem. Soc., *97*, 7220, (1975).

41. G.H.F. Dierckson and W.P. Kraemer, Chem. Phys. Lett., *6*, 419, (1970).

42. L.A. Curtiss and J.A. Pople, J. Mol. Spectrosc., *61*, 1, (1976).

43. S.F. Boys and F. Bernadi, Mol. Phys., *19*, 558, (1970).

44. T.P. Green and F.B. van Duijneveldt, unpublished work.

45. H. Lischka, J. Am. Chem. Soc., *96*, 4761, (1974).

46. S. Yamabe and K. Morokuma, J. Am. Chem. Soc., *97*, 4458, (1975).

47. H. Umeyama and K. Morokuma, J. Am. Chem. Soc., *99*, 1316, (1977).

48. P. Kollman, J. McKelvey, A. Johansson and S. Rottenberg, J. Am. Chem. Soc., *97*, 955, (1975); P. Kollman, J. Am. Chem. Soc., *99*, 4875, (1977); G. Leroy, G. Louterman-Leloup and P. Ruelle, Bull. Soc. Chim. Belg., *85*, 393, (1976); S. Nagase and T. Fueno, Theoret. Chim. Acta., *35*, 217, (1974).

49. D.R. Yarkony, S.V. O'Neill, H.F. Schaefer III, C.P. Baskin and C.F. Bender, J. Chem. Phys., *60*, 855, (1974).

50. M.L. Klein, I.R. McDonald and S.F. O'Shea, J. Chem. Phys., *69*, 63, (1978); M.L. Klein and I.R. McDonald, J. Chem. Phys., *71*, 298, (1979).

51. L.L. Poulsen, G.D. Billing and J.I. Steinfeld, J. Chem. Phys., *68*, 5121, (1978); G.D. Billing and L.L. Poulsen, J. Chem. Phys., *68*, 5128, (1978); Chem. Phys., *36*, 271, (1979).

52. W.L. Jorgensen, J. Am. Chem. Soc., *100*, 7824, (1978); W.L. Jorgensen and M.E. Cournoyer, J. Am. Chem. Soc., *100*, 4942, (1978); W.L. Jorgensen, J. Chem. Phys, *70*, 5888, (1979); G.A. Parker, R.L. Snow and R.T. Pack, Chem. Phys. Lett., *33*, 399, (1975), (electron gas calculation).

53. H. Lischka, Chem. Phys. Lett., *66*, 108, (1979).

54. M.H. Alexander and A.E. DePristo, J. Chem. Phys., *65*, 5009, (1976).

55. M.H. Alexander, P.J. Dagdigian and A.E. DePristo, J. Chem. Phys., *66*, 59, (1977); M.H. Alexander and A.E. DePristo, J. Chem. Phys., *66*, 1334, (1977).

56. H.C. Longuet-Higgins, Mol. Phys., *6*, 445, (1963).

57. K. Yamada and M. Winnewisser, J. Mol. Spectrosc., *68*, 307, (1977).

58. J. Singer, Elements of Numerical Analysis, (Academic Press, N.Y., 1964), chapter 7; the matrix diagonalisation is by Householder's method using ICL Scientific subroutines, subroutine FPROOT1, 1974.

59. S.T. Epstein, J. Chem. Phys., *65*, 5526, (1976).

60. J.S. Muenter, J. Chem. Phys., *56*, 5409, (1972).

61. F.H. DeLeeuw and A. Dymanus, J. Mol. Spectrosc., *48*, 427, (1973).

62. R.C. Kerns and L.C. Allen, J. Am. Chem. Soc., *100*, 6587, (1978).

63. R.F.W. Bader, I. Keaveny and P.E. Cade, J. Chem. Phys., *47*, 3381, (1967).

64. D.U. Webb and K.N. Rao, J. Mol. Spectrosc., *28*, 121, (1968).

65. P.E. Cade and W.Huo, J. Chem. Phys., *47*, 614, (1967).

66. B.J. Howard, private communication; M.H. Alexander and A.E. DePristo, J. Chem. Phys., *66*, 2166, (1977).

Appendix A Refocussing of molecules in electric deflection experiments

1. Second-order moments

In the Oxford spectrometer the quadrupole fields are charged to a potential difference of V volts, two of the rods being earthed. The absolute value of the electric field at a particular radius r is given by (see chapter 2)

$$|E| = VR^{-2}r \qquad \text{(A1.1)}$$

where R is the quadrupole 'lens' diameter. Considering a second-order Stark effect, for example, the $K = 0$ states of a symmetric top molecule, the Stark energy is given by[1]

$$W^{(2)} = \frac{\mu^2E^2}{2\bar{B}} \cdot \frac{\{J(J+1) - 3M^2\}}{J(J+1)(2J-1)(2J+3)} \qquad \text{(A1.2)}$$

and equation A1.2 may be re-written as

$$W^{(2)} = \frac{\mu^2V^2r^2}{2R^4\bar{B}} f(J,M) \qquad \text{(A1.3)}$$

where f(J,M) is the J,M dependence of the Stark effect. The force on a molecule is given by

$$F = -\nabla W = -\frac{\mu^2V^2r}{R^4\bar{B}} f(J,M) \qquad \text{(A1.4)}$$

and hence focussing states have positive Stark effects. Within a quadrupolar lens the equation of motion[2] for molecules with mass m is given by

$$r = r_o\cos\left(\frac{\mu^2V^2f(J,M)}{mR^4}\right)^{\frac{1}{2}}t + \dot{r}_o\left(\frac{\mu^2V^2f(J,M)}{mR^4}\right)^{-\frac{1}{2}}\sin\left(\frac{\mu^2V^2f(J,M)}{mR^4}\right)t \qquad \text{(A1.5)}$$

where r_o is the initial radius entrance position to the lens. Molecules travel through the lens with velocity u, and hence the distance through the lens is given at time t by $t = z/u$, where the lens axis is the z axis. Equation A1.5 then becomes

$$r = r_o\cos pz + \dot{r}_o(pu)^{-1}\sin pz \qquad \text{(A1.6)}$$

where

$$p = \left(\frac{\mu^2 V^2 f(J,M)}{mu^2 R^4 \bar{B}}\right)^{\frac{1}{2}} \tag{A1.7}$$

p depends only on the geometry of the system.

Equation A1.6 and its derivative can be combined and written as a matrix equation for a lens of length l as[3]

$$\begin{pmatrix} r \\ \dot{r}/u \end{pmatrix} = \begin{pmatrix} \cos pl & p^{-1} \sin pl \\ -p \sin pl & \cos pl \end{pmatrix} \begin{pmatrix} r_o \\ \dot{r}_o/u \end{pmatrix} \tag{A1.8}$$

and for a field-free region of length z the equations are of the form

$$\begin{pmatrix} r \\ \dot{r}/u \end{pmatrix} = \begin{pmatrix} 1 & z \\ 0 & 1 \end{pmatrix} \begin{pmatrix} r_o \\ \dot{r}_o/u \end{pmatrix} \tag{A1.9}$$

In the Oxford spectrometer the distance from the source to the A field entrance z_o is ~ 15 cm. The length of both quadrupole fields, l, is 39 cm, and the field-free region between the A and B field (z_i) is ~ 41 cm. Experimentally, it is observed that for optimum focussing the B field voltage is ~ 2/3 A field voltage. p', the inverse length characteristic of the B field is then put to 2/3 of that of the A field (p). The refocussing matrix transformation for a molecule in the beam is then

$$\begin{pmatrix} 1 & z_f \\ 0 & 1 \end{pmatrix} \begin{pmatrix} \cos p'l & p'^{-1} \sin p'l \\ -p' \sin p'l & \cos p'l \end{pmatrix} \begin{pmatrix} 1 & z_i \\ 0 & 1 \end{pmatrix} \begin{pmatrix} \cos pl & p^{-1} \sin pl \\ -p \sin pl & \cos pl \end{pmatrix}$$

$$\times \begin{pmatrix} 1 & z_o \\ 0 & 1 \end{pmatrix} \tag{A1.10}$$

The focussing condition is that the upper right hand matrix element of this product be zero, or approximately so since we have only estimated the effect of the B field. This is

$$(\cos p'l - z_f p' \sin p'l)(z_o \cos pl - p^{-1} \sin pl) + (z_i \cos p'l - z_i z_f p' \sin p'l$$

$$+ p'^{-1} \sin p'l - z_f \cos p'l)(\cos pl - z_o p \sin pl) \simeq 0 \qquad \text{(A1.11)}$$

The value of p nearest zero is at 2.8×10^{-2} (equation A1.11 ~ 0.6). It is then possible to calculate the A-focussing voltage required for a second-order Stark molecule by transposing equation A1.7

$$V = \frac{R^2 up}{\mu} \left[\frac{m\bar{B}}{f(J,M)} \right]^{\frac{1}{2}} \qquad \text{(A1.12)}$$

Substituting the most probable velocity $u = (3kT/m)^{\frac{1}{2}}$ [4] for the seeded beam of molecules along the beam axis gives the final voltage dependence as

$$V = \frac{R^2 p}{\mu} \left[\frac{3kT\bar{B}}{f(J,M)} \right]^{\frac{1}{2}} \qquad \text{(A1.13)}$$

and this is the origin of the $\mu B^{-\frac{1}{2}}$ dependence in comparing focussing characteristics of atom-diatom complexes in chapter 6.

The minimum second-order dipole moment that could be calculated at an A field of 30 kV is given from equation A1.13. The state with the fastest positive Stark effect is the J,M = 1,0 state. In the CO_2 expansion in argon the minimum dipole moment that can be refocussed in the spectrometer is approximately

$$\mu \geq \frac{R^2 p}{V_{max}} \left[\frac{3kT\bar{B}}{f(1,0)} \right]^{\frac{1}{2}} \simeq 0.07_5 \text{ Debyes} \qquad \text{(A1.14)}$$

where V_{max} is the A field voltage (see chapter 2).

2. First-order moments

A crude estimate of the refocussability of $(CO_2)_2$ is given by

$$\text{refocussing (r)} \propto Q_{ROT}^{-1} \sum_{J=2}^{\infty} \sum_{K=2}^{J} \sum_{M=0}^{J} \frac{\mu EMK}{J(J+1)} \exp -(\{\bar{B}J(J+1) - [A-\bar{B}]K^2\}/kT) \qquad \text{(A2.1)}$$

where the sum over K is for even values only, and $\bar{B}$ represents $\frac{1}{2}(B+C)$.

The summations may be replaced by integrations yielding

$$r \propto \frac{\mu E}{2Q_{ROT}} \sum_{J=2}^{\infty} \exp-(\bar{B}J(J+1)/kT) \int_{3/2}^{J+\frac{1}{2}} K \exp-(K^2[A-\bar{B}]/kT)\,dK \qquad (A2.2)$$

$$r \propto \frac{\mu E}{4Q_{ROT}} \cdot \frac{kT}{[A-\bar{B}]} \left[\exp(9[A-\bar{B}]/4kT) \int_{3/2}^{\infty} \exp-(\bar{B}J(J+1)/kT)\,dJ - \int_{3/2}^{\infty} \exp -\{(AJ(J+1)/kT + [A-\bar{B}]/4kT\}dJ \right] \qquad (A2.3)$$

$$r \propto 208\ \mu E Q_{ROT}^{-1} \simeq 0.060\ \mu E \qquad (A2.4)$$

where Q_{ROT} is the rotational partition function for the dimer and is approximately half the value of the corresponding asymmetric top (see chapter 2) because states with odd values of K are forbidden by symmetry considerations.

References to Appendix A

1. H.W. Kroto, Molecular Rotation Spectra, (Wiley, London, 1975), chapter 7.

2. W.E. Falconer, A. Büchler, J.L. Stauffer and W. Klemperer, J. Chem. Phys., *48*, 312, (1968); *ibid.*, *43*, 2416, (1965).

3. S. Penner, Rev. Sci. Instrum., *32*, 150, (1961).

4. N.F. Ramsey, Molecular Beams, (OUP, Oxford, 1956), chapter 2.

Appendix B Spin-spin and spin-rotation interactions in van der Waals molecules

1. Spin-spin interactions in van der Waals molecules

From Ramsey[1], page 200, the Hamiltonian is given by:

$$H_{SS} = \frac{2d_a}{(2J-1)(2J+3)}\left[\frac{3}{2}(I_1.J)(I_2.J) + \frac{3}{2}(I_2.J)(I_1.J) - (I_1.I_2)J^2\right] \quad (B1.1)$$

where $d_a = \left\langle \frac{g_1 g_2 \mu_N^2}{r^3} \right\rangle \times \langle P_2(\cos\theta)\rangle = d^{HCl}\langle P_2(\cos\theta)\rangle$

and g_1, g_2 are the gyromagnetic ratios of nucleus 1 and 2, μ_N is the nuclear magneton, and r is the H-Cl distance. Considering nucleus 1 as completely coupled and nucleus 2 as decoupled from J, *i.e.* $|f\rangle \equiv |J_1 I_1; F_1 M_{F_1}; I_2 M_{I_2}\rangle$ yields:

$$I_1.I_2 = \frac{(I_1.F_1)(F_1.I_2)}{F_1(F_1+1)} \quad (B1.2)$$

$$I_1.J = \tfrac{1}{2}\{F_1(F_1+1) - I_1(I_1+1) - J(J+1)\} \quad (B1.3)$$

and similarly for $F_1.J$, $I_1.F_1$.

$$I_2.J = \frac{(I_2.F_1)(F_1.J)}{F_1(F_1+1)} \quad (B1.4)$$

so the diagonal matrix element is

$$3d_a\frac{[F_1(F_1+1) - I_1(I_1+1)]^2 - J(J+1)[2F_1(F_1+1) + 2I_1(I_1+1) + J(J+1)]}{2(2J-1)(2J+3)F_1(F_1+1)} \times F_1.I_2 \quad (B1.5)$$

$$= \alpha F_1.I_2 \quad (B1.6)$$

Now

$$F_1.I_2 = F_{1z}I_{2z} + \tfrac{1}{2}\{F_{1+}I_{2-} + F_{1-}I_{2+}\} \quad (B1.7)$$

where the z direction will be applied by the electric field. F_{1+} is a step-up operator in M_F (H.W. Kroto, Molecular Rotation Spectra, page 28). So for $M_F \neq \frac{1}{2}$ levels

$$\langle f|H_{SS}|f\rangle = \alpha M_{F_1} M_{I_2} \quad (B1.8)$$

which leads to symmetric splitting in KrHCl. With $|M_F| = \frac{1}{2}$, however, an off-diagonal matrix element exists linking $M_F = \pm\frac{1}{2}$ states. For example $F, M_F = \frac{1}{2}$, $M_{I_2} = -\frac{1}{2}$ are mixed with $F, M_F = -\frac{1}{2}$, $M_{I_2} = \frac{1}{2}$. As

$$F_{1-}|F_1, \tfrac{1}{2}\rangle = \{F_1(F_1+1) - \tfrac{1}{2}(\tfrac{1}{2}-1)\}^{\frac{1}{2}}|F_1, -\tfrac{1}{2}\rangle$$

$$= (F_1+\tfrac{1}{2})|F_1, -\tfrac{1}{2}\rangle \qquad \text{(B1.9)}$$

and

$$I_{2+}|\tfrac{1}{2}, -\tfrac{1}{2}\rangle = |\tfrac{1}{2}, \tfrac{1}{2}\rangle$$

So we need to diagonalise the matrix

$$\begin{pmatrix} -\alpha/4 & (F+\frac{1}{2})\alpha/2 \\ (F+\frac{1}{2})\alpha/2 & -\alpha/4 \end{pmatrix} \qquad \text{(B1.10)}$$

which gives energies (Kroto, page 9)

$$E = -\alpha/4 \pm (F+\tfrac{1}{2})\alpha/2 \qquad \text{(B1.11)}$$

As an example the splittings for the transitions in figure 4.3 may be calculated using the above equations (see figures B.1 and B.2). The transtions are:

a. $J = 2$, $F, |M_F| = 1/2, 1/2 \rightarrow 5/2, 3/2$ for $^{84}KrH^{35}Cl$

b. $J = 3$, $F, |M_F| = 3/2, 3/2 \rightarrow 7/2, 5/2$ for $^{86}KrH^{35}Cl$

and these represent typical splitting patterns, which are shown in figure B.3.

In the case of KrHCl the main spin-spin component is the directly coupled spin-spin magnetic interaction. d for HCl is 5.59(9) kHz [2]. Another mechanism of spin-spin interaction is the coupling (δ) via the magnetic interaction of the nucleus and its 'atomic' electrons, together with the exchange interaction with the other atom's electrons, and this orients the other magnetic nucleus. It is equivalent in second-order perturbation theory to the mixing in of excited triplet electronic states. It is however barely determined in HCl as 0.04(10) kHz.

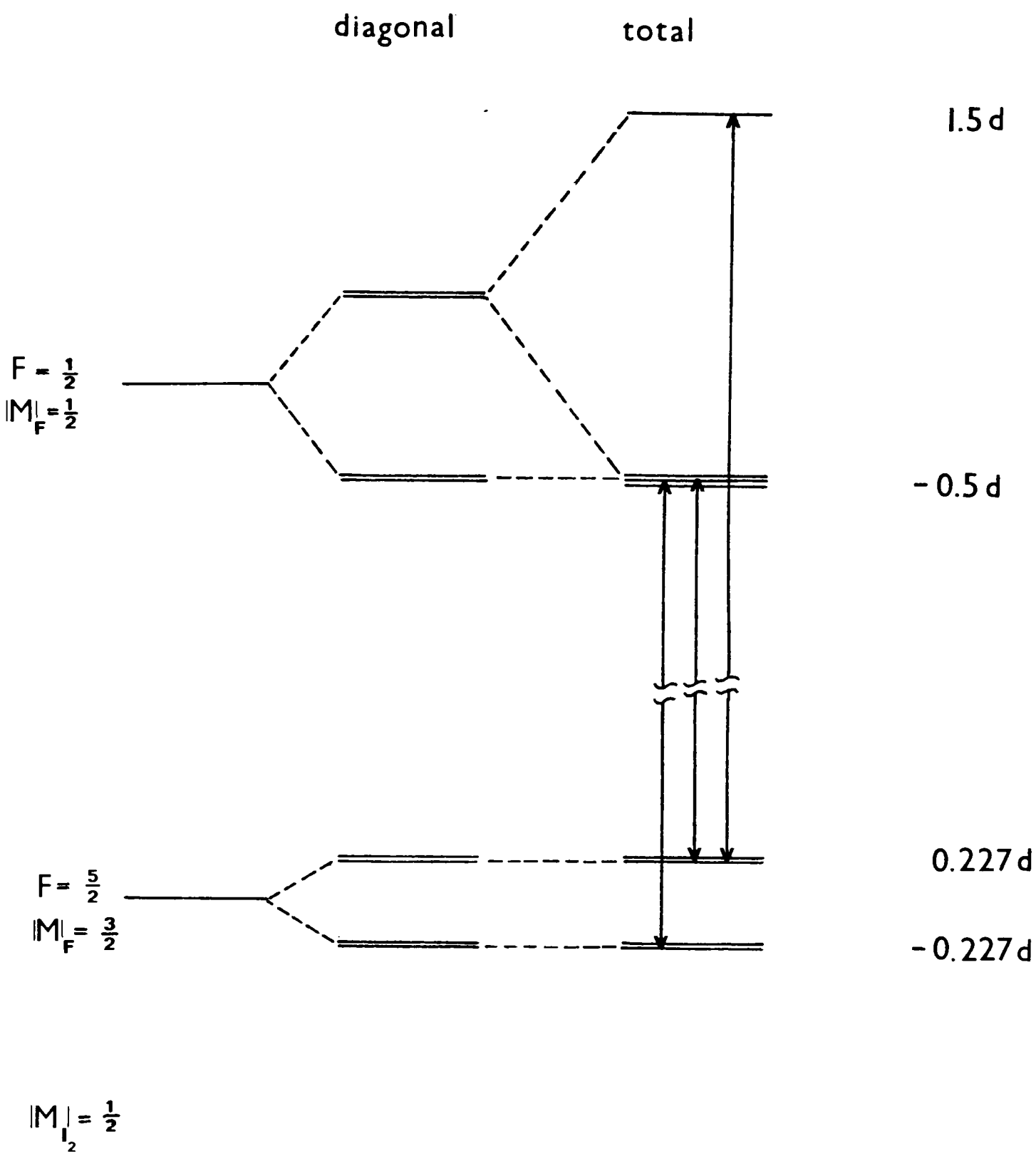

Figure B.1 Spin-spin analysis of $J = 2$, $F = 1/2 \rightarrow 5/2$, $M_F = 1/2 \rightarrow 3/2$ transtion.

b.

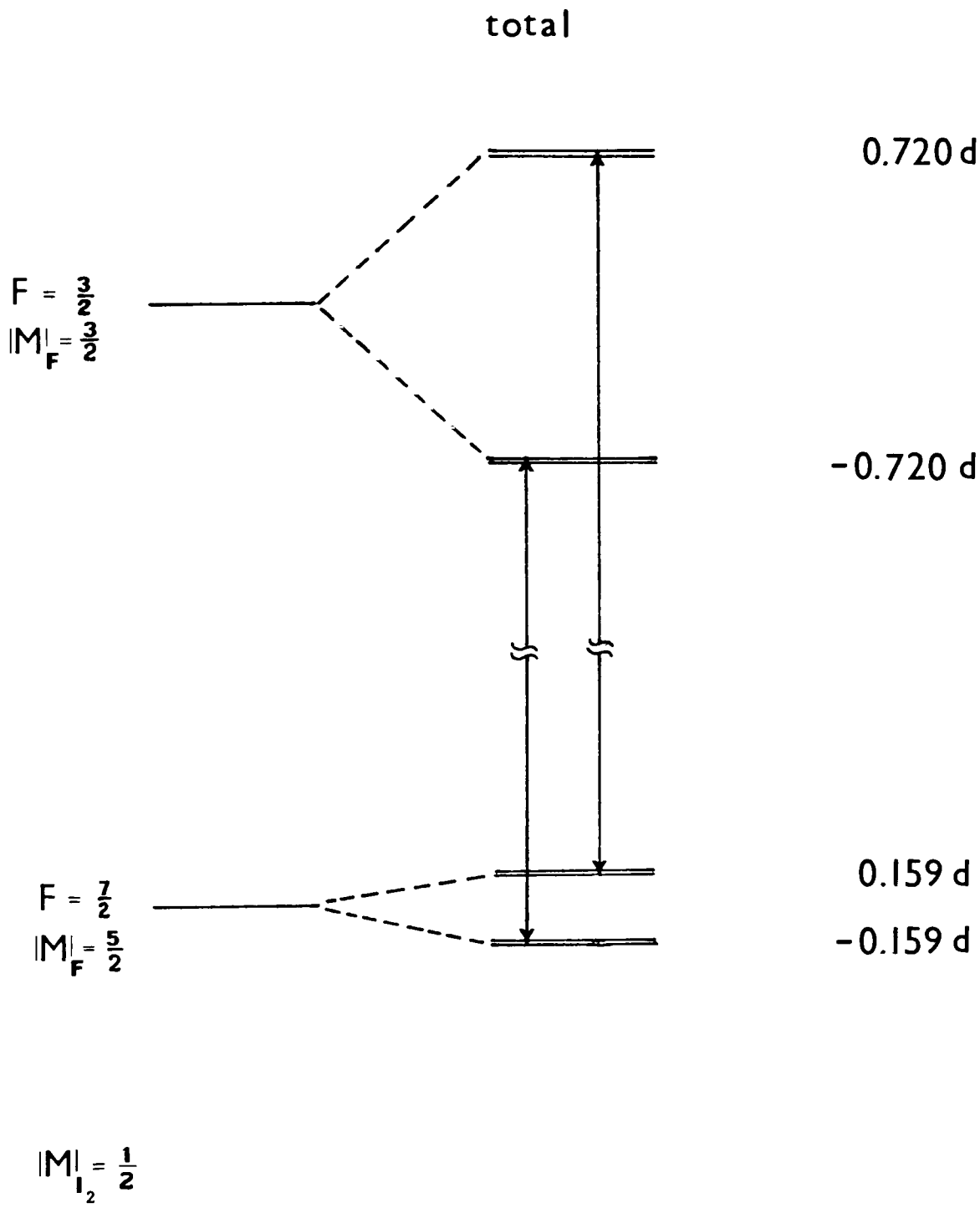

Figure B.2 Spin-spin analysis of $J = 3$, $F = 3/2 \rightarrow 7/2$, $M_F = 3/2 \rightarrow 5/2$ transition producing a symmetric doublet.

Figure B.3 Spin-spin splitting in KrHCl spectra (see text).

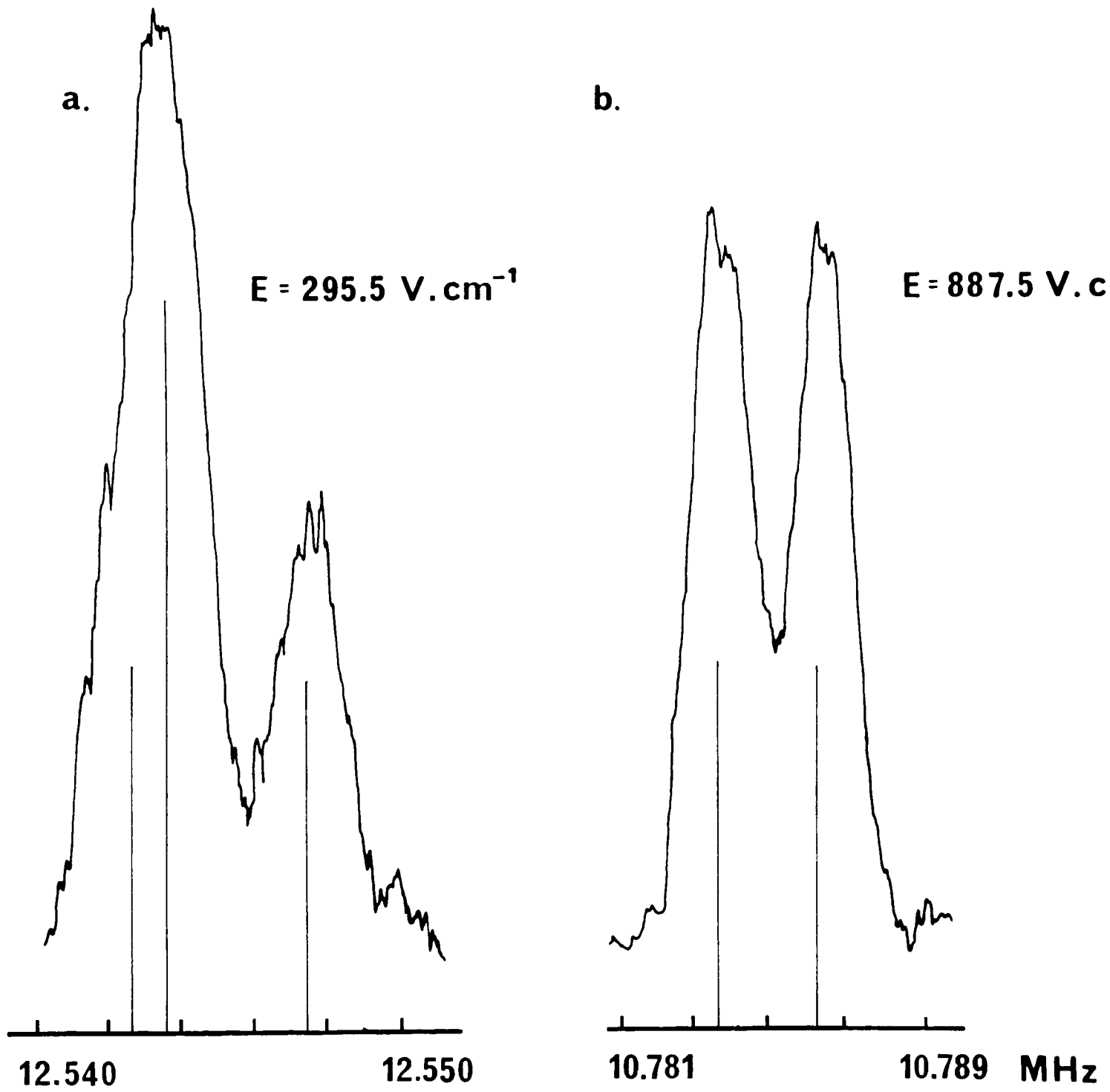
a.
E = 295.5 V.cm⁻¹
12.540
12.550
b.
E = 887.5 V.cm⁻¹
10.781
10.789
MHz

2. Spin-rotation interaction in van der Waals molecules

The spin-rotation interaction arises, in the absence of external fields, from the interaction of a nuclear magnetic moment with intramolecular fields set up at the nucleus. These fields arise from the rotation of both the electrons and the nuclear framework relative to the nucleus in question. The general Hamiltonian is written in the form

$$H_{SR} = I_K . M_K . J \qquad \text{(B2.1)}$$

where I_K is the nuclear spin and M_K is the spin-rotation tensor for nucleus K. The magnetic moment is related to the nuclear spin by the equation

$$\mu_K = \frac{g_K \mu_N}{\hbar} I_K \qquad \text{(B2.2)}$$

where g_K is the nuclear g-factor, and μ_N is the nuclear magneton. For the chlorine nucleus in HCl only one component of the tensor is unique or non-zero and that is the *bb* component (*a*,*b*,*c* are the inertial axes and $b \equiv c$ for a linear molecule and symmetric top). This can be related to known quantities by the relation[2]

$$C_b^{Cl} = (M^{Cl})_{bb} = (M^{Cl})^n_{bb} + (M^{Cl})^{el}_{bb} \qquad \text{(B2.3)}$$

where
$$(M^{Cl})^n_{bb} = - \frac{e\mu_o \mu_N g_{Cl} b_o}{h r_{HCl}} \qquad \text{(B2.4)}$$

and

$$(M^{Cl})^{el}_{bb} = \frac{\mu_o \mu_B \mu_N g_{Cl} b_o}{\pi} \sum_{n \neq 0} \frac{\langle 0|L_b|n\rangle\langle n|L'_b|0\rangle + \langle 0|L'_b|n\rangle\langle n|L_b|0\rangle}{E_n - E_o} \qquad \text{(B2.5)}$$

$(M^{Cl})^n_{bb}$ and $(M^{Cl})^{el}_{bb}$ refer to the nuclear and electronic contributions respectively. μ_o is the vacuum permeability and b_o is the rotational constant of HCl, with r_{HCl} the HCl bond length. The electronic contribution consists of a sum of matrix elements over excited electronic states, L_b being the total electronic angular momentum operator at the chlorine nucleus and $L'_b = \sum_i l^i_b / r^3_{iCl}$ where l^i_b is the angular momentum of

the i-th electron relative to the chlorine nucleus. The nuclear contribution is easily calculated as -2.07 kHz which means that the value for the electronic part is +55.91 kHz from the experimental value[2].

Thus the majority of the contribution to C_b^{Cl} comes from the

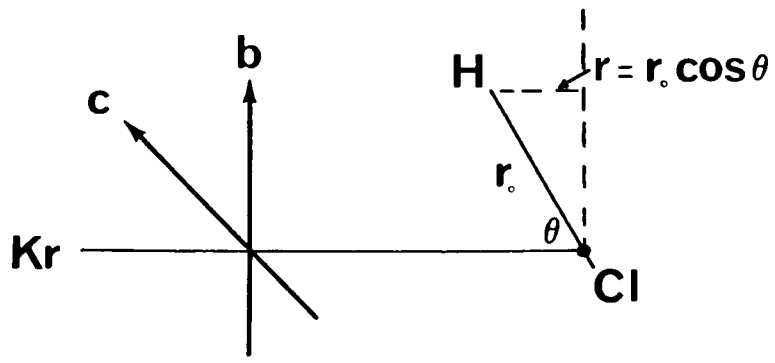

Figure B.4 Spin-rotation in KrHCl.

electronic part. For KrHCl if the complex is considered as a semi-rigidly bent molecule, orientation effects and the effects of the krypton will exist. The HCl complex is now rotating more slowly than the HCl subunit alone about an arbitrary axis by the ratio $\bar{B}/b_o$, where $\bar{B}$ is the complex rotational constant. Also the HCl subunit is orientated by θ with respect to the *b* axis. Since the magnetic field at the centre of a rotating charge is proportional to r^{-2} (Biot-Savart) then the C^{Cl} for the complex is given by:

for rotation around the *b* axis

$$C^{Cl} = C_{HCl}^{Cl} \frac{\bar{B}}{b_o} \langle \cos^2\theta \rangle \qquad \text{(B2.6)}$$

for rotation around the *c* axis

$$C^{Cl} = C_{HCl}^{Cl} \frac{\bar{B}}{b_o} \qquad \text{(B2.7)}$$

The measured spin-rotation constant in a K = 0 state is the mean of these and is given by the equation

$$C^{Cl} = C_{HCl}^{Cl} \frac{\bar{B}}{b_o} \left\{ \frac{1 + \langle \cos^2\theta \rangle}{2} \right\} \qquad \text{(B2.8)}$$

References to Appendix B

1. N.F. Ramsey, Molecular Beams, (OUP, Oxford, 1956).

2. F.H. de Leeuw and A. Dymanus, J. Mol. Spectrosc., *48*, 427, (1973).

Appendix C Deuterium quadrupole effects in van der Waals spectra

1. First order terms in $(eQq)^D$ using a high field basis set yield only one diagonal term of the form:

$$\langle JM_J;I_2M_{I_2}|H_{Q_2}|JM_J;I_2M_{I_2}\rangle = -(eQq)^D_a \frac{[3M_J^2 - J(J+1)][3M_{I_2}^2 - I_2(I_2+1)]}{4I_2(2I_2-1)(2J-1)(2J+3)} \quad (C1.1)$$

However, additional matrix elements also exist off-diagonal in M_{I_2} (K=0):

$$\langle JM_J;I_2M_{I_2}|H_{Q_2}|JM_J\pm1;I_2M_{I_2}\mp1\rangle$$

$$= -\frac{3(eQq)^D_a(2M_J\pm1)(2M_{I_2}\mp1)}{8I_2(2I_2-1)(2J-1)(2J+1)}\{(I_2\pm M_{I_2})(I_2\mp M_{I_2}+1)(J\mp M_J)(J\pm M_J+1)\}^{\frac{1}{2}} \quad (C1.2)$$

which links $M_{I_2} = 0$ to ±1.

$$\langle JM_J;I_2M_{I_2}|H_{Q_2}|JM_J\pm2;I_2M_{I_2}\mp2\rangle$$

$$= -\frac{3(eQq)^D_a}{8I_2(2I_2-1)(2J-1)(2J+3)}\{(J\mp M_J)(J\pm M_J+1)(J\pm M_J+2)(J\mp M_J-1)(I_2\pm M_{I_2})$$

$$(I_2\mp M_{I_2}+1)(I_2\mp M_{I_2}+2)(I_2\pm M_{I_2}-1)\}^{\frac{1}{2}} \quad (C1.3)$$

which links $M_{I_2} = \pm1$ to ∓1.

Both sets of matrix elements split the $M_{I_2} = \pm1$ transitions. A net shift of $M_{I_2} = 0$ also occurs. The effects are at the level of a few kHz as seen in table 4.7.

2. The interaction H_{Q_2} is much smaller than H_{Q_1} so the splittings of the zero field microwave spectrum are easily calculated following Townes and Schawlow[1]. The value of the spin-spin interaction matrix elements are given in Appendix B. The splitting is illustrated for the transition J,F = 2,1/2 → 1,3/2, figure 4.8, the splitting calculation of which is shown below.

J	F_1	F	W_{Q_2}	d
2	1/2	3/2	0.0	-1.0
		1/2	0.0	2.0
1	3/2	5/2	0.04	-1.360
		3/2	-0.16	0.906˙
		1/2	0.20	2.26˙

transitions

J,	F	→ J′,	F′	ΔWQ_2	d	rel.int.	Δ_{calc}/kHz
2	3/2	1	5/2	-0.04	0.360	50	-4.3_7
		1	3/2	0.16	-1.906˙	16	17.2_6
		1	1/2	-0.20	-3.26˙	2.4	-24.0_0
2	1/2	1	3/2	0.16	1.093	12	18.5_5
		1	1/2	-0.20	-0.26˙	16	-22.7_1

The relative intensities (rel.int.) are interpolations of Appendix I according to Townes and Schawlow, page 172, which leads to relative intensities of 0.37:1:0.56 compared with the experimental values of 0.45:1:0.67, (see figure C.1). Other effects caused by the different refocussing characteristics in the spectrometer are more difficult to calculate, but might be expected to be small for such near eigenstates.

Reference to Appendix C

1. C.H. Townes and A.L. Schawlow, Microwave Spectroscopy, (Dover Press, N.Y., 1975), chapter 6.6.

Figure C.1 *Phase-locked spectrum of $^{84}KrD^{35}Cl$ showing the splitting caused by the deuterium quadrupole coupling constant. The transition is $J,F_1 = 2,1/2 \rightarrow 1,3/2$, F being the total quantum number.*

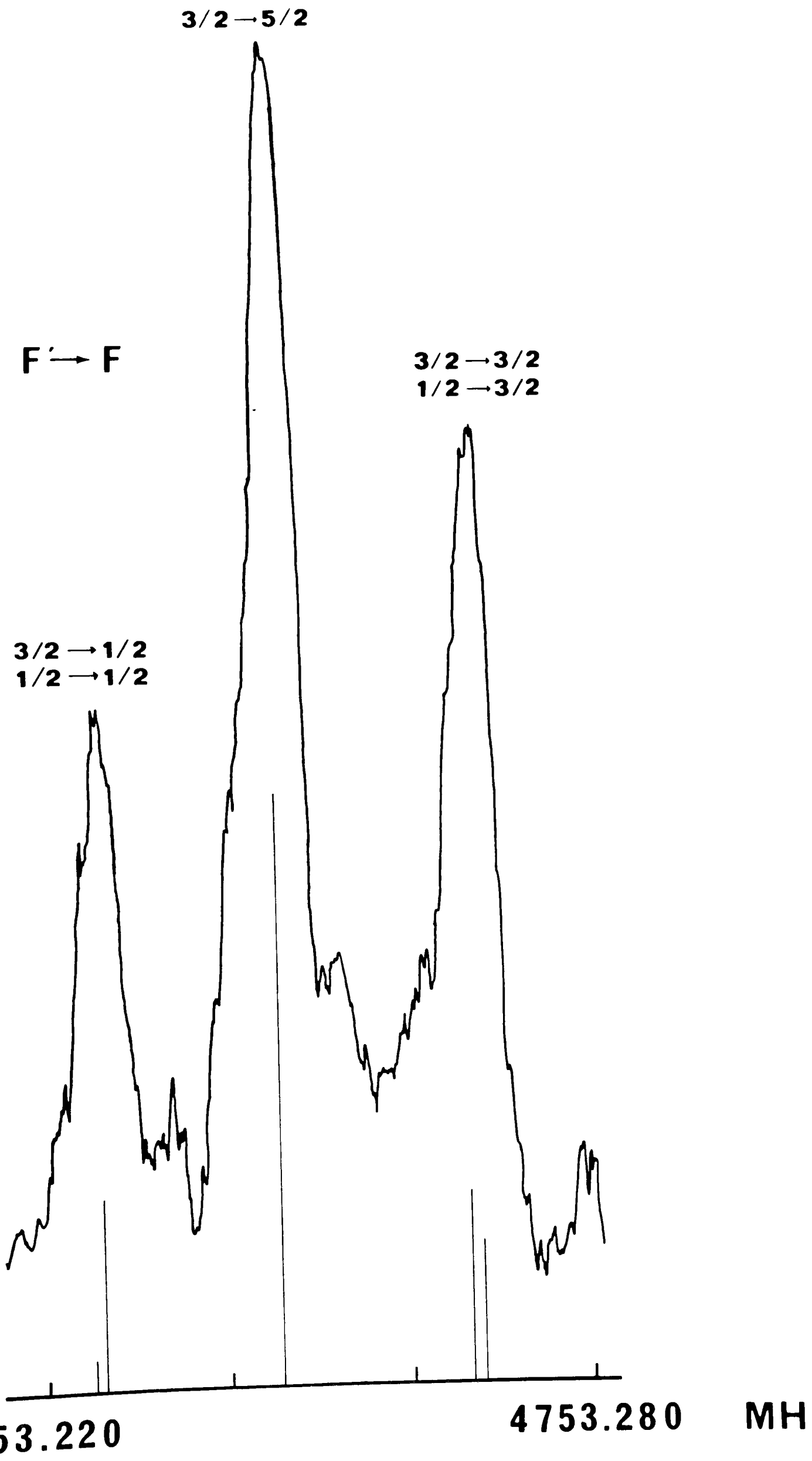
3/2 → 5/2
F' → F
3/2 → 3/2
1/2 → 3/2
3/2 → 1/2
1/2 → 1/2
4753.220
4753.280
MH

Appendix D Appendix to chapter 7

1. Matrix elements for the Born-Oppenheimer method

The matrix elements are integrals over spherical harmonics, denoted by $|jm\rangle$, and the appropriate ones are as follows:

$$\langle jm|P_n(\cos\theta)|j'm'\rangle = (-1)^m\left[(2j+1)(2j'+1)\right]^{\frac{1}{2}}\begin{pmatrix} j & n & j' \\ -m & 0 & m' \end{pmatrix}\begin{pmatrix} j & n & j' \\ 0 & 0 & 0 \end{pmatrix} \quad \text{(D1.1)}$$

from Edmonds (4.6.3) [1], since $Y^*_{j,m} = (-1)^m Y_{j,-m}$ (Brink, 2.7) [1].

The H_{NA} matrix elements take the following form

$$\langle v'b'K|H_{NA}|vbK\rangle = -\frac{\hbar^2}{2\mu}\int \chi_{v'b'}\left\{\left\langle b'\left|\frac{\partial^2}{\partial R^2}\right|b\right\rangle + 2\left\langle b'\left|\frac{\partial}{\partial R}\right|b\right\rangle\frac{\partial}{\partial R}\right\}\chi_{vb}dR$$

$$= -\frac{\hbar^2}{2\mu}\int \chi_{v'b'}\left\{\sum_j c_{b'j}\ddot{c}_{bj} + 2\sum_j c_{b'j}\dot{c}_{bj}\frac{\partial}{\partial R}\right\}\chi_{vb}dR \quad \text{(D1.2)}$$

where the c's are functions of R (see equation 7.8). The H_{ROT} matrix elements take the form

$$\langle v'b'K'|H_{ROT}|vbK\rangle = \langle v'b'|\hbar^2/2\mu R^2|vb\rangle\, J(J+1)\delta_{KK'} \quad \text{(D1.3)}$$

The matrix elements for H_{NA} of $\partial/\partial R$ and $\partial^2/\partial R^2$ may be obtained from the radial derivatives above by storing the c coefficients and either calculating $\dot{c}$ and $\ddot{c}$ by numerical differentiation or by re-writing the matrix elements in terms of the potential derivatives. For example $\langle b'|\partial/\partial R|b\rangle = -\langle b'|\partial V/\partial R|b\rangle/(U_{b'} - U_b)$ for $b' \neq b$ (see chapter 7, ref 2). The latter technique is used for the atom-diatom complexes, but for $(HF)_2$ the potential does not take a simple form and numerical differentiation is quicker.

2. Spectroscopic parameters from KrHCl 4-angle fitting (5 parameter fit)

Contributions to various spectroscopic observables from the approach decribed in chapter 7

	$KrH^{35}Cl$	$KrD^{35}Cl$
Ground state energies/cm^{-1}		
Zeroth-order	-157.005	-167.719
Second-order non-adiabatic	-0.440	-0.319
Third-order non-adiabatic	0.014	0.019
Total	-157.431	-168.019
Rotational constants/MHz		
Zeroth-order	1200.5935	1187.2463
Non-adiabatic	3.3539	2.6363
Third-order non-adiabatic	-0.1663	-0.1503
Coriolis correction	-3.1109	-7.1564
Non-adiabatic Coriolis	-0.0509	-0.0636
Total	1200.6193	1182.5121
Centrifugal distortion constant/kHz		
Zeroth-order	7.3379	6.6700
Coriolis correction	-0.0226	-0.1276
Total	7.3153	6.5424
Expectation values of P_2:		
Zeroth-order	0.43185	0.60215
First-order non-adiabatic	0.00349	0.00473
Second-order non-adiabatic	-0.00350	-0.00284
Coriolis - C21 correction	0.00026	0.00041
Total	0.43211	0.60445
Zeroth-order P_1:	0.73124	0.83992
Centrifugal distortion of P_2/ppm		
Zeroth-order	9.53	6.01
Non-adiabatic	-0.45	-1.17
Coriolis	1.99	3.65
Total	11.07	8.50

3. KrHCl: 4-angle potential surface parameters

	5 parameter fit	(1) [1]	(2) [1]	(3) [1]
ε/cm^{-1} [3]	224.22(45)	224.04(53)	214.28(66)	234.04(57)
ε/cm^{-1} [4]	160.16(1.18)	159.38(61)	149.65(78)	169.30(62)
ε/cm^{-1} [5]	142.72	143.43	133.17	153.51
$R_e/Å$ [3]	$4.085_9(3)$	$4.086_4(3)$	$4.084_7(4)$	$4.088_0(3)$
$R_e/Å$ [6]	$3.978_6(5)$	$3.978_2(3)$	$3.974_8(6)$	$3.981_6(3)$
M [3]	13.25(32)	13.24(25)	13.98(44)	12.60(23)
M [6]	{13.25(32)}	13.52(66)	14.76(1.08)	12.43(63)
γ	10.0	10.0	10.0	10.0
χ^2	4.08	3.80	4.05	3.83
$\varepsilon_{iso}/cm^{-1}$	155.0	155.0	145.0	165.0
$\Delta R/Å$ [2]	0.107(6)	0.108(5)	0.110(7)	0.106(4)

[1] 6 parameter least-squares fits (1,2,3) varying the well depth.
[2] $\Delta R = R_e(\theta = 0°) - R_e(\theta = 60°)$.
[3] for $\theta = 0°$.
[4] for $\theta = 60°$.
[5] for $\theta = 120°$, $180°$.
[6] for $\theta = 60°$, $120°$, $180°$.

4. Matrix elements for diatom-diatom systems

(i) The basic matrix element for the diatom-diatom program takes the form

$$\langle jm|C_{kq}|j'm'\rangle = (-1)^m \left[(2j+1)(2j'+1)\right]^{\frac{1}{2}} \begin{pmatrix} j & k & j' \\ 0 & 0 & 0 \end{pmatrix} \begin{pmatrix} j & k & j' \\ -m & q & m' \end{pmatrix} \qquad \text{(D4.1)}$$

where $|jm\rangle$ is a spherical harmonic. Also

$$j_z|jm\rangle = m|jm\rangle \qquad \text{(D4.2)}$$

and

$$j_\pm|jm\rangle = \left[j(j+1) - m(m\pm1)\right]^{\frac{1}{2}} |jm\pm1\rangle \qquad \text{(D4.3)}$$

(ii) The potential function for $(HF)_2$ takes the form (chapter 7, ref. 12)

$$V_{el} = \frac{q_1 q_2}{R} + \frac{q_1 \mu_2}{R^2} C_{10}(2) - \frac{q_2 \mu_1}{R^2} C_{10}(1) + ... \qquad (D4.4)$$

and so defining $q_1 q_2 / R_{ref} = MNMN$, where q is a monopole, $q_1 \mu_2 / (R_{ref})^2 = MNDP$, a monopole - dipole type term etc., then the potential function may be written

$$\begin{aligned}
V = {} & MNMN - MNDP0\,[C_{10}(1) - C_{10}(2)] \\
& - 2DPDP0\,[C_{10}(1)C_{10}(2)] \\
& - DPDP1\,[C_{11}(1)C_{1-1}(2) + C_{1-1}(1)C_{11}(2)] \\
& + 3DPQD0\,[C_{20}(1)C_{10}(2) - C_{10}(1)C_{20}(2)] \\
& + \sqrt{3}DPQD1\,[\{C_{21}(1)C_{1-1}(2) + C_{2-1}(1)C_{11}(2)\} \\
& \qquad - \{C_{11}(1)C_{2-1}(2) + C_{1-1}(1)C_{21}(2)\}] \\
& + 6QDQD0\,[C_{20}(1)C_{20}(2)] \\
& + 4QDQD1\,[C_{21}(1)C_{2-1}(2) + C_{2-1}(1)C_{21}(2)] \\
& + QDQD2\,[C_{22}(1)C_{2-2}(2) + C_{2-2}(1)C_{22}(2)] \\
& - 4DPOC0\,[C_{30}(1)C_{10}(2) + C_{10}(1)C_{30}(2)] \\
& - \sqrt{6}DPOC1\,[\{C_{31}(1)C_{1-1}(2) + C_{3-1}(1)C_{11}(2)\} \\
& \qquad + \{C_{11}(1)C_{3-1}(2) + C_{1-1}(1)C_{31}(2)\}] \qquad (D4.5)
\end{aligned}$$

where $C_{kq}(1) \equiv C_{kq}(\theta_1 \phi_1)$ etc., and R_{ref} is the reference distance of 2.79 Å.

(iii) Alexander writes his potential function as a triple sum over spherical harmonics to facilitate semiclassical scattering calculations (chapter 7, ref. 66)

$$V(R) = \sum_{l_1 l_2 l} A_{l_1 l_2 l}(R) \sum_{m} \langle l_1 m_1 l_2 m_2 | lm \rangle\, Y_{l_1 m_1} Y_{l_2 m_2} Y^*_{lm} \qquad (D4.6)$$

$$= \sum_{l_1 l_2 l} A_{l_1 l_2 l}(R) \sum_{k_1 k_2} \langle l_1 k_1 l_2 k_2 | l0 \rangle\, Y_{l_1 k_1} Y_{l_2 k_2} \left[\frac{2l+1}{4\pi} \right]^{\frac{1}{2}} \qquad (D4.7)$$

$$= \sum_{l_1 l_2 l} A_{l_1 l_2 l}(R) \sum_{k} (-1)^{l_1-l_2} \frac{(2l+1)}{(4\pi)^{\frac{1}{2}}} \begin{pmatrix} l_1 & l_2 & l \\ k & -k & 0 \end{pmatrix} Y_{l_1 k} Y_{l_2 -k} \qquad \text{(D4.8)}$$

$$= \sum_{l_1 l_2 l} A_{l_1 l_2 l}(R) \sum_{k} \frac{(2l+1)}{(4\pi)^{\frac{3}{2}}} \left\{(2l_1+1)(2l_2+1)\right\}^{\frac{1}{2}} (-1)^{l_1-l_2} \begin{pmatrix} l_1 & l_2 & l \\ k & -k & 0 \end{pmatrix}$$

$$\times C_{l_1 k} C_{l_2 -k} \qquad \text{(D4.9)}$$

since chapter 7 uses the expansion

$$V(R) = \sum_{l_1 l_2 k} V_{l_1 l_2 k} C_{l_1 k} C_{l_2 -k} \qquad \text{(D4.10)}$$

then V and A can be related by the equation

$$V_{l_1 l_2 k} = (-1)^{l_1-l_2} \sum_{l} \frac{\left\{(2l_1+1)(2l_2+1)\right\}^{\frac{1}{2}}}{(4\pi)^{\frac{3}{2}}} (2l+1) \begin{pmatrix} l_1 & l_2 & l \\ k & -k & 0 \end{pmatrix} A_{l_1 l_2 l} \qquad \text{(D4.11)}$$

and the values of $V_{l_1 l_2 k}$ may then be calculated.

Reference to Appendix D

1. D.M. Brink and G.R. Satchler, Angular Momentum, (OUP, Oxford, 1968); A.R. Edmonds, Angular Momentum in Quantum Mechanics, (Princeton Univ. Press, 1957).